Erasmus MC
Universitair Medisch Centrum Rotterdam

Thoraxcentre

The 22nd European Symposium on Ultrasound Contrast Imaging

- An ICUS Conference -

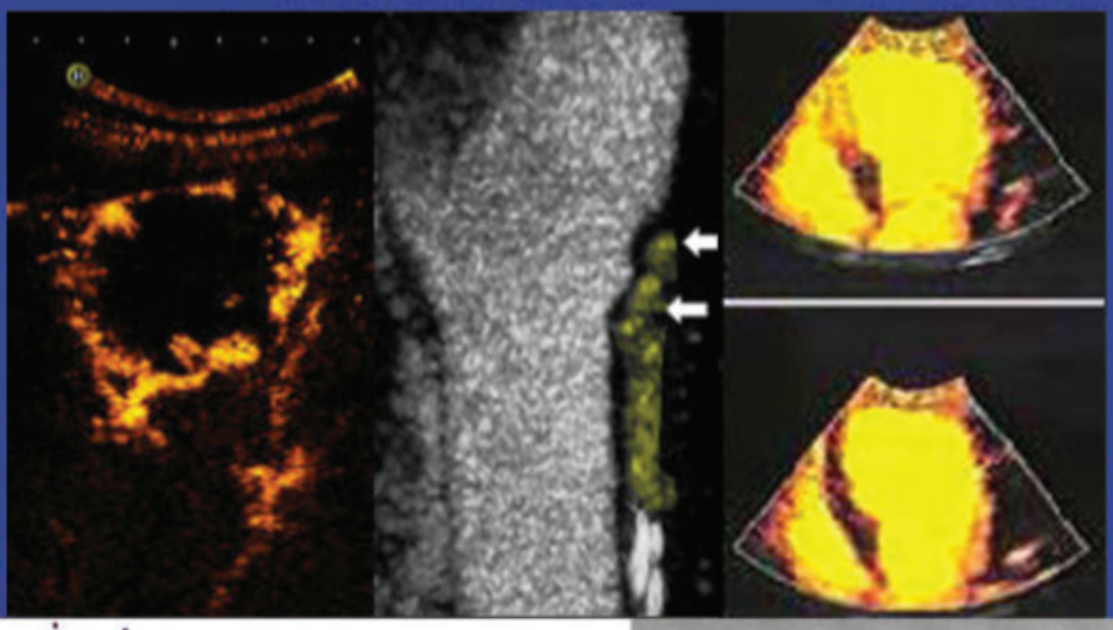

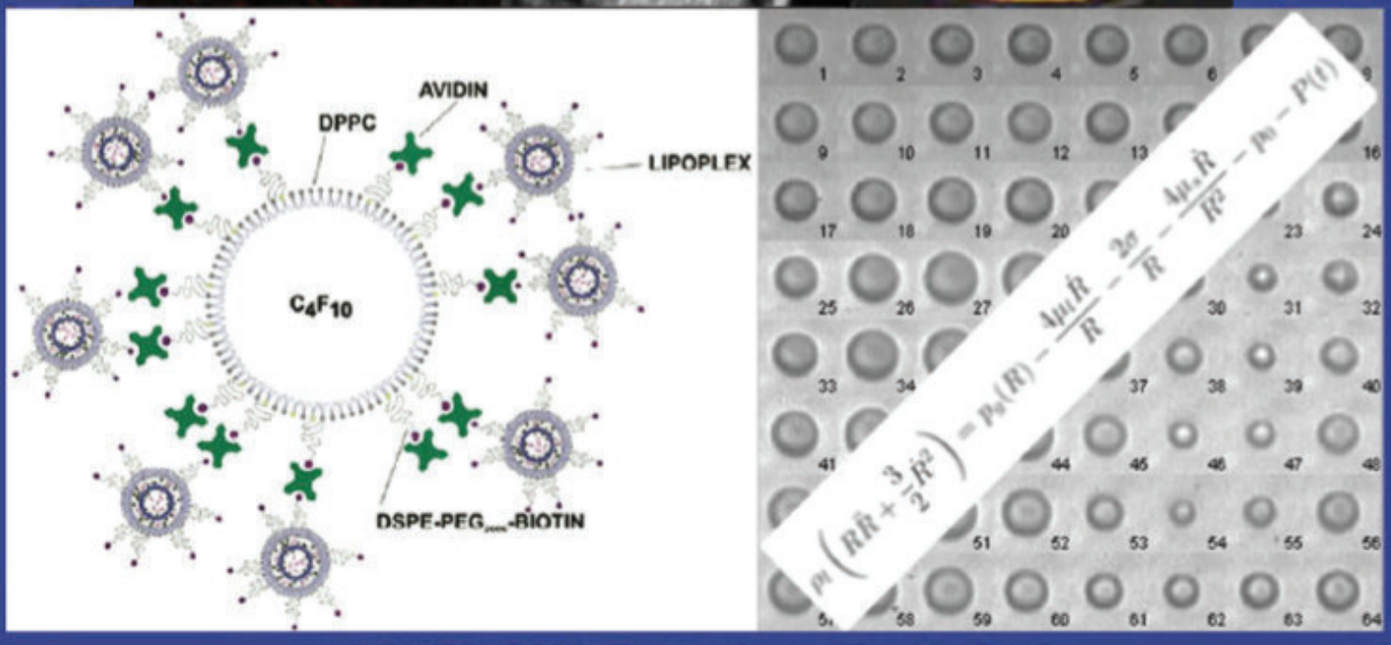

Abstract book

19-20 January 2017, Rotterdam, The Netherlands

Organised by Nico de Jong, Folkert ten Cate, Rik Vos, Klazina Kooiman, and Arend Schinkel

Erasmus MC Rotterdam

22nd EUROPEAN SYMPOSIUM ON ULTRASOUND CONTRAST IMAGING
19-20 JANUARY 2017, Rotterdam, The Netherlands

WEDNESDAY, 18 January 2017

13.30 PhD Defense (Erasmus MC) Tom van Rooij
"Ultrasound contrast agents for imaging and therapy"

18.00 – 20.00 Registration - Welcome Drinks [1st floor, Hilton Rotterdam]

THURSDAY, 19 January 2017

Oral program

08.00 – 09.00 Registration

09.00 – 09.10 Introduction and opening ..... *Eleanor Stride*

09.10 – 10.40 THERAPEUTIC CLINICAL TRIALS ..... *Chairpersons: Folkert ten Cate and Flemming Forsberg*

10.40 – 11.10 Intermission

11.10 – 12.40 UPCOMING CHALLENGES ..... *chairpersons: Peter Burns and Klazina Kooiman*

12.40 – 13.45 LUNCH

13.45 – 14.15 Dutch Heart Foundation lecture ..... *Chairperson: Francois Tranquart*

14.15 – 15.45 THERAPEUTICS / THERANOSTICS ..... *Chairpersons: Ine Lentacker and Arend Schinkel*

15.45 – 16.15 Intermission

16.15 – 17.45 CLINICAL CEUS ..... *Chairpersons: Steve Feinstein and Mike Averkiou*

18.30 – 22.30 EVENING PROGRAM (Incl. Dinner buffet)

22nd EUROPEAN SYMPOSIUM ON ULTRASOUND CONTRAST IMAGING
19-20 JANUARY 2017, Rotterdam, The Netherlands

FRIDAY, 20 January 2017

07.30 – 08.00 Registration

Poster sessions

22nd EUROPEAN SYMPOSIUM ON ULTRASOUND CONTRAST IMAGING
19-20 JANUARY 2017, Rotterdam, The Netherlands

FRIDAY, 20 January 2017

Oral program

Organised by: Nico de Jong, Folkert ten Cate, Rik Vos, Klazina Kooiman and Arend Schinkel

Scientific board: Mike Averkiou, Paolo Colonna, David Cosgrove, Edward Leen and Eleanor Stride

Thursday, 19 January 2017

Evening Program

"Euromast"

Parkhaven 20, Rotterdam

Buffet: around 19:30

Coaches will be leaving from Hilton at 18:30 and will be back in Hilton around 22:30

High Mechanical Index Impulses from a Diagnostic Ultrasound Transducer in Acute ST segment Elevation Myocardial Infarction: Initial Results and Future Applications

Thomas R. Porter, Wilson Mathias Jr, Jeane M Tsutsui, Bruno G Tavares, Miguel O Aguiar Jr, Mucio T Oliveira, Alexandre Soeiro, Pedro A Lemos, Jose Ramires, Roberto Kalil Filho, Sebastiaan T. Roos, Lynda JM Juffermans, Niels van Royen, Albert C. van Rossum, Feng Xie, Yolande Appelman, Otto Kamp and the Microvascular Recovery in Acute Myocardial Infarction (MRUSMI) Working Group

Introduction

In patients with acute ST segment elevation myocardial infarction (STEMI), animal studies have demonstrated both a beneficial effect but also a dose response curve to diagnostic ultrasound (DUS) induced microbubble cavitation in acute coronary thrombosis. Preliminary clinical trials have demonstrated that high mechanical index (MI) impulses from a diagnostic ultrasound (DUS) transducer during a commercially available ultrasound contrast microbubble (MB) infusion have been shown to improve microvascular flow within the risk area, when administered before and immediately after emergent percutaneous coronary intervention (PCI).

Objective

This abstract reviews the results of ongoing clinical trials from the MRUSMI investigators in 2016 that have investigated the effect of DUS and MB on epicardial flow, microvascular flow, and adverse left ventricular remodeling (ALVR) at follow up.

Methods

A total of 37 patients with their first acute STEMI (24 left anterior descending, five circumflex, and eight right coronary artery) have been randomized in the Sao Paulo study group. These patients were randomized to randomized to receive an intravenous microbubble (Definity) infusion and either intermittent high MI (1.2) impulses at a short pulse duration (3-4 usec) when MB were visualized within the risk area (high MI + PCI) or low MI imaging alone (PCI only). Treatments were administered just prior to PCI as well for 30 additional minutes following PCI. Recanalization rates prior to PCI and TIMI flow following PCI were compared. Microvascular flow (as assessed by low MI imaging and MB at hospital discharge and one month follow up) was also compared. ALVR was defined as a >20% increase in left ventricular end diastolic volume at one month follow up. In the Netherlands group, six patients have received high MI impulses at a longer pulse duration (20 usec) during the same intravenous Definity infusion.

Results

In the Sao Paulo study, door to dilation times were not different between groups. However, epicardial recanalization rates prior to PCI were higher in the high MI + PCI group (58% versus 11%; p=0.005). ALVR at one month follow up was seen in nine of the patients treated with PCI only, but only three of patients treated with high MI + PCI (p = 0.035). In the Netherlands sub-group, three of six patients receiving the longer 20 usec pulse duration high MI impulse experienced coronary vasoconstriction of the culprit artery,

unresponsive to nitroglycerin. These vasoconstrictor responses in response to high MI 20 usec pulse duration impulses during a Definity microbubble infusion have been reproduced in a large animal coronary artery balloon injury model only when arterial thrombus is also present at the balloon injury site.

Conclusions

The addition of high MI short pulse duration impulses from a DUS transducer improves microvascular recovery in acute STEMI patients treated with PCI, and prevents ALVR at follow up. Longer pulse duration high MI impulses in this setting appear to also induce epicardial coronary vasoconstriction in the regions where acute thrombi are still present.

Ultrasound and microbubbles for anticancer drug delivery: from physics to clinics

A. Bouakaz,[1] J.M. Escoffre,[1] A. Novell[1] and T. Lecomte[2]

[1]Inserm UMR 930, Imagerie et Cerveau, Université François Rabelais, Tours, FRANCE
[2]Service d'Hépato-gastroentérologie et de Cancérologie Digestive, CHRU Trousseau, Tours, FRANCE

Ultrasound (US) in combination with gaseous microbubbles has come into focus as a potential new drug delivery technology [1]. Indeed, beyond their exploitation for diagnosis, microbubbles and US, today represent an emerging approach for localized drug delivery. Recent research shows that under the action of US waves, microbubbles transiently perforate biological barriers (e.g . cell membrane, endothelial barrier) thus leading to the uptake and enhanced accumulation of drugs in the targeted region [2]. In this way, the bioavailability of therapeutic agents is site-specifically augmented only in the zone where the US waves are focused. Commonly referred to as sonoporation, it offers real promises as a drug delivery tool with potential of alleviating the limitations encountered by traditionally available therapeutic arsenal.

Sonoporation can indeed potentiate the extravasation of a wide range of therapeutic molecules including chemotherapeutic agents, nucleic acids (e.g. siRNA, miRNA, mRNA, oligonucleotides, plasmid DNA), therapeutic peptides, and monoclonal antibodies. Preclinical studies demonstrating proof of concept have been shown in various organs as well as clinical indications in a number of small animal models including both ectopic and few orthotopic models.

Nevertheless, a number of evaluation and clinical validation issues need to be tackled including standardization of US parameters, selection of appropriate microbubbles, identification of optimal clinical indications and drugs before further translation to the clinic.

To facilitate US and microbubbles drug delivery to the clinic, a number of questions need to be addressed such as: which organ should be targeted? Which drugs are suitable for sonoporation drug delivery? If cancer is the clinical target, which lesions (solid tumors or metastases) should be considered? Since microbubbles need to be localized within the target organ or zone for better drug extravasation, should considerations concerning the perfusion of the target lesion take precedence? What US parameters (frequency, pressure/MI, exposure time and duty cycle) should be used to activate the microbubbles to induce drug uptake? A number of studies show that sonoporation efficiency is strongly correlated with the concentration of microbubbles in the target zone, suggesting that UCA concentration is a crucial sonoporation parameter. Accordingly, what microbubble concentrations should be used? Similarly, the appropriate method of microbubble administration, that is, bolus injection or continuous infusion delivered intra-arterially or intravenously needs careful consideration. Similarly, the treatment schedule is of significant importance, since administration of microbubbles and drugs should be performed in a prescribed manner and US insonation timing (duty cycle) should be synchronized to coincide with the arrival of elevated microbubble concentrations in the targeted regions. The type of microbubbles employed is also of significant importance because their response to US activation depends on their physical properties. Pragmatically, it should be easier and faster to evaluate drug delivery using clinically available microbubbles, as that will facilitate quick translation to clinic. Whether US scanners operated in specific modes (such as Doppler mode) can deliver US sequences capable of inducing drug delivery; are just some of the questions that also need addressing for the effective translation of this therapeutic technology to the clinic.

In this talk, we will discuss how this therapeutic approach developed from basic equation developments (Rayleigh-Plesset) to preclinical evaluation and to clinical proof of concept. We will also review on going and future clinical trials in the field of drug delivery using sonoporation.

1. *Sennoga CA, Kanbar E, Auboire L, Dujardin PA, Fouan D, Escoffre JM, Bouakaz A (2016) Microbubble-mediated ultrasound drug delivery and therapeutic monitoring. Expert Opin. Drug. Deliv., in press.*
2. *Bouakaz A, Zeghimi A, Doinikov AA (2016) Sonoporation: Concept and Mechanisms. Adv. Exp. Med. Biol., 880:175-89.*

Neurorestoration of the nigrostriatal pathway through multiple treatments with FUS-facilitated brain drug delivery

***Elisa E. Konofagou*[1,2]**

[1]*Department of Biomedical Engineering, Columbia University, New York, NY*
[2]*Department of Radiology, Columbia University, New York, NY*
ek2191@columbia.edu

Current treatments of neurological and neurodegenerative diseases are limited due to the lack of a truly non-invasive, transient, and regionally selective brain drug delivery method. The brain is particularly difficult to deliver drugs to because of the blood-brain barrier (BBB). The impermeability of the BBB is due to the tight junctions connecting adjacent endothelial cells and highly regulatory transport systems of the endothelial cell membranes. The main function of the BBB is ion and volume regulation to ensure conditions necessary for proper synaptic and axonal signaling. However, the same permeability properties that keep the brain healthy also constitute the cause of the tremendous obstacles posed in its pharmacological treatment. The BBB prevents most neurologically active drugs from entering the brain and, as a result, has been isolated as the rate-limiting factor in brain drug delivery. Until a solution to the trans-BBB delivery problem is found, treatments of neurological diseases will remain impeded. In this presentation, neuroprotection and neurorestoration of the dopaminergic pathway will be shown in a Parkinsonian mouse model. We have found that FUS-induced BBB opening allows the delivery of neurotrophic factors and adeno-associated viruses that express those factors as well as protection (before the MPTP toxin is administered) and restoration (after the toxin is administered) of the dopaminergic neurons. Gene delivery induced neuroprotection in the dopaminergic pathway. In protein delivery, comparable findings in dendritic density in the substantia nigra region of the mouse brain was found between a single and a triple delivery regimen. However, in the caudate putamen region, the triple regimen was found to significantly increase the terminal density which indicated restoration of the neuronal processes through collateral sprouting. This finding is in accordance with prior reports on neurotrophic proteins restoring impaired neurons. These findings indicate the therapeutic effect that FUS could induce in dopaminergic neurons through the enhanced drug delivery dose.

Keywords- blood-brain barrier, drug delivery, focused ultrasound, mechanism,microbubble

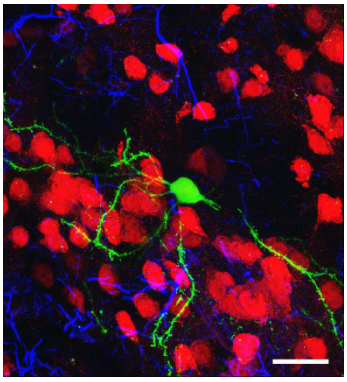

Neuronal GFP expression using gene delivery through the blood-brain barrier

Focused ultrasound enhanced delivery of therapeutic agents into the brain - A review of progress towards clinic use

K. Hynynen

Department of Medical Biophysics and Institute of Biomaterials and Biomedical Engineering, University of Toronto and Physical Sciences Platform, Sunnybrook Research Institute and Physical Sciences Platform, Toronto, Ontario, Canada

Microbubbles can concentrate ultrasound energy at macroscopic levels. In vivo experiments have shown that intravascular bubbles can enhance vascular permeability and increase local diffusion of drugs from blood to tissue. This has been shown to be important especially in brain where the Blood-Brain barrier prevents the diffusion of most molecules from the blood into the tissue. The locations of microbubbles can be mapped using acoustic methods by using receiver arrays to capture the ultrasound signals scattered. The spectral information of these scattered signals can be used to quantify and control the exposure such that desired bio-effects are achieved. In this talk we review our progress towards clinical treatments of brain tumors and Alzheimer`s Disease and discuss the future clinical potential of the proposed methods.

Development of an Implantable Ultrasonic Device for Enhancing the Delivery of Chemotherapy to the Brain

Lafon C,[1,5] Canney M,[2] Beccaria K,[3] Horodyckid C,[3] Vignot A,[2] Chapelon JY,[1] Idbaih A,[3] Carpentier A[3,4]

[1]LabTAU, INSERM, University of Lyon, France
[2]Carthera SAS, Lyon, France
[3]Assistance Publique Hôpitaux de Paris, Paris, France
[4]Sorbonne University, Paris 6, France
[5]University of Virginia, Charlottesville, VA

Treating brain tumors remains a serious challenge. Depending on tumor type, stage or location, treatments combining surgery, radiotherapy and chemotherapy are proposed. However, the blood brain barrier (BBB) impedes the intracerebral diffusion of drugs and limits the effectiveness of systemically administered chemotherapy. It has been shown in preclinical studies that pulsed ultrasound, coupled with injection of microbubbles, can be an effective method for enhancing the delivery of drugs to the brain.

To enhance the delivery of chemotherapy to patients with brain tumors, a practical ultrasonic approach was developed. It consisted of implanting an ultrasound device in the skull and opening the BBB just before each chemotherapy session. Thus, the ultrasonic beam was not distorted or attenuated when propagating through the skull. Activation of the device for BBB disruption was a simple procedure that was performed in less than 15 minutes. Real-time MRI monitoring, head shaving, and placement of stereotaxic frames were not required, making the procedure much simpler than that required for transcranial ultrasound devices.

The ultrasound device was unfocused and operated at a frequency of 1MHz. After injection of an ultrasound contrast agent, an in situ acoustic pressure of 0.5-1.1 MPa was delivered for 120-150 s to transiently open the BBB. In pre-clinical studies, significant intracerebral enhanced diffusion of various drugs was observed in the sonicated region of rabbits and non-human primates. The feasibility of repeated, safe opening of the BBB with this device was also demonstrated in non human primates. The device was left implanted for three months and BBB opening was performed every 15 days without observing any adverse side effects.

With these supportive preclinical data, a phase 1 clinical trial was conducted on patients with recurrent glioblastoma. Patients underwent ultrasound sonications for disrupting the BBB and carboplatin-based chemotherapy on a monthly basis. BBB disruption was assessed immediately after sonication using dynamic contrast T1-weighted MRI. Fifteen patients were included in this ultrasound dose escalation study. BBB disruption was observed in 28 out of 41 ultrasound treatments, with the probability of opening increasing to 100% at the highest acoustic pressure levels (1.1 MPa). The procedure is rapid (<15 min) and safe. No acute vascular or inflammatory incidents were observed in post-sonication MRI. Interestingly, no tumor recurrence occurred at 4 months on a patient who had repeated opening of the BBB at the highest acoustic pressure levels. This first clinical trial paves the way for new therapeutic strategies for brain tumors.

Current Clinical Trials: what is needed to be successful?

François Tranquart

Advice-Us Consulting, France

The use of an ultrasound contrast agent together with an ultrasound equipment has opened a wide domain of research from the simple use of these agents as image enhancers to innovative domains of therapy mediated by these contrast agents and ultrasound molecular imaging. This is now time for conducting several clinical trials to demonstrate the clinical benefit in terms of efficacy and safety before a routine adoption and an approval by health authorities.

The combination of ultrasound waves (a medical device) together with an ultrasound contrast agent (a drug) induces specific considerations when conducting the required clinical trials. Typically, when the objective is to get an approval of this drug, each pharma company is following a path which has been clearly defined for any drug from a Phase I to a Phase III addressing the specific requirements for demonstrating the efficacy and the safety of the selected agent. This has been done by all companies for the four agents currently approved and marketed. This is completed by several Phase IV or post-marketing studies to collect additional data for a specific population or for an extended indication. As such the situation is quite simple with clear milestones and endpoints.

The situation is becoming more complex when dealing with molecular imaging and further with therapeutic treatment. For the specific case of a molecular imaging agent, following extensive pre-clinical validation according to the guidelines, the underlying mechanism of interaction between the targeting moiety and the endothelium must be carefully explored to envision the binding mechanism of this agent in patients. The translation of animal results into clinics could not be straightforward requiring a specific validation in humans. It is well-known that the expression of some receptors could differ significantly between animals and patients. In that perspective, performing an exploratory phase in patients could satisfy the validation step by ensuring the possible detection of this agent in humans according to the receptor's expression. In some cases, the absence of animal model or the impossibility to use the selected ligand in animal models to the species specificity could require this clinical phase for agent validation. This exploratory phase, if positive, will precede the full clinical development as for therapeutic drugs. This means that assessing efficacy and safety during clinical trials cannot rely on a simple assessment of an improved detection or characterization of any lesion but should clarify extensively the underlying mechanism by providing evidence on the selectivity and accuracy of an increased presence of the agent in certain location. As such, the design of the clinical trials should integrate these objectives in the definition of the endpoints and a specific attention should be paid to the three pillar proofs i.e. mechanism, principle and concept for an acceptation by health authorities.

To some extent, the story is about the same for any therapeutic therapy intent with additional complexities. Indeed, the objective is to use a microbubble together with an ultrasound equipment and sometimes another drug for an indication which is not covered by respective approval. Each element is used outside the approved indication (microbubble for therapy instead of imaging, ultrasound equipment with higher MI than clinically approved by FDA) and combined to deliver a local effect. Some key questions need to be addressed before engaging any company or academic group in a clinical trial: how to consider the selected bubble, as a drug or as a device? How to get authorisation for using an ultrasound equipment outside the currently approved specifications? How to combine a drug in this new setting? This means that, on top of a proof of efficacy (and safe use), there will be some regulatory hurdles to be considered seriously. The response is not so simple due to the ambiguity of the selected domain since the bubbles will act as a pure mechanical agent to facilitate the incorporation of a drug or to enlarge some lesions without any intrinsic drug effect. Even though many preclinical data tend to support a therapeutic effect of this interaction, the clinical translation requires some efforts for convincing first the authorities then pharma companies about the effectiveness of this innovation. First of all is a proof of mechanism to clarify how it works then a proof of principle demonstrating a significant increase in the local delivery of the selected drug. This cannot be based simply on surrogate markers as the tumour response but on a direct measurement of the incorporation of the drug in selected tissues in comparison to non-treated areas. Do we have collected such evidence so far?

Therefore, beyond the unrivalled accuracy of contrast-enhanced ultrasound imaging in so many indications, the current developments in molecular imaging and more specifically for a therapeutic treatment call for a well-defined clinical strategy for demonstrating the efficacy and safety of these innovative methods. At the moment, despite promising pre-clinical results, the lack of obvious proof of mechanism and proof of principle represents a limitation for considering a full clinical development of these techniques. This will be the focus of the planned first-in-man studies before considering a more conventional clinical development. A close interaction between the various stakeholders including health authorities may greatly help in the way of a successful development and ultimately approval of these new techniques.

Molecular Engineering of Microbubble Resonance

Mark Borden

University of Colorado Boulder

Is it possible to engineer the resonance frequency of a microbubble by manipulating the lipid shell? In this talk, a recent study will be discussed that attempts to answer this question for very small-amplitude oscillations. A molecular model for the lipid shell will be introduced that provides calculation of the shell elasticity directly from first-principle intermolecular pair potentials. This elasticity is strictly valid for very small intermolecular displacements, and was tested experimentally for microbubbles with different lipid shell compositions. Individual gold-nanoparticle-coated, plasmonic microbubbles of 2-6 μm radius were photothermally activated with a short laser pulse, and the subsequent nanometer-scale radial oscillations during ring-down were monitored by optical scatter. The method provided average dynamic response measurements of single microbubbles. Each microbubble was modeled as an underdamped, linear oscillator to determine the damping ratio and eigenfrequency, and thus the lipid monolayer viscosity and elasticity. As predicted by the model, a significant increase in surface elasticity was observed for lipid acyl chain length of 16 to 20 carbons. The surface viscosity was found to be equivalent for these lipid shells. We also observed an anomalous decrease in elasticity and increase in viscosity when increasing the acyl chain length from 20 to 22 carbons, indicating that microstructural effects may be important for such small displacements. The talk will conclude with insights gleaned from the molecular model on resonance effects for larger amplitude oscillations.

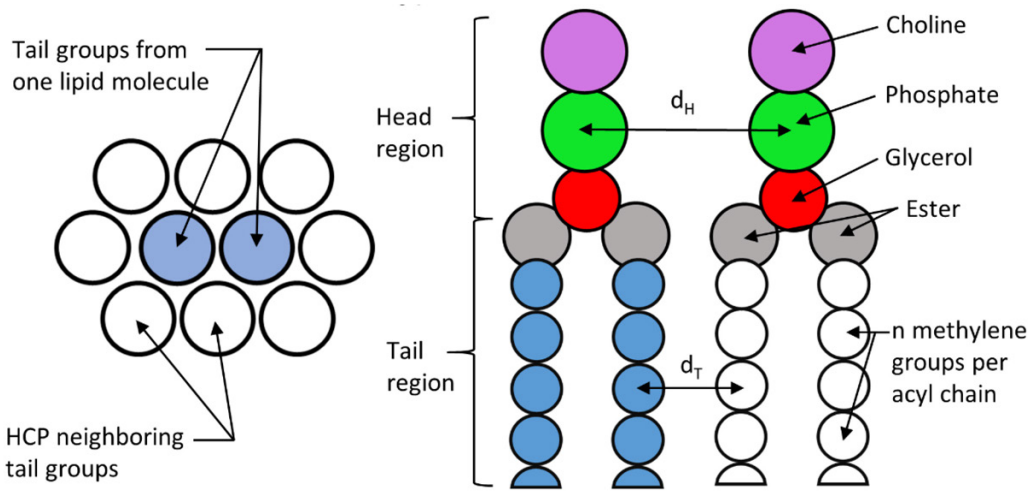

Nanobubbles for Ultrasound Contrast Imaging: The Final Frontier

Katsuro Tachibana

Department of Anatomy, Fukuoka University School of Medicine, Fukuoka, Japan

Background and Aim

Ultrasound contrast agents (UCA) have been used in clinical diagnosis for several decades. UCA usually is a microbubble with shells composed of lipids, proteins, sugar or polymers (1-10μm). Microbubbles also plays an important role for sonoporation (1, 2).

In this study, we devised a revolutionary method to produce nano-sized bubbles (100-700nm) from biocompatible liquids such as saline, distilled water and various injectable drugs. Furthermore, we developed a new system to accurately measure the size distribution, concentration and mass of the nanobubbles. Based on these vast amounts of information, several types of nanobubble were evaluated for possible use as a new ultrasound contrast agent.

Materials and Methods

NanoSight (LM-10, Malvern Instruments Ltd, UK) captures a video file of laser scattering images of bubbles, moving under Brownian motion. The Nanoparticle Tracking Analysis (NTA) software tracked the nanobubbles individually and using the Stokes Einstein equation calculated their hydrodynamic diameters.

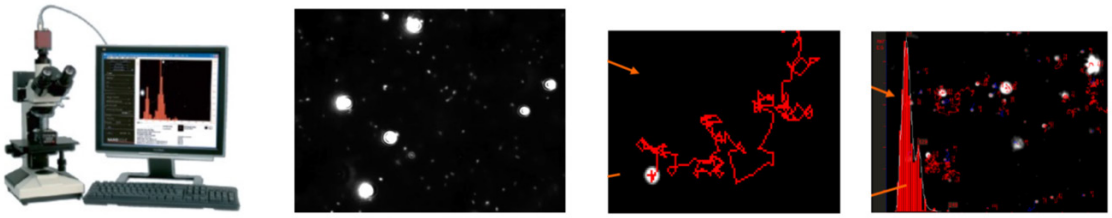

Particle mass was measured by Archimedes (Malvern Instruments Ltd, UK) which is a high-performance system based on the resonant mass measurement method (figure below). High frequency ultrasound imaging system (Prospect, S-Sharp Corporation, Taiwan) was used to evaluate visibility of nanobubbles in a flow model phantom.

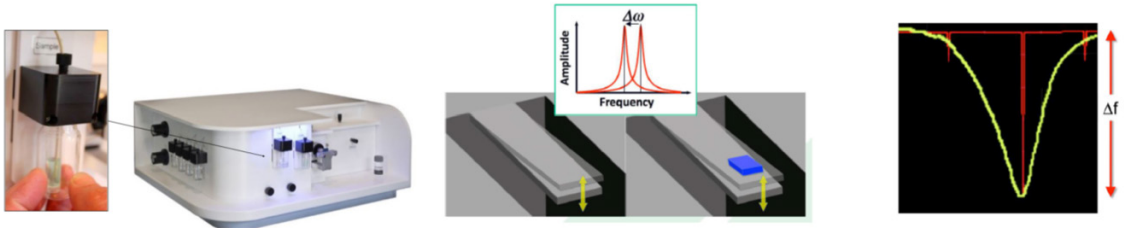

Nanobubbles were produced in customized 2 ml air tight, robust plastic containers which were filled by various liquids/gas and shaken at very high velocity (6500rpm) for 30 second duration under pressurized environment. The samples were later centrifuged to eliminate micro-sized bubbles before nanobubble size and mass measurements.

Results

The two figures below show the size distribution and mass measurent of 0.06% Human Albumin based nanobubbles produced by the above method.

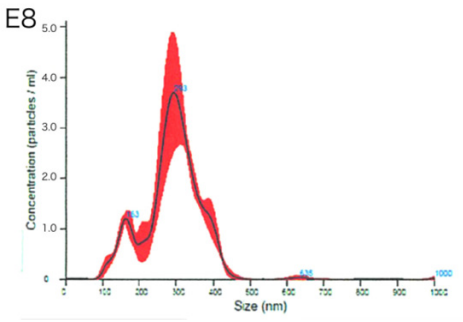

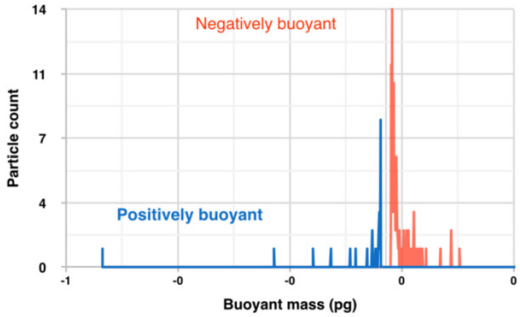

Observation by ultrasound imaging (40MHz) showed nanobubbles in the artificial flow model. Below figure shows movies before and after nanobubble administration.

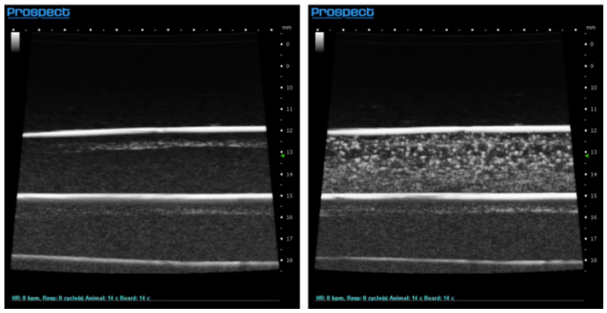

Conclusion

Conventional nanobubble production uses a system with pressurized water jetting through a nozzle which requires liters of circulating liquid. Whereas our new method needs only 2ml of liquid per sample which permits us to evaluate hundreds of type of materials that may be used as nanobubble UCA. In addition, this could only be fully realized with stable nanobubble measurement information feedback. Lastly, nanobubbles have the potential to become a drug delivery or sonoporation modality, opening up a whole new field in nano-level “Theranostics” in medicine.

References

1. *Induction of cell-membrane porosity by ultrasound, K Tachibana, T Uchida, et al, The Lancet 1999, 353 (9162), 1409*
2. *Albumin microbubble echo-contrast material as an enhancer for ultrasound accelerated thrombolysis, K Tachibana, S Tachibana, Circulation 1995, 92 (5), 1148-1150*

In vitro and *in vivo* evaluation of sub-micron phase-shift droplets: Portrait of a complex agent

Paul S. Sheeran,[1,2] Kimoon Yoo,[2] Wesley Walker,[2] Ross Williams,[2] Charles Tremblay-Darveau,[1,2] and Peter N. Burns[1,2]

[1]Department of Medical Biophysics, University of Toronto, Toronto, Ontario, Canada
[2]Sunnybrook Research Institute, Toronto, Ontario, Canada

Introduction

Alongside the clinical successes of contrast-enhanced ultrasound have come significant advances in the development of experimental contrast agents that overcome some of the inherent limitations of microbubbles. One of the most commonly researched microbubble alternatives is the phase-shift perfluorocarbon droplet. In its liquid state, the phase-shift droplet is designed to circulate in the bloodstream as a bubble precursor until a high-intensity acoustic field initiates vaporization and the agent expands to form a vapour bubble approximately 5-6 times the droplet diameter. Thus, the phase-shift droplet combines the high echogenicity of a microbubble with the prospect of spatiotemporal control over the change in size, density, and compressibility – creating bubbles 'on-demand'.

A number of tradeoffs are involved in the design of droplets that impact *in vivo* efficacy[1,2]. While these tradeoffs have produced a wealth of research on vaporization physics and characterizations of the vaporization threshold over a wide parameter space, few studies have explored the role of droplet encapsulation on *in vivo* circulatory kinetics. With the goal of developing insight for *in vivo* use, we here survey our recent work to develop long-circulating phase-shift droplets for drug delivery applications by optimizing droplet encapsulation and developing practical activation parameters to maximize contrast production at human imaging frequencies.

Methods

Phospholipid-encapsulated droplets with decafluorobutane cores were produced according to previously developed protocols[3]. Previous studies have shown that longer acyl chain lengths can greatly improve droplet stabilization when subjected to repeated vaporization and condensation[4]. Here, we extend this concept by testing the role of acyl chain length on droplet dissolution rate and circulatory lifetime. Four different encapsulations were tested that span primary phospholipid chain length and encapsulations common to commercial microbubbles: (1) DPPC:DPPE-PEG5000, (2), DPPC:DPPA:DPPE-PEG5000, (3) DSPC:DPPE-PEG5000, and (4) DBPC:DPPE-PEG5000. Emulsion degradation (via droplet dissolution) was measured at physiologic temperature in a vessel flow phantom by periodically activating highly dilute droplets with a 7.5 MHz piston transducer. The decay in the bubble intensity produced by activation over time was measured by a co-aligned clinical linear array probe (Philips iU22, L9-3) in B-mode and analyzed offline. *In vivo* circulatory persistence was measured in the mouse kidney using a VisualSonics Vevo2100 with a 30 MHz imaging probe. Following bolus injection, droplets were activated every 10 minutes by increasing the B-mode imaging power on the scanner using a method previously described[3]. The images produced during these activation scans were filtered offline to isolate signals produced by droplet vaporization and the drop in signal resulting from agent decay and clearance was quantified. The encapsulation that performed best in these persistence experiments was then tested in the vessel flow phantom to determine optimal acoustic activation choices. Three piston transducers (2.25, 5, 7.5 MHz) were used to activate dilute droplet samples at physiological temperature in the

vessel at flow rates near 3 mm/s. Each sample was exposed to a range of pressures (0.5 – 5 MPa), pulse repetition periods (0.1 – 2 seconds), and pulse lengths (2, 5, 10 cycles). Contrast enhancement as a function of the vaporization parameters was measured with a co-aligned linear array probe (described above) and analyzed offline.

Results, and Discussion, and Conclusions

Changes in encapsulation produced relatively similar droplet size distributions and level of contrast enhancement *in vitro* and *in vivo*, but significantly different persistence properties (**Figure 1**) – with the most rigid phospholipid shell (DBPC:DPPE-PEG5000) providing a decay half-life as much as 30 times longer than the least rigid shell (DPPC:DPPE-PEG5000). Thus, encapsulations that are typically thought of as ideal for microbubble imaging (less rigid monolayers that respond to acoustic pulses more dynamically) have substantial drawbacks in use as droplet encapsulations with regard to dissolution rate. Future work on encapsulation may further improve circulatory stability to produce contrast agents that last for many hours in circulation, which is ideal for many therapeutic/theranostic applications.

As has been previously reported for other droplet formulations[5,6], vaporization thresholds decreased with increasing frequency between 2.25 and 7.5 MHz for the long-circulating DBPC-encapsulated droplets. At 5 and 7.5 MHz the activation threshold fell within the FDA output limits for diagnostic imaging, but at 2.25 MHz activation was not produced without exceeding these limits. At flow rates near 3 mm/s, very short pulse repetition periods at 2.25 MHz had the capability of almost completely destroying contrast from the previous pulse at the high pressures required for vaporization, but this effect was less substantial for 5 and 7.5 MHz due to lower peak pressures and narrower beam profiles. Increasing pulse length increased the probability of observing a vaporization event – lowering the threshold at each frequency by as much as 50 kPa when increasing from a 2 to 10 cycle activation pulse. However, the marginal decrease in the threshold came at the cost of lower mean enhancement and higher variation from pulse to pulse (**Figure 2**). This effect was highly significant for 7.5 MHz but less so at 2.25 MHz, even though the peak negative pressures required at 7.5 MHz were substantially lower in magnitude (and mechanical index) than those at 2.25 MHz. This suggests that bubble susceptibility to destruction from long vaporization pulses is likely a function of bubble resonance as the bubble grows through the pulsing period. Interestingly, the negative impacts of pulse repetition period seem to be dominant at lower frequencies, while the negative impacts of pulse length seem to be dominant at higher frequencies in the clinical imaging range. Thus, in developing practical activation parameters to maximize contrast enhancement from sub-micron droplets, several tradeoffs exist, two of which are common to the field, and one of which is not as obvious: 1) the desired activation depth in tissue must be balanced with the maximum regulatory outputs available (for activation with diagnostic scanners) and the improved activation at higher frequencies; 2) pulse repetition should be chosen carefully depending on flow rate, frequency, and beam width (F/#) to maximize bubble formation without destroying contrast from previous pulses; and 3) the improved vaporization probability with long pulses and at higher frequencies must be carefully balanced with disruption of bubbles from the same pulse if the bubble grows through resonant sizes coincident with the vaporization frequency.

These results highlight the promise but also the complexity of the phase-shift droplet as a contrast agent, and much work remains to improve ease of use to the point that it becomes a compelling clinical agent.

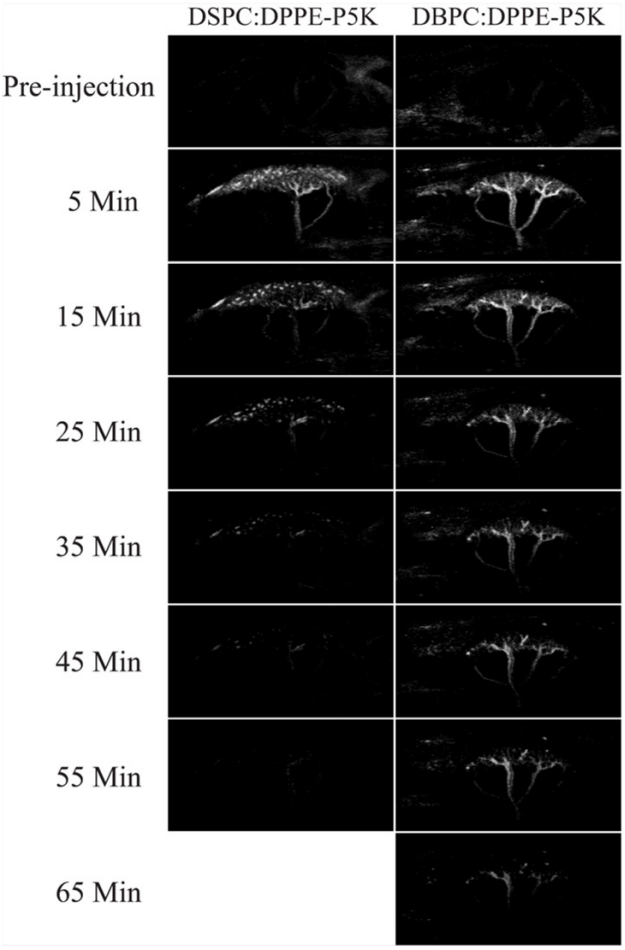

Figure 1. Post-processed B-mode images of droplet activation in the mouse kidney at 10 minute intervals. The change in activation over time depended strongly on the primary phospholipid used for encapsulation, with more rigid phospholipids providing circulatory half-lives on the order of 20 minutes.

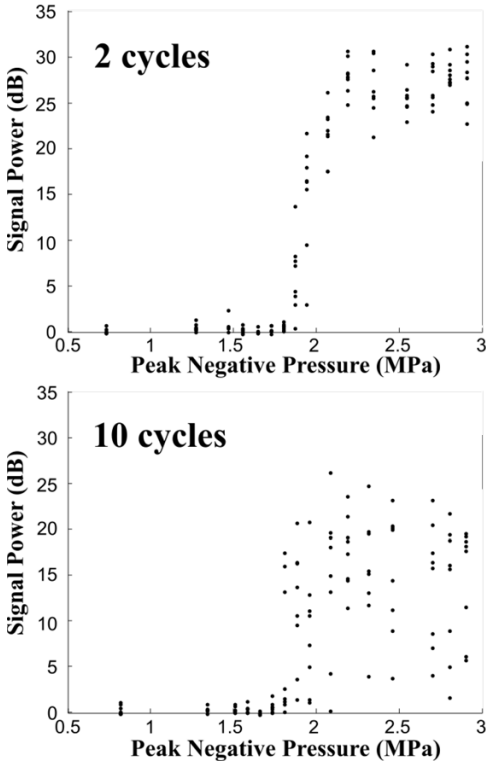

Figure 2. Droplet activation at 7.5 MHz in a vessel flow phantom produced signal enhancement on the order of 25 dB in B-mode as measured with an iU22 (L9-3 probe). Each point represents the signal enhancement resulting from a single pulse within the same sample (8 measurements at each pressure). Use of a longer activation pulse diminished the level of contrast remaining and significantly increased variability from pulse to pulse.

References

1. *Sheeran, P. S. & Dayton, P. A. Phase-change contrast agents for imaging and therapy. Curr. Pharm. Des.* ***18,*** *2152–2165 (2012).*
2. *Mountford, P. A. & Borden, M. A. On the thermodynamics and kinetics of superheated fluorocarbon phase-change agents. Adv. Colloid Interface Sci.* ***237,*** *15–27 (2016).*
3. *Sheeran, P. S. et al. Image-Guided Ultrasound Characterization of Volatile Sub-Micron Phase-Shift Droplets in the 20-40 MHz Frequency Range. Ultrasound Med. Biol.* ***42,*** *795–807 (2016).*
4. *Mountford, P. A., Smith, W. S. & Borden, M. A. Fluorocarbon Nanodrops as Acoustic Temperature Probes. Langmuir* ***31,*** *10656–10663 (2015).*
5. *Kripfgans, O. D., Fowlkes, J. B., Miller, D. L., Eldevik, O. P. & Carson, P. L. Acoustic droplet vaporization for therapeutic and diagnostic applications. Ultrasound Med Biol* ***26,*** *1177–1189 (2000).*
6. *Shpak, O. et al. Acoustic droplet vaporization is initiated by superharmonic focusing. Proc. Natl. Acad. Sci.* ***111,*** *1697–1702 (2014).*

Contrast Enhanced UltraSound IntraCardiac Echography (CEUS-ICE) with a 9-french intracardiac echographic probe

Ludwig Steffgen,[1,2] Hans Bosch,[3] Nico de Jong,[3] Hendrik Vos,[3] Tamas Szili Torok,[4] Daphne Merkus,[5] Maaike Visser-te Lintel Hekkert,[5] Ching Hua Chou,[2] Glen McLaughlin[2]

[1] *Trainings-Zentrum Ultraschall-Diagnostik LS GmbH, Mainleus, Germany*
[2] *Zonare Medical Systems, Mountain View, California, USA*
[3] *Biomedical Engineering, Thorax center, Erasmus MC, Rotterdam, the Netherlands*
[4] *Cardiology, Thorax center, Erasmus MC, Rotterdam, the Netherlands*
[5] *Experimental Cardiology, Thorax center, Erasmus MC, Rotterdam, the Netherlands*

Introduction

Intracardiac echography (ICE), in which an ultrasound catheter is inserted into the femoral vein and guided to the right atrium or ventricle, is used for visually guiding interventions such as closure of atrial septal defects, closure of the left atrial appendage, catheter-based aortic valve repair, and ablations around the atrioventricular node. Compared to conventional fluoroscopic guidance, it reduces the amount of radiation during intervention for both the patient and the professionals. Compared to transoesophageal echo (TEE) in which patients need to be under general anaesthesia, the need for only mild sedation for ICE-guided interventions reduces the costs and the procedure time, and makes it a more suitable modality during paediatric interventions. Yet, clinical impact may be further improved if the ICE catheter can image intracardiac blood flow patterns, left-right shunts, and myocardial perfusion. Our aim here is to show the proof-of-principle of **C**ontrast-**E**nhanced **U**ltra**S**ound (CEUS) with an ICE probe in an animal model.

Materials and Method

We used a 9 french -2.9mm diameter- ICE catheter (7 MHz, Viewflex, St. Jude) with insertion length of 0.90 m. The catheter tip allowed a 4-way bending up to 120°. The acoustic aperture contains 64 elements with an 11-mm lens. The probe was connected via a connector board to a ZS3 ultrasound system (Zonare medical systems, Mountain View, CA, USA) with custom software in Contrast Enhanced Ultrasound mode. Recorded data was shown in real-time, and stored for offline post-processing and documentation. Digital clips of up to 8 minutes were recorded.

Upon start of the procedure, a 67 kg farm pig was sedated by injection of Zoletil (Tiletamine/Zolazepam; 5mg/kg), Rompun (Xylazine; 2.25mg/kg), and Atropine (1ml), anesthesized with Pentobarbital (10-15 mg/kg/h), and connected to an ECG and blood pressure monitoring system. The animal was mechanically ventilated. A 1cc Sildenafyl bolus before each contrast bolus was administered to prevent shock in the pig. The contrast agent was SonoVue (Bracco).

The catheter was inserted into the femoral vein and led through the inferior vena cava to the right atrium, into its so-called right-atrial home view. Thanks to the steerability the ICE catheter could also enter the right ventricle, to visualize the left ventricle and all associated structures through the ventricular septal wall.

Before contrast administration, all regular clinical ultrasound data were recorded, i.e., B-Mode, M-Mode, and Colour-Doppler Velocity images, from both the right-atrial home view and from the right ventricle.

Upon contrast administration, the probe was in the right atrium, and boluses of 1.2 ml and 2.4 ml were injected per recording.

Results

The injected bubbles of the contrast agent followed the venous flow, as such first beeing visible in the right heart and, with a temporal delay of several seconds, appearing in the left heart. The behaviour of the blood pool enhancement by the contrast agent and flow patterns became apparent in the movies. During and after wash-out from the cavities, a mild opacification of the myocardial tissue became visible.

Discussion

This proof-of-principle study shows that intracardiac echography can be combined with a Contrast Enhanced Ultrasound imaging modality. CEUS-ICE may enable further visualisation of clinically relevant parameters such as myocardial perfusion/reperfusion after percutaneous angioplasty, or residual valve or septal defect leakage during and after intervention.

Acknowledgment

We would like to acknowledge all support from Experimental Cardiology, Thorax center, Erasmus MC, during the animal experiment.

High Frame Rate Cardiac Contrast Enhanced Ultrasound

M. Toulemonde,[1] R. Corbett,[2] V. Papadopoulou,[1] N. Chahal,[3] Y. Li,[1] S. Lin,[1] M. Butler,[4] W C. Duncan,[5] DO. Cosgrove,[6] V. Sboros,[4] RJ. Eckersley,[7] R. Senior,[3] N. Duncan,[2] M-X Tang[1]*

*[1]Department of Bioengineering, Imperial College London, London, U.K. *mengxing.tang@ic.ac.uk*
[2]Imperial College Renal and Transplant Centre, Hammersmith Hospital, London
[3]Department of Echocardiography, Royal Brompton Hospital, London
[4]Institute of Biological Chemistry Biophysics, and Bioengineering, Heriot-Watt University, Edinburgh
[5]MRC Centre for Reproductive Health, The University of Edinburgh, Edinburgh
[6]Hammersmith Hospital, Imperial College London, London
[7]Biomedical Engineering Department, King's College London, London

The introduction of microbubble contrast agents in echocardiography has significantly advanced our capability for assessing cardiac function, including improved visualization of endocardial borders and the quantification of myocardial perfusion[1][2]. However, there is an ongoing engineering challenge to produce cardiac contrast enhanced ultrasound images of good spatial resolution and signal to noise ratio, as well as sufficient temporal resolution. The maximum imaging frame rate is fundamentally limited by the time required for the transmitted ultrasound pulse to travel to and from the deepest target of interest (up to ~20cm in cardiac applications), and also by the number of pulses transmitted per image. In standard CEUS techniques obtained with line by line scanning, at least tens of pulse transmissions are required for each image. Contrast specific pulse sequences, required to extract microbubble signals from tissue background [3], further reduce the imaging frame rate by a factor of two or more. This provides little scope to further compromise frame rate in order to achieve better image quality, particularly with stress echocardiography where the heart rate is significantly higher than at rest.

High frame-rate (HFR) ultrasound has shown promise in non-contrast cardiac imaging [4][5]. An increase in frame rate of up to two orders of magnitude can be achieved using diverging transmission waves. However, when the ultrasound transmission is unfocused, it is difficult to achieve a similar Mechanical Index (MI) as that used in existing tissue harmonic imaging in deep tissues, consequently compromising the image quality. Multi-line focused transmissions can be used to increase the MI achievable, but frame rate improvement under such transmission is limited.

This key limitation of HFR ultrasound disappears when it is combined with CEUS. Existing microbubble contrast agents require very low MIs to generate a contrast signal, typically in the range of 0.05-0.2. This has offered a significant opportunity for improving the existing cardiac CEUS in evaluating cardiac functions. While a number of recent studies have investigated the application of HFR CEUS in vascular imaging [6-10], they all used clinical linear array high frequency probes (typically between 3 and 15 MHz).

In this work we present the first, as far as we are aware, HFR cardiac CEUS imaging methodology, and demonstrate its feasibility in an *in vitro* phantom, a sheep model, and in an ethically-approved study involving healthy human volunteers. CEUS images at thousands of frames per second are acquired using low MI diverging waves and pulse inversion sequences implemented on an ultrasound research platform and a phased array low frequency probe [11]. A destruction pulse sequence has also been implemented. When comparing to standard CEUS and given the same display frame-rate, HFR cardiac CEUS is shown to be able to generate images of significantly improved contrast and spatial resolution. Replenishment of contrast signal after the destruction pulse sequence, as well as some individual microbubble events, are observed in the myocardium. Microbubble destruction between standard cardiac CEUS and HFR cardiac CEUS is also compared and the results show that HFR cardiac CEUS can generate better images without significant microbubble destruction.

Finally, some blood flow velocity modulation of image intensity in HFR CEUS is also observed and discussed.

In conclusion, we have demonstrated the feasibility of HFR cardiac CEUS in vivo. The initial results show great potential for its application to improve clinical imaging and quantification of cardiac function.

Acknowledgement

This work is funded by the UK Engineering and Physical Sciences Research Council (EPSRC) grant EP/M011933/1 and grant EP/M010961/1 and the NIHR Imperial Biomedical Research Centre.

References

1. *K. Wei, A. R. Jayaweera, S. Firoozan, A. Linka, D. M. Skyba, and S. Kaul, "Quantification of Myocardial Blood Flow With Ultrasound-Induced Destruction of Microbubbles Administered as a Constant Venous Infusion", Circulation, vol. 97, no. 5, pp. 473-483, 1998.*
2. *J. R. Lindner, "Microbubbles in medical imaging: current applications and future directions," in Nature Reviews Drug Discovery, vol. 3, no. 6, pp. 527-533, 2004.*
3. *A. Stanziola, M. Toulemonde, Y. O. Yildiz, R. J. Eckersley, and M. X. Tang, "Ultrasound Imaging with Microbubbles [Life Sciences]", IEEE Signal Processing Magazine, vol. 33, no. 2, pp. 111-117, 2016.*
4. *M. Tanter, and M. Fink, "Ultrafast imaging in biomedical ultrasound", IEEE Trans. on UFFC, vol. 61, no. 1, pp. 102-119, 2014.*
5. *J. Provost, C. Papadacco, J. E. Arango, M. Imbault, M. Fink, J. L. Gennison, M. Tanter, and M. pernot, "3D ultrafast ultrasound imaging in vivo", Phys. Med. Biol., vol. 59, no. 19, pp. L1-L13, 2014.*
6. *O. Couture, S. Bannouf, G. Montaldo, J. F. Aubry, M. Fink, and M. Tanter, "Ultrafast Imaging of Ultrasound Contrast Agents", Ultrasound in Medicine & Biology , vol. 35, no. 11, pp. 1908-1916, 2009.*
7. *C. Tremblay-Darveau, R. Williams, L. Milot, M. Bruce, and P. N. Burns, "Combined perfusion and doppler imaging using plane-wave nonlinear detection and microbubble contrast agents", IEEE Trans. on UFFC, vol. 61, no. 12, pp. 1988-2000, 2014.*
8. *C. Errico, J. Pierre, S. Pezet, Y. Desailly, Z. Lenkei, O. Couture, and M. Tanter, "Ultrafast ultrasound localization microscopy for deep super-resolution vascular imaging", Nature, vol. 527, no. 7579, pp. 499-502, 2015.*
9. *C. H. Leow, E. Bazigou, R. J. Eckersley, A. C. H. Yu, P. D. Weinberg, and M. X. Tang, "Flow Velocity Mapping Using Contrast Enhanced High-Frame-Rate Plane Wave Ultrasound and Image Tracking: Methods and Initial in Vitro and in Vivo Evaluation", Ultrasound in Medicine & Biology, vol. 41, no. 11, pp. 2913-2925, 2015.*
10. *A Stanziola and M-X Tang, Temporal and spatial processing of high frame-rate contrast enhanced ultrasound data, Proceedings of the 21st European Symposium on Ultrasound Contrast Imaging, p160-162, Rotterdam, January 2016*
11. *M. Toulemonde, Y. Lin, S. Lin, M. Butler, R. Eckersley, W C. Duncan, V. Sboros, and M.X. Tang, "Cardiac imaging with high frame rate contrast enhanced ultrasound: in-vivo demonstration", Proceedings of the IEEE International Ultrasonics Symposium (IUS), Tours, September 2016.*

Oxygen Loaded Microbubbles for Sonodynamic Therapy

Eleanor Beguin, Joshua Owen, Jason Sheng, Heather Nesbitt, Conor McEwan, Lester Barnsley, Mark Borden, Anthony McHale, John Callan, Eleanor Stride

[1]Institute of Biomedical Engineering, University of Oxford, UK
[2]Biomedical Sciences Research Institute, Ulster University, Coleraine, Northern Ireland, UK
[3]Materials Science & Engineering, University of Colorado, Boulder, Colorado, USA

Hypoxia, i.e. a reduction in dissolved oxygen concentration below physiologically normal levels, has been identified as playing a critical role in the progression of many types of disease and as a key determinant of the success of cancer treatment. It poses a particular challenge for treatments such as radiotherapy, photodynamic and sonodynamic therapy which rely on the production of reactive oxygen species. Strategies for treating hypoxia have included the development of hypoxia-selective drugs as well as methods for directly increasing blood oxygenation, e.g. hyperbaric oxygen therapy, pure oxygen or carbogen breathing, ozone therapy, hydrogen peroxide injections and administration of suspensions of oxygen carrier liquids. To date, however, these approaches have delivered limited success either due to lack of proven efficacy and/or unwanted side effects. Gas microbubbles, stabilised by a biocompatible shell have been used as ultrasound contrast agents for several decades and have also been widely investigated as a means of promoting drug delivery. The aim of our research has been to determine whether microbubbles could be used to deliver both a sonodynamic therapy drug and oxygen simultaneously to a tumour to facilitate treatment.

In the initial study, 1,2-Distearoyl-sn-glycero-3-phosphocholine (DSPC) coated microbubbles containing either oxygen (O_2) or sulphur hexafluoride (SF_6) were produced by sonication and conjugated to a sonosensitiser (Rose Bengal RB) via an Avidin-Biotin linker. Tumours were induced in BALB/c SCID mice using the BxPc-3 human pancreatic cell line and exposed to ultrasound for 3.5 mins (3.5 Wcm^{-2} at 1MHz centre frequency, 100 Hz pulse repetition frequency and 30% duty cycle) following intratumoural injection of either O_2 or SF_6 microbubbles. Five days after treatment a 45% reduction in tumour volume was seen in the mice receiving the O_2 bubbles, compared with a 35% increase in volume for those receiving the SF_6 microbubbles. As shown in Fig.1, the control groups (no ultrasound) showed an increase of 180% in tumour volume over the same period. Fibre optic oxygen probe measurements and subsequent analysis of the levels of hypoxia inducible factor (HIF1-α) confirmed an increase in the partial pressure of oxygen in the tumour.

For eventual clinical use however, achieving adequate microbubble stability and targeting to enable intravenous microbubble administration represents a considerable challenge. The next phase of the work therefore investigated whether reformulating the microbubbles and functionalising them with magnetic nanoparticles could both improve their longevity and enable localisation of the microbubbles to a target site.

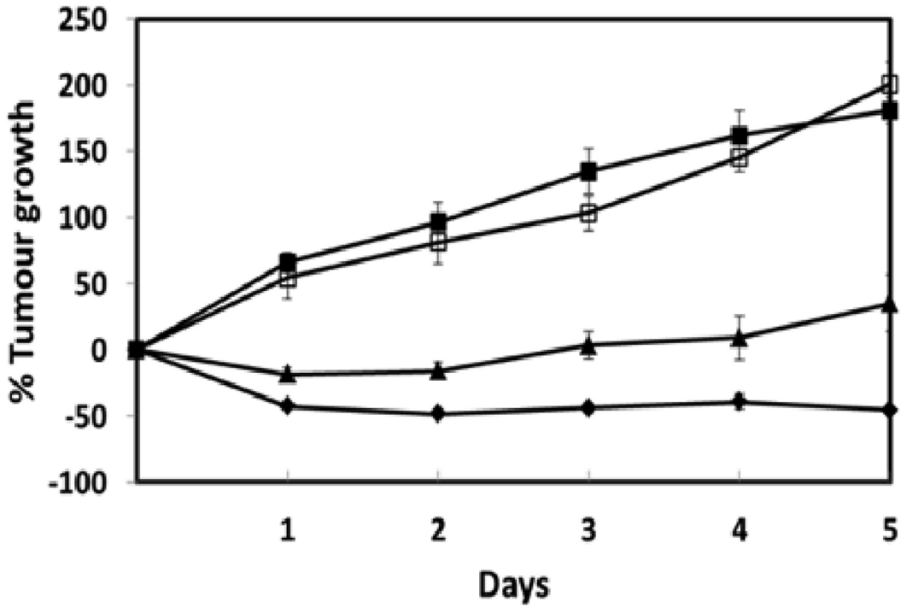

Fig.1: Plot of % tumour growth against time for mice bearing BxPc-3 tumours and treated with (i) O_2-RB microbubbles and ultrasound (filled diamonds) (ii) O_2-RB microbubbles only (open squares) (iii) SF6-RB microbubbles and ultrasound (filled triangles) (iv) SF_6-RB microbubbles only (filled squares) (n = 3) (McEwan et al 2015)[1].

1,2-dibehenoyl-sn-glycero-3-phosphocholine coated microbubbles containing oxygen and 50nm spherical magnetite particles were produced by sonication and conjugated to the SDT drug Rose Bengal via an Avidin-Biotin linker. The substitution of the phospholipid was found to substantially enhance the stability of the microbubbles to changes in size and concentration. Orthotopic tumours were induced in BALB/c SCID mice using the BxPc-3 human pancreatic cell line and exposed to ultrasound for 3.5 mins ($3.5Wcm^{-2}$ at 1MHz centre frequency, 100Hz pulse repetition frequency, 30% duty cycle) following intravenous injection of the microbubbles with or without application of a 0.1T magnetic field.

38 days post implantation the tumours treated with both ultrasound and the magnet were 50% smaller than the control tumours and exhibited a 3-fold increase in active caspase as a marker of apoptosis (Fig. 2). There was no statistically significant effect of ultrasound alone. The results indicate that intravenously administered oxygen filled microbubbles can temporarily reduce tumour hypoxia and facilitate sonodynamic therapy and efficacy can be enhanced by magnetic targeting. This potentially represents a new treatment option for recalcitrant tumours for which existing therapeutic options are extremely limited.

1. *C. McEwan, J. Owen , E. Stride, C. Fowley, H. Nesbitt, D. Cochrane, C. Coussios, M. Borden, A. McHale and J. Callan. Oxygen Carrying Microbubbles for Enhanced Sonodynamic Therapy of Hypoxic Tumours. Journal of Controlled Release 2015; 203: 51–56.*

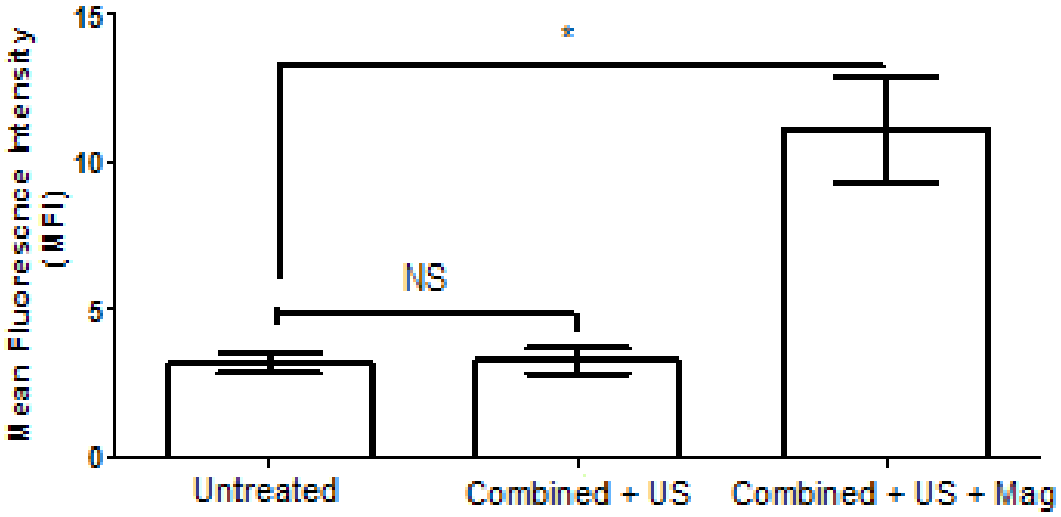

Fig. 2: Active caspase expression in suspensions of cells excised from orthotopic BxPc-3 tumours in mice treated with (i) sham exposure (ii) O_2-RB magnetic microbubbles and ultrasound (ii) O_2-RB magnetic microbubbles, magnetic field and ultrasound (n = 8).

ACKNOWLEDGEMENTS

We thank the Engineering and Physical Sciences Research Council for supporting this work through EP/I021795/1. John Callan thanks Norbrook Laboratories Ltd. for an endowed chair.

Sonoporation in 3D endothelialized microvascular networks

Ine De Cock, Eric Juang, Christina Keravnou, Sara Keller, Madison Gallagher, Ying Zeng, Mike Averkiou

Department of Bioengineering, University of Washington, Seattle, USA

Introduction

Although promising *in vitro* and *in vivo* results have shown the feasibility and demonstrated the potential of ultrasound and microbubbles to enhance drug uptake, there is still no consensus on the optimal ultrasound conditions and therapy protocol to use *in vivo*. Many *in vitro* studies have been investigating the effect of ultrasound parameters on drug uptake enhancement and the underlying biophysical mechanisms [1]. However, *in vitro* studies are typically conducted in a simplified environment, with stationary microbubbles in direct contact with a monolayer of the target cells. *In vivo*, microbubbles are circulating in the vasculature and are only in direct contact with endothelial cells lining the blood vessels, while the target cells are often in the interstitium beyond the vasculature. Therefore, there is an imminent need for more realistic *in vivo* models to study and fully understand ultrasound mediated drug delivery and to translate this technique to the clinic. Recent developments of microfabrication techniques have enabled the production of advanced 3D cell and tissue models. Our objective was to develop a 3D microvascular network mimicking the *in vivo* vasculature, perfuse it with microbubbles, and use it to study sonoporation and ultrasound mediated particle extravasation.

Methods

The 3D microvascular networks consist of endothelialized microchannels embedded in a collagen matrix (see Fig. 1). By connecting the microvascular networks to a syringe pump (see Fig. 2), the microvessels were perfused with microbubbles ($1.2x10^8$microbubbles/mL) at a flow rate of 10 µL/min, which is similar to physiological rates in the microvasculature. In addition, propidium iodide (25 µg/mL) was added to the perfusion mixture as a model drug to study sonoporation, while 40 nm fluorescent polystyrene beads (25 µg/mL) were used to assess ultrasound induced extravasation. Microvessels were exposed to ultrasound by coupling a transducer to the networks via hydrogel. The following ultrasound parameters were used: frequency of 1 MHz, acoustic pressure of 1.4 MPa (corrected for any pressure losses through the network's outer enclosure), pulse length of 500 cycles, duty cycle of 5% and exposure time of 5 sec. The glass coverslip at the bottom of the networks offered an optical window to observe microbubble-cell interactions via bright-field imaging at frame rates of approximately 30 fps, while drug uptake was assessed via fluorescence microscopy.

Fig. 1. Z-stack projection of horizontal confocal sections of endothelialized microvessels: (i) overall network, (ii) views of corner (iii) and branching sections. Red, CD31; blue, nuclei. (Scale bar: 100 µm.)

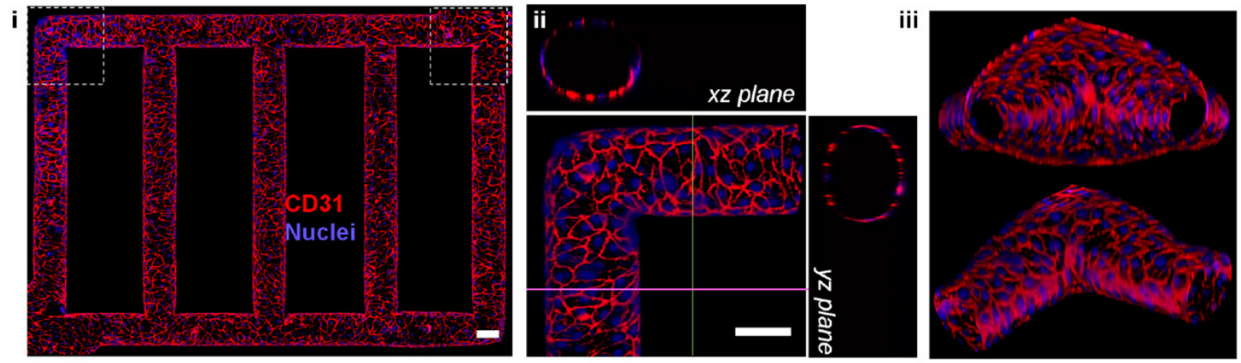

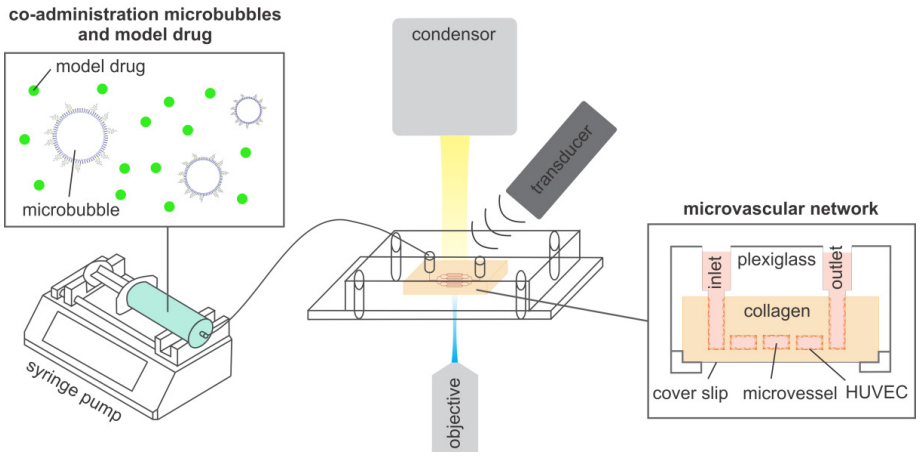

Fig. 2. Schematic of the experimental setup.

Results

The endothelialized microvascular networks were successfully perfused with microbubbles at physiological flow rates (10 µL/min). When exposing the networks to ultrasound in the presence of microbubbles, the cell membrane of a significant amount of endothelial cells was permeabilized (see Fig. 3), allowing the uptake of propidium iodide in the cells. We have noticed that areas in the microvascular networks where microbubbles were sticking to the endothelial wall due to flow variation, displayed a higher number of permeabilized cells than those where microbubbles were freely flowing. This may indicate the need for having the microbubbles adhering to the vessel wall in order to affect the endothelial cells, suggesting the utility of targeted microbubbles.

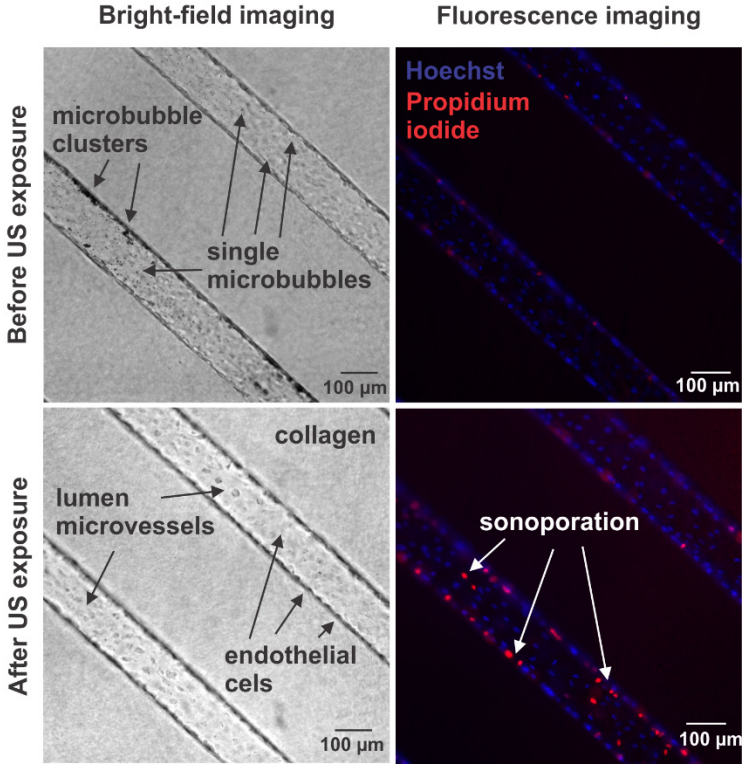

Fig. 3. Bright-field images (left column) and fluorescence images (right column) with the endothelial cell nuclei stained in blue with Hoechst and propidium iodide uptake depicted in red. Images were acquired before (top row) and after (bottom row) ultrasound exposure. Sonoporation, indicated by propidium iodide uptake, was mainly observed in areas where microbubbles were sticking to the vessel wall.

In addition, in preliminary experiments, we observed that microbubble cavitation upon ultrasound exposure could cause some degree of microvessel poration and induce extravasation of 40 nm fluorescent beads (see Fig. 4) into the collagen matrix. Although the extent of extravasation was limited, this was still significant since 40 nm beads are too large to naturally penetrate into the collagen matrix. In future experiments, we will investigate the effect of changing the model drug size as well as the effect of ultrasound parameters on sonoporation.

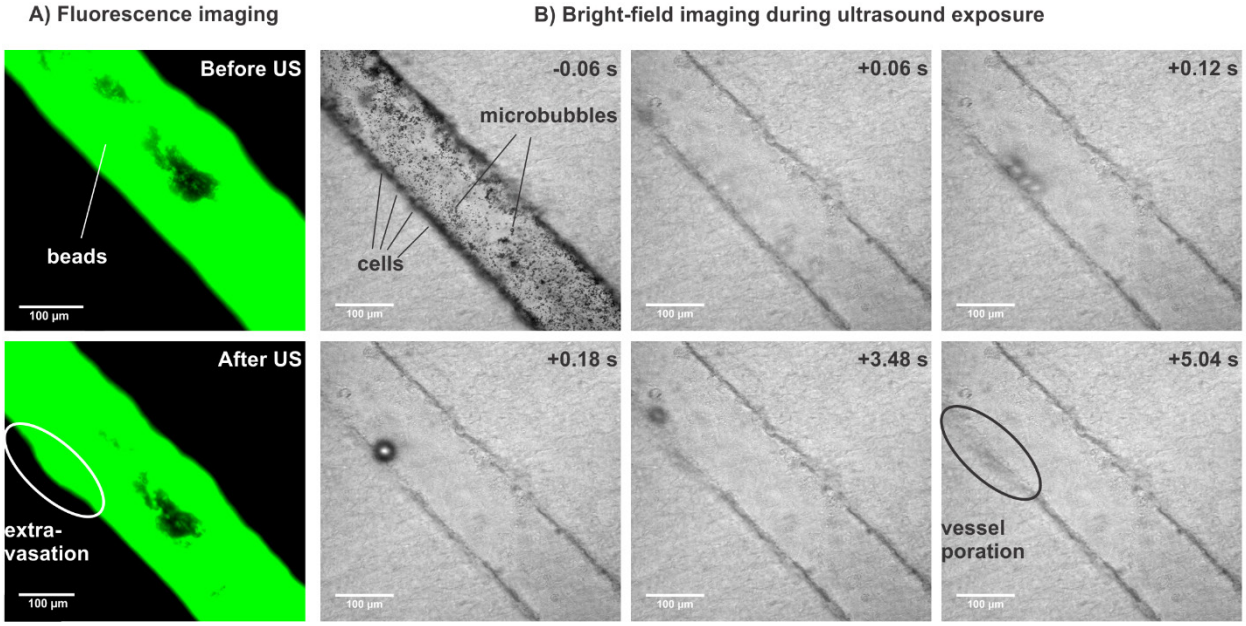

Fig. 4. A) Fluorescent images acquired before and after ultrasound exposure. B) Still frames of a bright-field recording acquired during ultrasound exposure (starting at t=0s and ending at t=5s). Upon ultrasound exposure, microbubbles oscillate, cluster and coalesce into a large microbubble (frame +0.18s), leading to the disruption of the endothelial vessel wall (frame +5.04s). The fluorescent image acquired after ultrasound exposure indicates that beads have extravasated from the microvessel into the collagen matrix.

Discussion and Conclusion

The novel 3D microvascular network model described in the present work is a clinically relevant model mimicking the *in vivo* vasculature and therefore offers an excellent platform to study sonoporation and extravasation in a realistic environment [2]. So far we have successfully perfused the 3D microvascular networks and performed initial investigations on sonoporation and drug delivery to endothelial cells and particle extravasation. In the future, we plan to produce more detailed studies of drug uptake enhancement and offer new insights into the associated mechanisms. By inducing neoagiogenesis in such a system we plan to evaluate sonoporation with antiangiogenic drugs.

References

1. *Lentacker I, De Cock I, Deckers R, De Smedt SC, Moonen CT, Understanding ultrasound induced sonoporation: definitions and underlying mechanisms, Adv. Drug Deliv. Rev, 72 (2016), 49-64.*
2. *Zheng Y, Chen J, Craven M, Choi NW, Totorica S, Diaz-Santana A, Kermani P, Hempstead B, Fischbach-Teschl C, López JA, Stroock AD, In vitro microvessels for the study of angiogenesis and thrombosis, Proc. Natl. Acad. Sci. USA, 109 (2012) 9342-7.*

The Role of Nitric Oxide during Sonoreperfusion of Microvascular Obstruction

François T.H. Yu, PhD,[1] Varun Avula, Xucai Chen, PhD,[1] Adam Straub, PhD,[2] Linda Lavery,[1] Flordeliza Villanueva, MD and John J. Pacella, MS, MD[1]

Rationale

Microembolization during PCI for acute myocardial infarction can cause microvascular obstruction **(MVO)**. MVO severely limits the success of reperfusion therapies, is associated with additional myonecrosis, and is linked to worse prognosis, including death. We have shown, both in *in vitro* and *in vivo* models, that ultrasound **(US)** and microbubble **(MB)** therapy relieves MVO and restores perfusion (termed "sonoreperfusion" or "**SRP**") but the underlying mechanisms remain to be established.

Objective

Both mechanical (thrombus dissolution) and biological processes (endothelial effects) are posited to play a role in SRP. In this study, we investigated the role of nitric oxide (**NO**) during SRP.

Methods and results

Using Western blotting and immunostaining methods, we first demonstrated that US-stimulated MB oscillations induced a 6-fold increase in endothelial nitric oxide synthase **(eNOS)** phosphorylation *in vitro* ($p<0.05$), compared to baseline. We then monitored the kinetics of intramuscular NO and perfusion flow rate responses following 2-min of SRP therapy in the rat hindlimb muscle, with and without blockade of eNOS with LNAME. Following SRP, we found that starting at 6 minutes intramuscular NO increased significantly over 30 min and was higher than baseline after 21 min ($p<0.05$). Concomitant contrast enhanced burst reperfusion imaging confirmed that there was a marked increase in perfusion flow rate at 6 and 10 min post SRP compared to baseline (>2.5 fold, $p<0.05$). The increases in intramuscular NO and perfusion rate were completely blunted with LNAME. Finally, we tested the hypothesis that NO plays a role in SRP by assessing reperfusion efficacy in a previously described rat hindlimb model of MVO during blockade of eNOS. After US treatment 1, MBV was restored to baseline in the MB+US control group ($p<0.05$ vs MVO stage), but remained low in the LNAME group (p=ns vs MVO stage). Perfusion rates increased in the MB+US control group after US treatment 2 ($p<0.05$ vs MVO stage) but not in the MB+US+LNAME group.

Conclusions

These data strongly support that MB oscillations can activate the eNOS pathway leading to increased blood perfusion and NO plays a significant role in SRP efficacy.

Reduction in Dissolved Oxygen Resulting from Acoustic Droplet Vaporization

Karla Mercado,[1] Kirthi Radhakrishnan,[1*] Christy Holland,[1,2] Kevin Haworth[1,2]

[1] Department of Internal Medicine, University of Cincinnati, Cincinnati, OH, USA 45267-0586
[2] Biomedical Engineering Program, University of Cincinnati, Cincinnati, OH, USA 45267-0586
[*] Now with Philips Electronics North America, 3000 Minuteman Road, Andover, MA 01810

Background and Objective

Microbubbles can be formed *in situ* using acoustic droplet vaporization (ADV) (Kripfgans et al. 2000), which is the ultrasound-mediated phase transition of liquid perfluorocarbon droplets into gas microbubbles. ADV has potential diagnostic (Kripfgans et al. 2002; Sheeran et al. 2015) and therapeutic (Burgess and Porter 2015; Fabiilli et al. 2010; Fabiilli et al. 2013; Kopechek et al. 2014) applications. After the phase transition, dissolved gases diffuse into the ADV-converted microbubble due to a gas concentration gradient across the bubble surface (Kripfgans et al. 2000; Reznik et al. 2012; Sheeran et al. 2011) (Figure 1). The objective of this study was to determine the magnitude of the reduction in the dissolved oxygen in the fluid following acoustic droplet vaporization as the ultrasound insonation pressure amplitude, droplet size distribution, and droplet concentration were varied.

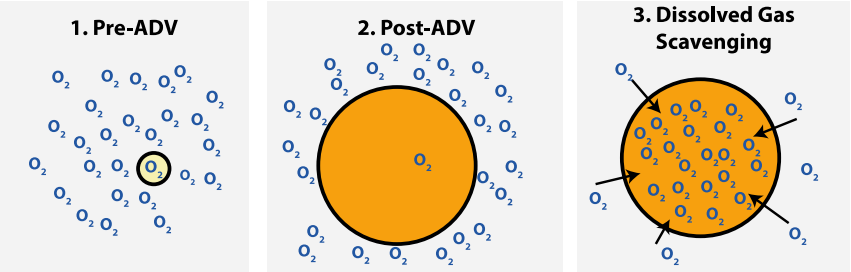

Figure 1: A schematic representation of how oxygen, a representative gas, can be sequestered in microbubbles formed via acoustic droplet vaporization (ADV). Prior to ADV, the dissolved oxygen inside the droplets is at equilibrium with the dissolved oxygen in the surrounding fluid (panel 1). Upon phase transition, the microbubble forms rapidly and is undersaturated with oxygen (panel 2). Following in-gassing, the amount of dissolved oxygen in the surrounding fluid is decreased (panel 3).

Methods

Perfluorocarbon droplets were manufactured using high speed shaking which resulted in a polydisperse size distribution of droplets between 0.6 and 18 μm (Radhakrishnan et al. 2016). Differential centrifugation was used to size-isolate the droplet populations between 1 and 3 μm or 2 and 5 μm (Mercado et al. 2016). Both polydisperse droplets and size-isolated droplets were used in this study. Perfluorocarbon droplets were diluted to droplet concentrations between 2.4×10^6 and 4×10^8 droplets/mL in saline and pumped through a flow phantom in a 37 ºC water bath at volumetric flow rates of 5 ml/min or 10 ml/min, mimicking branching arteries. The droplets were exposed to pulsed ultrasound at a center frequency of 2 MHz (10 cycles, 100 Hz pulse repetition frequency, and peak negative pressures ranging from 0 to 12.2 MPa) or 5 MHz (10 cycles, 500 Hz pulse repetition frequency, and 4.25 MPa peak negative pressure). Dissolved oxygen sensors were

placed proximal and distal to the ultrasound insonation location. The effluent of the system was collected, and the size distribution and concentration of the droplets in the effluent were measured with a Coulter counter (Multisizer 4). The ADV transition efficiency was determined as the percent difference of the number of droplets at each diameter in the effluent before and after ADV. An empirical model was developed to predict the extent of dissolved oxygen scavenging based on the volume of perfluorocarbon that was transitioned into gas microbubbles. The model was based on equal partial pressures of dissolved gases in the perfluorocarbon droplets, perfluorocarbon microbubbles, and surrounding liquid at equilibrium and conservation of the mass for the dissolved gases before and after ultrasound exposure. The surface tension, γ, was set as either 0 mN/m and 68 mN/m.

Results

A statistically significant reduction in the dissolved oxygen in the fluid containing 4×10^8 polydisperse droplets/mL was observed after exposure to 2 MHz ultrasound with peak negative pressures higher than the ADV threshold, 4.2 MPa peak negative pressure. The dissolved oxygen content in the fluid predicted by the model, using surface tension values of 0 mN/m and 68 mN/m, was not significantly different than the experimentally measured dissolved oxygen after ADV (Figure 2). A smaller fraction of the polydisperse droplet population was transitioned into gas bubbles compared to the size-isolated droplets (Figure 3). For size-isolated droplets exposed to 5 MHz pulsed ultrasound, the transition efficiency and magnitude of dissolved oxygen scavenging varied non-monotonically as the concentration of size-isolated droplets increased (Table 1). B-mode imaging showed that the ADV microbubbles caused acoustic shadowing, with more shadowing occurring with polydisperse droplets in the flow phantom relative to the size-isolated droplets.

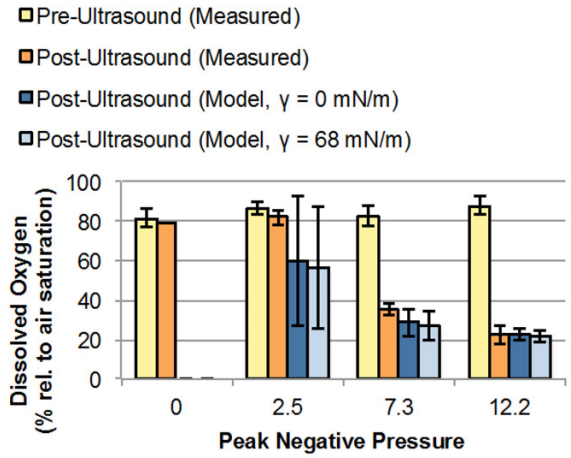

Figure 2: The dissolved oxygen measured before (yellow) and after (orange) 2 MHz pulsed ultrasound exposure at 0 MPa, 2.5 MPa, 7.3 MPa, and 12.2 MPa peak negative pressure. Dissolved oxygen scavenging was observed only when the ultrasound pressure amplitude exceeded the ADV threshold (4.2 MPa). The model for predicting the decrease in dissolved oxygen in the fluid, with surface tension of 0 mN/m and 68 mN/m, were not statistically significantly different than the measured change in dissolved oxygen.

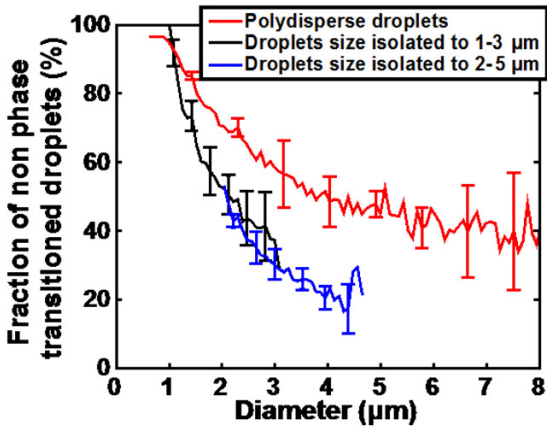

Figure 3: The number of droplets measured in the flow phantom effluent with and without 5 MHz ultrasound exposure (4.25 MPa peak negative pressure) was used to calculate the fraction of droplets that did not transition to gas. The fraction of non-transitioned droplets decreased with increasing droplet diameter. For a fixed droplet diameter, there were more non-transitioned droplets from the polydisperse distribution. The polydisperse distribution also produced more acoustic shadowing on a B-mode image.

Table 1: The droplet transition efficiency and magnitude of dissolved oxygen scavenging as the droplet concentration is varied.

Pre-ultrasound droplet concentration (droplets/mL)	Post-ultrasound droplet concentration (droplets/mL)	Transition efficiency (%)	Magnitude of dissolved oxygen scavenging (%)
2.4×10^6	1.2×10^6	52	17
5.2×10^6	2.1×10^6	59	25
10×10^6	8.8×10^6	12	15

Discussion and Conclusions

The magnitude of the oxygen scavenging was observed to be a function of the volume of perfluorocarbon droplets that transitioned to gas per unit volume of the surrounding fluid. It was demonstrated that the extent of gas scavenging can be predicted using a relatively simple model. Changing the modeled surface tension from 0 mN/m to 68 mN/m did not significantly change the predicted dissolved oxygen scavenging, likely due to the relatively large size of the microbubbles produced. The measurements of dissolved oxygen scavenging and transition efficiency revealed non-monotonic relationships with droplet size distribution and concentration. The reduction in transition efficiency with increasing droplet concentration may be due to acoustic shadowing, which has implications for the maximum oxygen scavenging that can be induced. The beneficial and negative bioeffects of gas scavenging caused by ADV may need to be considered when investigating potential clinical applications of ADV.

Acknowledgements

This work was supported by the United States National Institutes of Health through grants KL2TR000078, KL2TR001426, and K25HL133452, and the American Heart Association through grant 16SDG27250231.

References

1. *Burgess MT, Porter TM. Acoustic Cavitation-Mediated Delivery of Small Interfering Ribonucleic Acids with Phase-Shift Nano-Emulsions. Ultrasound Med Biol 2015;41:2191–2201.*
2. *Fabiilli ML, Haworth KJ, Sebastian IE, Kripfgans OD, Carson PL, Fowlkes JB. Delivery of Chlorambucil Using an Acoustically-Triggered Perfluoropentane Emulsion. Ultrasound Med Biol 2010;36:1364–1375.*
3. *Fabiilli ML, Wilson CG, Padilla F, Martín-Saavedra FM, Fowlkes JB, Franceschi RT. Acoustic droplet-hydrogel composites for spatial and temporal control of growth factor delivery and scaffold stiffness. Acta Biomater 2013;9:7399–7409.*
4. *Kopechek JA, Park E-J, Zhang Y-Z, Vykhodtseva NI, McDannold NJ, Porter TM. Cavitation-enhanced MR-guided focused ultrasound ablation of rabbit tumors in vivo using phase shift nanoemulsions. Phys Med Biol 2014;59:3465–3481.*
5. *Kripfgans OD, Fowlkes JB, Miller DL, Eldevik OP, Carson PL. Acoustic droplet vaporization for therapeutic and diagnostic applications. Ultrasound Med Biol 2000;26:1177–1189.*
6. *Kripfgans OD, Fowlkes JB, Woydt M, Eldevik OP, Carson PL. In vivo Droplet Vaporization for Occlusion Therapy and Phase Aberration Correction. IEEE Trans Ultrason Ferroelectr Freq Control 2002;49:726–738.*
7. *Mercado KP, Radhakrishnan K, Stewart K, Snider L, Ryan D, Haworth KJ. Size-isolation of ultrasound-mediated phase change perfluorocarbon droplets using differential centrifugation. J Acoust Soc Am 2016;139:EL142–EL148.*
8. *Radhakrishnan K, Holland CK, Haworth KJ. Scavenging dissolved oxygen via acoustic droplet vaporization. Ultrason Sonochem 2016;31:394–403.*
9. *Reznik N, Seo M, Williams R, Bolewska-Pedyczak E, Lee M, Matsuura N, Gariepy J, Foster FS, Burns PN. Optical studies of vaporization and stability of fluorescently labelled perfluorocarbon droplets. Phys Med Biol 2012;57:7205.*
10. *Sheeran PS, Rojas JD, Puett C, Hjelmquist J, Arena CB, Dayton PA. Contrast-enhanced ultrasound imaging and in vivo circulatory kinetics with low-boiling-point nanoscale phase-change perfluorocarbon agents. Ultrasound Med Biol 2015;41:814–831.*
11. *Sheeran PS, Wong VP, Luois S, McFarland RJ, Ross WD, Feingold S, Matsunaga TO, Dayton PA. Decafluorobutane as a Phase-Change Contrast Agent for Low-Energy Extravascular Ultrasonic Imaging. Ultrasound Med Biol 2011;37:1518–1530.*

Improved Drug Distribution using Rapid Short-Pulse (RaSP) Sequences *In Vivo* to Open the Blood-Brain Barrier

Sophie Morse, Antonios N Pouliopoulos, Julien Lin, Tiffany Chan, James J Choi

Noninvasive Surgery and Biopsy laboratory, Department of Bioengineering, Imperial College London, London, SW7 1AZ, United Kingdom

Introduction

One third of the worldwide disease burden – number of years lost due to disease – is caused by brain diseases, such as dementia, Parkinson's and brain cancer (DiLuca and Olesen 2014). With an aging population, this burden is expected to rise. Despite the global effort to develop new treatments, there are still no effective drugs for these diseases. One of the major reasons for the lack of successful therapies is that the majority of drugs cannot enter the brain due to the blood-brain barrier (BBB) (Lu *et al* 2014). A promising solution to this problem is the use of focused ultrasound and microbubbles to locally and noninvasively open the BBB so that therapeutic agents can enter the brain (Hynynen *et al* 2001). Since its inception, ultrasound technology has been shown to deliver a range of drugs across the BBB (Burgess *et al* 2015). However, several underlying factors, such as concerns of efficacy and safety, have prevented its clinical translation in human patients (Baseri *et al* 2010, Choi *et al* 2007, Pouliopoulos *et al* 2016). We have previously shown that current ultrasound technology produces a poor drug distribution and damages arteries (Choi *et al* 2010). This efficacy-safety limit is likely a result of the use of conventional ultrasound pulse shapes and sequences, which have poor control over cavitation dynamics, generating a mixture of desired and undesired cavitation activity (Choi and Coussios 2012). We have recently developed and tested a new low pressure rapid short-pulse (RaSP) sequence *in vitro*, designed to promote the desired cavitation activity in the correct location (Pouliopoulos *et al* 2016). This new sequence will be evaluated here for its ability to improve the efficacy and safety of ultrasound-mediated drug delivery to the brain *in vivo*.

Methods

Rapid short-pulse (RaSP) sequences consist of short pulses emitted at high pulse repetition frequencies separated by off-time intervals in the range of microseconds. *In* vitro studies have shown that these sequences prolong the lifetime of microbubbles and increase their mobility during the off-time intervals, enhancing both the temporal and spatial distribution of acoustic cavitation activity (Pouliopoulos *et al* 2016). In this work, RaSP sequences were tested *in vivo* at a peak-negative pressure of 400 kPa for their ability to efficiently and safely open the blood-brain barrier (pulse length (PL): 5 cycles; pulse repetition frequency (PRF): 1.25 kHz; burst length: 10 ms). Drug delivery patterns produced using these sequences were compared against those produced by conventionally used long-pulse sequences at the same acoustic pressure (PL: 10,000 cycles; PRF: 0.5 Hz; burst length: 10 ms). Fluorescently-tagged (Texas Red) 3 kDa dextran and microbubbles were intravenously injected in mice while sonicating the left hippocampus with a 1 MHz focused ultrasound transducer. A 7.5 MHz passive cavitation detector captured the microbubble-seeded acoustic emissions. The relative dose and distribution of the drug were quantified by calculating the normalised optical density (NOD, the average increase in fluorescence in the targeted area normalised by the control) and the coefficient of variation (COV, the ratio of the standard deviation by the average fluorescent intensity in the targeted region). Safety was assessed by haematoxylin and eosin (H&E) histological staining.

Results

Despite emitting 150 times less acoustic energy, RaSP sequences delivered a dextran dose of the same order of magnitude as the long-pulse sequences (Fig.2). Moreover, the drug distribution was significantly more

uniform using RaSP sequences (Fig.1), as indicated by the coefficient of variation (Fig.2). Unlike the long-pulse sequences, RaSP sequences did not produce as prominent vascular effects, where dextran accumulates in the large vessels (Fig.1c). Acoustic emissions from the short-pulses were more stable than those from the long-pulses, with the energy smoothly decreasing with time. Based on H&E analysis, the dextran delivery was considered to be safe as no tissue damage or haemorrhage was observed in the targeted region.

Conclusion

These results suggest that RaSP sequences can generate a more uniform distribution of acoustic activity in space and time, leading to an improved spatial distribution of dextran. Low pressure RaSP sequences could result in a more efficient and safe delivery of agents across the blood-brain barrier to treat diseases such as Alzheimer's, Parkinson's and brain cancer.

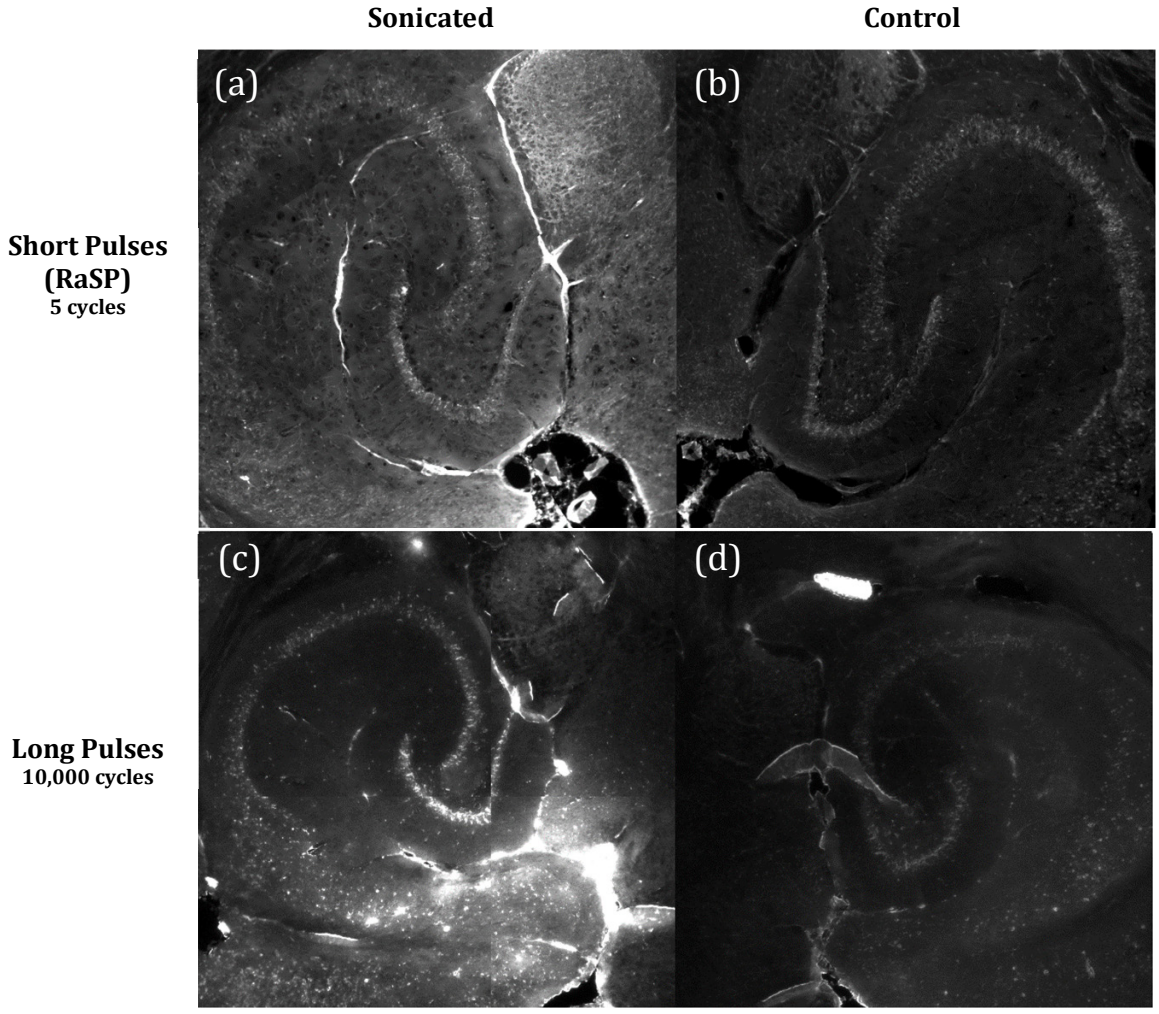

Figure 1. Comparison of the drug delivery distributions for RaSP and conventional long-pulse sequences. Fluorescent 3 kDa dextran (Texas Red) delivered to the left hippocampus (**a,c**) at 400 kPa peak-negative pressure using RaSP pulse sequences (**a,b**) and conventional long-pulse sequences (**c,d**). The right hippocampus was used as a control (**b,d**). Artefacts are present in the conventional long-pulse fluorescent control image, where folds and ventricle fluorescence is present (**d**).

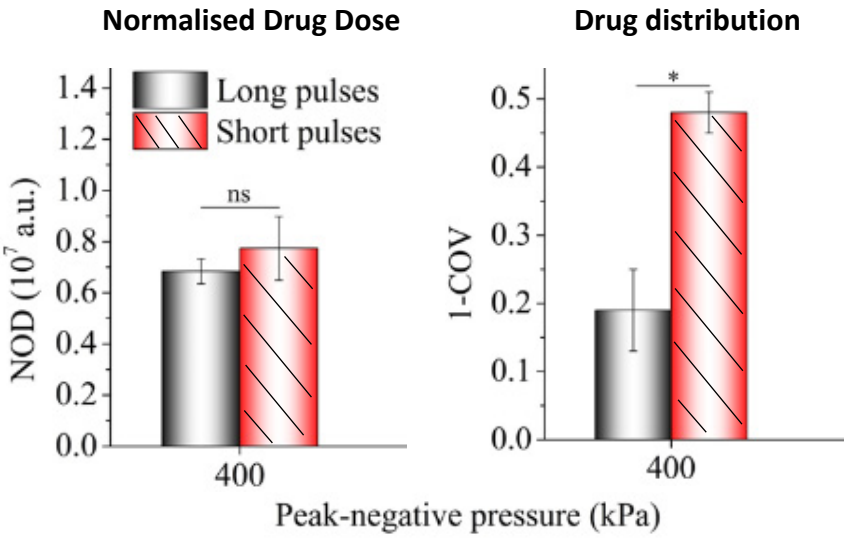

Figure 2. Quantification of the normalised drug dose and drug distribution created using RaSP and conventional long-pulse sequences. Normalised optical density (NOD), calculated as a measure of the normalised drug dose, and coefficient of variation (COV), as a measure of the drug distribution, shown for the RaSP and conventional pulse sequences at 400 kPa peak-negative pressure (* $p < 0.01$; ns = not significant). The drug distribution is plotted as (1 - COV) to show the better distribution of the short-pulse sequences (RaSP).

References

1) *Baseri B, Choi J J, Tung Y S and Konofagou E E 2010 Multi-modality safety assessment of blood-brain barrier opening using focused ultrasound and definity microbubbles: A short-term study Ultrasound Med. Biol. 36 1445–59*
2) *Burgess A, Shah K, Hough O and Hynynen K 2015 Focused ultrasound-mediated drug delivery through the blood-brain barrier. Expert Rev. Neurother. 15 477–91*
3) *Choi J J and Coussios C-C 2012 Spatiotemporal evolution of cavitation dynamics exhibited by flowing microbubbles during ultrasound exposure. J. Acoust. Soc. Am. 132 3538–49*
4) *Choi J J, Pernot M, Small S A and Konofagou E E 2007 Noninvasive, transcranial and localized opening of the blood-brain barrier using focused ultrasound in mice Ultrasound Med. Biol. 33 95–104*
5) *Choi J J, Wang S, Tung Y S, Morrison B and Konofagou E E 2010 Molecules of Various Pharmacologically-Relevant Sizes Can Cross the Ultrasound-Induced Blood-Brain Barrier Opening in vivo Ultrasound Med. Biol. 36 58–67*
6) *DiLuca M and Olesen J 2014 The cost of brain diseases: A burden or a challenge? Neuron 82 1205–8*
7) *Hynynen K, McDannold N, Vykhodtseva N and Jolesz F a 2001 Noninvasive MR imaging-guided focal opening of the blood-brain barrier in rabbits. Radiology 220 640–6*
8) *Lu C T, Zhao Y Z, Wong H L, Cai J, Peng L and Tian X Q 2014 Current approaches to enhance CNS delivery of drugs across the brain barriers Int. J. Nanomedicine 9 2241–57*
9) *Olesen J and Leonardi M 2003 The burden of brain diseases in Europe Eur. J. Neurol. 10 471–7*
10) *Pouliopoulos A N, Li C, Tinguely M, Garbin V, Tang M-X and Choi J J 2016 Rapid short-pulse sequences enhance the spatiotemporal uniformity of acoustically-driven microbubble activity during flow conditions J. Acoust. Soc. Am. 140 2469–80*

Quantitative Subharmonic Imaging and Pressure Estimation *In Vivo*

F. Forsberg

Department of Radiology, Thomas Jefferson University, Philadelphia, PA 19107.

Objective

Our group has previously shown the subharmonic amplitude of microbubble-based ultrasound contrast agents is a good indicator of hydrostatic pressure *in vitro* and has developed a noninvasive pressure measurement technique, known as subharmonic-aided pressure estimation (SHAPE), based on this principle. Noninvasive SHAPE measurements may be a useful alternative to catheter-based measurements of cardiac conditions or portal hypertension as well as other conditions. Here, we present results from our pre-clinical and clinical trials on the utility of quantitative SHAPE as a novel biomarker.

Methods

SHAPE was implemented on a Sonix RP scanner (Analogic Ultrasound, Richmond, Canada) using a phased array transducer (PA4-2) with a transmit/receive frequency of 2.5/1.25 MHz and pulse inversion imaging. Nine canines received 0.015 μl/kg/min infusions of Sonazoid (GE Healthcare, Oslo, Norway). Simultaneous, closed chest, pressure measurements were acquired over 5 s with SHAPE and with an invasive, 5F high-fidelity manometer-tipped pressure catheter (SPC-350; Millar Instruments, Houston, TX). Data were collected in triplicate from the right atrium (RA), right ventricle (RV), left atrium (LA), left ventricle (LV) and aorta. The subharmonic signal amplitudes were extracted using a bandpass filter and fitted to the reference standard using linear regression analysis. In our first-in-humans liver trial, 45 patients received a co-infusion of Sonazoid (0.72 μL microbubbles/kg/hour; GE Healthcare, Oslo, Norway) and saline (120 ml/hour) following transjugular liver biopsy. Subjects were scanned with a modified Logiq 9 scanner (GE Healthcare, Milwaukee, WI). The acoustic output for optimal SHAPE sensitivity was determined and used for pressure estimation. Radiofrequency data from the portal and hepatic veins were collected for 5 s (n = 3). Subharmonic amplitudes were extracted off-line and compared to catheter-based hepatic venous pressure gradients (HVPG) determined as part of clinical care. Subsequently, we have initiated clinical trials in cardiac patients undergoing right and left heart catheterizations (n = 15) and in women with breast cancer undergoing neoadjuvant chemotherapy where SHAPE is being used to measure interstitial fluid pressures as a new biomarker for treatment response (17 subjects have been enrolled).

Results

The maximum absolute errors for mean LV diastolic, minimum LV diastolic, LV end-diastolic and mean LV pressures and the range of LV pressures were 2.5, 2.4, 8.9, 6.0 and 4.5 mmHg, respectively. For the right heart peak systolic, mean diastolic, end diastolic and minimum pressures and RV relaxation (isovolumic -dp/dt) were within 2.3, 1.3, 1.3, 0.9 mmHg and 1.5 mmHg/s, respectively, of the measured pressures. In the human liver study, adequate contrast signals were obtained from 34 of the 45 patients. The SHAPE gradient between the portal and hepatic veins in those patients was in good overall agreement with HVPG (r = 0.82). Subjects with portal hypertension (HVPG > 10 mmHg) showed significantly higher subharmonic gradients compared

to those with lower HVPGs (1.37 ± 0.59 vs. -1.68 ± 0.27, $p < 0.001$) with a sensitivity of 89 % and a specificity of 88 %. In our biomarker trial of women undergoing neoadjuvant chemotherapy we found that results from 10% completion of the therapy showed the subharmonic signal increased more in the tumor than in the surrounding area for complete responders compared to partial/non responders (3.23 ± 1.41 dB vs. -0.88 ± 1.46 dB; $p = 0.001$ from SHAPE and 1.32 ± 0.73 dB vs. -0.82 ± 0.88 dB; $p = 0.002$ from SHI).

Conclusions

First-in-human results show SHAPE may be a useful, noninvasive biomarker for assessing portal hypertension. Other areas that could benefit from noninvasive, quantitative pressure measurements (e.g., primary diagnosis of heart disease and treatment monitoring for breast cancer neoadjuvant chemotherapy) are actively being pursued.

CEUS and Malignant Liver Lesions: The Challenge to Differentiate HCC from CCC

Carla Serra

The use of microbubble ultrasound contrast agents for the evaluation on focal liver lesions has overcome several limits of conventional B-mode and Doppler ultrasound techniques. Contrast-enhanced patterns of liver lesions can be evaluated during all vascular phases (arterial, portal venous, late phases), as in contrast-enhanced computed tomography (CT) and contrast-enhanced magnetic resonance imaging (MRI), but it has the advantage of being performed in real time under the direct control of the operator. Furthermore, the use of contrast-enhanced ultrasound (CEUS) to characterize focal lesions, both in cirrhotic and non-cirrhotic liver is recommended in the clinical practice guidelines issued by the European Federation of Societies for Ultrasound in Medicine and Biology (EFSUMB).

The majority of clinical applications of CEUS in the abdomen are for the liver and the principal aim of CEUS in the liver is the characterization of focal liver lesions (FLLs). In particular, CEUS evaluation of FLLs in late and post-vascular phase provides important information about their malignant potential: the majority of malignant lesions are hypo-enhancing, whereas most solid benign lesions are iso- or hyper-enhancing.

A special issue most be considered the evaluation of FLL in cirrhotic and screening for HCC. Although macro-regenerative and dysplastic nodules generally do not present early contrast uptake, resembling liver parenchymal behaviour, the typical CEUS pattern of HCC in liver cirrhosis is hyper-enhancement in the arterial phase, followed by wash-out in the late phase. This pattern correlates to HCC in more than 97 % of cases but has also been described in peripheral CCC and hepatic lymphoma in 1–3 % of cases. Furthermore, wash-out characterizes HCC with poorer grades of differentiation, whereas well-differentiated HCC tends to be iso-enhanced with respect to the parenchyma in the portal venous or late phase and a wash-out, when present tends to start later in HCC, generally not before 60 s after injection, and in one-fourth of cases appears only after 180 s.

The presence of early wash-out has been described in poorly differentiated HCCs and in cases of non-hepatocellular cancers, for example, in peripheral CCC. In the arterial phase CCC may show different enhancement patterns: usually it shows a quick rhim-like enhancement (50 % of cases), but it may show be homogeneous to the surrounding parenchyma or hypoenhancing. The main feature of CCC at CEUS is the presence of a quick and early wash out present at less than 60 s after injection. CEUS enhancement patterns of CCC are consistent with those on CECT in the arterial phase, while in the portal phase, CCC fades out more obviously on CEUS than on CECT and in the late phase, all CCCs show washout on CEUS whereas sustained enhancement on CECT. Despite the removal of CEUS from AASLD and EASL guidelines on the management of HCC, due to the difficulty to differentiate HCC from CCC described in a controversial study, it maintains a reasonable role in the imaging armamentarium, in a field where also other imaging techniques have some limitations.

A Phase 3 Multicentre, Randomised, Non-inferiority Study of the Efficacy and Safety of SonazoidTM and SonoVue® in Patients with Focal Liver Lesions Undergoing Pre- and Post-Contrast Ultrasound Imaging

Yuxin Jiang,[1] Ke Lv,[1] Ping Liang,[2] Huixiong Xu,[3] Lianfang Du,[4] Xiaoyan Xie,[5] Christina Kalli,[6] Geir Torheim,[7] Wenping Wang[8]

[1]Peking Union Medical College Hospital
[2]Chinese PLA General Hospital
[3]Tenth People's Hospital of Tongji
[4]Shanghai First People's Hospital
[5]The First Affiliated Hospital of Sun-Yat sen University
[6]GE Healthcare Life Sciences
[7]GE Healthcare AS
[8]Zhongshan Hospital Fudan University

The purpose of this phase 3 study was to assess the efficacy of Sonazoid for characterizing focal liver lesions in large series of patients. A second objective was to demonstrate equivalent diagnostic efficacy with SonoVue® which is already used in subjects with focal liver lesions (FLLs). This has been achieved by comparing pre- and post-contrast ultrasound examination findings with regards to aspects of lesion diagnosis, including diagnosis as benign versus malignant, specific lesion diagnosis (haemangioma, focal nodular hyperplasia, other benign; hepatocellular carcinoma, metastasis, other malignant), and confidence in diagnosis.

Materials and Methods

The study was conducted at 17 centres in China and Korea. Before enrolling 'efficacy' patients, up to 4 Sonazoid training cases alternating with up to 4 SonoVue training cases per site were enrolled to train each ultrasound operator. SonoVue training cases could be omitted at centres where use of SonoVue was established. A total of 424 patients received an injection of Sonazoid (0.12 μL microbubbles/kg) or SonoVue (2.4 mL) for contrast-enhanced ultrasound (CEUS) imaging. A total of 338 patients were included in the efficacy population (169 each in the Sonazoid and SonoVue groups, respectively). Three trained and qualified independent blinded readers (1 from Europe and 2 from China) evaluated pre- and post-contrast images and characterized the target FLLs (1 per patient) as benign or malignant. The criterion for non-inferiority was that the upper bound of the exact binomial 95% confidence interval (CI) for the difference in accuracy improvement between the 2 groups was less than the pre-specified non-inferiority margin of 20% for a minimum of 2 out of 3 blinded readers. Contrast-enhanced CT (CE-CT), CE-MRI, or biopsy provided the reference diagnosis.

Results

The proportions of subjects with each type of reference diagnosis were similar in the Sonazoid (50% benign; 50% malignant) and SonoVue (56% benign; 46% malignant) groups. With respect to the classification of lesions as benign or malignant, the study was successful as the difference in accuracy improvement between the Sonazoid and SonoVue groups was <20% for all 3 blinded readers. Regarding the assignment of specific lesion diagnoses, the difference in accuracy improvement between the 2 groups was <20% for 2 out of 3 blinded readers. There was a clear improvement in all 3 readers' level of confidence in post-contrast diagnosis relative to unenhanced ultrasound. Sonazoid-enhanced ultrasound provided a statistically significant improvement in specificity for all 3 readers (p=0.0093, <0.0001, 0.0011), as did SonoVue-enhanced

ultrasound for two readers, i.e. Reader 1 (p=0.0023) and Reader 2 (p=0.034). There was a statistically significant improvement in accuracy for Reader 2 (p=0.033) with Sonazoid and for Reader 1 (p=0.012) with SonoVue.

Both contrast agents were well tolerated.

Conclusion

Data from this study clearly demonstrate that the efficacy of Sonazoid in diagnosing FLLs as benign or malignant or assigning a specific diagnosis is very comparable to that of SonoVue. In the majority of pre-contrast cases level of confidence was ‘probable’ (i.e., the reader would have ordered another diagnostic imaging test such as MRI or CT) whereas in the majority of post-contrast cases it was ‘definite’ (i.e., the reader was sufficiently confident that another diagnostic imaging test such as MRI or CT was unnecessary) with both Sonazoid and SonoVue. Results underline the benefit of CEUS with Sonazoid imaging over non-enhanced imaging in reaching a confident diagnosis without having to refer patients for additional imaging exams.

Optimized quantification of thyroid nodular vascularization from 3-D contrast-enhanced ultrasound images

C. Caresio,[1] M. Caballo, M. Deandrea,[2] R. Garberoglio,[3] A. Mormile,[2] R. Rossetto,[4] P. Limone,[2] F. Molinari[1]

[1]*Biolab, Department of Electronics and Telecommunication, Politecnico di Torino, Turin, Italy*
[2]*Endocrinology Section "Umberto I" Hospital, Ordine Mauriziano di Torino, University of Turin, Turin, Italy*
[3]*Fondazione Scientifica Mauriziana ONLUS, Torino, Italy*
[4]*Division of Endocrinology, Diabetology and Metabolism, Department of Medical Sciences, University of Turin, Turin, Italy*

Introduction

Thyroid nodules represent a common finding in clinical practice and occur in up to 50% of the worldwide population. Even if the number of new thyroid cancers has considerably risen in the last decade, only 5% of thyroid nodules are malignant (incidence: 2.1%, mortality 0.5%, Globocan 2012). Differential diagnosis is, therefore, of paramount importance for a correct treatment of the nodule. Conventional ultrasound imaging has a moderate diagnostic accuracy (sensitivity: 68-100%, specificity: 67-94%, [1]) in the differentiation of thyroid nodules, and it must be coupled to fine needle aspiration (FNA) biopsy. However, FNA biopsy is an invasive procedure subject to inconclusive diagnosis in about 25% of the cases [2], possibly leading to overtreatment and unneeded surgery.

Contrast-enhanced ultrasound imaging (CEUS) has been introduced to improve the differential diagnosis of solitary thyroid nodules [1], [3], [4] . CEUS results in a better vasculature representation of thyroid healthy tissue and nodules compared with conventional Doppler imaging ([1], [5]). CEUS can boost the differential diagnosis of thyroid nodules if a quantitative and robust characterization of the vascularization is made possible.

Hence, the aim of our study was to develop a quantitative methodology for 3-D analysis of thyroid nodules' vascular network based on 3-D CEUS images. In this work, we improved a previous method [5] by optimizing the representation of the vascular tree.

Methods

Patients and ultrasound equipment

Twenty patients (3 Males, age 43.00 ± 10.40 y, 17 Females, age 46,00 ± 13.28 y) with solitary solid thyroid nodule were selected in the study. All subjects underwent a clinical examination, hormonal profiling, and FNA biopsy. Among the 20 nodules, 10 were benign and 10 had confirmed histological diagnosis of malignancy. 3-D CEUS volumes were acquired after the injection of 2.5-ml ultrasound contrast agent (SonoVue Bracco, Milan, Italy) using a MyLab™ Twice ultrasound device (Esaote, Genova, Italy), equipped with a linear-volumetric array transducer with 4-13 MHz variable frequency.

3-D vascular segmentation algorithm

We developed an innovative technique for rapid and automated representation and quantification of cancer vascular architecture. The algorithm consists of the following steps: i) starting from the CEUS volume (Figure 1.b) an initial step of preprocessing based on a Vessel Enhancement Filter [6] for noise suppression and contrast improvement (Figure 1.c) is performed; ii) a 3-D iterative thinning process is used to obtain the

morphological skeleton of the tumor vascular network (Figure 1.d); iii) a mathematical-based centerline extraction is applied [7] (Figure 1.e and 1.f). The skeleton in Figure 1.f is used for the quantitative analysis.

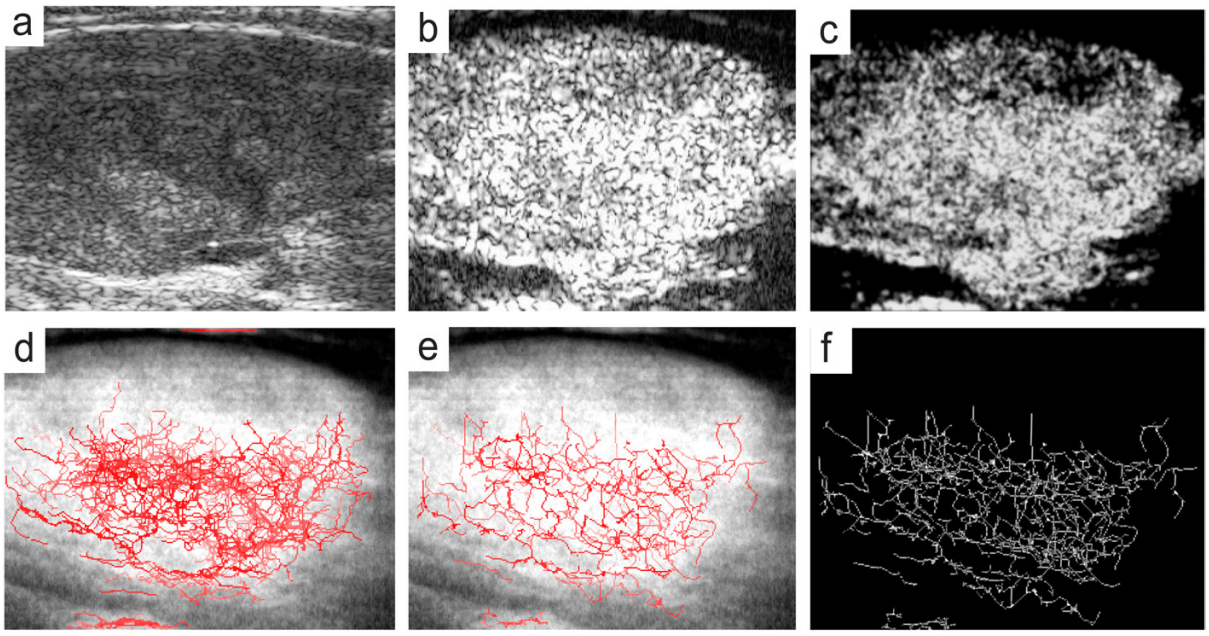

Figure 1: Vascular segmentation algorithm steps: (a) B-Mode slice of a malignant nodule; (b) CEUS slice; (c) Vessel enhancement filtering; (d) Morphological skeleton (e) Intensity flow centerline (f) 3- D skeleton rendering.

Features extraction and data analysis

Seven features were calculated from the 3-D skeleton. The first three were tortuosity metrics [8]: Distance Metric (DM), Inflection Count Metric (ICM) and Sum Of Angles Metric (SOAM). The last four were architectural parameters [9]: number of trees (NT), number of branches (NB), vascular volume density (VVD) and spatial vascularity pattern (SPV). The parameter SPV provided a discrete result of the spatial distribution of blood vessels in the tumor as perilesional or intranodular. For the two group of tumors, mean values and standard deviation for the continuous features were reported. The comparison between benign and malignant nodules was performed using a non-parametric Mann-Whitney U-test.

Multivariate Analysis of Variance (MANOVA) was used to test the equality of the means between benign and malignant nodules, considering the patient age, patient gender and the seven vascular features.

Results

In Table 1, mean values ± standard deviations of the six continuous features and the discrete parameter SVP are reported for the two nodules groups. Vascular continuous parameters are all higher for malignant nodules. The result of the Mann-Whitney U-test shows a significant difference between the benign and malignant nodules. For the SVP feature, 6 out of 10 benign nodules were labelled as perilesional while malignant nodules were all classified as intranodular (10/10). To conduct MANOVA, after removing the collinear variables, five features were left (ICM, VVD, NT, SVP and patient age). The MANOVA dimension of the group means was equal to 1 ($p << 0.001$), which indicated that, in the MANOVA hyperplane, the first canonical variable is discriminant for the nodule type and benign and malignant nodules can be linearly separated (Figure 2).

CEUS	Benign Nodules	Malignant Nodules	p-value
DM (a.u.)	13.91 ± 8.31	82.93 ± 49.38	<< 0.05
ICM (a.u.)	35.78 ± 18.63	227.62 ± 93.97	<< 0.05
SOAM (a.u)	4.28 ± 3.19	26.51 ± 21.19	<< 0.05
VVD (%)	30.30 ± 11.40	60.30 ± 7.11	<< 0.05
NT (a.u.)	5.30 ± 1.34	8.40 ± 2.79	<< 0.05
NB (a.u.)	18.30 ± 5.83	53.70 ± 17.72	<< 0.05
SVP (a.u.)	6/10	10/10	<< 0.05

Table 1: Mean values ± standard deviation and p-value of the 6 vascular features analyzed for CEUS volumes. The SVP is reported as a fraction of perilesional benign tumor and intranodular malignant tumors on the total number of tumor of the respective group.

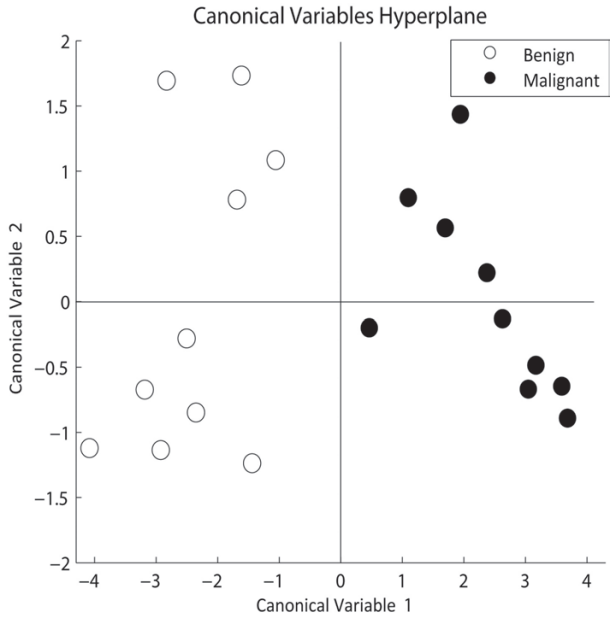

Figure 2: Representation of patients in the plane of the first two canonical variables obtained by MANOVA. The vascular features ICM, VVD, NT, SVP and patient age allow for a clear separation of the patients on the basis of the tumor type (benign or malignant).

Conclusions

In this work, a new methodology applied on 3-D contrast-enhanced ultrasound images was presented in the characterization of thyroid nodules. Innovative image processing techniques combined with vascular features extraction enabled the assessment of thyroid nodules; in fact, malignant lesions showed higher vascular features compared to benign nodules. These findings suggest that malignant lesions are highly perfused due to the increase in the overall density of the vasculature in the lesion. In future work, the proposed methodology could be extended and applied to CEUS volumes in the characterization and localization of prostate cancer, complementing existing dynamic CEUS features [10], [11].

References

1. *D. Yu, Y. Han, and T. Chen, "Contrast-enhanced ultrasound for differentiation of benign and malignant thyroid lesions: meta-analysis.," Otolaryngol. Head. Neck Surg., vol. 151, no. 6, pp. 909–15, 2014.*
2. *D. N. Poller, Z. W. Baloch, G. Fadda, S. J. Johnson, M. Bongiovanni, A. Pontecorvi, and B. Cochand-Priollet, "Thyroid FNA: New classifications and new interpretations," Cancer Cytopathol., pp. 1–10, 2016.*
3. *X. Sui, H.-J. Liu, H.-L. Jia, and Q.-M. Fang, "Contrast-enhanced ultrasound and real-time elastography in the differential diagnosis of malignant and benign thyroid nodules.," Exp. Ther. Med., vol. 12, no. 2, pp. 783–791, 2016.*
4. *U. Nemec, S. F. Nemec, C. Novotny, M. Weber, C. Czerny, and C. R. Krestan, "Quantitative evaluation of contrast-enhanced ultrasound after intravenous administration of a microbubble contrast agent for differentiation of benign and malignant thyroid nodules: Assessment of diagnostic accuracy," Eur. Radiol., vol. 22, no. 6, pp. 1357–1365, 2012.*
5. *F. Molinari, A. Mantovani, M. Deandrea, P. Limone, R. Garberoglio, and J. S. Suri, "Characterization of Single Thyroid Nodules by Contrast-Enhanced 3-D Ultrasound," Ultrasound Med. Biol., vol. 36, no. 10, pp. 1616–1625, 2010.*
6. *A. F. Frangi, W. J. Niessen, K. L. Vincken, and M. a Viergever, "Multiscale vessel enhancement filtering," Medial Image Comput. Comput. Invervention - MICCAI'98. Lect. Notes Comput. Sci. vol 1496, vol. 1496, pp. 130–137, 1998.*
7. *S. R. Aylward and E. Bullitt, "Initialization, noise, singularities, and scale in height ridge traversal for tubular object centerline extraction," IEEE Trans. Med. Imaging, vol. 21, no. 2, pp. 61–75, 2002.*
8. *E. Bullitt, G. Gerig, S. M. Pizer, W. Lin, and S. R. Aylward, "Measuring Tortuosity of the Intracerebral Vasculature from MRA Images," IEEE Trans Med Imaging, vol. 22, no. 9, pp. 1163–1171, 2003.*
9. *S. Huang, R. Chang, S. Member, W. K. Moon, Y. Lee, D. Chen, and J. S. Suri, "Analysis of Tumor Vascularity Using Ultrasound Images," Vascular, vol. 27, no. 3, pp. 320–330, 2008.*
10. *R. van Sloun, L. Demi, A. Postema, J. de la Rosette, H. Wijkstra, and M. Mischi, "Entropy of Ultrasound-Contrast-Agent Velocity Fields for Angiogenesis Imaging in Prostate Cancer," IEEE Trans. Med. Imaging, vol. 62, no., 2016.*
11. *R. J. van Sloun, L. Demi, A. W. Postema, J. J. de la Rosette, H. Wijkstra, and M. Mischi, "Ultrasound-contrast-agent dispersion and velocity imaging for prostate cancer localization," Med. Image Anal., vol. 35, pp. 610–619, 2017.*

Synovial vascular perfusion parameters derived from quantitative analysis of contrast-enhanced ultrasound correlates with pathogenic CD4+ T17 cells lineages in the psoriatic arthritis joints

E.Grisan,[1] G. Rizzo,[1] M. Tonietto,[1] A. Coran,[3] B. Raffeiner,[2,4] A. Scanu,[2] V. Martini,[2] D. Sacerdoti,[2] R. Stramare,[2] U. Fiocco[2]

[1] Department of Information Engineering, University of Padova, Padova (Italy)
[2] Department of Medicine, University of Padova, Padova (Italy)
[3] Veneto Institute of Oncology, Padova (Italy)
[4] Rheumathology Unit, Bolzano Hospital, Bolzano (Italy)

Background

Psoriatic arthritis (PsA) is a systemic immune-mediated disease, characterized by enthesitis, synovitis and osteitis, associated to skin psoriasis, with marked clinical heterogeneity. The interleukin IL23 pathway and IL17 cytokine axis play a critical role in the joint inflammation in PsA. The upregulation of the pro-inflammatory IL17 and IL23 axis in synovial tissue (ST) and synovial fluid (SF) induces a cascade of effects among which the production of IL-17$^+$ CD4$^+$ T helper cells (Th17) that showed a significant relation to the systemic disease activity, both at the onset and the progression of PsA and rheumatoid arthritis.

Objectives

The distinctive pathophysiology of PsA synovitis is characterized by a rapid vascular growth and tortuous blood vessels with inhomogeneous distribution: we aim at investigating the relationship between synovial perfusion patterns as seen by contrast enhanced ultrasound (CEUS) and Th17 cells expression.

Methods

Eight consecutive patients who fulfilled the Classification of Psoriatic ARthritis (CASPAR) criteria were enrolled in this study.

Each patient underwent ultrasound examination of the knee: gray scale and Power-Doppler ultrasound (PDUS) examination were performed immediately after the clinical examination, for anatomical reference and for the identification of the knee joint recess indicating the strongest vascularity. The latter was chosen for contrast-enhanced examination. A pixel-wise analysis of perfusion kinetics was performed. For each patient, a distribution of synovial perfusion parameters (time to peak, peak value, raise time, mean transit time, blood volume index) are summarized by four statistical descriptors (mean, standard deviation, 25th percentile and 75th percentile).

Additionally, synovial fluid samples were collected from the swollen knees. After centrifugation, the synovial fluid mononuclear cells were isolated, plated and incubated and immunostained. Mononuclear cells were treated with commercially available anti-CD4 antibodies. CD4$^+$ T cells were gated and then divided by FACS into the different CD4$^+$ T cells lineages that are linked to IL23-IL17 immune axis: CD4$^+$, CD4$^+$IL23$^+$, CD4$^+$IL17A-F$^+$, CD4$^+$IL17A-F$^+$IL23$^+$.

Results

We found that the local expression levels of 3 different Th17 cell lineages were significantly correlated with imaging perfusion estimates. In particular, $CD4^+$ T cells expression resulted correlated with the variability (as standard deviation) of the time to peak (ρ = -0.90 $p<0.01$), BVI (ρ = -0.86, $p<0.01$) and raise time (ρ = -0.86 $p<0.01$) and with the average MTT (ρ = 0.81 $p<0.05$). $CD4^+$ $IL17^+$ $IL23^+$ levels were correlated with the 75^{th} percentile of the peak value (ρ = 0.74, $p<0.05$), with the 25^{th} percentile of the MTT (ρ = -0.85, $p<0.01$), and with the 75^{th} percentile of the BVI (ρ = 0.80, $p<0.05$).). $CD4^+$ $L23^+$ levels did not resulted significantly correlated with any computed parameter, whereas $CD4^+$ $IL17^+$ levels were correlated with the average BVI (ρ = 0.71, $p<0.05$), and with the 75^{th} percentile of the BVI (ρ = 0.76, $p<0.05$).

Conclusions

Quantitative pixel-wise analysis of CEUS data allows the computation of perfusion parameters that are strongly correlated with expression of specific $CD4^+$ Th17 cells lineages, suggesting the possibility of their monitoring through accurate non-invasive CEUS perfusion imaging.

Safe and temporal opening of the blood brain barrier using Acoustic Cluster Therapy

Andreas K.O. Åslund,[1] Sofie Snipstad,[1] Andrew Healey,[2] Svein Kvåle,[2] Sverre H. Torp,[3,4] Per C. Sontum,[2] Catharina de Lange Davies,[1] Annemieke van Wamel[1].

[1] Department of Physics, Norwegian University of Science and Technology (NTNU), Trondheim, Norway;
[2] Phoenix Solutions AS, Oslo, Norway;
[3] Department of Pathology and Medical Genetics, St. Olavs University Hospital, Trondheim, Norway;
[4] Department of Laboratory Medicine, Children's and Women's Health, NTNU, Trondheim, Norway.

Introduction

The blood-brain barrier (BBB) maintains the homeostasis of the brain and protects it from unwanted or harmful substances. Unfortunately, the BBB also blocks >98% of small drugs (<600 Da) and all larger therapeutic molecules from entering the brain, unless active transport of the substances is possible [1]. Thus, the blood-brain barrier (BBB) is a major obstacle in drug delivery for diseases of the brain, and today there is no standardized route to surpass it.

One technique to locally and transiently disrupt the BBB, is focused ultrasound in combination with gas-filled microbubbles. Since its introduction in 2001 [2], focused ultrasound (FUS) in combination with microbubbles has been explored to increase the permeability of the BBB in various pre-clinical settings [3]. Whereas the concept clearly holds merit, it also has limitations. The microbubbles need to be close to the endothelial wall to maximize biomechanical effects [4,5]. Regular contrast microbubbles are small (1-3 μm), and their average distance to the vessel wall is often too large to induce a significant biomechanical effect. Furthermore, the circulation lifetime of most microbubbles is typically in the order of 2-3 min, thus limiting the exposure time. Although conventional microbubbles have shown promise for opening the BBB and for drug delivery to the brain, these microbubbles were developed for diagnostic imaging, not for therapy.

A recently proposed concept for ultrasound mediated, targeted drug delivery; Acoustic Cluster Therapy (ACT), makes use of similar mechanisms as regular microbubbles, but addresses important shortcomings of the latter. Details of the ACT formulation concept are described previously [6-7]. The concept is visualized in figure 1. The ACT formulation is a mix of negatively charged microbubbles and positively charged microdroplets, with the ensuing formation of microbubble/microdroplet clusters from the electrostatic attraction between the two components. The ACT Cluster Dispersion for Injection may be co-administered with a regular medicament (e.g. chemotherapeutic) to induce locally enhanced uptake of the systemically injected drug. The clusters are small enough to be free flowing in the microvasculature after i.v. injection. When insonated with ultrasound, the microbubbles transfers energy to the microdroplets that vaporizes, forming bigger microbubbles. In this study, this activation step is done using a calibrated 1 MHz single element transducer (Imasonic SAS) at an MI of 0.28, a 4 μs pulse length, a pulse repetition frequency (PRF) of 1 kHz, for a duration of 30 sec, directed to a small section in one of the hemispheres in the rat brain. The 20-30 μm large bubbles transiently deposit in the local microvasculature, stopping the blood flow for some 5-10 minutes. Post activation, low MI (0.09) US with same frequency, pulse length, and PRF was applied for 10 minutes to induce controlled volume oscillations

Figure 1
Acoustic Cluster Therapy (ACT) mediated drug delivery to the brain

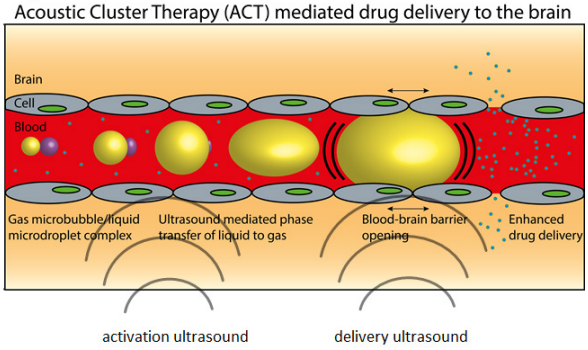

ensuing biomechanical effects to allow for enhanced extravasation and distribution of drug molecules to the targeted tissue.

Under gas anesthesia, healthy female Sprague Dawley rats (NTac:SD; Taconic, 8-12 weeks old, 240-280 grams) got the above described ACT treatment (1/8 diluted ACT formulation, 1 ml/kg) while Omniscan (1 ml/kg, 0.5 mmol gadododiamide/kg) and the near IRDye 800CW-PEG (10 nmol/kg) were circulating in the blood. BBB opening was confirmed with MR and Near IR imaging as seen in figure 2. The contralateral side of the treated position was used as an internal negative control. 1 h after ACT treatment, the animals were injected with pentobarbital and perfused with PBS, before the brain was removed and imaged with an infrared imager (Pearl Impulse Imager, LI-COR Biosciences Ltd.). Some animals only received Omniscan during ACT treatment. After BBB opening was confirmed, the rats were allowed to recover to be imaged with contrast MRI again at 3 days post treatment. A little gadodiamide extravasation into the brain was detectable for some animals, indicating that the BBB was close to or fully recovered.

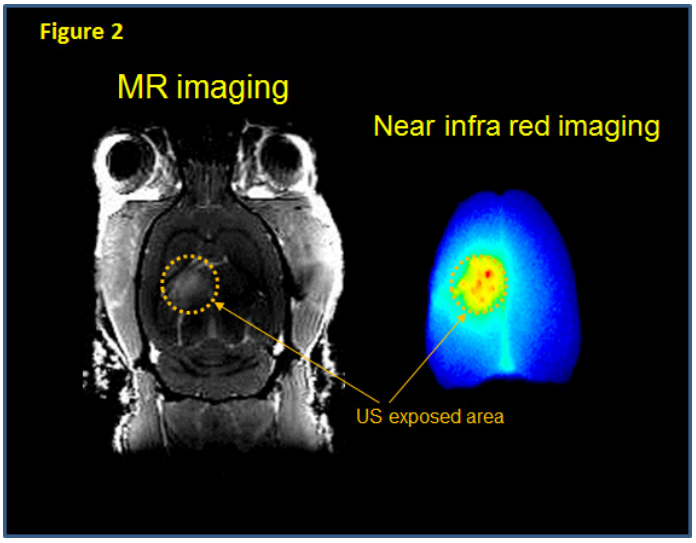

The in situ MI applied in this study was well below the threshold for what has previously been published as risk for damage to the brain/vasculature [8]. This is corroborated by the T1-FLASH MRI and haematoxylin-eosin-saffron-staining, which revealed no signs of hemorrhage. Only a few occurrences of focal micro-hemorrhages were found, but the damage scored mild and were of no clinical relevance. No signs of eosinophilic degeneration of neurons, gliosis, inflammation, or microglial/macrophage reaction were detected.

In conclusion, ACT was able to safely and temporarily permeabilize the BBB, using an acoustic power 5-10 times lower than applied for conventional microbubbles, and successful deliver small and large molecules into the brain.

References

1. *Pardridge WM. J Cereb Blood Flow Metab. 2012; 32: 1959-72.*
2. *Hynynen K, McDannold N, Vykhodtseva N, Jolesz FA. Radiology. 2001; 220: 640-6.*
3. *Etame AB, Diaz RJ, Smith CA, Mainprize TG, Hynynen K, Rutka JT.. Neurosurg Focus. 2012; 32: E3.*
4. *Liu HL, Fan CH, Ting CY, Yeh CK. Theranostics. 2014; 4: 432-44.*
5. *Kooiman K, Vos HJ, Versluis M, de Jong N. Adv Drug Deliv Rev. 2014; 72: 28-48.*
6. *P.C. Sontum, et al., Int J of Pharmaceutics, 2015; 495: 1019–1027.*
7. *A. J. Healey, et al., Ultrasound Med Biol, 2016; 42: 1145-66*
8. *McDannold N, Vykhodtseva N, Hynynen K. Ultrasound Med Biol. 2008; 34: 834-40.*

Sonoporation-sensitization by microbubble constituents?

Miles Aron,[a] Dario Carugo,[a] Oliver Vince,[a] Valerio Pereno,[a] Shamit Shrivastava,[a] Joshua Owen,[a] Erdinc Sezgin,[b] Jorge Bernardino de la Serna,[b] Marina Kuimova,[c] Christian Eggeling,[b,d] and Eleanor Stride[a]

[a]Department of Engineering Science, Institute of Biomedical Engineering, University of Oxford, Oxford OX3 7DQ, United Kingdom
[b]MRC Human Immunology Unit, Weatherall Institute of Molecular Medicine, University of Oxford, Headley Way, Oxford OX3 9DS, United Kingdom
[c]Department of Chemistry, Imperial College London, London SW7 2AZ, United Kingdom
[d]Wolfson Imaging Centre, Weatherall Institute of Molecular Medicine, University of Oxford, Headley Way, Oxford OX3 9DS, United Kingdom

The mechanisms underpinning sonoporation – the permeabilization of cell membranes following exposure to ultrasound and microbubbles – remain a source of considerable uncertainty[1]. Moreover, recent studies have indicated that reversible permeabilisation can be induced by extremely mild ultrasound exposure conditions[2,3]. In this study we investigate whether exposure to microbubbles *prior* to ultrasound exposure sensitizes cells to sonoporation through temporary modification of cell membrane physicochemical properties.

We employed quantitative fluorescence microscopy techniques to investigate microbubble–membrane interactions in both artificial and biological membrane bilayers in an acoustofluidic system. Material transfer from microbubbles to fluorescently-labelled cell membranes was observed following exposure to microbubbles containing a lipid mimetic fluorescent probe, DiI, and ultrasound (970 kHz, ~210 kPa, 60 s continuous wave). The lipid order of cell membranes, a key determinant of biophysical properties, was quantified before and after exposure using spectral imaging with polarity sensitive probe, C-Laurdan. The effects of ultrasound exposure, microbubble lipid chain length, polyethylene glycol (PEG) concentration, and microbubble washing by centrifugation, on the cell membrane response were evaluated. In parallel, sonoporation and viability were measured via propidium iodide and calcein AM fluorescence.

It was found that 1) the PEG used in many microbubble formulations, including clinically-available Definity® and SonoVue®, has a major impact on the cell membrane prior to ultrasound exposure and 2) lipid transfer, a candidate mechanism for enhanced drug delivery with encapsulated microbubbles[4–6], occurs in a microbubble formulation-dependent manner and can be quantified as a change in membrane lipid order.

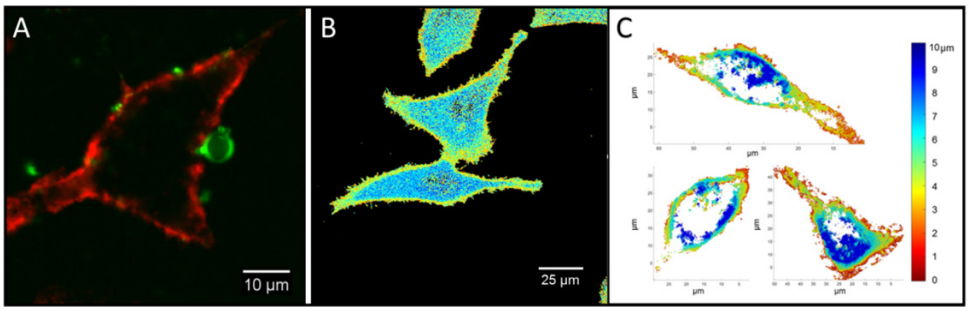

Figure: (a) DSPC-PEG40S microbubble labelled with DiI, a lipid-mimetic fluorescent probe (green) attached to an A-549 cell membrane (CellMask, red). (b) Map of the lipid order of cells quantified by generalised polarization from spectral imaging with polarity-sensitive probe, C-Laurdan. Lipid order increases from blue to red. (c) Maps of the 3D colocalization of DiI with A-549 cell membranes following ultrasound exposure of DiI-loaded DSPC-PEG40S microbubbles.

References

1. *Lentacker, I., De Cock, I., Deckers, R., De Smedt, S. C. & Moonen, C. T. W. Understanding ultrasound induced sonoporation: Definitions and underlying mechanisms. Adv. Drug Deliv. Rev.* ***72,*** *49–64 (2014).*
2. *Kooiman, K., Foppen-Harteveld, M., Der Steen, A. F. W. Van & De Jong, N. Sonoporation of endothelial cells by vibrating targeted microbubbles. J. Control. Release* ***154,*** *35–41 (2011).*
3. *Fan, Z., Liu, H., Mayer, M. & Deng, C. C. X. Spatiotemporally controlled single cell sonoporation. Proc. Natl. Acad. Sci. U. S. A.* ***109,*** *16486–16491 (2012).*
4. *Der Loughian, C. et al. Jumping acoustic bubbles on lipid bilayers. Soft Matter 3460–3469 (2015). doi:10.1039/c5sm00427f*
5. *Luan, Y. et al. Lipid shedding from single oscillating microbubbles. Ultrasound Med. Biol.* ***40,*** *1834–1846 (2014).*
6. *De Cock, I., Lajoinie, G., Versluis, M., De Smedt, S. C. & Lentacker, I. Sonoprinting and the importance of microbubble loading for the ultrasound mediated cellular delivery of nanoparticles. Biomaterials* ***83,*** *294–307 (2016).*

Simplified preparation of targeted bubbles for $\alpha_v\beta_3$ integrin based on a clinically available ultrasound contrast agent: Validation in a tumor-bearing mouse model

Kentaro Otani

Department of Regenerative Medicine and Tissue Engineering,
National Cerebral and Cardiovascular Center Research Institute, Suita, Japan

Background and aims

The usefulness of ultrasound molecular imaging with αvβ3 integrin-targeted bubbles for detecting tumor angiogenesis has been demonstrated. Recently, we developed αvβ3 integrin-targeted bubbles by modifying clinically available bubbles (Sonazoid) with lactadherin [1]. The aims of this study were to simplify the preparation of lactadherin-bearing Sonazoid by determining the optimal mixing ratio of lactadherin and Sonazoid, and to examine the diagnostic utility of lactadherin-bearing Sonazoid for αvβ3 integrin-expressing tumor vessels.

Materials ad Methods

Sonazoid (1.2 × 107 bubbles) was incubated with various amounts of Alexa Fluor 488-labeled lactadherin for 15 min at room temperature. By FACS analysis, the fluorescence intensity and labeling ratio of lactadherin-bearing Sonazoid prepared with ("conventional") or without ("w/o washing") the washing and centrifugation process were compared. The diagnostic utility of lactadherin-bearing Sonazoid for αvβ3 integrin-expressing tumor vessels was examined in SK-OV-3-tumor–bearing mice. Ten minutes after the intravenous infusion of lactadherin-bearing Sonazoid (6 × 106 bubbles), ultrasound molecular imaging with low mechanical index was performed; the increment in video intensity (ΔVI) was calculated and compared with that of Sonazoid.

Results

Although the fluorescence intensity of lactadherin-bearing Sonazoid increased concomitant with the added dose of Alexa Fluor 488–lactadherin, the labeling ratio reached a plateau between 1.0 μg and 10 μg Alexa Fluor 488–lactadherin (Figure 1). By incubating 1.2 × 107 Sonazoid bubbles with 1.0 μg lactadherin, lactadherin-bearing Sonazoid could be prepared by the "w/o washing" method, with no significant reduction in labeling ratio (w/o washing, 65.1% ± 4.2%, vs. conventional, 68.1% ± 2.1%). At day 8–9 after xenograft transplantation, the ΔVI value was significantly larger for lactadherin-bearing Sonazoid prepared by the w/o washing method (4.36 ± 1.39) than for Sonazoid (2.92 ± 0.82) (Figure 2).

Conclusion

This study demonstrated that the lactadherin-bearing Sonazoid is an easily prepared and potentially clinically translatable targeted bubble for $\alpha_v\beta_3$ integrin-expressing vessels.

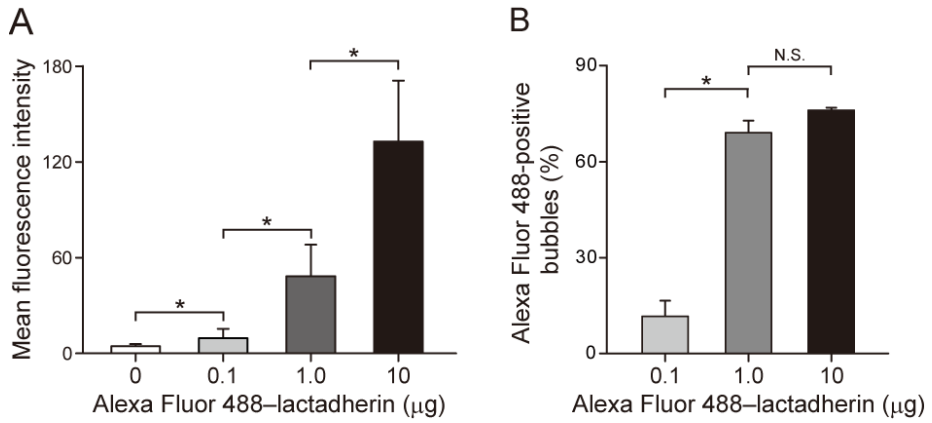

Figure 1. Mean fluorescent intensity and labeling ratio of Alexa Fluor 488-conjugated lactadherin-bearing Sonazoid. A) Mean fluorescence intensity of Sonazoid increased concomitant with the added dose of Alexa Fluor 488–lactadherin. B) Although the labeling ratio increased significantly between 0.1 and 1.0 μg of Alexa Fluor 488–lactadherin, a significant increase in labeling ratio did not occur between 1.0 and 10 μg of Alexa Fluor 488–lactadherin. N.S.; not significant, * $P < 0.05$.

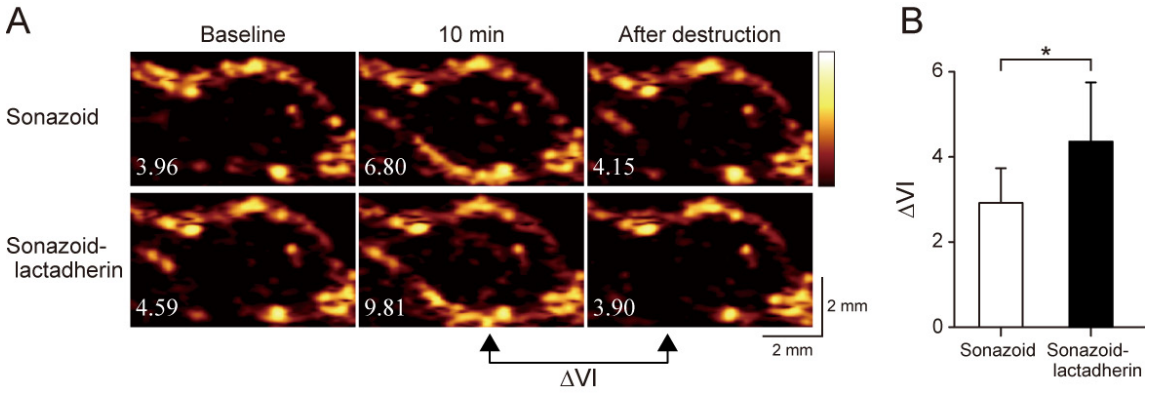

Figure 2. Ultrasound molecular imaging in tumor-bearing mice. A) Representative contrast images of tumors before (Baseline), 10 minutes after the administration of Sonazoid or lactadherin-bearing Sonazoid (10 min), and after the transient high-power ultrasound pulses (After destruction). Values in the lower left corner of each panel indicate the VI of the tumor. B) Comparison of ΔVI between Sonazoid and lactadherin-bearing Sonazoid. * $P < 0.05$.

Reference

1. *Otani K and Yamahara K. Feasibility of lactadherin-bearing clinically available microbubbles as ultrasound contrast agent for angiogenesis. Mol Imaging Biol 2013;15:534-41.*

Nanoparticle-stabilized microbubbles for ultrasound-mediated drug delivery and treatment of human breast adenocarcinoma in mice

Sofie Snipstad[1*], Sigrid Berg[2,3], Ýrr Mørch[4], Astrid Bjørkøy[1], Einar Sulheim[1,4], Rune Hansen[2,3], Annemieke van Wamel[1], Astri F. Maaland[1], Sverre H. Torp[5,6], Catharina de Lange Davies[1]

[1]Department of Physics, Norwegian University of Science and Technology (NTNU), Trondheim, Norway; [2]SINTEF Technology and Society, Trondheim, Norway; [3]Department of Circulation and Medical Imaging; NTNU, Norway; [4]SINTEF Materials and Chemistry, Trondheim, Norway; [5]Department of Laboratory Medicine, Children's and Women's Health, NTNU, Trondheim, Norway; [6]Department of Pathology and Medical Genetics, St. Olavs University Hospital, Trondheim, Norway; [*]Corresponding author: sofie.snipstad@ntnu.no

The use of multifunctional nanoparticles (NPs) opens new possibilities in cancer diagnostics and therapy. Leaky tumor vessels and nonfunctional lymphatics enable selective extravasation and accumulation of NPs in tumors. Encapsulation of drugs in NPs can thus improve pharmacokinetics, increase efficacy and reduce toxicity of the drugs compared to conventional chemotherapy. However, the permeability and vascularization varies greatly within and between tumors. Therefore, delivery of NPs is often insufficient, and the distribution of NPs in tumor tissue heterogeneous, so that the NPs and encapsulated drugs do not reach all the cells. Focused ultrasound (FUS), in particular when combined with gas filled microbubbles (MBs), has been reported to non-invasively improve the delivery of drugs and NPs to tumor tissue. At relatively low pressures, the acoustic pressure waves will cause stable cavitation of the MBs, resulting in microstreaming in the vasculature, and shear stresses on the blood vessel wall. At higher pressures, the oscillation will result in inertial cavitation and a violent collapse of the bubble, which leads to the formation of shock waves and jet streams in the vasculature. These effects can cause formation of small pores and increase the vascular permeability, increase extravasation across the capillary wall and potentially improve penetration through the extracellular matrix, thereby improving the uptake and distribution of NPs and drugs in tumors.

A novel multifunctional drug delivery system consisting of MBs stabilized by polymeric NPs to be used in ultrasound (US)-mediated drug delivery has been developed[1], as shown schematically in figure 1. These biodegradable poly(alkyl cyanoacrylate) (PACA) NPs can be prepared in a one-step synthesis, they can encapsulate drugs or contrast agents with high loading capacity, and can be functionalized with polyethylene glycol (PEG). We have previously characterized their cellular uptake and degradation[2], and shown that this platform can be employed to improve delivery of NPs to xenograft tumors in mice[3] and across the blood-brain barrier in healthy rats[4]. The main aim of the present study was to investigate the mechanisms of US-mediated delivery, to determine whether stable or inertial cavitation is the major mechanism for improved extravasation and enhanced NP delivery. The goal was to determine acoustically safe amplitudes which enhance the delivery of the nanomedicine to the tumor tissue, and to determine if the increased delivery has a therapeutic benefit. In previous work, poly(butyl cyanoacrylate) (PBCA) NPs were used, whereas poly(isohexyl cyanoacrylate) (PIHCA) NPs were used here. Due to a longer and branched alkyl monomer chain, they have a slower degradation rate, which might be therapeutically favorable.

To achieve successful and sufficient delivery of NPs to tumor tissue, the NPs have to circulate in blood for a sufficient amount of time, extravasate from the vasculature, penetrate the extracellular matrix and deliver their payload to the intracellular targets. Various aspects of these transport steps were investigated for our NPs. The

NPs were characterized with respect to in vitro cellular uptake in a breast cancer cell line (MDA-MB-231), using confocal laser scanning microscopy (CLSM) and flow cytometry. In vivo circulation half-life was determined by post-injection blood sampling from the saphenous vein in mice. The biodistribution of NPs was determined by imaging using a near infrared whole animal scanner. Circulation of the MBs was evaluated using contrast enhanced US imaging. To study how FUS combined with MBs enhances uptake of NPs in tumors, subcutaneous breast cancer xenografts were grown in athymic mice. MBs stabilized by NPs were injected intravenously before tumors were exposed to US treatments of various pressures and pulse lengths. A center frequency of 1MHz was used, with 10.000 cycles every 100 ms (local PRF 10 Hz) for 0.5 s, followed by 1.5 s break (global PRF 0.5 Hz, and total duty cycle 2.5 %), with acoustic pressures of 0.1, 0.25, 0.5 and 1 MPa. For the highest pressure, a short flash of 3 cycles was also investigated. The total treatment time was 2 min. The microdistribution of NPs was imaged on frozen tumor sections using CLSM, and the total uptake was quantified. No effects of low pressures (mechanical index (MI) 0.1 and 0.25) were observed, whereas collapse cavitation at higher pressures (MI 0.5) improved the tumor uptake by 2.5 times. An MI of 1 increased NP uptake with the longer pulse length, whereas the short flash did not. Except for the highest MI of 1, which caused substantial visual hemorrhage, evaluation of hematoxylin-eosin-saffron-stained tumor sections showed that all other FUS treatments were considered safe. This indicates a window where enhanced uptake can be achieved without damaging the tissue.

The therapeutic effect of our novel NP-MBs encapsulating the anticancer cytotoxic drug cabazitaxel in combination with US was demonstrated in a proof of concept study. Untreated animals showed a continuous tumor growth. All tumors treated with NP-MBs with cabazitaxel responded to treatment, and showed a reduced growth compared to control animals, but continued to grow 4 weeks after treatment. The tumors that received both NP-MBs with cabazitaxel and FUS, however, went into complete remission. This suggests that US treatment improved the accumulation and distribution of drug, and that this NP-MB platform is highly promising for controlled drug delivery and for future clinical applications.

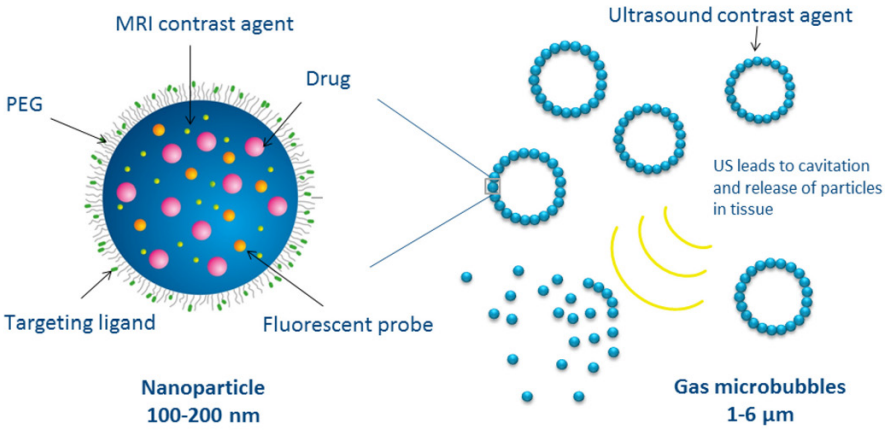

Figure 1: Schematic illustration of the NP-stabilized MBs to be used in US-mediated drug delivery[1].

References

1. *Y. Mørch et al., Contrast Media Mol Imaging 2015, 10, 356–366.*
2. *E. Sulheim et al., J Nanobiotechnology 2016, 14, 1.*
3. *S. Eggen et al., J Control Release 2014, 10, 39-49.*
4. *A. Åslund et al., J Control Release 2015, 28, 287-94.*

Spatial and Temporal Window for cisplatin delivery in a 3D culture model

Noboru Sasaki[1], Nobuki Kudo[2], Shouta MM.Nakayama[1], Kensuke Nakamura[1], Keitaro Morishita[1], Hiroshi Ohta[1], Mitsuyoshi Takiguchi[1]

[1] Graduate School of Veterinary Medicine, Hokkaido University, Sapporo, Japan
[2] Graduate School of Information and Sciences, Hokkaido University, Sapporo, Japan

Introduction

Multi-modality treatment for bladder cancer aims selective organ preservation with favorable outcome. Local delivery of chemotherapeutic agents may improve local disease control. Ultrasound-triggered microbubble cavitation is one of the promising drug delivery technologies for bladder cancer. Efficient drug penetration in tumor tissue and an increase in intracellular drug concentration are critical to developing clinical relevant US-mediated intravesical chemotherapy. Using a bladder cancer mimicking three-dimensional (3D) culture model, we investigated i) intracellular delivery of cisplatin; ii) extracellular delivery of cisplatin; iii) enhanced cytotoxic effect of cisplatin by US-triggered microbubble cavitation. We changed the culture volume of the 3D model in order to evaluate penetration profile of cisplatin into a 3D structure. In addition, an interval between sonication and addition of cisplatin was optimized.

Materials and Methods

Human urinary bladder cancer cells were mixed with collagen type-I and were seeded into a 35 mm culture dish at the volume of 50, 100, 150 and 200 microL. After culturing for 3 days, the gel mixture was exposed to non-focused ultrasound (center frequency 1 MHz, duty factor 50%, intensity 90 mW/cm^2, exposure time 1 min) in the presence of 6 microg/mL cisplatin and 1.3×10^6 microbubbles/mL. For platinum measurement, cells were harvested by collagenase from the gel right after the sonication and were separated from the dissolved gel. Cisplatin concentration was determined by measuring ^{195}Pt with an inductively coupled plasma mass spectrometer. For assessing cell viability, cells were culture for 4 days in the gel after the sonication; thereafter cells were harvested and counted manually. For the optimization of the interval between sonication and cisplatin, 100 microL of the cell-collagen mixture was seeded into a 35 mm culture dish. Ultrasound was exposed to the gel as mentioned above. Ultrasound was exposed to cells at the presence of cisplatin (i.e. 0 hr), 30 min, 1 hr, or 2 hr before addition of cisplatin. The cell viability was evaluated 4 days after the treatments.

Results

Intracellular Platinum concentration

Ultrasound-triggered microbubble cavitation increased the intracellular platinum concentration at the culture volume of 50 and 100 microL compared to cisplatin only, while not at the culture volume of 150 or 200 microL.

Extracellular platinum concentration

Sonication, either with or without microbubbles, did not increase the platinum level in the supernatant of dissolved gel at any culture volumes.

Cell viability

Ultrasound-triggered microbubble cavitation enhanced the cytotoxic effect of cisplatin at the culture volume of 50 and 100 microL, but not at the culture volume of 150 or 200 microL

Interval between sonication and cisplatin

Ultrasound-triggered microbubble cavitation enhanced the cytotoxic effect of cisplatin when ultrasound was exposed 1 hr, 30 min, or 0 hr before addition of cisplatin.

Discussion

The results of this study suggest that US-triggered microbubble cavitation delivers cisplatin into cells and thus enhances the cytotoxic effect of cisplatin at the culture volume of 50 and 100 microL. Because the culture surface area of the dish is approximately 10 cm^2, US-triggered microbubble cavitation in our setup may deliver cisplatin into cells at the distance of 100 micrometers from the gel surface. Moreover, the effects of US-triggered microbubble cavitation may continue for 1 hr after sonication. Although the effects of US-triggered microbubble cavitation were limited, optimization of US parameters and repetition of the treatments may improve the therapeutic efficacy. Further studies using the 3D culture will contribute to developing the US-assisted intravesical drug delivery for bladder cancer.

Microbubble and ultrasound-mediated mRNA transfection of porcine lymph nodes *in vivo*: Parameters, parameters, parameters…

Heleen Dewitte[a,b], Katrien Vanderperren[c], Emmelie Stock[c], Rein Verbeke[a], Benedicte Descamps[d], Christiaan Vanhove[d], Stefaan C. De Smedt[a] & Ine Lentacker[a]

[a]Laboratory for General Biochemistry and Physical Pharmacy, Faculty of Pharmacy, Ghent University, Ghent, Belgium. Heleen.Dewitte@UGent.be
[b]Laboratory of Molecular and Cellular Therapy, Department of Biomedical Sciences, Vrije Universiteit Brussel, Brussels, Belgium.
[c]Department of Veterinary Medical Imaging and Small Animal Orthopaedics, Faculty of Veterinary Medicine, Ghent University, Merelbeke, Belgium.
[d]Infinity in vivo small animal imaging lab, Ghent University, Ghent, Belgium.

Introduction & aim

Cancer immunotherapy, where a patient's own immune system is harnessed in the battle against a tumor, is still on the rise. In order to activate dendritic cells (DCs), the most important initiators of immunity, they should be loaded with tumor antigens and activation signals. This way, these cells prime other cells of the immune system to selectively target and destroy cancerous cells[1]. As such, many efforts have been made to directly target these antigens and activation signals towards DCs *in vivo*. We previously reported on our strategy that uses microbubbles for ultrasound-triggered delivery of mRNA which encodes both tumor antigens as well as these activation signals. Using this strategy, we have been able to induce mRNA transfection in DCs, which were in turn capable of initiating powerful anti-tumor immune responses in mice[2].

To evaluate the *in vivo* potential of this strategy, this project aims to investigate the efficiency of microbubble-mediated delivery of mRNA in the lymph nodes of pigs, as these organs contain large numbers of DCs.

Study design

Freshly euthanized pigs were either injected subcutaneously (at the ankle) or intranodally (in the popliteal lymph nodes) with luciferase mRNA-loaded microbubbles or with mRNA-nanoparticles. In both cases, the presence of the microbubbles in the popliteal node was confirmed via contrast-enhanced ultrasound imaging (CEUS) using a 12-5 MHz linear transducer of a Philips iU-22 US scanner (MI=0.08). To achieve microbubble destruction in the lymph nodes, various strategies were used: (a) the preset "burst" function on the scanner, (b) the Power Doppler mode of the scanner, set at 100% amplitude or (c), the sonitron2100 at 1MHz with varying duty cycles and acoustic powers (MI=1.1 to 1.6). After exposure to ultrasound, the lymph nodes were excised, kept at 37°C until analysis via bioluminescence imaging 5h later.

Results & discussion

First of all, corresponding to our previous results in dogs[3], the microbubbles quickly and extensively drained to the lymph nodes upon subcutaneous injection. No difference in CEUS enhancement of the lymph nodes could be observed between intranodal or subcutaneous injection of the microbubbles.

When looking at microbubble disruption using the 3 different ultrasound protocols, it was clear that microbubble disruption was incomplete when the "burst" function on the scanner was used. More, but still incomplete disruption was observed with the Power Doppler function, but using the sonitron2100, all ultrasound settings resulted in complete microbubble destruction. When the microbubbles had been injected

subcutaneously, replenishment of the lymph node with newly draining microbubbles could be observed within seconds after bursting the microbubbles.

When looking at the luciferase expression 5h after ultrasound application to the lymph nodes using an IVIS scanner, it was clear that the mRNA nanoparticles did not result in any transfection if no microbubbles or ultrasound were used, corresponding to our precious results[4]. In contrast, mRNA-loaded microbubbles injected intranodally and exposed to ultrasound, did show significant protein expression (Figure 1). As expected, the ultrasound settings are clearly crucial to achieve effective mRNA delivery, as only the sonitron2100 at different ultrasound settings could cause any measurable transfection.

As a conclusion, it is clear that the optimization of ultrasound parameters is one of the most crucial parts in translating *in vitro* to *in vivo* results. Unfortunately, none of the parameters tested on the imaging scanner sufficed to effectively implode the microbubbles and deliver the mRNA. On the other hand, the sonitron2100 did allow sonoporation, but this device merely allows limited control over the acoustic parameters, rendering it difficult to determine the optimal parameters for sonoporation *in vivo*. This underscores the need for novel, more controllable devices that allow both CEUS imaging and sonoporation.

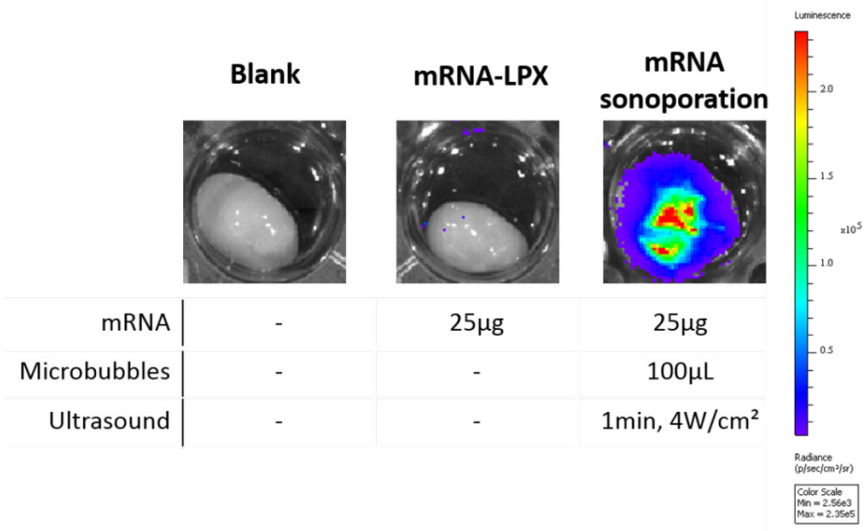

Figure 1: luminescence imaging of porcine lymph nodes 5h after injection with saline (blank), mRNA nanoparticles (mRNA-LPX) or mRNA-loaded microbubbles followed by ultrasound exposure using the sonitron2100 at 4W/cm² (~1.5MPa) (mRNA sonoporation).

References

1. *Palucka, K. & Banchereau, J. Dendritic-Cell-Based Therapeutic Cancer Vaccines. Immunity **39**, 38-48 (2013).*
2. *Dewitte, H. et al. The potential of antigen and TriMix sonoporation using mRNA-loaded microbubbles for ultrasound-triggered cancer immunotherapy. Journal of Controlled Release **194**, 28-36 (2014).*
3. *Dewitte, H. et al. Theranostic mRNA-loaded microbubbles in the lymphatics of dogs: implications for drug delivery. Theranostics **5**, 97-109 (2015).*
4. *De Temmerman, M.L. et al. mRNA-Lipoplex loaded microbubble contrast agents for ultrasound-assisted transfection of dendritic cells. Biomaterials **32**, 9128-9135 (2011).*

The effect of pulse length on perfusion kinetics following sonoreperfusion therapy

François T.H.Yu, Gary Yu, Xucai Chen, Linda Lavery, Flordeliza Villanueva and John Pacella

Center for Ultrasound and Molecular Imaging and Therapeutics, University of Pittsburgh School of Medicine, Pittsburgh, Pennsylvania, USA,

Background

Microembolization during PCI for acute myocardial infarction can cause microvascular obstruction (MVO). MVO severely limits the success of reperfusion therapies, is associated with additional myonecrosis, and is linked to worse prognosis, including death. A recent clinical trial showed that adjunct short pulse MB+US therapy prior to and following PCI in patients presenting with a first STEMI, not only improved angiographic recanalization prior to PCI, but also decreased the proportion of obstructed microvascular segments and improved ejection fraction at 1 month.1 This study demonstrated the clinical potential of short pulse high mechanical index MB+US as an adjunct therapy for patients presenting with STEMI. Based on our historical success with using long tone burst ultrasound for SRP in a rat hindlimb model of MVO, 2 we sought to compare the use of short (5 cycles) and long (5000 cycles) ultrasound pulsing schemes for sonoreperfusion therapy.

Methods

In an intact rat hindlimb, we applied therapeutic ultrasound with a single element transducer (A302S, 0.5 inch, Olympus, Waltham, MA) using long pulses (1 MHz, 1.5 MPa, 5000 cycles, 3 sec pulse interval) or bursts of short pulses (1 MHz, 1.5 MPa, 5 cycles, 1 ms pulse interval, 1 sec ON, 2 sec OFF) with the same total number of acoustic cycles, for 2 min, during intra-femoral infusion of lipid encapsulated perfluorobutane filled microbubbles (3.5 ±1.5 μm). Burst-replenishment imaging of the rat hindlimb muscle was performed using a clinical Sequoia ultrasound scanner in contrast mode (CPS, 7 MHz, 0.2 MI) during jugular venous infusion of Definity (2 mL/hr) to monitor the kinetics of perfusion for 30 min following therapeutic ultrasound (4-5 rats/group). Image intensities of the acquired perfusion cineloops were measured in regions of interest located under the therapeutic ultrasound beam to calculate the percentage of bright pixels (arbitrary threshold) and the perfusion rate (A×B) in the microvasculature. Statistical analysis was performed using 2-way ANOVA and Sidak post-hoc testing (Prism 6, Graphpad software, La Jolla, CA).

Results

Typical frames at 1 sec post burst in the burst replenishment cineloops are shown in figure 1 at different time points after 2 min of SRP therapy for the short and the long cycle pulses. Both short and long pulses resulted in increased perfusion (brightness), however the temporal responses were distinct. For the short pulses, brightness immediately increased post SRP but dissipated over 30 min. Conversely, with the long pulses, brightness increased starting at 6 min post SRP and persisted up to 30 min post SRP.

We further quantified these video sequences by computing the % bright pixels in the ROI at 1 sec post burst and the microvascular flow rate (A×B) in the ROI (excluding the large vessels). For the short pulse, the % bright pixels at 1 sec post burst was significantly higher post SRP compared to baseline (55.5±13.1% vs. 22.3±15.5%, $p<0.05$) and was statistically higher than that with the long pulse. The flow rate numerically increased post SRP but the difference did not reach statistical significance compared to baseline. However, the flow rate was higher than that with the long pulse immediately post SRP. With the long pulse, the % bright pixels gradually increased from 10.5±3.7 % at baseline to 75.1±13.7 % ($p<0.05$) at 10 min and 79.4±12.8% ($p<0.05$) at 30 min post SRP. These values were also significantly higher than that with the short pulse. The

flow rate initially dropped but started increasing at 3 min post SRP and reached 14.1±7.9 dB/s at 10 min post SRP and 10.4±4.4 dB/s at 30 min post SRP, which were both significantly higher than baseline (3.1±1.2 dB/s) and higher than that with the short pulse.

Conclusions:

These data strongly support that short and long pulses can both improve sonoreperfusion therapy as measured using contrast burst-replenishment imaging. The short pulse increased perfusion immediately following SRP but the effect started to decrease with time. Conversely, the long pulse caused a delayed effect with a sustained improvement in perfusion starting at 6 min and persisting for at least 30 min after therapy.

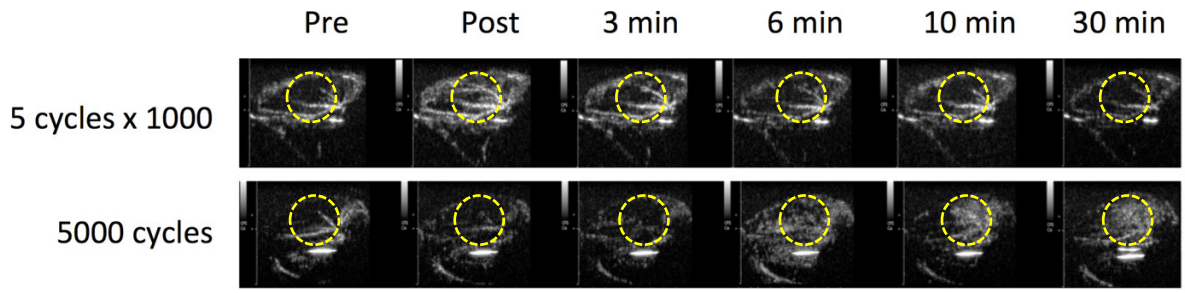

Figure 1: Typical still frames taken 1s post burst in burst reperfusion cineloops at different time points after SRP therapy using either short or long pulse therapeutic ultrasound. Yellow circles indicates location of therapeutic ultrasound beam

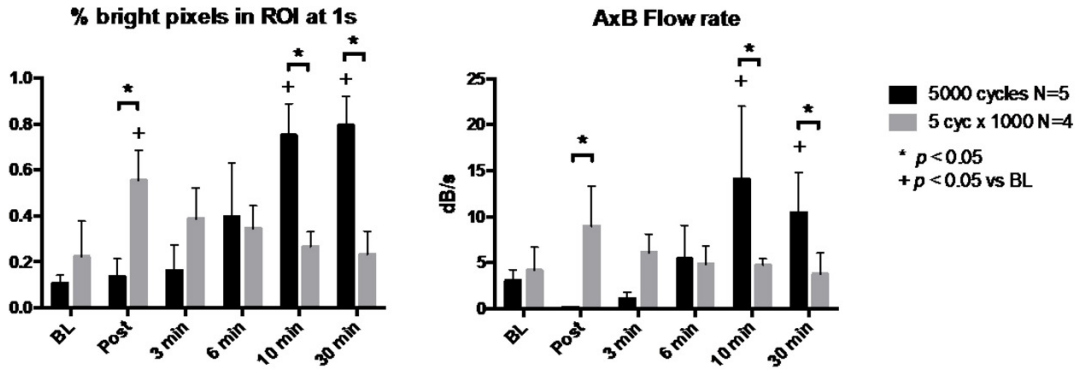

Figure 2: (a) Percentage of bright pixels (above arbitrary threshold) in ROI at 1 sec post burst and (b) Microvascular flow rate at different time points following SRP therapy for short and long SRP pulses.

References

1. *Mathias W, Jr., Tsutsui JM, Tavares BG, Xie F, Aguiar MO, Garcia DR, Oliveira MT, Jr., Soeiro A, Nicolau JC, Lemos PAN, Rochitte CE, Ramires JA, Kalil RF and Porter TR. Diagnostic Ultrasound Impulses Improve Microvascular Flow in Patients With STEMI Receiving Intravenous Microbubbles. J Am Coll Cardiol. 2016;67:2506-15.*
2. *Pacella JJ, Brands J, Schnatz FG, Black JJ, Chen X and Villanueva FS. Treatment of microvascular micro-embolization using microbubbles and long-tone-burst ultrasound: an in vivo study. Ultrasound Med Biol. 2015;41:456-64.*

Sonobactericide as an adjunct therapy to treat infective endocarditis: an *in vitro* demonstration of an ultrasound, microbubble, and thrombolytic-based treatment

Kirby R. Lattwein[1, 2, 3], Himanshu Shekhar[2], Willem J.B. van Wamel[3], Andrew B. Herr[4], Christy K. Holland[2], and Klazina Kooiman[1]

[1]Dept. of Biomedical Engineering, Thorax Center, Erasmus MC, Rotterdam, the Netherlands
[2]Dept. of Internal Medicine, Div. of Cardiovascular Health and Diseases, U. Cincinnati, Cincinnati, OH, USA
[3]Dept. of Medical Microbiology and Infectious Diseases, Erasmus MC, Rotterdam, the Netherlands
[4]Div. of Immunobiology, Cincinnati Children's Hospital MC, Cincinnati, OH, USA

Introduction

Infective endocarditis (IE) is a bacterial infection of the endocardial and prosthetic valvular surfaces in the heart. IE is associated with high morbidity and mortality (15-40% in-hospital and 35-69% 5-year mortality rates) [1, 2, 3]. The predominant bacteria causing this infection are Staphylococci, with *Staphylococcus aureus* (*S. aureus*) having the single highest prevalence (30-31%), associated with higher mortality, and a worse prognosis [1, 2]. These bacteria can bind to existing thrombi and generate vegetations (biofilms) on heart valves. IE is challenging to cure because both the immune system and antibiotics are often ineffective against the biofilm-encased bacteria [1, 2, 3]. In this *in vitro* study, we report a novel strategy called sonobactericide to treat IE using ultrasound and an ultrasound contrast agent, in combination with an antibiotic and a thrombolytic.

Methods

We developed an *in vitro* model of IE vegetations using human whole blood clots retracted around a silk suture, infected with the bacteria, *S. aureus* (Fig. 1A). Clots were manufactured with human blood drawn according to an institutional review board approved protocol. Histological examination using hematoxylin and eosin (H&E) staining and crystal violet (CV) staining was performed to assess the structure of clots qualitatively to validate the IE model. The viability of bacteria in the infected clots was determined using confocal laser scanning microscopy with fluorescence from the LIVE/DEAD® BacLight™ kit. Infected clots were treated in an established *in vitro* flow model (Fig.1B) and lytic efficacy was assessed by analyzing time-lapse microscopy images over 30 minutes using custom MATLAB program [4, 5]. Infected clots were exposed to continuous human plasma flow (0.65 mL/min) either alone or with different combinations of the following: oxacillin (clinical dose of 172 µg/mL), recombinant tissue plasminogen activator (rt-PA; clinical dose of 3.15 µg/mL), intermittent (50 s on, 30 s off) continuous-wave ultrasound (120 kHz, 0.44 MPa peak-to-peak pressure), and ultrasound contrast agent Definity (2 µl/ml). The fractional clot width loss at 30 min was used to quantify the extent of infected clot degradation, and was computed for each treatment arm.

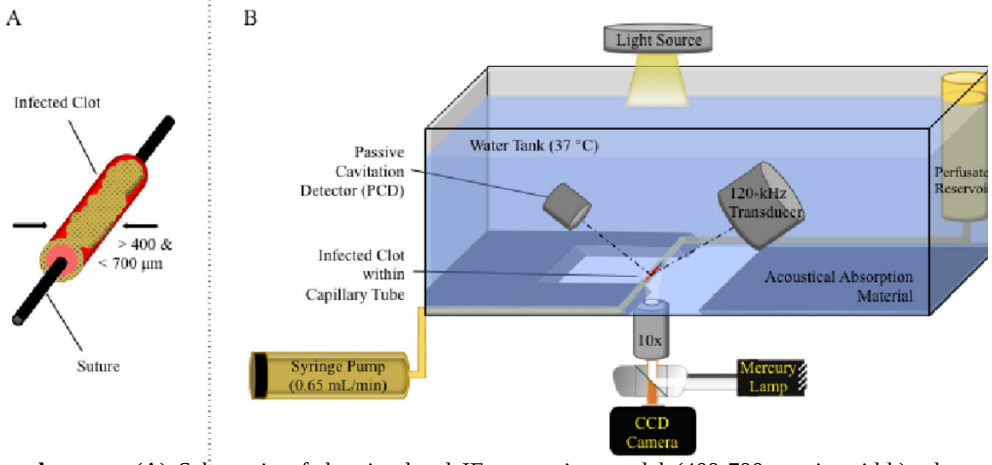

Figure 1. Experimental set-up. (A) Schematic of the simulated IE vegetation model (400-700 µm in width) where the infected clot composed of bacteria (yellow) and clot (red) are produced on a suture (black) (not drawn to scale). (B) Illustration depicting the combined optical imaging and acoustical field set-up of the in vitro infected clot on a suture flow model (not drawn to scale).

Results and Discussion

A cross section of the infected clot stained with H&E (Fig. 2A) revealed a dense erythrocyte mass (dark pink) around a suture (black arrow with solid line). The inner portions of the clots were comprised of fibrin, erythrocytes, and sporadic immune cells. H&E revealed an outer layer of biofilm consisting of bacteria embedded in a fibrin mesh, which was confirmed with CV-stained gram-positive bacteria (Fig. 2B). Confocal

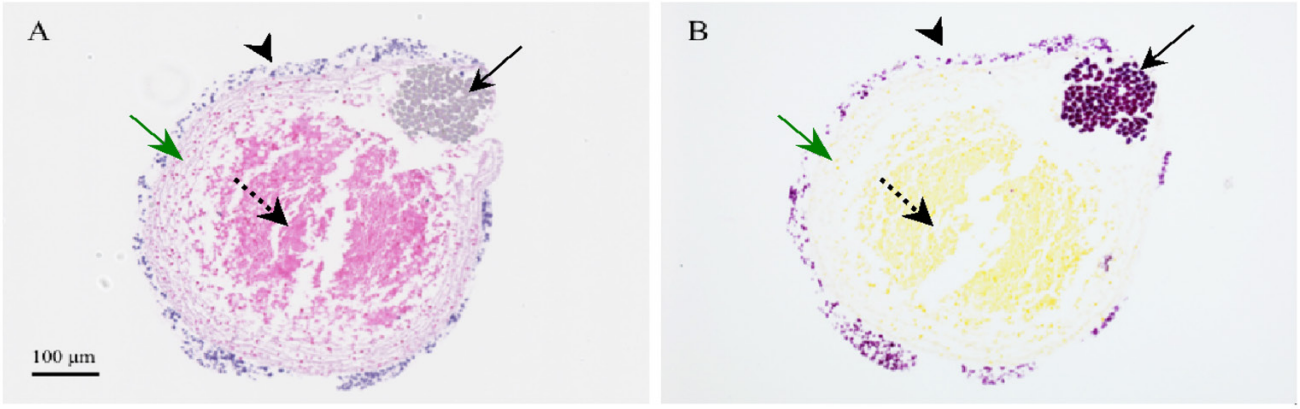

Figure 2. Cross-sectional histological staining of infected clots. Hematoxylin-eosin staining is depicted in (A) and crystal violet in (B). Black arrows indicate the suture within the clot. The black arrowhead without a line indicates bacteria (purple in (A) and (B)), a green arrow for fibrin (light pink in (A), light yellow in (B)), and a black arrow with a dashed line for erythrocytes (dark pink in (A), dark yellow in (B)). Both photographs are at 10x magnification.

microscopy images showed biofilms lining the clots, which were comprised of predominately viable bacteria. Both histology and confocal microscopy showed that the biofilms were heterogeneous of variable thickness, which is typical of biofilm growth [6]. These findings are consistent with the structure of IE vegetations found in patient samples [7].

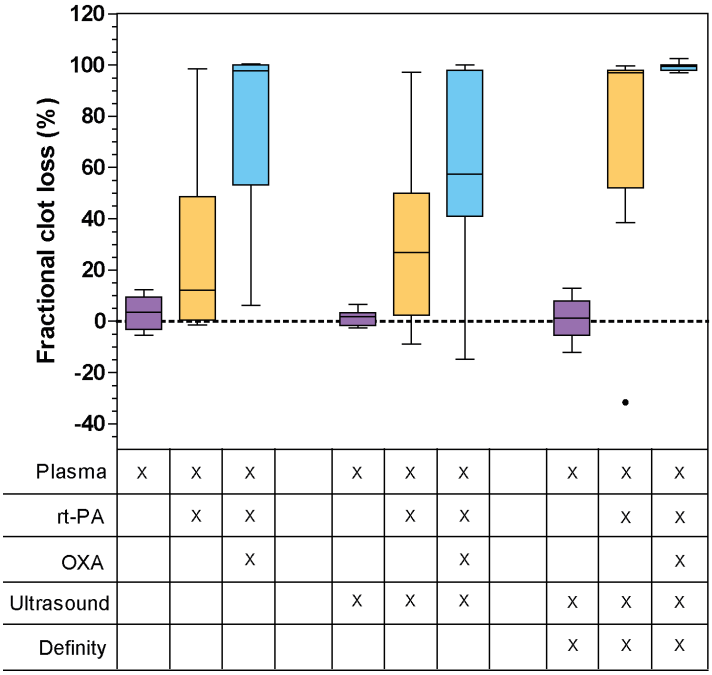

Figure 3. Fractional clot width loss of infected clots after treatment. Boxes represent the interquartile range. The lines within the boxes represent the median and the whiskers indicate 1.5 times the interquartile range. The circle depicts an outlier using Tukey method. The treatment conditions are given in the table below the graph. OXA = antibiotic.

As shown in Figure 3, the flow rate provided minimal degradation of the infected clot due to the mechanical shear stress and endogenous t-PA from plasma flow alone. When rt-PA was added, clot width loss was highly variable with an average loss of 26%. After the addition of the antibiotic with rt-PA and plasma, the average clot width loss increased to 78%. Similar amounts of degradation as the plasma alone group were seen when ultrasound alone, or ultrasound with Definity, was used as a treatment. Infected clots exposed to the combination of oxacillin, rt-PA, ultrasound, and Definity achieved almost 100% loss (99.3 ± 1.7%) for all clots, which was more than any of the other treatment arms.

Conclusion

This study presents a novel method termed sonobactericide, which may have potential as an adjunct therapy for IE. The IE vegetation model developed for this research resembled the initial pathogenesis of IE, and composed of the similar components as IE vegetations found in patient samples. The simulated IE vegetations were treated under flow *in vitro*. The use of ultrasound and Definity, in combination with oxacillin and rt-PA, achieved almost 100% vegetation loss. Further investigation is necessary to establish sonobactericide as a novel therapeutic strategy for treating IE and possibly other biofilm diseases.

Acknowledgements

This research was financially supported by the Netherlands Heart Foundation (student grant 2016SB001 to K.R.L., E. Dekker program), the I & I Fund (Infection and Immunity Master Program, Molecular Medicine Postgraduate School, Erasmus MC; grant to K.R.L.), and the Erasmus Medical Center (fellowship to K.K.). The authors thank all the members from the Image-guided Ultrasound Therapeutics Laboratories at the U. of Cincinnati, Tammy Gonzales from the Div. of Immunobiology at Cincinnati Children's Hospital, for their technical assistance and useful discussions. The authors are grateful to Joel Mortensen (Cincinnati Children's Hospital, Dept. of Laboratory Medicine) for providing the clinical bacterial isolate, and David Witte (Cincinnati Children's Hospital, Dept. of Pathology) and King Lam (Erasmus MC, Dept. of Pathology) for interpretation of histology.

References

1. *Werdan K., et al. (2014) Nature Reviews Cardiology; 11: 35-50.*
2. *Cahill T.J., et al. (2016) Lancet; 387: 882-93.*
3. *Mirabel M., et al. (2014) Eur Heart J; 35: 1195-204.*
4. *Bader K.B., et al. (2015) Ultrasound in Medicine and Biology; 41(1): 187-96.*
5. *Gruber M.J., et al. (2014) Journal of Acoustical Society of America; 135(2): 646-653*
6. *Archer N.K., et al. (2011) Virulence; 2: 445-59.*
7. *Thiene G., et al. (2006) Cardiovasc Pathol; 15: 256-63.*

Velocity vector imaging based on time-delay estimation: applications to angiogenic perfusion and cardiac flow analysis

Ruud JG van Sloun[1], Libertario Demi[1], Arnoud W Postema[2], Salvatore Saporito[1], Ingeborg HF Herold[3], Patrick Houthuizen[3], Hendrikus HM Korsten[3,1], Hessel Wijkstra[2, 1] and Massimo Mischi[1]

[1]Dept. of Electrical Engineering, Lab. of Biomedical Diagnostics, Eindhoven University of Technology, the Netherlands
[2]AMC University Hospital, Amsterdam, the Netherlands.
[3]Catharina Hospital, Eindhoven, the Netherlands.

Introduction

Visualization and interpretation of blood flow patterns is of interest in several healthcare applications ranging from cardiology to oncology. In cardiology, blood flow through the ventricles is determined by the valves, chamber geometry and wall motion, and carries relevant information linked to myocardial morphology and function of the cardiovascular system. A tool that permits its visualization may hence provide clinicians with important diagnostic and prognostic clues related to ventricle dysfunction and cardiac disease. Velocity vector imaging with echocardiographic particle velocimetry is such a tool [1]. Supported by recent advances in ultrafast ultrasound imaging, this approach typically exploits high frame rate ultrasound to facilitate accurate and reliable velocity estimation based on speckle-tracking techniques.

In oncology, visualization of flow patterns can be exploited to reveal tumor-driven angiogenesis; an important marker for cancer disease progression. Blood flow in angiogenic vasculature is complex and heterogeneous, governed by factors such as increased microvascular density, arteriovenous shunting, irregular branching, vessel tortuosity, and increased flow resistance. In this regard, characterizing the macroscopic flow patterns that arise from these contributions may provide diagnostic value. The state-of-art speckle-tracking methods in echographic particle image velocimetry are however not directly applicable to this problem.

The main argument against the use of these approaches is that the movement of the underlying scatterers (microbubbles) that form the local speckle pattern cannot be modelled as a simple translation from one frame to the next. Block matching algorithms for speckle-tracking require this condition to be valid at least to some extent. Where frame-to-frame de-correlation already presents problems for the high and complex flow in the cardiac chamber (in particular for lower frame-rates [2]) the complex microbubble kinetics in the microvasculature yields almost instantaneous speckle de-correlation. To avoid this problem, super-localization technologies aim at isolating single microbubbles that can be tracked using ultrafast ultrasound. Reconstruction of the complete velocity field would require relatively long acquisition times however.

Here we describe a new dynamic contrast-enhanced ultrasound (DCE-US) method that enables velocity vector imaging in both perfused organs as well as large blood pools as found in the cardiac chambers. The method estimates time delays amongst the indicator dilution curves measured at a set of pixels to infer a local velocity vector. The proposed method is applied to two cases: We first test the method's applicability to angiogenesis imaging in prostate cancer, by analyzing and characterizing the velocity vector images obtained from DCE-US acquisitions in 24 patients to predict the histopathological outcome [3]. We then show an initial proof-of-concept for the method's applicability to time-varying cardiac flow visualization using DCE-US imaging data acquired at a frame rate as low as 23 Hz.

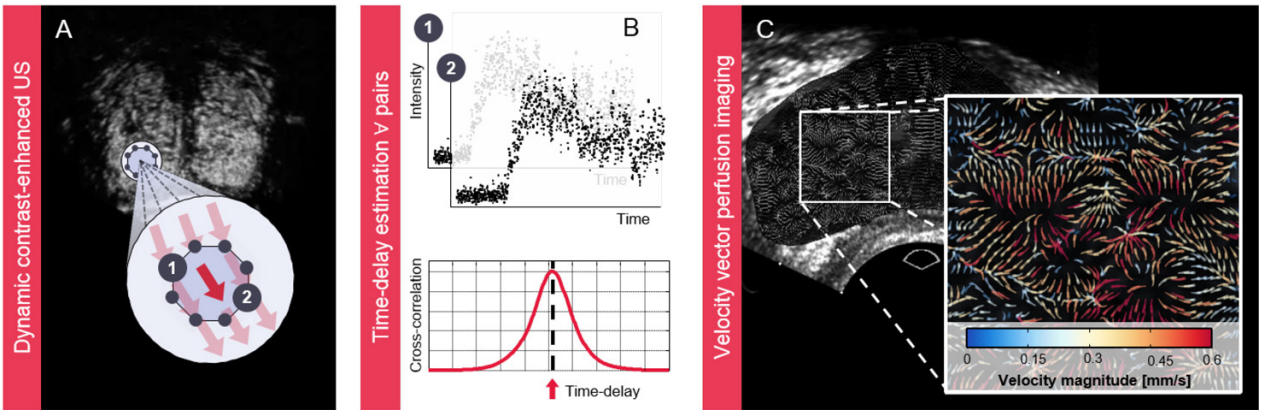

Figure 1 (A,B) Overview of the proposed velocity vector imaging method. First, the time-delays amongst all pairs of time-intensity curves obtained at a set of pixels in the DCE-US video are estimated by maximizing their cross-correlation vectors. Then, the least squares problem relating these time-delays to inter-pixel distance vectors is solved to retrieve a dominant velocity vector. (C) This procedure is repeated to form a vector velocity image, as shown here for an acquisition of the prostate. Note the ability to measure apparent velocities well below 1 mm/s.

Methods

Data acquisition

The DCE-US prostate investigations were performed at the AMC University Hospital (Amsterdam, The Netherlands). In total, 24 patients with biopsy-proven prostate cancer scheduled for radical prostatectomy were included in this study. An intravenous injection of a 2.4-mL SonoVue® (Bracco, Milan, Italy) bolus was administered, after which its passage through the prostate was imaged using a 2D transrectal ultrasound probe (C10-3v) and a Philips iU22 ultrasound scanner (Philips Healthcare, Andover, MA, USA). A power-modulation pulse scheme at 3.5 MHz was used to enhance sensitivity to microbubbles while suppressing linear backscattering from tissue. The mechanical index (MI) was set to 0.06. The frame rate was 10 Hz.

DCE-US echocardiography of a heart-failure patient was performed at the Catharina Hospital (Eindhoven, The Netherlands) three months after cardiac resynchronization therapy. The patient was a non-responder and had an ejection fraction of 10.6%. An intravenous injection of a 1:100 saline-diluted 10-mL SonoVue® (Bracco, Milan, Italy) bolus was administered, and trans-thoracic imaging was performed using an S5-1 sector array transducer and a Philips iE33 ultrasound scanner (Philips Healthcare, Andover, MA, USA). A power modulation pulse scheme was employed. The MI was 0.19 and the frame rate was 23 Hz.

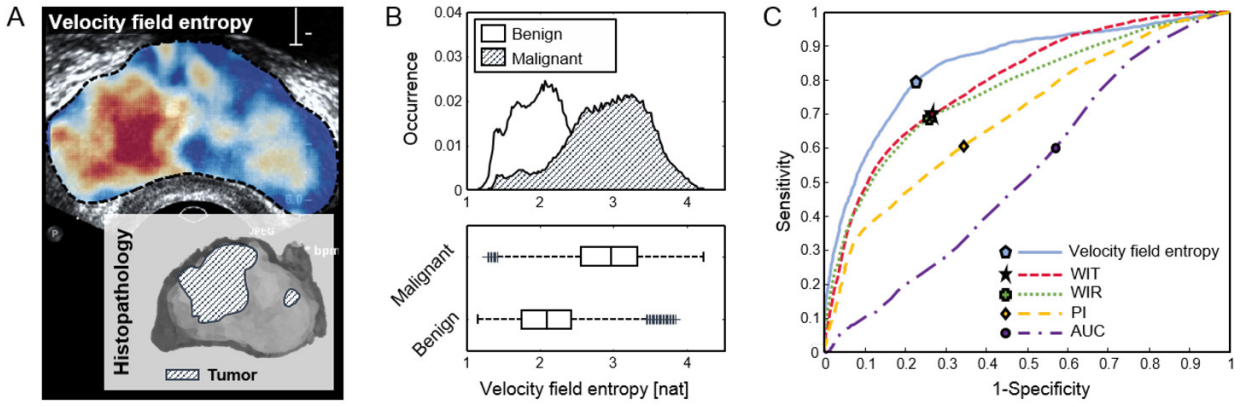

Figure 2 Statistical characterization of velocity vector fields for angiogenesis imaging. (A) The entropy of the velocity vector field qualitatively indicates the tumor location as confirmed by histopathology. (B) Histograms and box-plots of benign and malignant pixels taken from regions of interest distributed across 24 patients. (C) Receiver-operator-characteristics curve of pixel-based classification with velocity field entropy compared against those obtained using wash-in time (WIT), wash-in rate (WIR), peak intensity (PI) and area under the dilution curve (AUC).

Velocity vector imaging

For the purpose of estimating the velocity vector at a certain location, we consider the indicator dilution curves (IDCs) that are measured at a specific set of imaging pixels around this location: N pixels distributed on a circle with radius R (see figure 1). Assuming the transport of ultrasound contrast agents between two distinct pixels in this set to be convection-dominated, the measured IDC at one pixel may be modelled as a time-delayed version of another. This time-delay can be estimated by maximizing the cross correlation function between the two IDCs. We then collect all time delays amongst all the IDCs from the set in an array $\boldsymbol{\tau}$. The relation between $\boldsymbol{\tau}$, the matrix describing all inter-pixel distance vectors, D, and the dominant local velocity vector, $\vec{v}$, can be described as $\vec{v}^T\boldsymbol{\tau} = D$, which is solved for $\boldsymbol{v}$ by least squares minimization. This procedure is repeated for all pixels covering the prostate to produce a velocity vector image.

Angiogenesis characterization

Angiogenic flow characterization was performed by computing the local entropy of the velocity vector fields. This measure of flow heterogeneity was then validated against histopathology in 24 patients with prostate cancer. In total, 52 benign regions-of-interest and 53 malignant regions of interest were considered. The kernel parameters N and R were set to 8 and 0.9 mm, respectively.

Cardiac flow patterns

Time-varying cardiac flow patterns were derived by performing time-delay estimation on a moving window basis. The cross-correlation function was interpolated by fitting a parabola around its peak to facilitate the extraction of high resolution time-delay estimates that are required for high flow rates. The kernel parameters N and R were set to 12 and 3 mm, respectively.

Results

Figure 1C shows an example of velocity vector imaging in a human prostate. Figure 2 indicates that the velocity field entropy is significantly higher in areas with malignancy. Its classification performance for detecting prostate cancer was assessed and compared to other quantification methods (figure 2C), yielding a receiver-operator-characteristics curve area of 0.85, along with an optimal sensitivity and specificity of 80% and 79%, respectively. These statistics where lower for all other evaluated parameters. In Figure 3, an example of velocity vector imaging for left ventricular blood flow analysis is given. One can appreciate the time-varying flow patterns and vortex formation that are typical for the left ventricular blood flow [4],[5].

Conclusions

We presented a new method for DCE-US velocity vector imaging based on time-delay estimation that is applicable to quantification of flow in perfused organs (such as the prostate), as well as analysis of flow patterns in large blood pools such as the left ventricle. While the method's application for angiogenesis characterization already shows diagnostic relevance, clinical suitability for cardiac flow visualization remains to be validated. In this context, studying vortex formation related to cardiac pathology is of interest.

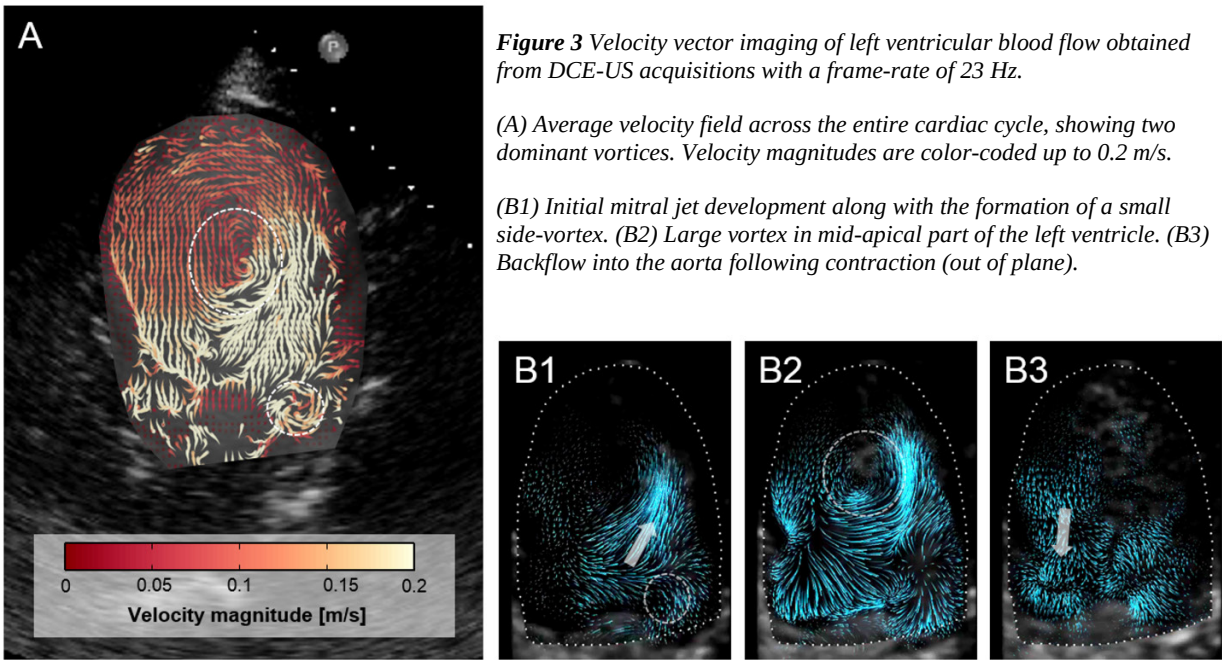

Figure 3 *Velocity vector imaging of left ventricular blood flow obtained from DCE-US acquisitions with a frame-rate of 23 Hz.*

(A) Average velocity field across the entire cardiac cycle, showing two dominant vortices. Velocity magnitudes are color-coded up to 0.2 m/s.

(B1) Initial mitral jet development along with the formation of a small side-vortex. (B2) Large vortex in mid-apical part of the left ventricle. (B3) Backflow into the aorta following contraction (out of plane).

References

1. *A. Kheradvar, H. Houle, G. Pedrizzetti, G. Tonti, T. Belcik, M. Ashraf, J. R. Lindner, M. Gharib, and D. Sahn, "Echocardiographic Particle Image Velocimetry : A Novel Technique for Quantification of Left Ventricular Blood Vorticity Pattern," J. Am. Soc. Echocardiogr., vol. 23, no. 1, pp. 86–94, 2010.*
2. *H. Gao, P. Claus, M. Amzulescu, I. Stankovic, J. D'hooge, and J. Voigt, "How to optimize intracardiac blood flow tracking by echocardiographic particle image velocimetry ? Exploring the influence of data acquisition using computer-generated data sets," Eur. Heart J., vol. 13, pp. 490–499, 2012.*
3. *R. J. G. Van Sloun, L. Demi, A. W. Postema, J. JMCH, D. Rosette, H. Wijkstra, and M. Mischi, "Entropy of Ultrasound-Contrast-Agent Velocity Fields for Angiogenesis Imaging in Prostate Cancer," IEEE Trans. Med. Imaging, 2016.*
4. *H. Abe, G. Caracciolo, A. Kheradvar, G. Pedrizzetti, B. K. Khandheria, J. Narula, and P. P. Sengupta, "Contrast echocardiography for assessing left ventricular vortex strength in heart failure : a prospective cohort study," Eur. Heart J., vol. 14, no. 11, pp. 1049–1060, 2013.*
5. *S. Cimino, G. Pedrizzetti, G. Tonti, E. Canali, V. Petronilli, L. De Luca, C. Iacoboni, and L. Agati, "European Journal of Mechanics B / Fluids In vivo analysis of intraventricular fluid dynamics in healthy hearts," Eur. J. Mech. B/Fluids, vol. 35, pp. 40–46, 2012.*

Stabilization and Coalescence of Monodisperse Microbubbles formed by Flow focusing

Tim Segers*, Anne Lassus, Philippe Bussat, Emmanuel Gaud, Samir Cherkaoui, and Peter Frinking

Bracco Suisse S.A., Geneva, Switzerland
**e-mail: tim.segers@bracco.com*

Monodisperse microbubbles may increase the sensitivity of contrast enhanced ultrasound imaging. Even more interestingly, they may improve the efficiency of therapeutic applications with microbubbles and ultrasound, such as drug or gene delivery, sonoporation and blood-brain barrier opening. It has been demonstrated that monodisperse phospholipid-coated microbubbles can be directly produced in a flow-focusing device. However, only very specific phospholipid mixtures at high concentrations were shown to be able to sufficiently stabilize freshly formed bubbles against coalescence [1,2]. Moreover, microfluidically formed microbubbles appeared to be inherently unstable until they dissolved to reach their final size [1,3]. To date, the importance of the different components present in a typical lipid dispersion on coalescence and long-term stability are unknown. Here, we characterized coalescence and long-term size stability of microbubbles formed using lipid mixtures containing DPPC, DPPA, and DPPE-PEG, and we studied the effects of lipid concentration, PEG molecular weight, PEG molar ratio, and the temperature at which the bubbles are formed.

For all lipid formulations studied, a concentration-independent ratio between the initial and the final microbubble size was found for concentrations ranging from 1.0 to 40.0 mg/mL, indicating that the gas-liquid interface was fully saturated with lipids even at the lowest concentrations. However, coalescence was found to decrease quadratically with a linear concentration increase showing that the presence of liposomal particles between two colliding bubbles results in a repulsive colloidal force.

The role of the lipopolymer chain length on microbubble stabilization and coalescence was investigated at PEG molecular weights of 1000, 2000, 3000, and 5000. The pegylated lipids were mixed with DPPA and DPPC at a 1:1:8 molar ratio, respectively. It was found that the ratio of the size of the freshly formed bubble to that of the stable bubble increases with PEG molecular weight from a factor of 1.5, 1.7, 2.0, up to 2.3 for PEG molecular weights of 1000, 2000, 3000, and 5000, respectively, indicating that the size decrease during stabilization can be mainly attributed to a change in conformation of the polymer headgroup. Coalescence was found to decrease exponentially with PEG molecular weight revealing the importance of the steric repulsion force between pegylated liposomes and colliding microbubbles.

The effect of the relative amount of pegylated molecules with respect to the primary lipid components was studied at PEG molar ratios of 5, 10, 15, and 20% while the molar ratio between DPPC and DPPA was as before (8:1). The linear increase of the PEG molar ratio resulted in a linear increase of the ratio of the initial to the final bubble size. On the other hand, coalescence probability decreased exponentially with a linear increase in PEG molar ratio through an increase in liposome concentration, which is effectively due to a decrease in liposome size.

Temperature is known to have a strong influence on the conformation of phospholipid molecules in liposomes and monolayers. Therefore, coalescence and size stability were measured for temperatures ranging from well below, to well above, the phase transition temperature of the lipid dispersion. Coalescence was found to decrease exponentially with a linear temperature increase. This confirms the linear temperature dependence of steric and structural forces resulting from the liposomes [4]. Size decrease during stabilization was found to increase with temperature due to an increased surface area per lipid molecule at elevated temperatures.

This work therefore gives a fundamental insight in the physiochemical and thermodynamic properties of phospholipid monolayers adsorbed to microbubbles formed by flow-focusing. Moreover, it reveals the role of colloidal and surface forces in the stable production of monodisperse bubbles, and it provides a practical guide to the successful preparation of lipid mixtures suitable for stable monodisperse microbubble synthesis.

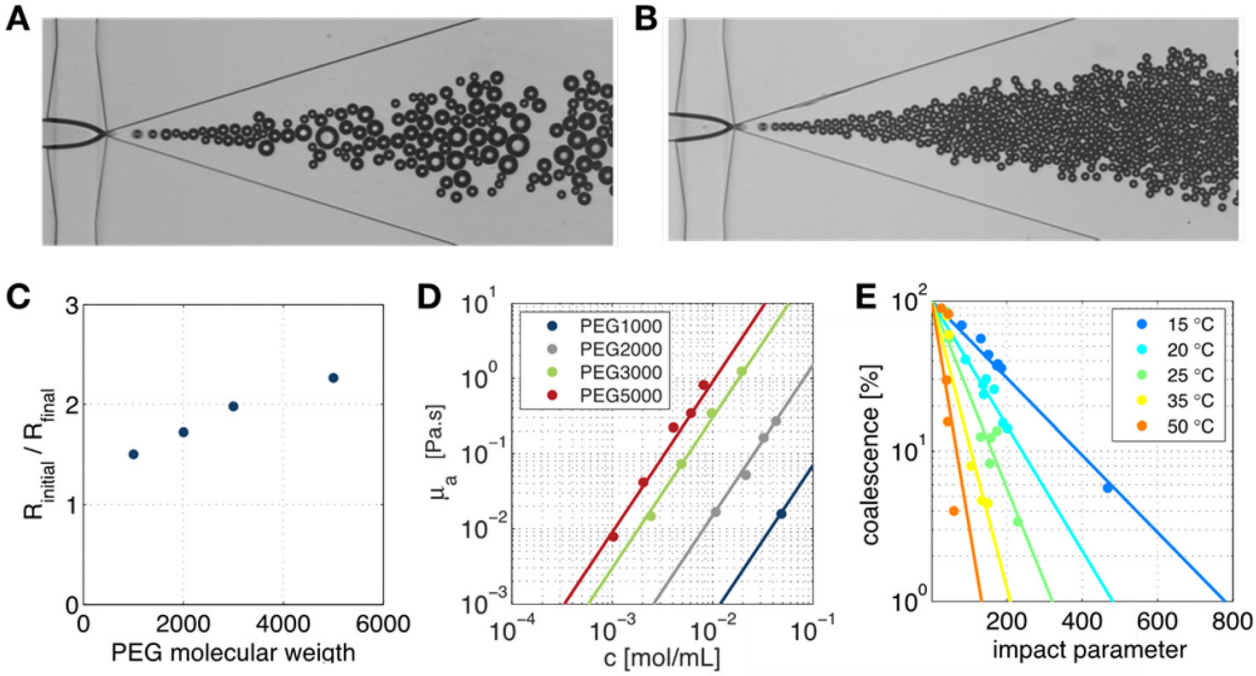

Figure 1 (A) Severe bubble coalescence is observed when a formulation with PEG2000 is used. (B) Coalescence decreases when DPPE-PEG5000 is used. (C) The ratio between the initial bubble size and the stable bubble size as a function of the PEG molecular weight. (D) The apparent viscosity increases quadratically with the lipid concentration and bubble coalescence decreases thereby quadratically with the lipid concentration. Moreover, coalescence decreases exponentially with PEG molar weight. (E) Coalescence decreases exponentially with a linear temperature increase.

References

1. *T. Segers, L. de Rond, N. de Jong, M. Borden, and M. Versluis, "Stability of monodisperse phospholipid-coated microbubbles formed by flow-focusing at high production rates," Langmuir 32(16), 3937–3944 (2016).*
2. *K. Hettiarachchi, E. Talu, M. L. Longo, P. A. Dayton, and A. P. Lee, "On- chip generation of microbubbles as a practical technology for manufacturing contrast agents for ultrasonic imaging," Lab. Chip 7(4), 463–468 (2007).*
3. *E. Talu, K. Hettiarachchi, R. J. Powell, A. P. Lee, P. A. Dayton, and M. L. Longo, "Maintaining monodispersity in a microbubble population formed by flow-focusing," Langmuir 24, 1745–1749 (2008).*
4. *Israelachvili, J. N. Intermolecular and Surface Forces, Vol. 2; Academic Press: Waltham, MA, USA, 1992.*

Microbubble Trapping, Imaging and Destruction for Targeted Drug Delivery

Luzhen Nie[1], Sevan Harput[1,2], David Cowell[1], Thomas Carpenter[1] , James McLaughlan[1,3], Steven Freear[1]

[1]School of Electronic and Electrical Engineering, University of Leeds, UK. LS2 9JT
[2]Department of Bioengineering, Imperial College London, London, SW7 2BP
[3]Division of Biomedical Imaging, University of Leeds, UK. LS2 9JT

Introduction

Accumulating therapeutic microbubbles (MBs) and releasing payload only at targeted sites offer great potential to improve the drug efficacy and minimize the systemic adverse effects. Previously MB manipulation with ultrasound mediated trapping force at physiologically relevant flow rates has proved feasible to facilitate targeted drug delivery [1, 2]. And in this work, steering of MBs, fast imaging and destruction sequences are interleaved with a same linear array medical ultrasound transducer. Once MBs are trapped, destructive pulses are applied to deliver therapeutic payload for therapy. Simultaneous fast imaging depicts the flow dynamics.

Verification of the simultaneous operation of trapping, destruction and imaging sequences is performed using microscopy. Optical imaging clarifies MBs can still be trapped during the fast switch between different excitation schemes.

Methods

A 128-element linear array medical probe is connected to the bespoke Leeds Ultrasound Array Research Platform II (UARP II) [3, 4] which undertakes arbitrary excitation generation and plane wave imaging (PWI). The ability to quickly switch between MB trapping, monitoring and destruction excitation schemes at kilo-Hertz results in high efficacy targeted drug delivery and ultrasound imaging at 1000 frames per second.

For the first instance, the probe is separated into two parts with equal 64 elements, out of phase pulses from two sub-apertures are transmitted simultaneously to destructively interfere along the center. Pressure null at the central line realizes an ultrasonic trap to stop MBs relying on steep pressure gradients [2]. The intensity of inlet beam is optimized by using aperture apodization and pulse width modulation [5] to attenuate MB velocity and also ensure MBs inflow to the trap region. Fig.1 details the calibrated pressures in water at the depth of 35 mm used in experiments.

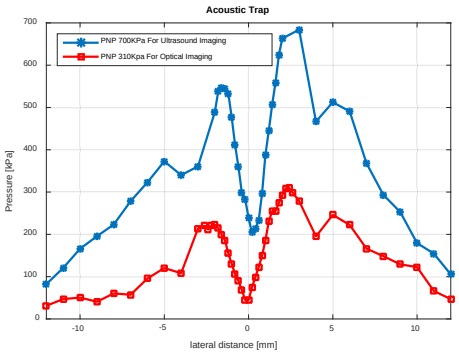

Fig.1. Beam profiles of two plane wave trapping beams with π phase shift for tissue mimicking flow phantom and flow cell under microscope at 35mm depth.

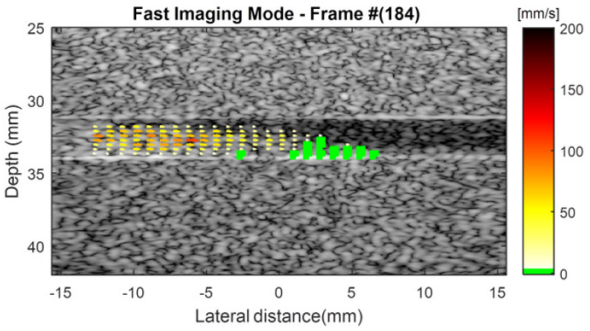

Fig.2. 2D encoded velocity map superimposed on corresponding B-mode image.

Focused beam with mechanical index of 0.7 with 10 us duration was prepared by transmitting 4.8 MHz sinusoidal excitations with the same transducer for destroying MBs. Imaging during trapping and destruction was achieved through single PWI pulse to retain MBs within the pressure null region when flow phantom was adopted.

Diluted MB solution was circulated through a 200 μm cellulose tube. Pure trapping sequence and trapping interleaved with pressure calibrated imaging pulse were transmitted respectively.

Preliminary Results and Discussions

MB solution with velocity up to 110 mm/s was flowed into a 3 mm wall-less tissue mimicking flow phantom, pulse repetition frequency (PRF) at 1 kHz for trapping and PWI imaging pulse switching. The 2D ultrasonic velocity map was encoded and superimposed on corresponding B-mode images (Fig.2). The trapping efficiency is refined by lower MB velocity than 4 mm/s (green dots in Fig.2) at designed trap site which ultimately increases the concentration of MBs. After undergoing ultrasound exposure from the inlet beam, it's not likely that speed of MBs reaches zero exactly. Ongoing flow was continuously impeded by the directly opposite radiation force from the outlet beam until the pressure summit which is located at the lateral profile of 2.5 mm in Fig.1. And after the peak pressure point, in-phase radiation force will push the MBs out of the trapping area and forward. This can clarify why green dots are denser just before MBs touch the peak pressure position in Fig.2.

Under microscope, the flow rate of 5 ml/h was set to achieve mean velocity of 28 mm/s [6] in the expanded cellulose tube when prefilled with water. Before the ultrasound source was activated, single flowing MBs are visible (Fig. 3a). Upon pure trapping sequence with PRF of 1 kHz, MB clusters with mean diameter around 20 μm were trapped still within the trapping region (several millimetres in length) for the whole period (25 seconds) when trapping force triggered (Fig. 3b). New MBs still continued to be flushed into the pressure null site but pushed to the far wall by the residual primary radiation force. Once the trapping sequence is stopped, MB clusters and MBs bonded to the back wall began dispersing (Fig. 3c). While high concentration of MBs can last for further several seconds in targeted site. Immediate MB rapture was achieved by subjecting MBs to high intensity acoustic field (Fig. 3d). No obvious experimental uncertainty was observed when interleaving trapping and pressure calibrated imaging sequences with the same PRF at 1 kHz. MB clusters can be also retained for the whole 25 seconds (Fig. 3e) and again MB accumulation along the back wall was refined by Fig. 3f when releasing trapping force. MBs vanish naturally with time, and same MB solution used through the experiment was contributed to fewer MB clusters as well as bonded MBs in Fig. 3f.

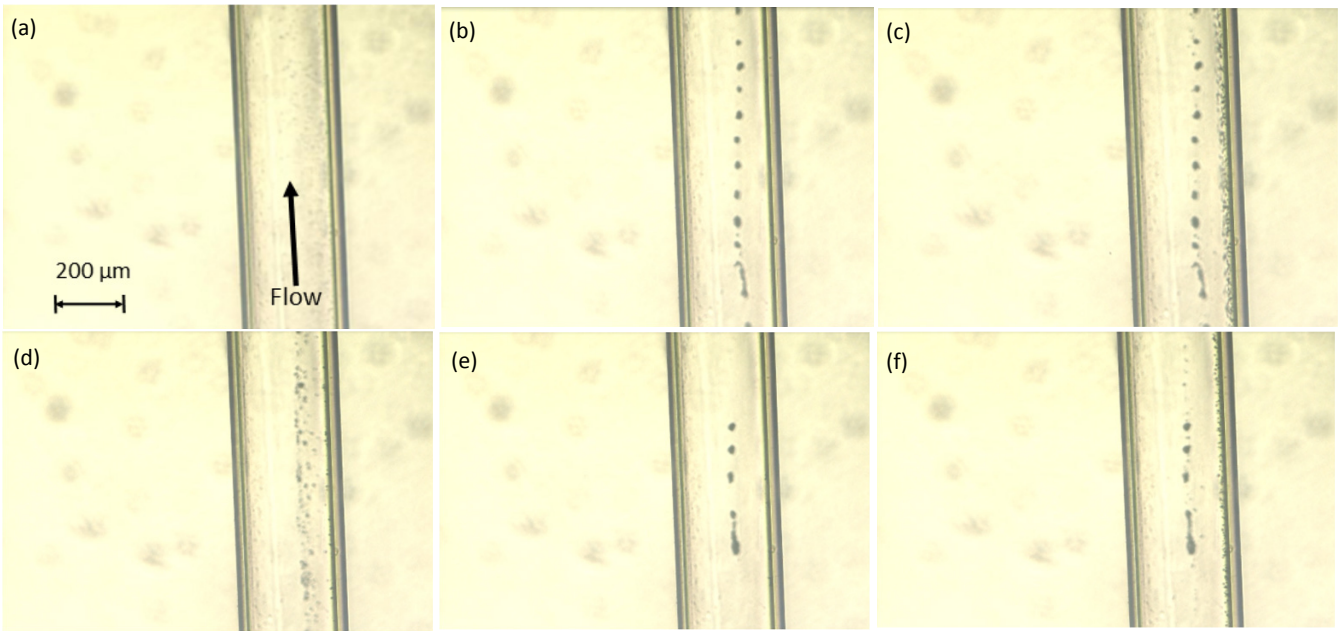

Fig.3. Micrograph images of microbubbles captured with the ultrasonic trap. (a) MBs in flow. (b) Trapped MB clusters. (c) High concentration can be reserved for further several seconds after release of the pure trapping sequence. (d) MB rapture. (e) Still MB clusters can be trapped when interleaving trapping and imaging sequences. (f) High concentration is observed which is similar to (c).

Conclusions

In conclusion, the ultrasonic trapping technique can increase the population of MBs at the target area. When coupled with destructive pulses, potentially localised drug release can occur and minimize systematic side effects. During therapy, PWI can monitor the process continuously while retaining MBs in targeted site at high frame rates, which is crucial for analysing the MB behaviour and flow dynamics. Preliminary optical imaging results indicate that interleaving trapping, imaging and destruction sequences with the same probe at KHz frame rate is realizable which finally provides a novel alternative for targeted drug delivery with therapeutic MBs.

References

1. *Harput, Sevan, et al. "Simultaneous trapping and imaging of microbubbles at clinically relevant flow rates." Ultrasonics Symposium (IUS), 2016 IEEE International. 2016.*
2. *Raiton, B., et al. "The capture of flowing microbubbles with an ultrasonic tap using acoustic radiation force." Applied Physics Letters 101.4 (2012): 044102.*
3. *Cowell, David MJ, Peter R. Smith, and Steven Freear. "Phase-inversion-based selective harmonic elimination (PI-SHE) in multi-level switched-mode tone-and frequency-modulated excitation." IEEE transactions on ultrasonics, ferroelectrics, and frequency control 60.6 (2013): 1084-1097.*
4. *Smith, Peter R., et al. "Ultrasound array transmitter architecture with high timing resolution using embedded phase-locked loops." IEEE transactions on ultrasonics, ferroelectrics, and frequency control 59.1 (2012): 40-49.*
5. *Smith, Peter R., David MJ Cowell, and Steven Freear. "Width-modulated square-wave pulses for ultrasound applications." IEEE transactions on ultrasonics, ferroelectrics, and frequency control 60.11 (2013): 2244-2256.*
6. *Tremblay-Darveau, Charles, et al. "Visualizing the Tumor Microvasculature With a Nonlinear Plane-Wave Doppler Imaging Scheme Based on Amplitude Modulation." IEEE transactions on medical imaging 35.2 (2016): 699-709.*

Questions in Super-Resolution Ultrasound Imaging with Microbubbles

J. Brown[a], K. Christensen-Jeffries[a], S. Harput[b], P. Aljabar[a], M. X. Tang[b†], C. Dunsby[c, d†], and R. J. Eckersley[a†].

[a] Biomedical Engineering Department, Division of Imaging Sciences, King's College London, London SE1 7EH, UK.
[b] Department of Bioengineering, Imperial College London, London SW7 2AZ, UK.
[c] Department of Physics, Imperial College London, London SW7 2AZ, UK.
[d] Centre for Histopathology, Imperial College London, London W12 0NN, UK.
[†] These authors contributed equally to this work.

There is a clinical need to detect changes to the microvasculature for diagnosis and treatment of diseases such as cancer and diabetes. Super-resolution ultrasound circumvents the fundamental physical limit on the smallest dimensions that can be visualised to enable imaging at the micron scale. By localising the isolated point spread functions of microbubbles, points within the vasculature can be found. Using either standard focused wave or plane wave imaging, an image with resolution beyond the diffraction limit can be generated by plotting the localisations of bubbles across the field of view.

There is widespread interest in super-resolution ultrasound [1-5]. The focus of this work is on techniques which rely on isolated signals from microbubbles. Isolated signals can be achieved by extracting the separated bubble signals from a low concentration of bubbles; or using variation between frames to generate individual signals from a cloud of scatterers.

There have been various processing approaches; pulse inversion (PI) extracts the non-linear bubble response, differential imaging (DI) generates signal from bubble movement or destruction, and applying a singular value decomposition filter can discriminate between bubble and tissue signal. Each approach must be combined with carefully chosen acquisition parameters and bubble concentration if isolated signals are to be produced. This work serves as an exploration of the available techniques for those using super-resolution ultrasound.

Successful super-resolution requires us to ask:

How does the choice of signal processing algorithm affect the localisation accuracy and precision?

What is the optimum concentration of microbubbles for a given situation?

How should the acquisition parameters be optimised?

These questions have been studied through simulation and experiment. The bubble response to plane wave ultrasound has been modelled and the effects of different processing algorithms, pulse centre frequencies, and bubble concentrations simulated. For comparison with experiment, in vitro data were also collected for microbubble flow in 200μm cellulose tubes.

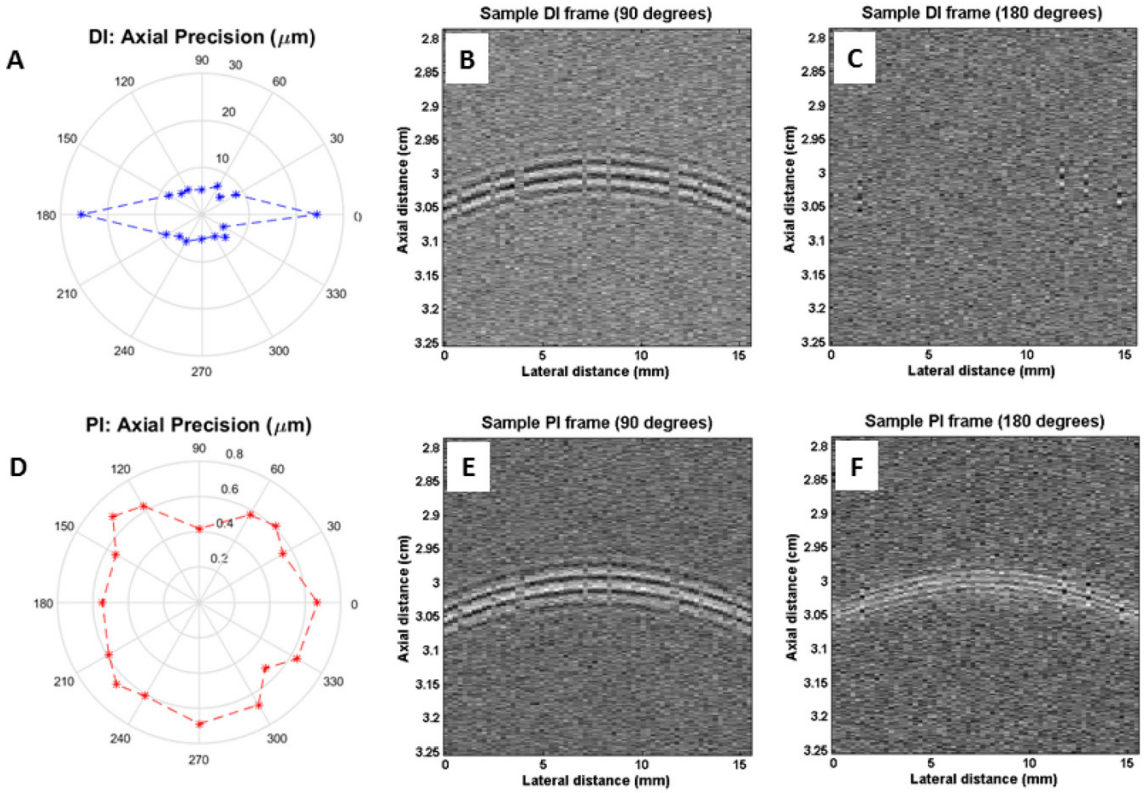

Figure 1: Simulated data comparing the use of pulse inversion (PI) with differential imaging (DI). Axial localisation precision with respect to bubble flow direction for signals generated using DI is shown in (A) with the simulated radio frequency frames for bubbles moving axially and laterally shown in (B) and (C) respectively. This can be compared with the axial localisation precision for PI shown in (D) and the radio frequency data shown for axial (E) and lateral (F) motion.

The results illustrated the interplay between bubble concentration, processing choice and acquisition parameters. The choice of image processing algorithm had important implications on how well the microbubbles could be localised. When processing methods which detect movement between adjacent frames were used, such as differential imaging, the accuracy and precision of the bubble localisation was affected by the bubble speed and direction. Figure 1 (A) and (D) show the simulation results comparing the axial localisation precision of differential imaging and pulse inversion imaging for the full range of bubble flow directions. The difference between signals received when the bubble is moving laterally and axially is also shown in Figure 1 and qualitatively shows why signals generated from lateral movement are difficult to localise. Introducing a higher bubble concentration creates further challenges as conveyed in Figure 2 - where the acquisition parameters and processing technique have not generated the required isolated signals. Appropriate choices of pulse frequency and pressure can enable super-resolution from a high concentration but, clinically, it may not be possible to use the optimal parameters.

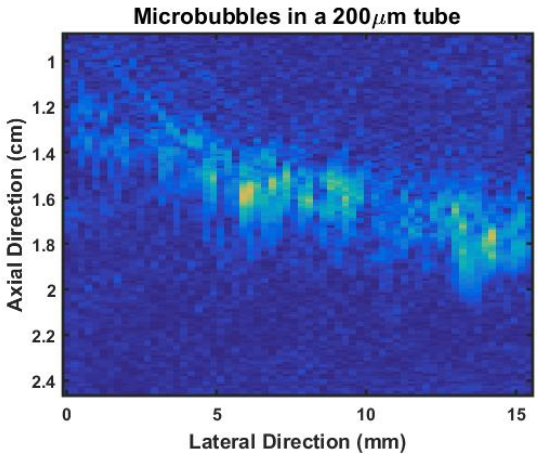

Figure 2: Example frame of a high microbubble concentration in a 200µm tube using imaging conditions that are unsuitable for generating isolated signals and thus unsuitable for super-resolution.

Overall the conditions required to generate isolated signals for each processing choice and at a range of bubble concentrations have been outlined. In the future, investigations of this type will allow those requiring super-resolution to generate images with the highest possible accuracy, and ultimately, resolution.

References

1. *Lin, F., J.D. Rojas, and P.A. Dayton. Super resolution contrast ultrasound imaging: Analysis of imaging resolution and application to imaging tumor angiogenesis. 2016 IEEE International Ultrasonics Symposium.*
2. *Errico, C., et al., Ultrafast ultrasound localization microscopy for deep super-resolution vascular imaging. Nature, 2015.* ***527****(7579): p. 499-502.*
3. *Foiret, J., et al. Super-localization of contrast agents in moving organs, first experiments in a rat kidney. 2016 IEEE International Ultrasonics Symposium.*
4. *Christensen-Jeffries, K., et al., In vivo acoustic super-resolution and super-resolved velocity mapping using microbubbles. Medical Imaging, IEEE Transactions on, 2015.* ***34****(2): p. 433-440.*
5. *Viessmann, O., et al., Acoustic super-resolution with ultrasound and microbubbles. Physics in medicine and biology, 2013.* ***58****(18): p. 6447.*

Wave propagation in the OrganoPlate™ for *in vitro* ultrasound-mediated drug delivery

Inés Beekers[1], Tom van Rooij[1], Martin D. Verweij[2], Michel Versluis[3], Nico de Jong[1,2], Sebastiaan J. Trietsch[4], Klazina Kooiman[1]

[1]Department of Biomedical Engineering, Erasmus MC, Rotterdam, the Netherlands
[2]Acoustical Wavefield Imaging, Delft University of Technology, Delft, the Netherlands
[3]Physics of Fluids, University of Twente, Enschede, the Netherlands
[4]Mimetas B.V., Leiden, the Netherlands

Introduction

Ultrasound insonification of gas-filled microbubbles can be used to locally enhance drug delivery by increasing the permeability of the vessel wall [1]. To better understand the underlying mechanisms, such as pore formation and opening of cell-cell junctions, we need an *in vitro* vessel model with 3D endothelial cell culture under flow. Therefore, we propose to use the OrganoPlate™: an elaborate microfluidic channel structure incorporated into a standard 384-well microtiter plate (Fig. 1). However, because the OrganoPlate™ has never been used for studies involving ultrasound, its acoustic properties are unknown. Since microbubble behavior highly depends on the acoustic pressure and frequency, the ultrasound transmission into the microchannels, encased between two 175 µm thin glass plates, needs to be fully characterized prior to studying the microbubble-cell interaction. By analyzing microbubble oscillation and modeling the acoustic pressure transmission in the microchannels, we assessed the feasibility of using the OrganoPlate™ for *in vitro* ultrasound-mediated drug delivery.

Microbubble oscillation

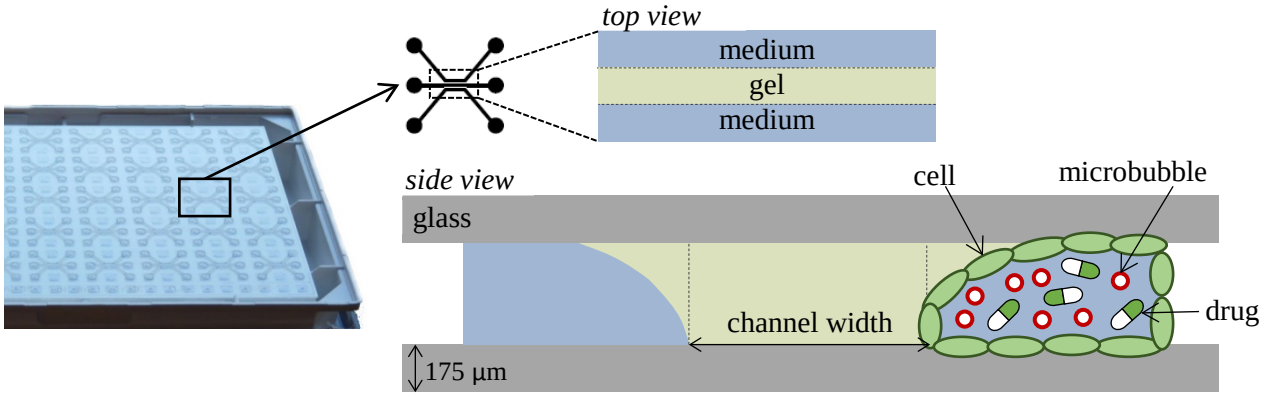

***Figure 1**: Bottom of the OrganoPlate™ [2] revealing the microchannel structure. The top view shows the three adjacent lanes, two for medium perfusion and one containing gel, allowing for culture on soft boundaries. The side view shows the microchannels encased between two glass plates. The bottom right illustration represents the desired in vitro setup with cultured endothelial cells and a flow of microbubbles and therapeutic agent in one of the medium channels. The channel width can be either 200 or 400 µm.*

Microbubbles with a C_4F_{10} gas core and a DSPC (1,2-distearoyl-sn-glycero-3-phosphocholine) based shell [3] were introduced in an OrganoPlate™ with a channel width of 400 µm. Microbubble spectroscopy [4] was performed by insonification with a focused transducer from 1 to 4 MHz (20 kPa, 8 cycles). The Brandaris 128 ultra-high-speed camera was used to record 38 single microbubbles upon insonification (~17 Mfps). The measured relative radial excursions of the microbubbles were compared to equivalent measurements previously performed in an acoustically transparent OptiCell [5] (Fig. 2A). Since the relative radial excursion (R) is proportional to the pressure amplitude experienced by the microbubble, the transmission into the OrganoPlate™ was determined by $T = R_{\text{OrganoPlate}}/R_{\text{OptiCell}}$ (Fig. 2B). The data revealed larger relative radial excursions in the OrganoPlate™ from 1 to 1.6 MHz, resulting from pressure amplification inside the microchannel.

Wave propagation model

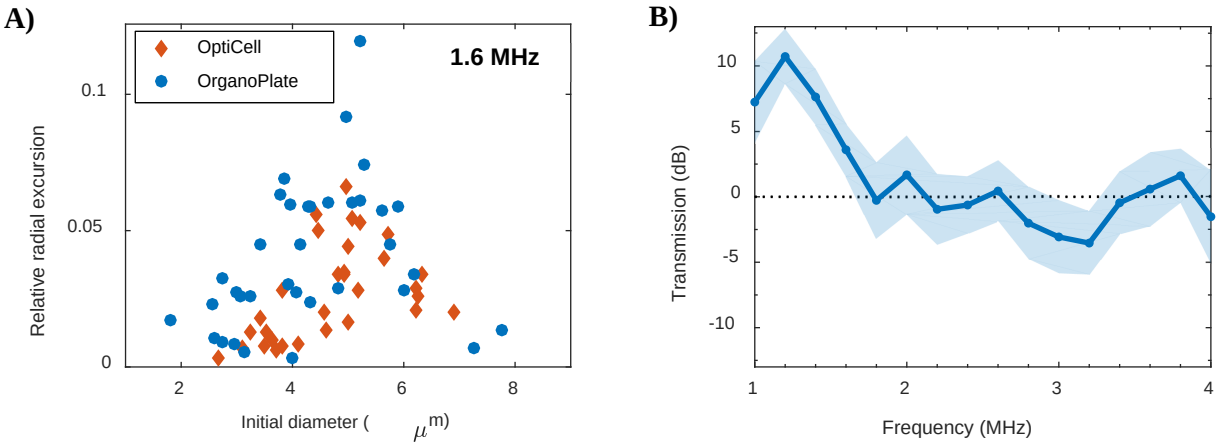

***Figure 2**: **A)** Relative radial excursions of microbubbles as a function of their initial diameter in an OrganoPlate™ ( ) or OptiCell ( ) when insonified at 1.6 MHz. **B)** Pressure transmission (dB) into the OrganoPlate™ determined by comparing relative radial excursions between microbubbles in an OrganoPlate™ and an acoustically transparent OptiCell. The shaded area corresponds to the standard deviation.*

The propagation of acoustic pressure into an OrganoPlate™ was simulated with a finite element model using *PZFlex*. We developed a 3D model of the microchannel structure, either for a channel width of 200 or 400 µm, and replicated the ultrasound insonification of the experimental setup (Fig. 3A). The pressure transmitted into the OrganoPlate™ was normalized to the incident pressure field and studied as a function of the applied frequency (Fig. 3B). The modeled wave propagation showed a more homogeneous transmission in the case of a channel width of 400 µm, with a root mean square deviation (RMSD) from zero of only 1.87 dB (Fig. 3A). The model validates the measured pressure transmission with a RMSD of 2.5 dB. Also, the frequency content was preserved after transmission into the microchannels.

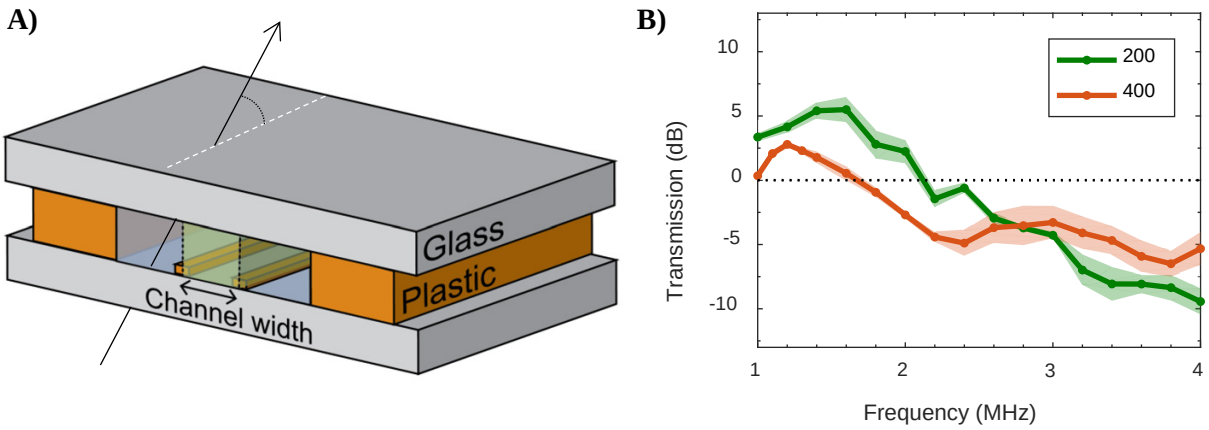

***Figure 3**: **A)** Sketch of the 3D model of the OrganoPlate™ (to scale); the microchannels are bound by plastic walls and incorporated between two 175 µm thin glass plates. The entire OrganoPlate™ was submersed in water and insonified at 45°. **B)** Transmission defined as the pressure amplitude in the focus normalized to the incident pressure field as a function of the applied frequency. The shaded area corresponds to the standard deviation.*

Conclusions

The homogeneous acoustic pressure and frequency transmission into the 400 µm wide microchannels of the OrganoPlate™ demonstrate its potential to create an ideal *in vitro* model for ultrasound-mediated drug delivery. An amplification of acoustic pressure of about 6 dB should be taken into account at frequencies between 1 and 1.6 MHz.

Acknowledgements

The authors would like to thank Robert Beurskens and Frits Mastik for their contributions to the experimental setup and Shreyas Raghunathan for assistance with PZFlex.

References

1. *K. Kooiman, et al., Adv. Drug Deliv. Rev., vol. 72, pp. 28–48, 2014.*
2. *S. J. Trietsch, et al., Lab Chip, vol. 13, no. 18, pp. 3548–3554, 2013.*
3. *K. Kooiman, et al., Eur. J. Lipid Sci. Technol., vol. 116, no. 9, pp. 1217–1227, 2014.*
4. *S. M. van der Meer, et al., J. Acoust. Soc. Am., vol. 121, no. 1, pp. 648–656, 2007.*
5. *T. van Rooij, et al., Ultrasound Med. Biol., vol. 41, no. 5, pp. 1432–1445, 2015.*

Numerical simulation of jet caused by ultrasonic irradiated microbubble near interface between two liquids

Koney Dupol Kanwar, Naohiro Sugita and Toshihiko Sugiura

Department of Mechanical Engineering, Keio University, Japan

Background

When a bubble near a wall is irradiated with sound wave in the vicinity of its eigenfrequency, it vibrates in a specific non-spherical shape. The resulting liquid jet and shock wave cause an erosion at the wall. One of the attempts to apply this phenomenon to medical treatment is a drug delivery system using sonoporation though the elucidation of the mechanism of sonoporation is on the road. We restrict our interest to the ratio of the specific acoustic impedance at which the microbubble in the vicinity of the liquid-liquid interface forms a jet by ultrasonic irradiation and to which of the shear stress and pressure mainly contributes to sonoporation.

Materials and Methods

The analytical model shown in Fig. 1 is axisymmetric and barotropic three phases flow of gas-liquid-liquid. We treated water (liquid 1) and highly viscous liquid (liquid 2) instead of blood and a vascular wall for simplicity. Tait equation for water and ideal gas law for air were used, and we set the density and the speed of sound in liquid 2 as constant values. The constrained interpolation profile scheme for advection terms, a pressure based solver for non-advection terms, the density functional method and the continuum surface force model were used.

Results

Time histories of non-dimensional pressure at the liquid-liquid interface on the axis of symmetry for some ratios of specific acoustic impedances Z_2/Z_1 are shown in Fig. 2. It shows that the smaller Z_2/Z_1 is, the slower the time when the liquid jet penetrates the bubble is and the larger the maximum pressure P_{max} is. P_{max}/P_0 where the liquid-liquid interface z/D_0=2.34 as functions of Z_2/Z_1, R_{max}/R_0 and the distance between the bubble surface and the liquid-liquid interface L_b/R_0 for $R=R_{max}$ are shown in Fig.3(a), (b) and (c), respectively. According to our numerical results, the liquid jet occurs only when Z_2/Z_1=2.00 at least with used parameters in this study. Finally, distributions of non-dimensional pressure on the axis of symmetry and those of non-dimensional shear stress in the radial direction at z/D_0=3 for Z_2/Z_1=2 are shown in Fig.4(a) and (b), respectively, for several elapsed times. They show that the pressure mainly contributes to sonoporation.

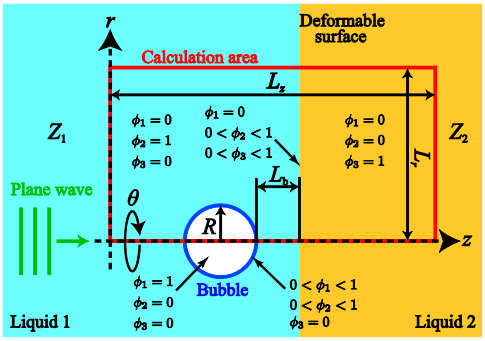

Figure 1: Schematic of initial bubble arrangement. Numerical parameters: initial bubble radius, $R=R_0$=3 μm, initial bubble position, L_b=6 μm, density functions, $\sum_{m=1}^{3}\phi_m=1$ ($0\leq\phi_m\leq1$), fluid viscosities, $\mu_{gas}=1.822\times10^{-5}$ Pa·s, $\mu_{liquid\ 1}=1.004\times10^{-3}$ Pa·s, $\mu_{liquid\ 2}$=0.096 Pa·s, spatial resolution, $\Delta r=\Delta z=0.04R_0$, temporal resolution, $\Delta t=4.0\times10^{-5}R_0/(P_0/\rho_0)^{1/2}$. We assumed a plane sinusoidal wave, whose acoustic pressure and frequency are 150 kPa and 1 MHz, respectively, incidents from z=0 plane.

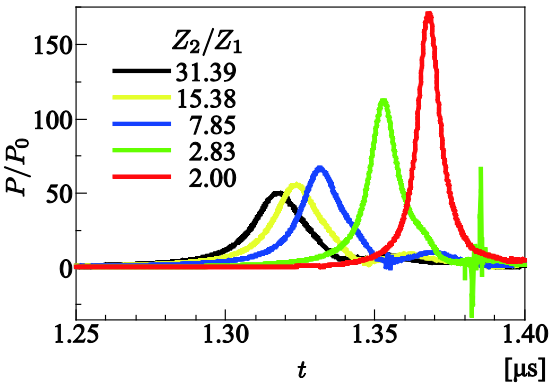

Figure 2: Time histories of non-dimensional pressure at the liquid-liquid interface on the axis of symmetry, with the initial position of liquid-liquid interface z/D_0=2.34. The pressure reaches its peak when collapses in every case.

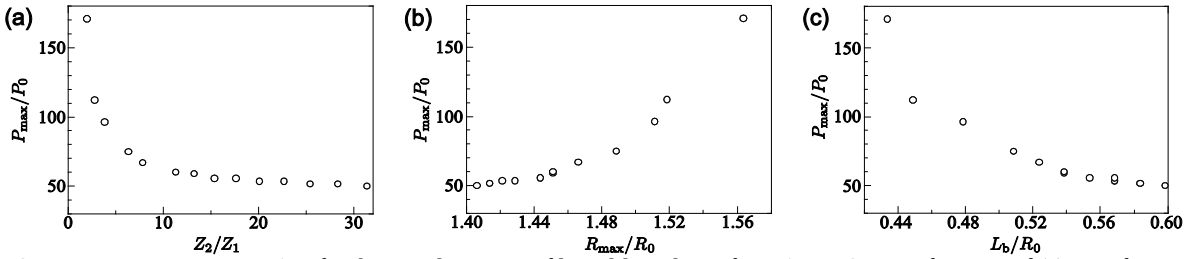

Figure 3: Maximum pressure P_{max}/P_0, for the initial position of liquid-liquid interface z/D_0=2.34, as a function of (a) specific acoustic impedance ratio Z_2/Z_1, (b) maximum bubble radius R_{max}/R_0 and (c) distance between bubble surface and liquid-liquid interface L_b/R_0 for $R=R_{max}$.

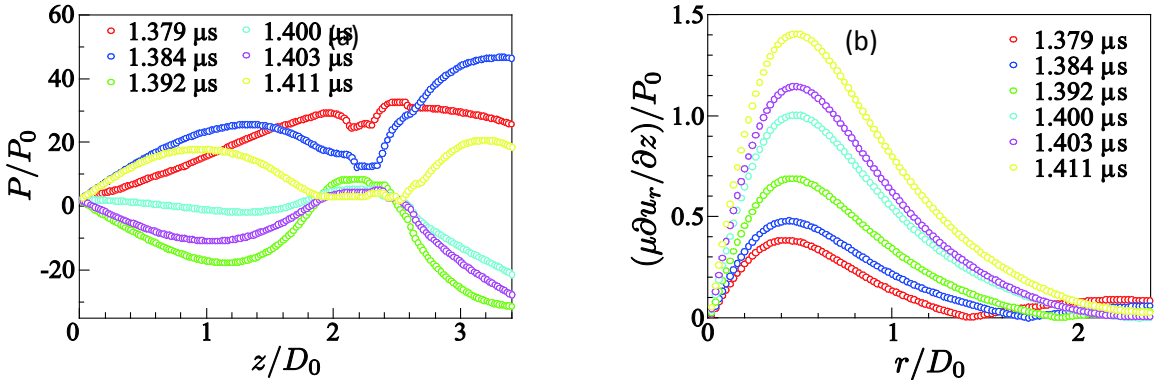

Figure 4: Distributions of non-dimensional pressure on the axis of symmetry (a), and those of non-dimensional shear stress in the radial direction at z/D_0=3 (b), for Z_2/Z_1=2.

Super contrast imaging using high frame-rate CEUS and spatial and temporal signal processing

Antonio Stanziola and Meng-Xing Tang

Department of Bioengineering, Imperial College London, London, U.K.
mengxing.tang@ic.ac.uk

Introduction

Contrast enhanced ultrasound (CEUS) with microbubbles enables imaging and quantification of micro-vascular flow and tissue perfusion, which has a wide range of applications in cardiovascular diseases and cancer. However, limited signal to noise ratio (SNR) of the images, especially in deeper tissues and for higher clinical ultrasound frequencies where microbubble are less active, can be challenging. Increase of transmitted ultrasound pressure can increase SNR, but it also increases the risk of bubble disruption.

Recent development of high frame-rate CEUS has opened up new opportunities for imaging macro- and micro-vascular flow and tissue perfusion [1-7]. The capability of obtaining a large amount of data during a short period of time allows new imaging and signal processing paradigms to be introduced to obtain superior image quality with very high SNR.

Methods and results

In this paper, we firstly report a new spatial-temporal signal processing technique - acoustic sub-aperture processing (ASAP) - capable of generating very high contrast images of macro and microvasculature by reducing the noise floor by up to 15 folds comparing to Power Doppler. In this approach received data are split into sub groups. As the signals from these groups are common but the noise is not, a simple coherence processing between the groups would be able to significantly reduce the noise. Furthermore, by carefully designing digital filters for the data, noise from side lobes can be suppressed. The approach is evaluated both in vitro and in vivo.

Secondly we compare this ASAP with a number of recently reported coherence based imaging approaches including spatial coherence based approach [8], temporal coherence based approach [9], and our previously reported spatial-temporal coherence based approach [6]. Their advantages and disadvantages are discussed. Example images using the same data but different coherence based approaches are shown in Fig1.

Figure1: In vivo microvascular CEUS image after (a) Spatial and temporal coherence processing as reported in [6]; (b) ASAP processing. The scale bar = 1mm.

Conclusion

We have presented a new signal processing technique capable of generating super contrast CEUS images, taking advantage of HFR data acquisition and spatial-temporal coherence of the data. A comparison with a few related techniques are also made.

Acknowledgement

We would like to thank members of the Ultrasound Laboratory for Imaging and Sensing (ULIS) group, Dr Robert Eckersley and Prof. David Cosgrove for their helpful discussion. We would also like to thank Dr Alfred Yu for his help with beamforming.

References

1. *C. Tremblay-Darveau, R. Williams, L. Milot, M. Bruce, and P. N. Burns, "Combined perfusion and doppler imaging using plane-wave nonlinear detection and microbubble contrast agents", IEEE Trans. on UFFC, vol. 61, no. 12, pp. 1988-2000, 2014.*
2. *C. Errico, J. Pierre, S. Pezet, Y. Desailly, Z. Lenkei, O. Couture, and M. Tanter, "Ultrafast ultrasound localization microscopy for deep super-resolution vascular imaging", Nature, vol. 527, no. 7579, pp. 499-502, 2015.*
3. *Avinoam Bar-Zion, Charles Tremblay-Darveau, Oren Solomon, Tamir Bendory, Dan Adam and Yonina C. Eldar, Fast and Background Free Super-Resolution Ultrasound Based on Fluctuation Statistics, Proceedings of the 21st European Symposium on Ultrasound Contrast Imaging, Rotterdam, January 2016*
4. *Yann Desailly, Jean-Michel Correas, Mickael Tanter, Olivier Couture, Contrast enhancement by real-time spatiotemporal filtering of ultrafast images, Proceedings of the 21st European Symposium on Ultrasound Contrast Imaging, Rotterdam, January 2016*
5. *C. H. Leow, E. Bazigou, R. J. Eckersley, A. C. H. Yu, P. D. Weinberg, and M. X. Tang, "Flow Velocity Mapping Using Contrast Enhanced High-Frame-Rate Plane Wave Ultrasound and Image Tracking: Methods and Initial in Vitro and in Vivo Evaluation", Ultrasound in Medicine & Biology, vol. 41, no. 11, pp. 2913-2925, 2015.*
6. *[A Stanziola and M-X Tang, Temporal and spatial processing of high frame-rate contrast enhanced ultrasound data, Proceedings of the 21st European Symposium on Ultrasound Contrast Imaging, p160-162, Rotterdam, January 2016*
7. *M. Toulemonde, Y. Lin, S. Lin, M. Butler, R. Eckersley, W C. Duncan, V. Sboros, and M.X. Tang, "Cardiac imaging with high frame rate contrast enhanced ultrasound: in-vivo demonstration", Proceedings of the IEEE International Ultrasonics Symposium (IUS), Tours, September 2016.*
8. *Lediju Bell MA1, Goswami R, Kisslo JA, Dahl JJ, Trahey GE, Short-lag spatial coherence imaging of cardiac ultrasound data: initial clinical results. Ultrasound Med Biol. 2013 Oct;39(10):1861-74. Epub 2013 Aug 9.*
9. *Charles Tremblay-Darveau, Avinoam Bar-Zion, Ross Williams, Paul S. Sheeran, Laurent Milot, Thanasis Loupas, Dan Adam, Matthew Bruce, Peter N. Burns, Improving contrastenhanced power Doppler using signal coherence, IEEE International Ultrasonics Symposium (IUS), Tours, September 2016.*

Multimodal left ventricular phantom for hemodynamic quantification studies

Jason Voorneveld[1], Timothy Hope[1], Geert Springeling[1], Sasa Kenjeres[2], Jos Westenberg [3], Frank Gijsen[1], Nico de Jong[1], Johan Bosch[1]

1Department of Biomedical Engineering, Thorax Center, Erasmus MC, Rotterdam, the Netherlands
2Transport Phenomena Section, Department of Chemical Engineering, Faculty of Applied Sciences, Delft University of Technology, Delft, the Netherlands
3Division of Image Processing, Department of Radiology, Leiden University, Leiden, the Netherlands

Introduction

Investigation of the complex intra-ventricular flow patterns remains a challenge in clinical ultrasound research. The combination of poor accessibility, large flow-rate range and three-dimensional flow patterns has rendered conventional Doppler techniques insufficient for full hemodynamic quantification.

Alternatively, echo-particle imaging velocimetry (ePIV) can estimate both velocity magnitude and direction. However, ePIV accuracy diminishes in the presence of fast flow due to the relatively large speckle displacement between frames [1]. The recent feasibility of ultrafast ultrasound acquisitions, using plane/spherical wave transmit protocols, has offered a possible solution to the aliasing limitations of ePIV.

Our previous work verified that ePIV accurately estimated the velocity of speckle/bubbles in a straight tube phantom at physiologically relevant velocities [2]. However, this simplified experiment was not able to capture the transient and multi-dimensional nature of intra-ventricular flow. Expanding on our previous work, we have developed an acoustically and optically transparent left-ventricular (LV) flow phantom to be used for laser, ultrasound (US) and magnetic resonance imaging (MRI) modalities.

This study describes the design of the (LV) phantom and some initial ultrasound acquisitions and ePIV results obtained from its use.

Methods and Materials

Left ventricular phantom

A compliant, optically and acoustically transparent silicone LV chamber (Fig. 1 - LV) was manufactured by painting silicone (HT 33 Transparente LT, Zhermack SpA, Rome, Italy), onto a 3D-printed mold of a LV. The 3D-printed mold was modelled on the statistical mean, end systolic phase, of a segmented 4D computed tomography dataset [3]. The silicone LV was then fitted with 3D-printed replicas of mitral (Fig. 1 – MV) and aortic (Fig. 1 – AoV) Björk-Shiley valves.

The LV was encased in a rigid, optically transparent acrylic box and connected to mitral and aortic valve ports, which were connected to an atrial and compliance chamber, respectively (similar in design to the phantom used in [4]. The acrylic box had one open port, which was connected to a programmable piston pump, programmed to reciprocate in a sinusoidal pattern with a frequency of 1.2 Hz with a 64-ml stroke volume. For this study degassed and deionized water was used as a pumping fluid.

The box had three open surfaces for laser/camera view access, as well as an US port on the underside of the box, sealed with a thin film. The orientation of the US and laser/camera ports allow for simultaneous acquisition of laser and echo PIV recordings. Additionally, the entire phantom (except the pump) was made from polymeric materials for MRI imaging.

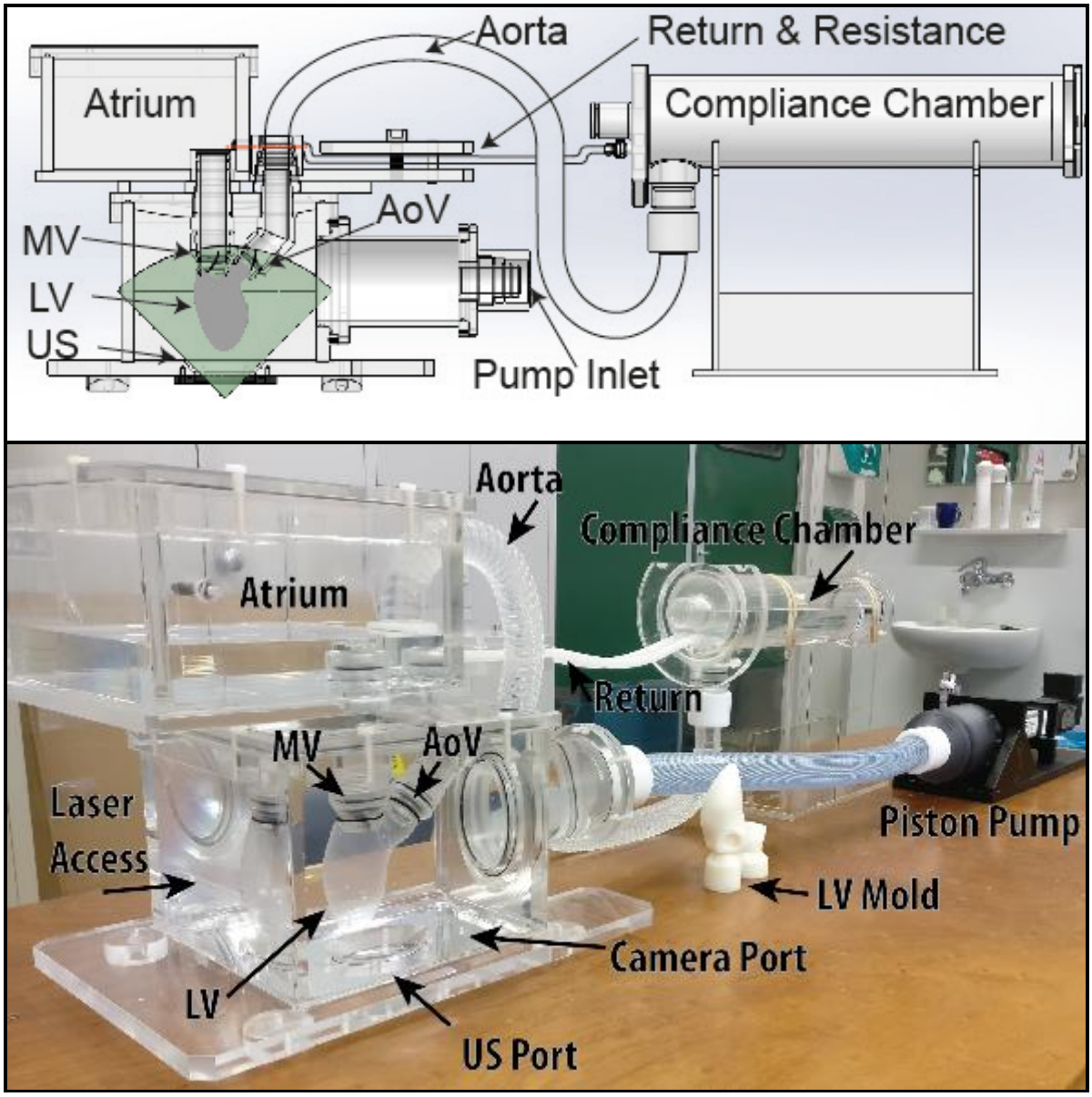

Figure 1: Diagrammatic (top) and photograph (bottom) of LV phantom. MV - mitral valve, AoV - Aortic Valve, US - Ultrasound, LV - left ventricle.

Ultrasound Acquisition

Beamformed image series were acquired with a Verasonics Vantage 256 system (Verasonics Inc., USA) using three different probes: L7-4 (5.0 MHz), C5-2 (3.125 MHz) and P4-1 (2.5 MHz). Spherical wave (plane wave for L7-4), 3-angled compounding acquisition protocol was used at a pulse repetition frequency of 3000 Hz (imaging at 1000 Hz). A diluted ultrasound contrast agent (UCA, 0.2 ml/l, SonoVue®, Bracco S.p.A) was used as a tracer particle for ePIV tracking.

Echo Particle Imaging Velocimetry

PIVlab (V1.41, [5]) was used as an ePIV implementation in Matlab (R2016b, The MathWords Inc., USA). In this study three tracking iterations were used, with kernel sizes of 9x4.5, 9x4.5 and 4.5x2.25 mm2 for each successive iteration, respectively.

For postprocessing, both median [6] and standard deviation based outlier removal tests were performed, replacing removed vectors with interpolated values from surrounding data. Finally, a moving average filter (5 ensembles) was applied along the time dimension of the data. No spatial smoothing was applied.

Results

The phantom expanded and contracted, filling and expelling water with the pump stroke (Fig 2).

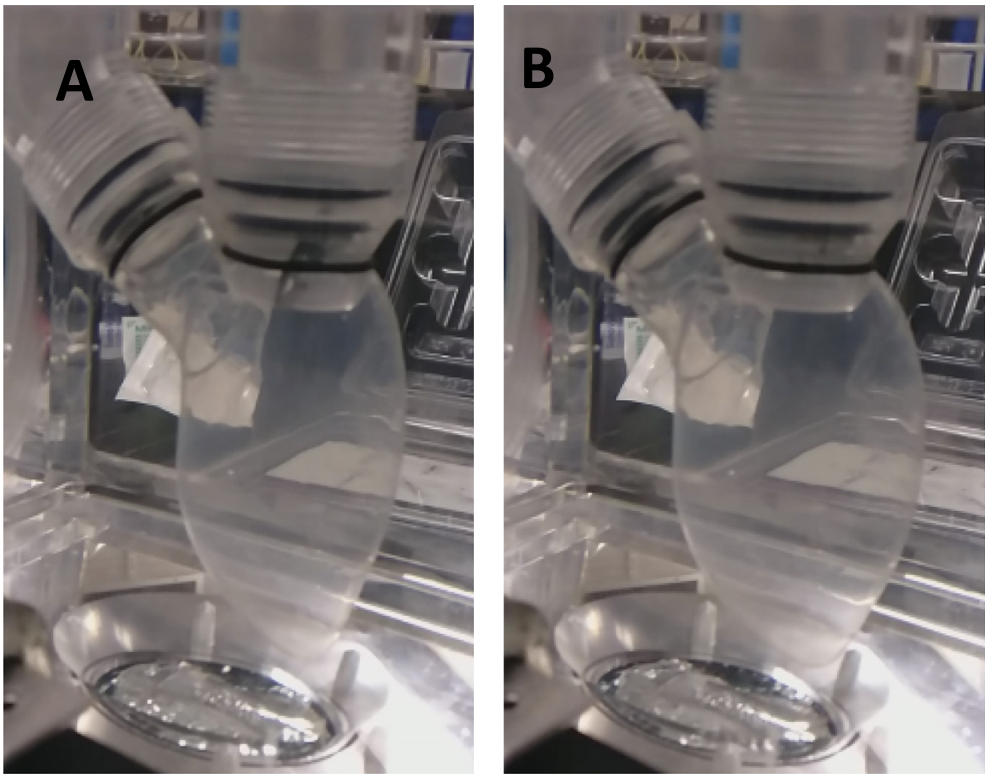

Figure 2: Photographs of LV phantom at A) maximum stroke and B) minimum stroke of sinusoid.

Example B-mode images for each probe are depicted in (Fig 3).

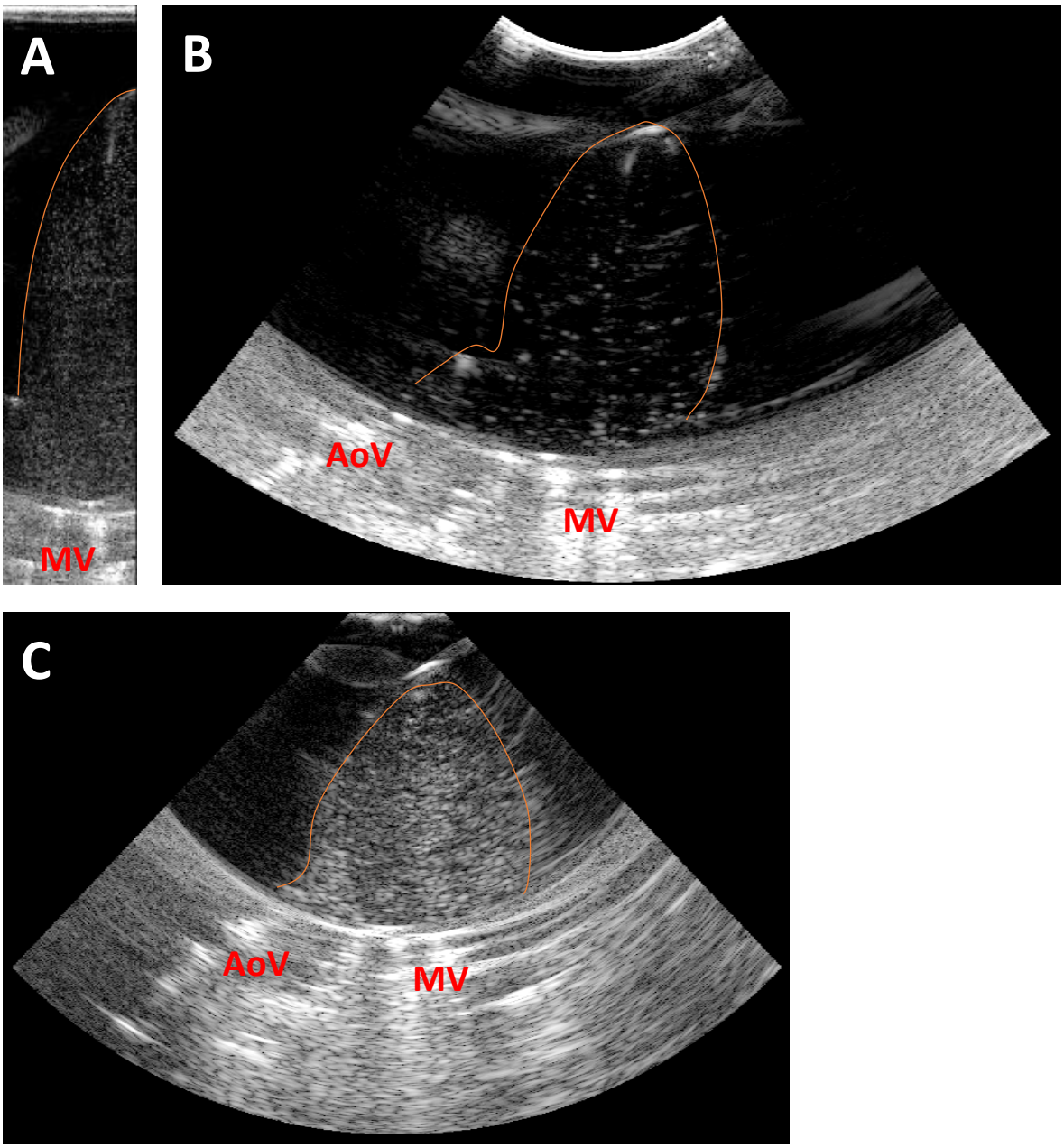

Figure 3: Bmode images of phantom for A) L7-4, B) C5-2 and C) P4-1. Mitral valve (MV) can be seen with all three probes and operates in plane, whereas the aortic valve (AoV) is not in the FOV of the L7-4 probe and operates out-of-plane. Approximate ventricleboundaries (red) are drawn to assist the reader.

Discussion

The L7-4 was not able to image the full LV cavity in its field of view (FOV) but provided the best speckle resolution of the three probes (Fig. 3A). The P4-1 probe comfortably imaged the full LV in its FOV but presented a much wider point spread function (PSF), especially at greater depth (Fig. 3C). The C5-2 also has a large enough FOV for the LV phantom and offered an intermediate PSF between the other two probes (Fig. 3B). It was difficult to ensure full contact with the C5-2's curved array on the flat film and loss-of-contactartifacts could be seen in some of the images.

In Fig 4. the ePIV derived velocity fields are displayed during a filling phase.

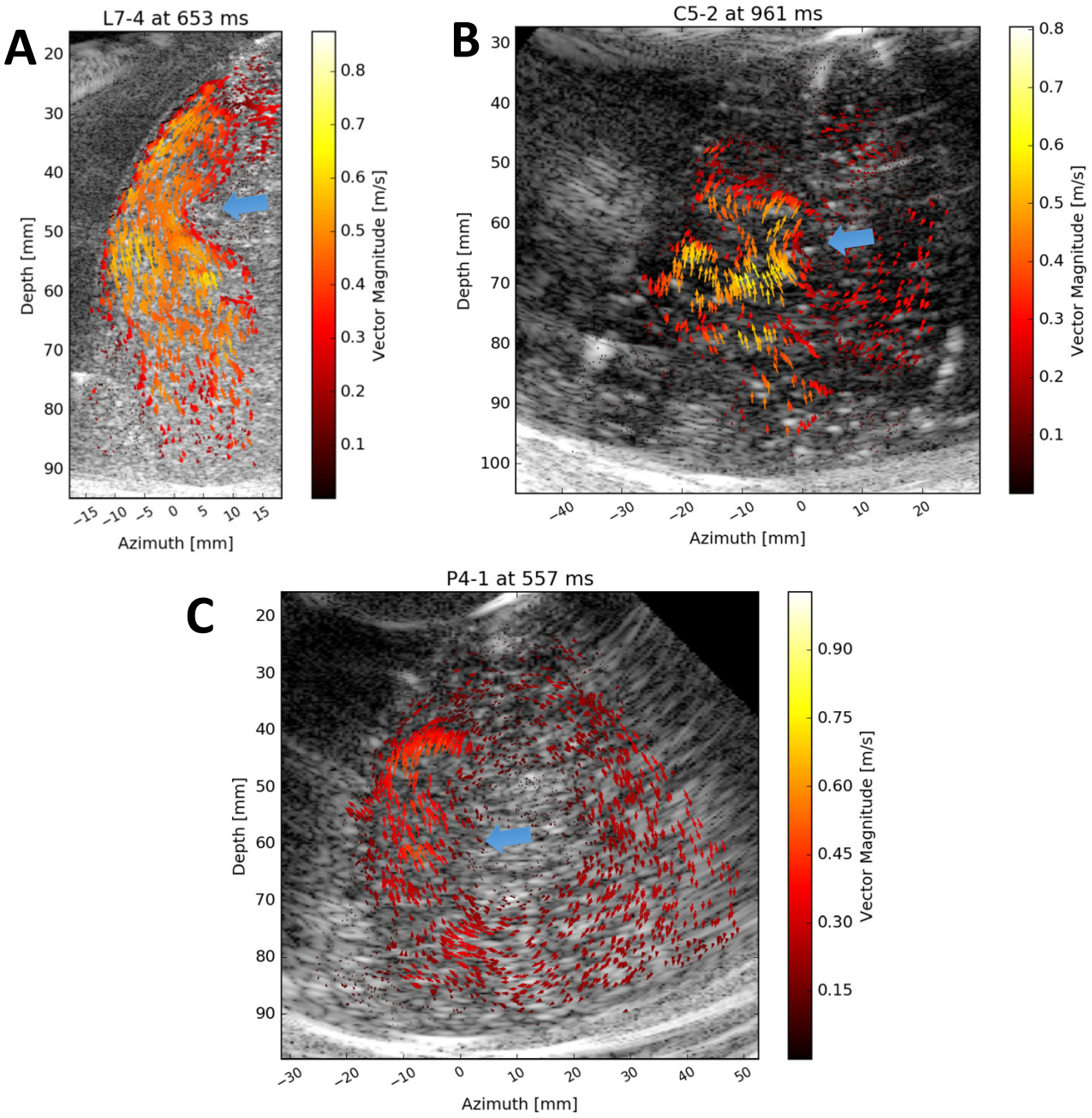

Figure 4: ePIV derived velocity maps during rapid filling with A) L7-4, B) C5-2 and C) P4-1 probes. Central vortex indicated with large blue arrow.

ePIV analysis on datasets obtained with all three probes revealed a well-defined central vortex. The maximum velocity magnitudes obtained were in the order of 1 m/s but require verification. Laser PIV will be used as a reference technique in assessing the accuracy of both ePIV and MRI based techniques in future.

Improvements to be considered in future will be triggered acquisitions to align acquisitions to a specific phase of the cardiac cycle and implementation of a more physiologically relevant stroke pattern.

Conclusion

The LV phantom allows for dynamic flow phenomena to be recorded using ultrafast US and ePIV. Laser PIV and phase-contrast MRI will be investigated in future for comparison between the three modalities.

Acknowledgements

The authors thank Robert Beurskens, Alex Brouwer and Michiel Manten for manufacturing the phantom and Marcel Rutten PhD for valuable advice on the phantom construction.

References

1. *C. Prinz, R. Faludi, A. Walker, M. Amzulescu, H. Gao, T. Uejima, A. G. Fraser, and J.-U. Voigt, "Can echocardiographic particle image velocimetry correctly detect motion patterns as they occur in blood inside heart chambers? A validation study using moving phantoms," Cardiovasc. Ultrasound, vol. 10, no. 24, p. 1, 2012.*
2. *J. Voorneveld, P. Kruizinga, H. J. Vos, F. J. H. Gijsen, E. G. Jebbink, A. F. W. van der Steen, N. de Jong, and J. G. Bosch, "Native blood speckle vs ultrasound contrast agent for particle image velocimetry with ultrafast ultrasound - in vitro experiments," in 2016 IEEE International Ultrasonics Symposium (IUS), 2016, no. Imdi, pp. 1–4.*
3. *C. T. Metz, N. Baka, H. Kirisli, M. Schaap, S. Klein, L. A. Neefjes, N. R. Mollet, B. Lelieveldt, M. De Bruijne, W. J. Niessen, and T. Van Walsum, "Regression-based cardiac motion prediction from single-phase CTA," IEEE Trans. Med. Imaging, vol. 31, no. 6, pp. 1311–1325, 2012.*
4. *H. Gao, N. Bijnens, D. Coisne, M. Lugiez, M. Rutten, and J. D'hooge, "2-D Left Ventricular Flow Estimation by Combining Speckle Tracking With Navier–Stokes-Based Regularization: An In Silico, In Vitro and In Vivo Study," Ultrasound Med. Biol., vol. 41, no. 1, pp. 99–113, 2015.*
5. *W. Thielicke and E. J. Stamhuis, "PIVlab – Towards User-friendly, Affordable and Accurate Digital Particle Image Velocimetry in MATLAB," J. Open Res. Softw., vol. 2, 2014.*
6. *J. Westerweel and F. Scarano, "Universal outlier detection for PIV data," Exp. Fluids, vol. 39, no. 6, pp. 1096–1100, 2005.*

Phospholipid microbubbles loaded with platinum complexes for Ultrasound-mediated treatment of brain cancer

Viviane Mawamba[a], Carsten Hagemann[b], Mario Löhr[b], Volker Sturm[b] and Ulrich Schatzschneider[a]

[a]Institut für Anorganische Chemie, Julius-Maximilians-Universität Würzburg, Am Hubland, D-97074 Würzburg, Germany
[b]Tumorlabor, Neurochirugische Klinik und Polyklinik, Uniklinik Würzburg, Joseph-Schneider Str.11/B1, D-97080 Würzburg, Germany
viviane.mawamba-kemo@uni-wuerzburg.de

Tumors of the central nervous system are among the most disabling and lethal types of cancer.[1] Because of their depth and location in functional inoperable areas, some brain cancers are surgically unreachable. Therefore, only standard treatment such as radio- and chemotherapy or a combination of both are possible. Chemotherapy has gained a lot of attention in the past two decades. Anti-cancer drugs are designed to kill malignant cells, but when administrated, only a small fraction of the injected dose reaches the target site, with the rest circulating through healthy tissue, resulting in dose-limiting side efffets. Encapsulation of drugs within microbubbles combined with local release triggered by focused ultrasound is thought to increase the local concentration of a chemotherapeutic agent at the site of disease while minimizing side effects on healthy tissue.[2,3]

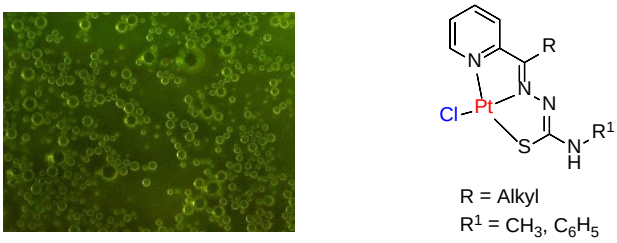

Figure 1: Fluorescence microscopy picture of octafluoropropane-filled lipid microbubbles stained with 1,1‘-dioctadecyl-3,3,3‘,3‘-tetramethylindocarbocyanine perchlorate (left) and general structure of membrane-affine cytotoxic platinum complex (right).

Microbubbles are gas-filled colloidal particles with a size range between 1-8 µm. In medicine, they are well-known as ultrasound contrast agents for imaging and diagnosis.[4] Our current work to be presented here is focused on the encapsulation of different platinum-based drug candidates within microbubbles, the study of their stability, and payload delivery *in vitro* under application of ultrasound as an external stimulus.

References

1. *S.A. Khuder, A. B. Mutgi, E.A. Schaub, Am. J. Ind. Med.* ***1998****, 34, 252-260.*
2. *Y. Liu, H. Miyoshi, M. Nakamura, J. Control. Release* ***2006****, 114, 89-99.*
3. *R. Deckers, C. T. W. Moonen, J. Control. Release* ***2010****, 148, 25-33.*
4. *S. Tinkov, R. Bekeredjian, G. Winter, C. Coester, J. Pharm. Sci.* ***2009****, 98, 1935-1961.*

Oral squamous cell carcinoma cell killing with ultrasound and cetuximab coated microbubbles in vitro

Kyouichi Narihira[1], Seyedeh Moosavi-Nejad[2], Akiko Watanabe[2], Sheng Hong[2], Katsuro Tachibana[2], Toshihiro Kikuta[1]

[1]*Department of Oral and Maxillofacial Surgery, Fukuoka University School of Medicine, Fukuoka, Japan*
[2]*Department of Anatomy, Fukuoka University School of Medicine, Fukuoka, Japan*

Background and Aim

Among cancers, head and neck region are the sixth most common cancers in the world. Oral squamous cell carcinoma (OSCC), originating in squamous cells that line the mouth and lips, makes around 90% of all oropharyngeal malignancies. Although traditional treatment remains the treatment of choice for many cases of OSCC at early stages, concerns over unwanted side effects following damages to the normal tissue have now become an important issue. As a result, there has been a considerable shift in the cancer therapies toward minimally invasive techniques for precisely targeting OSCC cells.

In this study, ~~i~~n order to obtain selective killing of oral squamous cancer cells, we prepared microbubbles by adding an antibody specific for OSCC. We added cetuximab (Erbitux), which is used recently in molecular targeted treatment of OSCC to the microbubbles (Figure 1). These microbubbles and ultrasound irradiation to in vitro cancer cell were evaluated whether there is a selective cell-killing effect to OSCC.

Materials and Methods

We used oral squamous carcinoma cell line HSC-2 and human leukemia cell line U937. The concentration of HSC-2 cells and U937 cells was 1×10^6 cell/ml.

The ultrasound irradiation was produced using a driving generator Sonopore 4000 (NepaGene, Japan). Center frequency was 1.011 MHz, sound intensity (I_{spta}) was 0.8, 0.9, 1.0 W/cm^2, duty ratio was 50%, PRF was 50Hz. Ultrasonic irradiation duration was 15 second.

Cetuximab-Albumin mixed microbubbles was added to cancer cells with ultrasonic irradiation in a experimental in vitro system. Effects were compared in different groups: molecular target drugs alone, ultrasonic irradiation alone, albumin bubble with ultrasound and molecular targeting albumin bubble with ultrasonic irradiation. Cell viability was measured trypan blue dye exclusion method. Apoptosis assay was detected by FITC-labeled annexin V and PI staining using Tali® Image-Based Cytometer (Life Technologies).

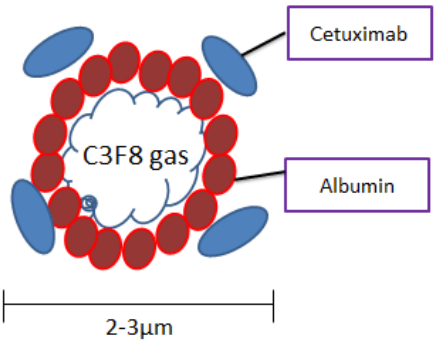

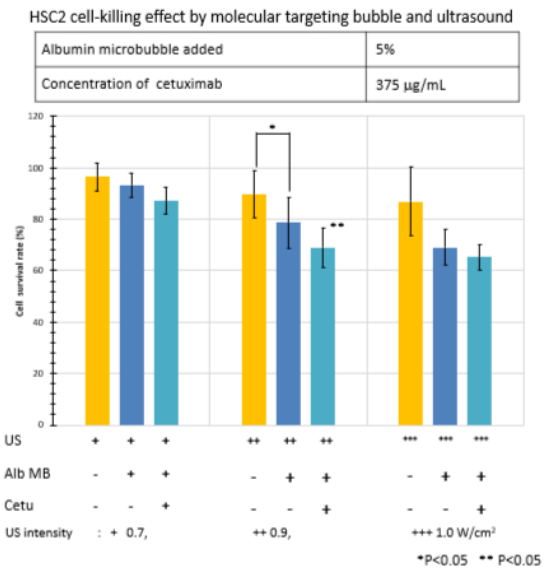

Results

There was a tendency for enhanced HSC2-cell killing effect with increasing cetuximab concentrations by ultrasonic

irradiation of molecular targeted albumin bubbles as compared to non-targeted albumin bubble (Figure 2).

Early apoptosis and secondary necrosis increased under ultrasound irradiation and the presence of Albumin-microbubbles and cetuximab as compared to control groups (P<0.5). On the other hand, for the U937 cells which was not specific for cetuximab showed less apoptosis in spite of the presence cetuximab coated microbubble during ultrasound irradiation (Figure 3).

Conclusion

We concluded that cetuximab coated microbubbles adhered more to the surface of cancer cells compared to the plain albumin-bubble, and showed an increase in cell-killing and apoptosis possibly due to the cavitation caused by ultrasound near the cell membrane.

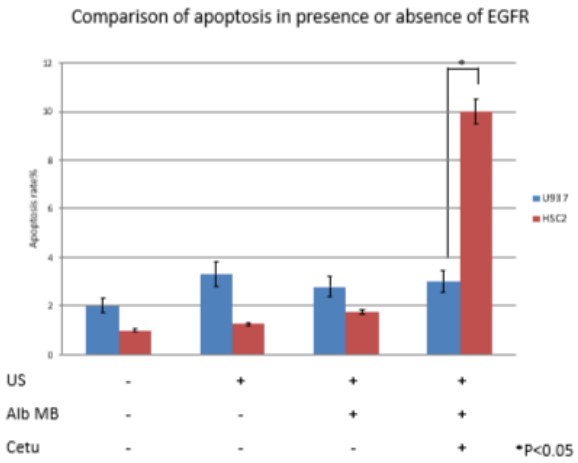

Reference

1. *Effect of cetuximab on proliferation of oral squamous cell carcinoma cells Ohnishi Yuichi, at el. Dent Med; 2014, 77, 59-65.*
2. *Ultrasound-Targeted Microbubble Destruction to Deliver siRNA Cancer Therapy. Andrew R, at el. Cancer Res; 2012, 72, 6191.*

Development of An Ultrasound-Activated Drug Delivery System for Chemoradiation Therapy in Bladder Cancer

Jia-Ling Ruan[1], Richard J. Browning[2], Jong-Wei Hsu[1], Yesna O. Yildiz[1], Jessica Gorrill[1], Borivoj Vojnovic[1], Eleanor Stride[2], and Anne E. Kiltie[1]

[1] Department of Oncology, Gray Institute for Radiation Oncology and Biology, University of Oxford, Oxford, United Kingdom
[2] Institute of Biomedical Engineering, University of Oxford, Oxford, United Kingdom
Email: jia-ling.ruan@oncology.ox.ac.uk

Bladder cancer is the fifth most common cancer in the US with a high relapse rate and a high incidence rate in the elderly population. Chemoradiation therapy has been shown to be an effective method for patients unsuitable for surgery in managing bladder cancers. However, although chemoradiation drugs like gemcitabine are able to enhance the radiosensitization of tumors, most of them still carry systematic side effects to normal tissues and were shown to be more toxic than radiotherapy alone. Here we have developed a drug delivery system for gemcitabine, which can be coupled with ultrasound for controlled drug release. Gemcitabine was incorporated into liposomal nanoparticles and these liposomes were then bio-conjugated to microbubbles using a modified method from previous studies[1,2]. The particle size, concentration, and morphology were characterized by dynamic light scattering, nanoparticle tracking analysis, and microscopy. The ultrasound-activated efficacy of the system was demonstrated on *in vitro* bladder cancer cell lines by microscopy using DiO to label the liposomal carriers. The result showed that the conjugation of liposome to microbubbles has better ultrasound-mediated delivery efficacy than using the liposomes and microbubbles separately (Figure 1). The enhanced cytotoxicity of the system was also studied. Our findings indicate that this system could be a promising new drug delivery vehicles to incorporate into the current chemoradiation therapy regime against bladder cancer.

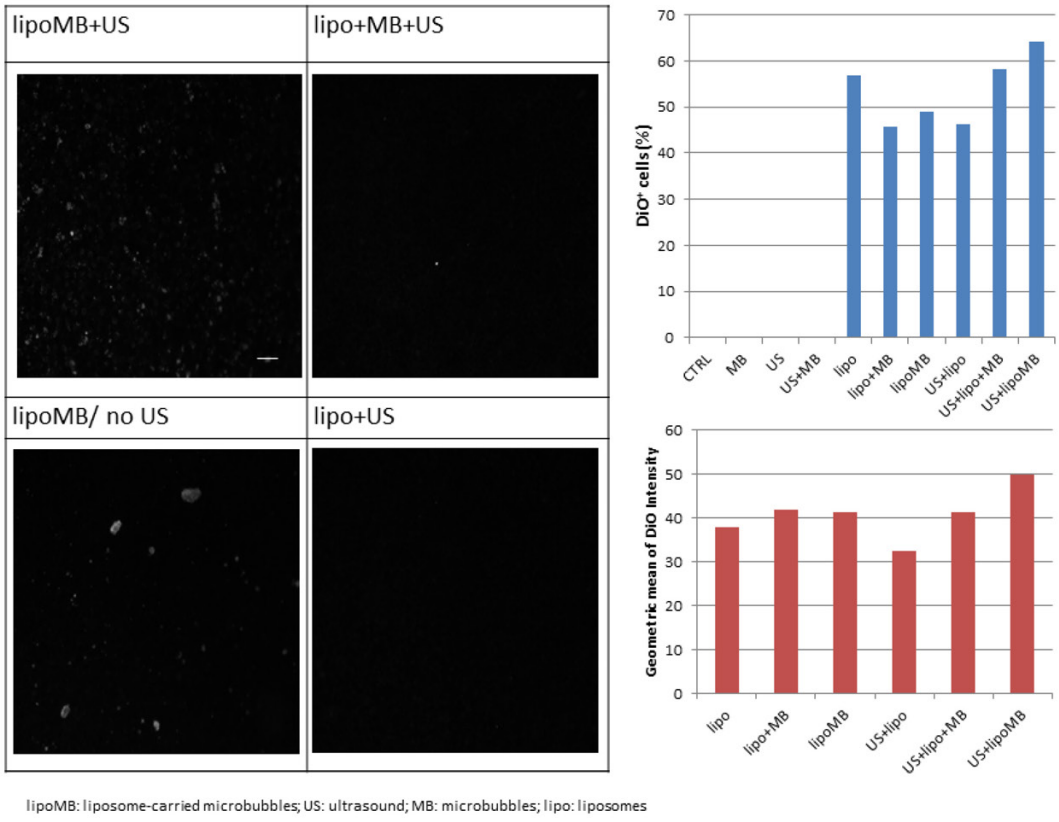

Figure 1. Efficiency of ultrasound-mediated delivery demonstrated by fluorescence microscopy and flow cytometry analysis using Dio-labeled liposomes. The scale bar is 50 µm.

Reference

1. *Kheirolomoom A, Dayton PA, Lum AFH, et al. Acoustically-active microbubbles conjugated to liposomes: Characterization of a proposed drug delivery vehicle. J Control Release. 2007;118(3):275-284. doi:10.1016/j.jconrel.2006.12.015.*
2. *Lentacker I, Geers B, Demeester J, De Smedt SC, Sanders NN. Design and evaluation of doxorubicin-containing microbubbles for ultrasound-triggered doxorubicin delivery: cytotoxicity and mechanisms involved. Mol Ther. 2010;18(1):101-108. doi:10.1038/mt.2009.160.*

Ultrasound-mediated delivery and distribution of polymeric nanoparticles in the normal brain parenchyma and melanoma metastases

Habib Baghirov[a], Sofie Snipstad[a], Einar Sulheim[a,b], Sigrid Berg[c,d], Mercy Afadzi[a], Rune Hansen[c,d], Frits Thorsen[f], Yrr Mørch[b], Catharina de Lange Davies[a], Andreas K.O. Åslund[a*]

[a] Department of Physics, The Norwegian University of Science and Technology (NTNU), 7491 Trondheim, Norway
[b] SINTEF Materials and Chemistry, 7465 Trondheim, Norway
[c] SINTEF Medical Technology, 7465 Trondheim, Norway
[d] Department of Circulation and Medical Imaging, NTNU, 7491 Trondheim, Norway
[e] Molecular Imaging Center and Kristian Gerhard Jebsen Brain Tumour Research Centre, Department of Biomedicine, University of Bergen, 5020 Bergen, Norway
**andreas.aslund@ntnu.no*

Introduction

Treatment of brain-related disorders is hindered by the blood-brain barrier (BBB), preventing most drugs from entering the brain.[1] Safe and transient opening of the BBB can be achieved with focused ultrasound (FUS) in combination with microbubbles, enabling delivery of drugs. To reduce toxicity and to increase targeting passively or actively, nanoparticles can be used for drug encapsulation. Previously we have shown that poly(butyl cyanoacrylate) nanoparticles stabilizing microbubbles can be used to open the BBB transiently.[2] Herein, microbubbles stabilized by poly(isohexyl cyanoacrylate) (PIHCA) nanoparticles were used to permeabilize the BBB and deliver nanoparticles to the brain in a melanoma brain metastasis model The uptake and displacement of nanoparticles from blood vessels determined.

Methods

A MR guided focused dual-frequency ultrasound transducer was used to open the BBB at 1.1 MHz (10 ms burst, 0.33 Hz, 5 min, PNP 0.32 MPa) in combination with nanoparticle-microbubbles, inducing cavitation. Post BBB-opening 7.8 MHz (5 ms burst, 1 Hz, 60 min, PNP 0.82 MPa) was applied to generate acoustic radiation force to push nanoparticles through the extracellular matrix. To evaluate the effect of BBB opening and acoustic radiation force, we quantified the extravasation and distribution of nanoparticles in the brain by confocal laser scanning microscopy. The extravasated amount of NPs was correlated to the extent of BBB opening, visualized by MRI and the MR contrast agent Omniscan. Microbubbles and nanoparticles were characterized by scanning electron microscopy (SEM) and super resolution optical microscopy.

Results

The nanoparticle-microbubbles have a shell consisting of a monolayer of nanoparticles, and acoustic characterization measurements showed that they burst at similar pressure levels as SonoVue and have similar echogenicity when imaged in contrast mode by a clinical ultrasound scanner. The concentration made is typically between 2e8 and 5e8 MB/ml, and the mean size is between 2.5 and 3.5 μm, with more than 90% of bubble being smaller than 5 μm.

We found that BBB transport and distribution of nanoparticles into the brain and melanoma metastases correlated with the extent of cavitation induced BBB opening. The extravasation and distribution of nanoparticles had a direct correlation to the, by MRI, immediately assessed BBB opening. Under the experimental conditions used, we were not able to detect any effect from the acoustic radiation force

experiments, possibly since nanoparticles were already well-distributed after BBB opening. In this study, we found that PIHCA nanoparticle-stabilized microbubbles can be used to achieve substantial accumulation and distribution of nanoparticles in the brain. This could potentially benefit the treatment in a multitude of disorders related to the brain, including brain-metastasized melanoma.

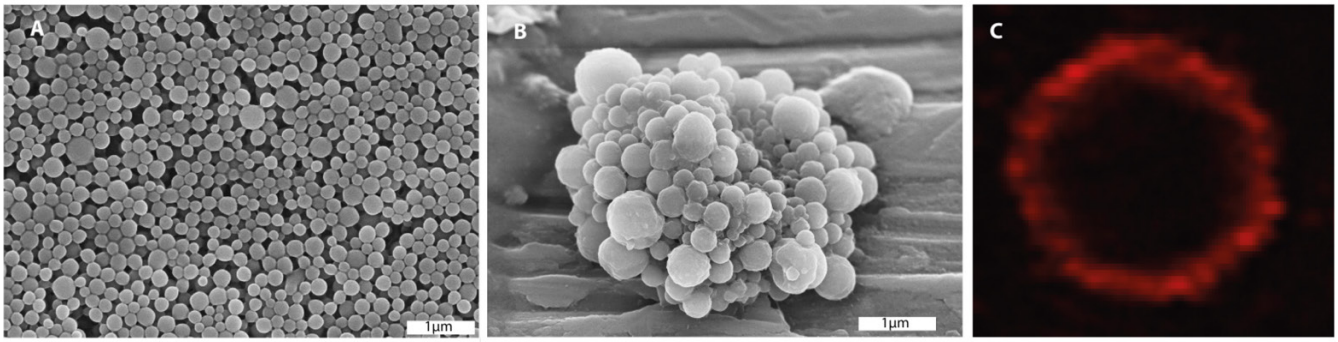

Fig. 1: A) SEM micrograph of PIHCA nanoparticles. B) SEM micrograph of a nanoparticle stabilized microbubble. C) Super resolution microscopy of a nanoparticle stabilized microbubble, showing that shell of the microbubble contains a layer of 1-2 nanoparticles thickness.

References

1. *Pardridge, W. M., Drug transport across the blood-brain barrier. J. Cereb. Blood Flow Metab.* ***2012,*** *32 (11), 1959-72.*
2. *Åslund, A. K. O.; Berg, S.; Hak, S.; Morch, Y.; Torp, S. H.; Sandvig, A.; Wideroe, M.; Hansen, R.; de Lange Davies, C., Nanoparticle delivery to the brain - By focused ultrasound and self-assembled nanoparticle-stabilized microbubbles. J. Control. Release* ***2015,*** *220 (Pt A), 287-94.*

Investigation of Sonodynamic Therapy Mechanisms with Oxygen Loaded Microbubbles

Estelle Beguin[1], Luca Bau[1], Yesna Yildiz[1], Joshua Owen[1], Paul Rademeyer[1], Richard Browning[1], John F. Callan[2], Anthony McHale[2] and Eleanor Stride[1]

[1]Department of Engineering Science, Institute of Biomedical Engineering, University of Oxford, Oxford OX3 7DQ, United Kingdom.
[2]Biomedical Sciences Research Institute, University of Ulster, Coleraine, Northern Ireland, BT52 1SA, United Kingdom.

Interest in the use of ultrasound (US) to trigger drug delivery is rapidly increasing due to the wide acceptance and low costs associated with US clinical systems. Sonodynamic Therapy (SDT) involves the use of drugs (sensitisers) that are only activated upon ultrasound exposure, thereby significantly reducing the risk of off-target side effects. It also offers the considerable advantages over the related technique of Photodynamic Therapy (PDT) in terms of penetration depth in human tissue. Both methods rely on the co-localisation of the sensitiser and molecular oxygen before application of a stimulus to generate cytotoxic singlet oxygen and other reactive oxygen species (ROS). In the case of PDT, the sensitiser is excited by light and singlet oxygen is generated through the quenching of excited sensitiser by ground state molecular oxygen. The mechanisms underpinning SDT, however, are currently poorly understood. Sonoluminescence and pyrolysis from US induced cavitation have been proposed as possible methods for ROS generation, but the evidence remains controversial. [1], [2]

Recent reports on the treatment of hypoxic tumours have identified oxygen microbubbles loaded with the sensitiser Rose Bengal as a promising SDT platform. [3], [4] The aim of this study was to investigate the mechanisms leading to Rose Bengal excitation and singlet oxygen generation from oxygen microbubbles and US. Microbubble cavitation was examined over a range of ultrasound parameters. Sonoluminescence was detected using a photomultiplier tube and the sonochemical analysis was carried out using fluorescence probes for relevant reactive oxygen species.

With the experimental apparatus and protocol used in this study we were not able to detect light emissions at the exposure conditions for which we have observed therapeutic effects (1 MHz, 3 Wcm^{-2} and 50% duty cycle). Neither were we able to activate Rose Bengal in the absence of US by exposure to ROS relevant to inertial cavitation (singlet oxygen, hydrogen peroxide and hydroxyl radicals). The implications of these findings and a possible alternative mechanism for the excitation of Rose Bengal will be discussed.

References

1. *V. Misík and P. Riesz, "Free radical intermediates in sonodynamic therapy.," Ann. N. Y. Acad. Sci., vol. 899, pp. 335–348, 2000.*
2. *I. Rosenthal, J. Z. Sostaric, and P. Riesz, "Sonodynamic therapy - a review of the synergistic effects of drugs and ultrasound," Ultrason. Sonochem., vol. 11, no. 6, pp. 349–363, 2004.*
3. *C. McEwan, J. Owen, E. Stride, C. Fowley, H. Nesbitt, D. Cochrane, C. C. Coussios, M. Borden, N. Nomikou, A. P. McHale, and J. F. Callan, "Oxygen carrying microbubbles for enhanced sonodynamic therapy of hypoxic tumours.," J. Control. Release, vol. 203, pp. 51–6, Apr. 2015.*
4. *C. McEwan, S. Kamila, J. Owen, H. Nesbitt, B. Callan, M. Borden, N. Nomikou, R. A. Hamoudi, M. A. Taylor, E. Stride, A. P. Mchale, and J. F. Callan, "Combined Sonodynamic and Antimetabolite Therapy for the Improved Treatment of Pancreatic Cancer using Oxygen Loaded Microbubbles as a Delivery Vehicle," Biomaterials, vol. 80, pp. 20–32, 2016.*

Adding an extra dimension to ultrasound-assisted drug delivery: multicellular 3D tumor models to evaluate interactions of drug-loaded microbubbles and ultrasound with a soft tissue environment

Roovers S.[1], Lajoinie G.[2], Dewitte H.[1], Versluis M.[2], De Smedt S.C.[1], Lentacker I.[1]

[1]Ghent Research Group on Nanomedicines, Ghent University, Ghent, Belgium.
[2]Physics of Fluids group, MIRA Institute for Biomedical Technology and Technical Medicine, University of Twente, Enschede, The Netherlands.
E-mail: Silke.Roovers@UGent.be

Drug-loaded microbubbles have shown to be efficient tools in ultrasound-targeted drug delivery in a variety of applications [1-3]. Currently, several research groups are trying to unravel which biophysical microbubble-cell interactions cause this improved drug delivery. For long, the two main mechanisms that were commonly believed to be responsible are sonoporation and enhanced endocytosis [4-6].

Sonoprinting

Recently, we have proposed a third possible mechanism, called '*sonoprinting'* [1]. This is defined as the direct deposition of elongated patches of nanoparticles along with parts of the bubble shell upon applying ultrasound to nanoparticle-loaded microbubbles.

The microbubble-cell interactions that lead to sonoprinting have been assessed in more detail using multiple imaging tools. Nanoparticle-loaded microbubbles were visualized during ultrasound exposure at a range of time scales and driven at different pressure levels. At lower pressures, the nanoparticles were transported away from the cell through microstreaming. However, when using high pressures and long ultrasound cycles, the bubble cores were rapidly moving due to acoustic radiation forces, dragging the nanoparticles with them which finally led to the deposition of these nanoparticles on the membrane surface of surrounding cells.

These could be important findings that could determine the way new drug-loaded microbubbles are formulated. However, it is important to realize that these observations might, in part, be influenced by the experimental *in vitro* set-up.

Towards a more suitable *in vivo*-like model

Earlier studies have shown that the presence of a stiff membrane on which the cells are cultured *in vitro*, can cause asymmetrical oscillations of microbubbles [7,8] and as such influence microbubble-cell interactions [9]. Therefore, this study has focused on developing multicellular tumor spheroids as a more suitable *in vivo*-like model to study biophysical interactions of microbubbles with a more complex and structured soft tissue model *in vitro.*

Besides reducing the possible influence of the rigid membrane on ultrasound experiments, 3D cultures have numerous other advantages over 2D cultures. The 3D micro-environment of the multicellular spheroids strongly resembles the *in vivo* situation, while maintaining the controlled setting of an *in vitro* study [10,11], as an extracellular matrix is formed that acts as a major physical barrier for drug penetration [10,12]. Moreover, the commonly observed necrotic core in rapidly-growing tumors has been seen in our 3D spheroid constructs as well (fig. 1B), which can contribute to drug resistance even further [12].

Spheroids of two different breast cancer cell lines, MCF-7 (human, fig. 1) and 4T1 (murine, fig. 2) are efficiently produced using a combination of the hanging drop technique with a gyratory shaking treatment.

The MF-7 spheroids are approximately 100 µm in size, while the 4T1 spheroids are roughly 200 µm in size and contain about 75,000 cells. To study microbubble-cell interactions, the spheroids can be transferred to collagen-coated CLINIcells® and left to attach for 4h after which microbubbles were added, as seen in figure 1B.

Using this model we aim to compare the efficacy of fluorescently labeled liposome-loaded microbubbles using live confocal imaging, combined with quantitative flow cytometry data and toxicological end point assays. As such this work intents to help close the gap between the complexity of the *in-vivo* situation and the more straightforward imaging and analysis in *in-vitro* monolayer cultures. This can provide new insights into the interaction of microbubble-liposome constructs with cells in a three dimensional context.

Figures

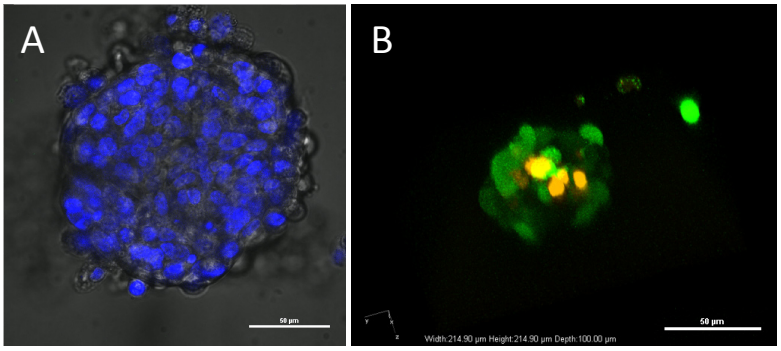

Fig 1: MCF-7 human breast cancer spheroids. A: MCF-7 spheroid stained with Hoechst 33342. B: maximum intensity projection of 101 cross sections of a MCF-7 spheroid stained with Calcein AM (green) indicating viable cells and PI (orange) representing dead cells. The occurrence of live cells in the periphery and dead cells in the inner layers reveals the presence of a necrotic core.

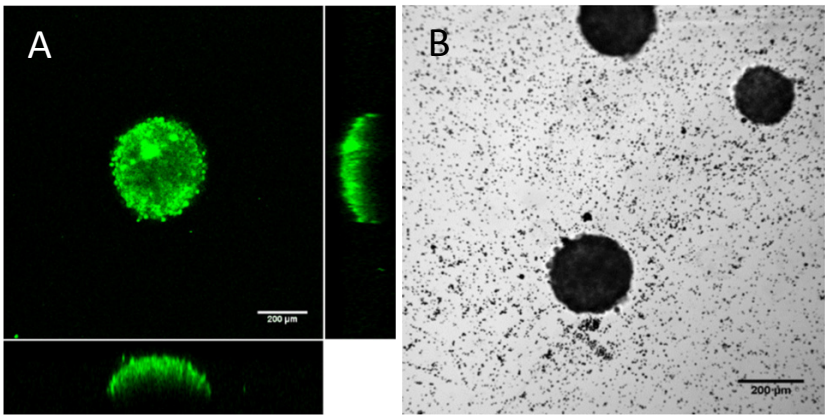

Fig 2: 4T1 mouse breast cancer spheroids. A: Orthogonal projection of 28 cross sections of a 4T1 spheroid stained with CellTrace™ CFSE. B: Bright field image of liposome-loaded microbubbles added to an acoustically transparent chamber (CLINIcell®), to which spheroids have attached.

References

1. *De Cock I, Lajoinie G, Versluis M, De Smedt SC, Lentacker I, Sonoprinting and the importance of microbubble loading for the ultrasound mediated cellular delivery of nanoparticles, Biomaterials, 2016.*
2. *Lentacker I, Wang N, Vandenbroecke RE, Demeester J, De Smedt SC, Sanders NN, Ultrasound exposure of lipoplex-loaded microbubbles facilitates direct cytoplasmic entry of lipoplexes, Mol. Pharm. 6 (2), 2009.*
3. *Lum AF, Borden MA, Dayton PA, Kruse BE, Simon SI, Ferrara KW, Ultrasound radiation force enables targeted deposition of model drug carriers loaded on microbubbles, JCR 111 (1-2) 2006.*
4. *Mehier-Humbert S, Bettinger T, Yan F, Guy PH, Plasma membrane poration induced by ultrasound exposure: Implication for drug delivery, JCR 104 (1), 2005.*
5. *Meijering BD, Juffermans LJ, Van Wamel A, Henning RH, Zuhorn IS, Emmer M, Versteilen AM, Paulus WJ, van Gilst WH, Kooiman K, de Jong N, Musters RJ, Deelman LE, Kamp O, Ultrasound and microbubble-targeted delivery of macromolecules is regulated by induction of endocytosis and pore formation. Circ. Res. 104 (5), 2009.*
6. *De Cock I, Zagato E, Braeckmans K, Luan Y, de Jong N, De Smedt SC, Lentacker I, Ultrasound and microbubble mediated drug delivery: Acoustic pressure as a determinant for uptake via membrane pores or endocytosis, JCR 197, 2015.*
7. *Doinikov AA, Aired L, Bouakaz A, Acoustic scattering from a contrast agent microbubble near an elastic wall of finite thickness, Phys Med Biol, 2011.*
8. *Zhang AM, Yao XL, Feng LH, The dynamic behavior of a gas bubble near a wall, Ocean Eng. 36, 2009.*
9. *Lajoinie G, Luan Y, Gelderblom E, Dollet B, Lentacker I, Dewitte H, de Jong N, Versluis M, Non-spherical oscillations drive the lipid shedding of microbubbles near a boundary, PhD thesis Guillaume Lajoinie, 2015.*
10. *Leong DT, Ng KW, Probing the relevance of 3D cancer models in nanomedicine research, Advanced drug delivery reviews 79-80, 2014.*
11. *Alemany-Ribes M, Semino CE, Bioengineering 3D environments for cancer models, Advanced drug delivery reviews 79-80, 2014.*
12. *Hirschhaeuser F, Menne H, Dittfeld C, West J, Mueller-Klieser W, Kunz-Schughart LA, Multicellular tumor spheroids:*

Monitoring of anti-angiogenic therapy by quantitative ultrasound molecular imaging

S. Turco[1], A. El Kaffas[2], Jianhua Zhou[2], Juergen K Willmann[2], H. Wijkstra[1,3], M. Mischi[1]

[1]Department of Electrical Engineering, Eindhoven University of Technology, the Netherlands
[2] Department of Radiology, Stanford Medicine, Stanford, CA, USA
[3]Department of Urology, Academic Medical Center, University of Amsterdam, the Netherlands

Introduction

Cancer growth and development requires angiogenesis, i.e., the formation of a blood supply to feed the tumor and enable metastatic spreading [1]. In cancer angiogenesis, pro-angiogenic factors are secreted to trigger the growth of new blood vessels and the recruitment of pre-existing vessels from surrounding tissue. The resulting vasculature is characterized by a chaotic network of abnormal micro-vessels exhibiting increased tortuosity and permeability, irregular diameters and branching, and arterio-venous shunting. This has led to a shift both in cancer diagnostics, whereby several *in-vivo* non-invasive imaging methods have been developed to assess the structural, functional, and molecular changes occurring due to cancer angiogenesis [2], and in cancer therapeutics, with the development of novel drugs aimed at inhibiting angiogenic processes and/or disrupting angiogenic tumor vasculature [3].

Ultrasound imaging of angiogenesis down to the molecular level has recently become possible thanks to the introduction of novel targeted ultrasound contrast agents (tUCA), which consist of gas-filled encapsulated microbubbles, whose shell has been functionalized with targeting ligands showing high-affinity for specific biomarkers involved in angiogenic processes [4]. One such biomarker, the vascular endothelial growth factor receptor 2 (VEGFR2) is recognized to play a major role in the growth and proliferation of endothelial cells [4]. In response, the first clinical-grade tUCA BR55 (Bracco Suisse SA, Switzerland) was recently developed, targeting VEGFR2, overexpressed in several types of cancers such as pancreatic, colon, rectal, prostate, breast, and ovarian cancer [4]. Thanks to their size (2-5 μm in diameter), targeted microbubbles can flow through the entire circulation remaining intravascular, and attach to the endothelial wall at locations where the target biomarker is overexpressed, thus causing selective enhancement in areas of active angiogenesis [4].

Separation of the contributions to the total acoustic signal from flowing and adherent microbubbles is thus crucial to assess the level of binding and quantify angiogenesis. Currently, this is done by looking at the late-enhancement, about 10 minutes after injection, and/or at the differential targeted enhancement (dTE), i.e., the difference in acoustic signal before and after the application of a destructive ultrasound (US) burst [4]. Besides providing only semi-quantitative measures, these methods lack reproducibility, being inherently dependent on machine settings and the time-points used for the analysis, they require long acquisitions, and, in case of dTE, the application of a destructive burst, with the associated risks of damage to the endothelial tissue [5]. These represent major limitations which may hamper clinical translation of ultrasound molecular imaging (USMI).

In response, we recently proposed a novel method for quantitative USMI by modeling the binding kinetics in the tUCA first-pass, providing quantitative assessment of microbubble binding based on 1-minute acquisition, with no need for a destructive burst [6]. After showing its feasibility for angiogenesis imaging in prostate-tumor bearing rats [6], in this work we tested the proposed method for its ability to monitor the respon\se to anti-angiogenic therapy in three colon cancer-bearing mice treated with Bevacizumab (Avastin®, Genetech/Roche), an antiangiogenic drug blocking the interactions with VEGFR2 receptors.

Methods

Modeling of tUCA binding kinetics

The first-pass binding (FPB) model [6] is proposed to describe the binding kinetics of tUCA. By this model, the total concentration of tUCA in a pixel of tissue is given by the weighted sum of the concentration of free microbubbles, described as a convective dispersion-process by the mLDRW model [7], and the concentration of bound microbubbles, which is modelled by a well-mixed, accumulating compartment under the assumption of negligible unbinding in the first-pass of the contrast bolus. Assuming high flow and using the adiabatic approximation, the FPB model is thus obtained as

$$C_t(t) = \alpha\sqrt{\frac{\kappa}{2\pi}}\left[v_f (t-t_0)^{-1/2} e^{\frac{-\kappa(t-t_0-\mu)^2}{2(t-t_0)}} + K_b \int_0^{\tau} (\tau - t_0)^{-1/2} e^{\frac{-\kappa(\tau-t_0-\mu)^2}{2(\tau-t_0)}} d\tau \right], \qquad (1)$$

where α is multiplicative factor depending on the injected dose and the blood flow, μ is the mean transit time of free microbubbles, t_0 is the theoretical injection time, κ is the dispersion parameter; and K_b is the first-pass binding rate.

Data acquisition

Colon cancer was established in three mice by injection of LS174T (n=2) or CT26 (n=1) cancer cell lines. At days 0/1, 3, and 7, one LS174T mouse (responder), and one CT26 (non-responder) received Bevacizumab, while one LS174T mouse (control) was treated with saline. 3D USMI was performed at days 0/1, 1/2, 3, 7, 10 by tail-vein injection of BR55, using an Epiq 7 ultrasound scanner (Philips Healthcare, Andover, MA, USA) with an X6-1 matrix array transducer operating at 3.2 MHz in power-modulation contrast-specific mode (mechanical index, MI = 0.09; volume sampling rate = 1 Hz; dynamic range = 52 dB; focal depth = 5 cm). About four minutes after injection ($t = t_{flash}$), a destructive US pulse was applied by switching the MI to 0.72. After the last USMI acquisition, tumors were extracted and frozen in 1-mm slices for histological quantification.

Data analysis

For each 2D plane of the 3D USMI dataset, time intensity curves (TICs) were extracted at each pixel and fitted by the FPB model in (1). Parametric maps of the binding rate K_b were obtained and compared to late-enhancement (signal intensity [SI] for $t = t_{flash} - 40s$) and dTE (average SI for $t_{flash}-130s < t < t_{flash}-30s$ subtracted by the average SI for $t_{flash} + 30s < t < t_{end}$). To evaluate the ability of the binding parameter K_b to monitor the response to anti-angiogenic therapy, regions-of interest (ROIs) around the cancer area were drawn in the three most central US planes. The average K_b, dTE, and late enhancement were calculated at days 0/1, 1/2, 3, 7, and 10, and the difference between the average parameter values at days 0/1 and 10 was tested by a two-sample Student t-test with level of significance $\alpha = 0.01$. The estimated ultrasound parameters were also compared with the corresponding histological quantification of frozen tumor slices, performed by evaluating VEGFR2 expression and percentage area blood vessels, by standard immunofluorescence and CD31 staining, respectively.

Results

The changes in the mean K_b, dTE, and late-enhancement values during treatment are shown in Fig. 1. The differences in the parameter values pre- (day 0/1) and post-treatment (day 10) are evaluated in Table I (two-sample Student t-test). Table II compares the values of the parameters post-treatment (day 10) with the histological quantification of the tumor after resection, evaluated in terms of VEGFR2 expression levels and percentage of blood-vessel area.

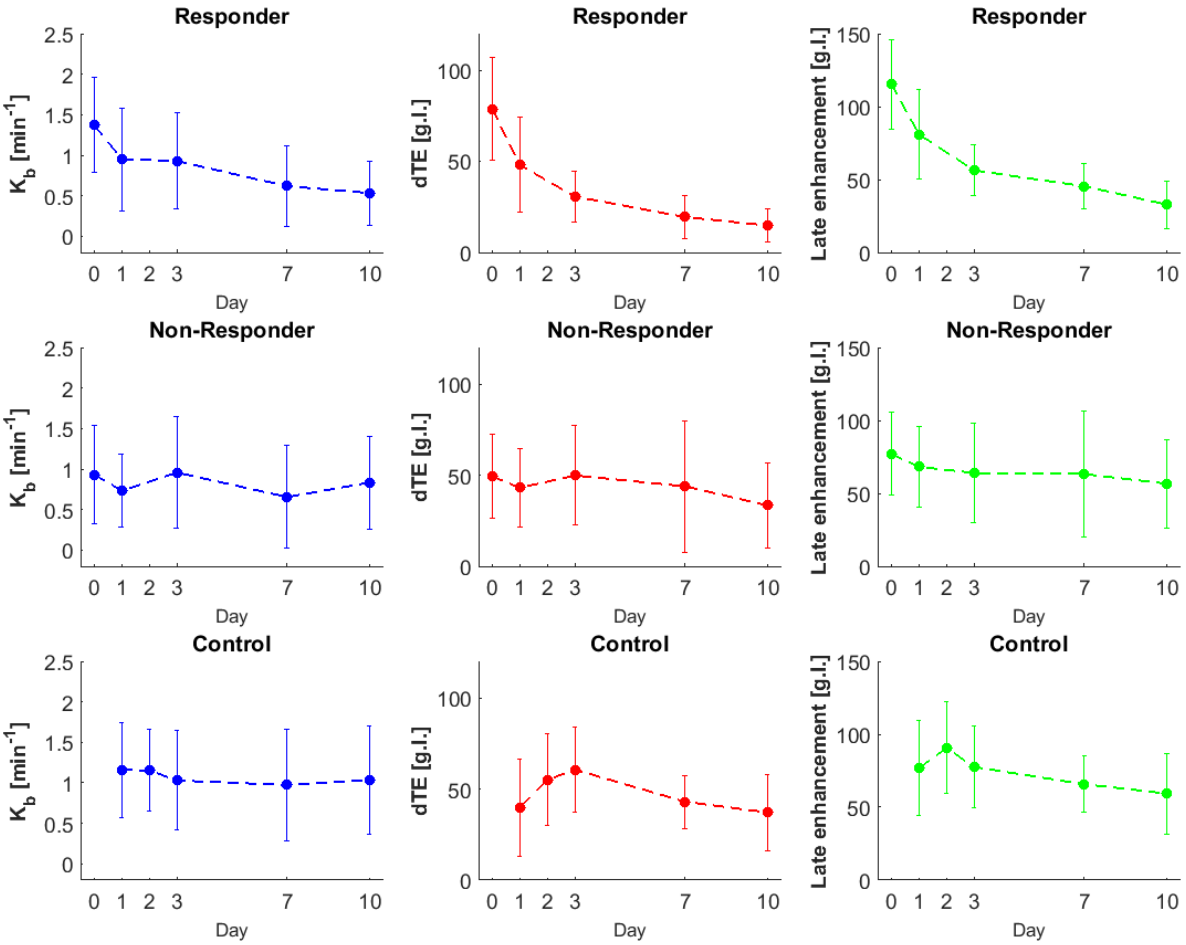

Fig. 1 Binding rate K_b (blue), dTE (red), and late enhancement (green) evaluated at five time points in one responder, one non-responder (treated with Bevacizumab), and one control (treated with saline). Error bars indicate the standard deviation.

Table I. Results of the teo-sample t-test comparing parameter values pre- and post-treatment (1 indicates a significant difference). P-values are given in parenthesis

	K_b [min^{-1}]	**dTE [a.u.]**	**Late-enhancement [a.u.]**
Responder	1 (<<0.1)	1 (<<0.1)	1 (<<0.1)
Non-responder	0 (0.03)	1 (<<0.1)	1 (<<0.1)
Control	0 (0.02)	0 (0.2)	1 (<<0.1)

Table II. Comparison between parameter values at day 10 and the histological quantification of VEGFR2 expression levels and percentage of blood-vessel area (CD31) of extracted tumors.

	K_b [min^{-1}]	dTE [a.u.]	Late-enhanc. [a.u]	VEGFR2 [a.u.]	CD31 [%]
Responder	0.53	14.8	32.8	$0.17 \cdot 10^3$	0.79
Non-responder	1.03	37.1	59.8	$1.21 \cdot 10^3$	5.33
Control	0.83	33.3	56.6	$1.28 \cdot 10^3$	4.62

Conclusions

In this work, a novel method for quantitative USMI by modeling the binding kinetics of tUCAs has been tested in the context of anti-angiogenic therapy monitoring on colon cancer-bearing mice treated with Bevacizumab. The proposed binding parameter K_b showed a significant decrease in the responder mouse, and no significant changes in the non-responder and control mice. Moreover, K_b values after treatment (day 10) were in agreement with the histological quantification of the resected tumors. Although further clinical and preclinical validation is needed, the binding parameter K_b looks a promising, quantitative biomarker for monitoring the tumor response to anti-angiogenic therapy, potentially overcoming some of the limitations of current techniques, including low reproducibility, long acquisition times, and the need for a high-pressure US pulse (dTE), and thus possibly facilitating clinical translation of USMI.

References

1. *J. Folkman, "Role of angiogenesis in tumor growth and metastasis," Seminars in Oncology, vol. 29, pp. 15-18, 12/16/ 2002.*
2. *S. Turco, H. Wijkstra, and M. Mischi, "Mathematical Models of Contrast Transport Kinetics for Cancer Diagnostic Imaging: A Review," IEEE Reviews in Biomedical Engineering, vol. 9, pp. 121-147, 2016.*
3. *A. Zámečníkova, "Novel approaches to the development of tyrosine kinase inhibitors and their role in the fight against cancer," Expert opinion on drug discovery, vol. 9, pp. 77-92, 2014.*
4. *L. Abou-Elkacem, S. V. Bachawal, and J. K. Willmann, "Ultrasound molecular imaging: Moving toward clinical translation," European journal of radiology, vol. 84, pp. 1685-1693, 2015.*
5. *D. L. Miller, "Overview of experimental studies of biological effects of medical ultrasound caused by gas body activation and inertial cavitation," Progress in biophysics and molecular biology, vol. 93, pp. 314-330, 2007.*
6. *S. Turco, P. J. Frinking, H. Wijkstra, and M. Mischi, "Quantification of the binding kinetics of targeted ultrasound contrast agent for molecular imaging of cancer angiogenesis," in Ultrasonics Symposium (IUS), 2015 IEEE International, 2015, pp. 1-4.*
7. *M. P. Kuenen, M. Mischi, and H. Wijkstra, "Contrast-ultrasound diffusion imaging for localization of prostate cancer," IEEE transactions on medical imaging, vol. 30, pp. 1493-1502, 2011.*

Microbubble Shells with Mesoscopic Colloidal Domains

Xianhe Liu and Marie Pierre Krafft

University of Strasbourg, CNRS, Institut Charles Sadron. F-67000 Strasbourg, France
xianhe.liu@ics-cnrs.unistra.fr

We will focus on the design, elaboration and study of innovative microbubbles (MBs) characterized by nanopatterned interfacial films and on the evaluation of their potential for diagnosis and therapy. Certain fluorinated amphiphiles (*e.g.* di- and tetrablock semi-fluorinated alkanes, *F*-alkylcarboxylic acids and phosphates) spontaneously self-assemble in the presence of phospholipids to form monodisperse domains of nano- or micrometric size when spread as 2D films at the air/water interface.[1] It is expected that these interfacial domains will endow microbubbles with specific elastic behaviour, which is supported by the fact that the surface domains form 2D physical gels at the air/water interface.[2]

We will first present a detailed characterization of the fluorinated surface domains in 2D films using atomic force microscopy (AFM), Brewster angle microscopy (BAM), infrared reflection absorption spectroscopy (IRRAS),[3] interfacial shear rheometry (ISR),[2] grazing-incidence X-ray scattering (GI-SAXS) and off-specular neutron scattering.

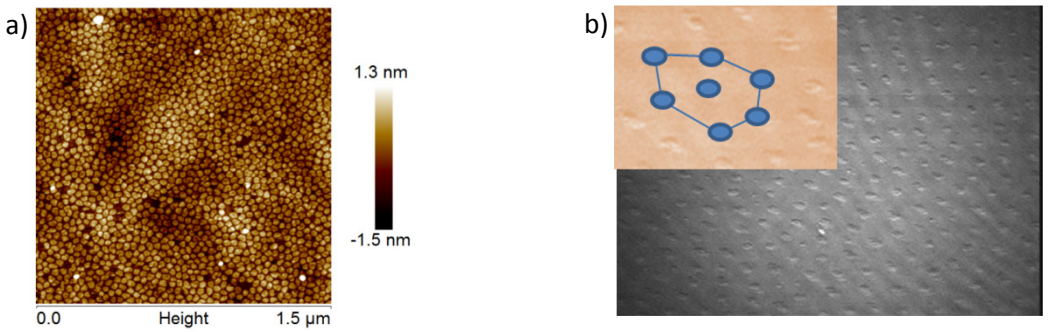

Figure 1. a) AFM image of surface domains of semi-fluorinated diblocks in 2D films and b) BAM image of surface domains of amphiphilic fluorinated phosphates.

Secondly, we will present our initial results on microbubbles stabilized by shells formed by fluorinated domains coexisting with a continuous phospholipid phase. The impact of the fluorinated domains on the bubbles' mean size, stability, hierarchical organisation within the shell, stability, echogenicity and mechanics is being investigated. The techniques used include optical microscopy, static light scattering (SLS), acoustical attenuation measurement and Flicker spectroscopy.

References

1. *M. P. Krafft, Acc. Chem. Res.* ***2012****, 45, 514-524; b) M. P. Krafft, J. G. Riess, Chem. Rev.* ***2009****, 109, 1714-1792.*
2. *T. Habe, M. Veschgini, S. Inoue, S. Mielke, X.-H. Liu, M. P. Krafft, M. Tanaka,* ***2016****, in preparation.*
3. *C. Schwieger, G. Westphal, X.-H. Liu, M. P. Krafft, Soft Matter,* ***2016****, to be submitted.*

Oil layer inside Microbubbles: A Novel route for the production of Hydrophobic Drug Delivery Vehicles

Adam H. Churchman, Victoria Mico, Julia Gala De Pablo, Sally A. Peyman and Stephen D. Evans*

**Molecular and Nanoscale Physics Group, School of Physics and Astronomy, University of Leeds, UK*

This paper reports a new and simple one-step method for the formation of hydrophobic drug delivery capsules with echogenic properties, termed oil layer inside microbubbles (OLI-MBs).

A large number of new, high potency anti-cancer drugs that have shown promising results *in vitro* exhibit poor water solubility, which makes them difficult to deliver *in vivo*, resulting in reduced drug efficacy and even toxicity. As a result there is an urgent need to develop novel systems for the *in vivo* delivery and release of hydrophobic drugs.

Microbubbles (MBs) are micrometer-sized, compressible gas cores stabilized by a lipid monolayer. Flow-focused (FF) microfluidics has emerged as a technique to produce MBs with fine control over their size [1]. MBs have been widely used as contrast agents for diagnostic ultrasound (US) imaging and have already been demonstrated as reliable vehicles for hydrophilic drug delivery [2]. Figure 1 shows an adaptation to the conventional MB architecture to allow hydrophobic drug delivery, through the incorporation of an oil layer between the gas core and lipid shell. Hydrophobic drugs are contained and protected in the inner oil layer before undergoing site-specific, triggered release using an US destruction pulse.

OLI-MB structures have been constructed previously using three-phase FF microfluidics, where gas, oil and lipid solution were brought together in a pinch-off regime. However, control of three phases on-chip is often unstable and requires careful consideration of oil viscosity, limiting the range of suitable oils.

We present a new method for OLI-MB formation utilizing simple microfluidics and nanoparticle self-assembly. As shown in figure 2, a solution of highly stable ~150 nm lipid (POPC) stabilized oil (squalane) nanodroplets, in PBS, were used as the aqueous phase in a FF device with C_4F_{10} as the core gas. During OLI-MB production the oil nanodroplets were found to self-assemble at the gas-water interface. To reduce the energy of the system further, the oil nanodroplets broke to form a thin layer of oil-lipid around the gas core. OLI-MB structures were produced at clinically relevant diameters (< 8 μm) of 2.4 ± 1.6 μm (figure 3), at a rate of ~$5x10^3$ bubbles/s, and an off chip concentration of 10^6 bubbles/ml. In order to visualize the thin oil layer, a hydrophobic fluorophore (DiI) was added to the oil and, as shown in figure 4, OLI-MBs were trapped in microfluidic particle traps so that any excess oil and lipid could be washed away [3]. As the fluorophore was in the oil fraction only, the fluorescent shell around the MB confirms the presence and stability of the oil layer (green).

Additionally, nanodroplet breakage was confirmed using mechanically agitated 10-40 μm OLI-MBs, made from fluorescence resonance energy transfer (FRET) enabled nanodroplets, and confocal microscopy. Here, donor (DiO) loaded nanodroplets and acceptor (DiI) loaded nanodroplets were mixed before OLI-MB formation. Figure 5 shows that FRET occurred only at the gas-water interface, confirming that the oil from both nanodroplet suspensions must have broken and mixed on the MB surface to allow energy transfer. Figure 6 shows how traps were used to confirm FRET OLI-MB stability after cleaning.

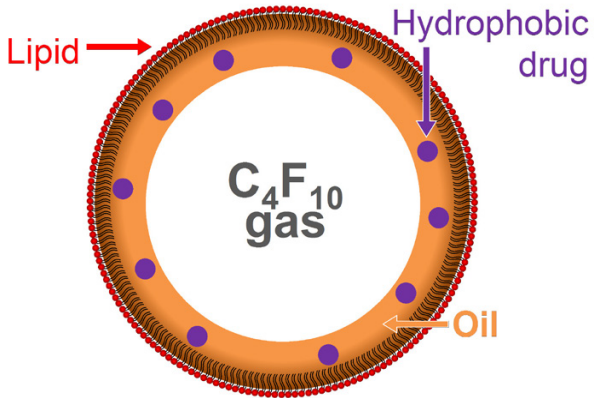

Figure 1: Schematic of the OLI-MB architecture.

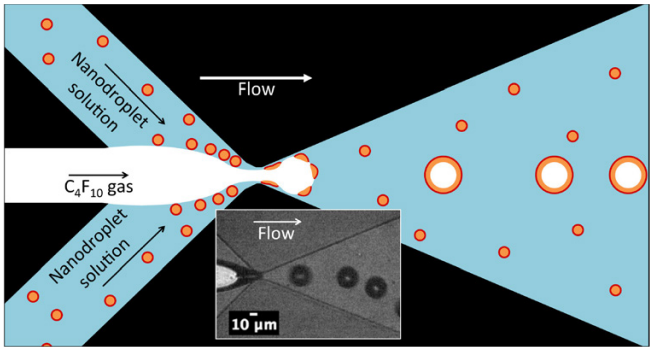

Figure 2: Schematic of proposed microfluidic OLI-MB formation. Inset image is a high frame rate image during production

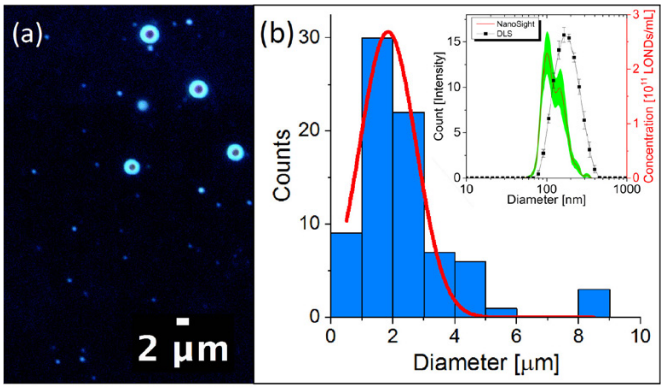

Figure 3: Dark field of (a) OLI-MBs off chip and (b) optical sizing. Insert image shows nanodroplet sizing and concentration using Dynamic Light Scattering and NanoSight

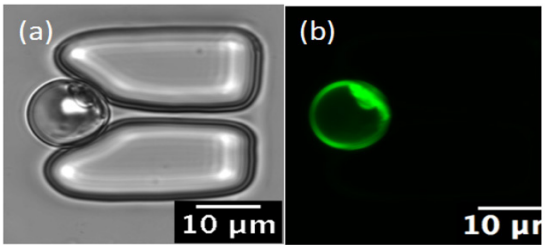

Figure 4: Confocal image of a trapped microfluidic OLI-MB, showing the stability of the fluorescent oil even after washing.

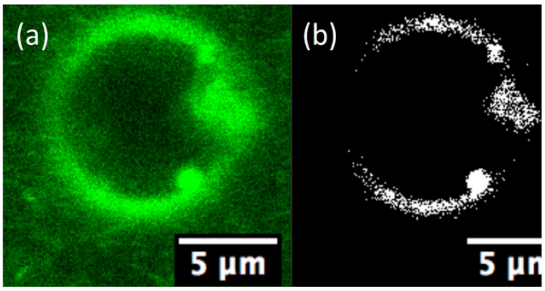

Figure 5: Confocal image of a mechanical agitation OLI-MB produced using FRET enabled LONDs, showing (a) the total fluorescence from the acceptor emission window, and (b) the FRET signal.

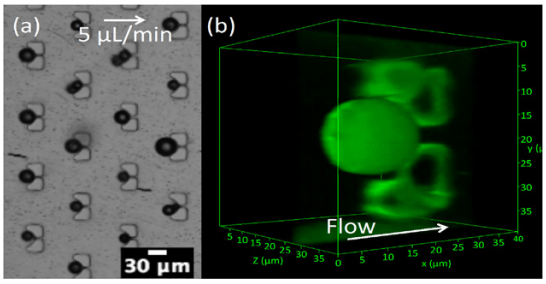

Figure 6: Confocal image of (a) trapped mechanical agitation OLI-MBs using particle traps, and (b) a confocal z-stack of an OLI-MB washed with PBS for 30 min.

References

1. *S.A. Peyman, R.H. Abou-Saleh, J.R. McLaughlan, N. Ingram, B.R.G. Johnson, K. Critchley, S. Freear, J.A. Evans, A.F. Markham, P.L. Coletta and S.D. Evans. Lab Chip, **12**, 4544 (2012).*
2. *A. Kheirolomoom, P.A. Dayton, A.F. Lum, E. Little, E.E. Paoli, H. Zheng and K.W. Feerara. J Control Release, **118**, 275 (2007).*
3. *D. Di Carlo, L.Y. Wu and L.P. Lee. Lab Chip, **6**, 1445–1449 (2006).*

Engineered 3D microvessels for the study of angiogenesis and sonoporation

Eric Juang, Ine De Cock, Christina Keravnou, Sara Keller, Madison Gallagher, Ying Zheng, and Mike Averkiou

Department of Bioengineering, University of Washington, Seattle, USA

Introduction

The microvasculature defines the physical and biochemical microenvironment within a tissue; it mediates the interaction between blood and tissue and plays a crucial role in the normal function of a tissue or the progression of diseases such as cancer. Delivering drugs and reagents through the vessels and into the cancer site has been a major thrust in cancer. In recent research, sonoporation, ultrasound-mediated cell membrane permeability change, has been demonstrated as a feasible method to increase drug uptake in cancer sites [1]. To investigate the process of sonoporation, most studies have focused on simple *in vitro* cell-monolayer setups due to the complexity of the biological environment. However, to understand the interaction between the microbubbles and vessel wall under physiological flow and shear at the molecular and the cellular level, it is necessary to develop a physiological microvascular model with *in vivo*-like 3D geometry, flow, and biotransport microenvironment.

Our group has successfully developed an endothelialized 3D microvascular model that recapitulates the complex structure and flow characteristics found *in vivo* [2]. Previously, we have demonstrated that these vessels exhibit proper intercellular junctions and have permeability and non-thrombogenic properties similar to those *in vivo*. In addition, we have also used this model to study the angiogenic properties of endothelial cells. In the present work, we further exploit the established microvessel models to study of microbubble-cell interactions during ultrasound induced sonoporation. Our objective is to develop a 3D microvascular network ideal for the study of sonoporation, perfuse it with microbubbles and induce *in vivo*-like flow conditions, and finally expose the microbubbles to ultrasound with various settings to induce sonoporation.

Materials and Methods

The 3D microvascular networks consist of three major components: an acrylic housing piece with inlet and outlet that enables the perfusion of human umbilical vein endothelial cells (HUVECs) and cell-culture medium, a block of micropatterened collagen, and another acrylic housing piece with a cover slide in the middle (Figure 1). The microvascular network is constructed in four steps: 1) fabrication of a polydimethylsiloxane(PDMS) positive-mold with soft lithography for collagen-patterning, 2) injection of type I collagen into the acrylic housings (injection molding), 3) gelation of the collagen and assembly of the device, 4) seeding of the microvascular channels with HUVECs. Type I collagen was prepared from rat tails to a stock concentration of 15mg/ml, which was further diluted and neutralized to 7.5mg/ml prior to microvessel fabrication.

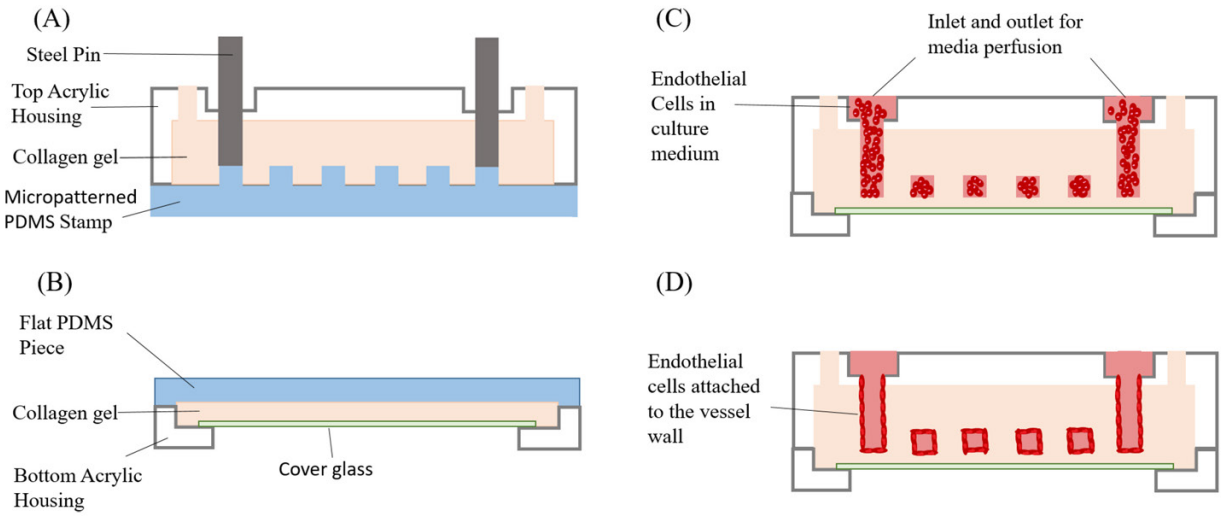

Figure 1. A schematic overview of the *in vitro* microvessel assembly and seeding procedures. (A) Microstructured collagen is molded with a micropatterned PDMS stamp in the top jig. (B) A flat collagen slab is molded with a flat PDMS piece in the bottom jig. (C) After collagen is sufficiently gelled, the top and bottom jigs are assembled together, and HUVECs are perfused into the microvascular network through the inlet and outlet by pipetting. (D) After two days of culture, endothelial cells attached to the vessel walls. *The relative proportions of the components are not to scale.

A syringe pump is used to perfuse a mixture of endothelial cell growth medium, microbubbles, and propidium iodide (PI) into the vascular channels. After fluid flow reaches steady state in the vascular channels, ultrasound (1 MHz, 500 cycles, 1.4 MPa, 5% DC, 5 sec exposure time) is applied. Bright-field microscopy at 30 fps is used to image microbubble perfusion in the network and microbubble-cell interactions upon the exposure of microvascular networks to ultrasound.

Results

Endothelialized 3D microvascular networks reached optimal condition in 3 days and remained viable over 7 days (Figure 2). The HUVECs distributed uniformly in the microvascular channels, covering and adhering to the walls of the channels. With calcein AM staining, we verified that the cells are viable after seeding (Figure 2). With immunostaining using endothelial-cell-specific markers (CD31), we also verified, in a separate microvessel, that these cells retained their endothelial phenotype and gene expression profile (Figure 3).

A flow rate of 10µl/min was found to create physiological shear at the blood-endothelium interface. The perfusion of microbubbles ($1.2x10^8$ microbubbles/ml) in the 3D networks was monitored with bright-field imaging. We observed no adverse effects on the endothelium as the microbubbles do not interact with the endothelium.

Destruction of microbubbles was evidently observed in microvascular channels during exposure to ultrasound (Figure 4). We noticed significant PI uptake in cells proximal to the destructed microbubbles, which indicates permeabilization of the plasma membrane or sonoporation. Cells next to microbubble clusters showed a higher degree of sonoporation.

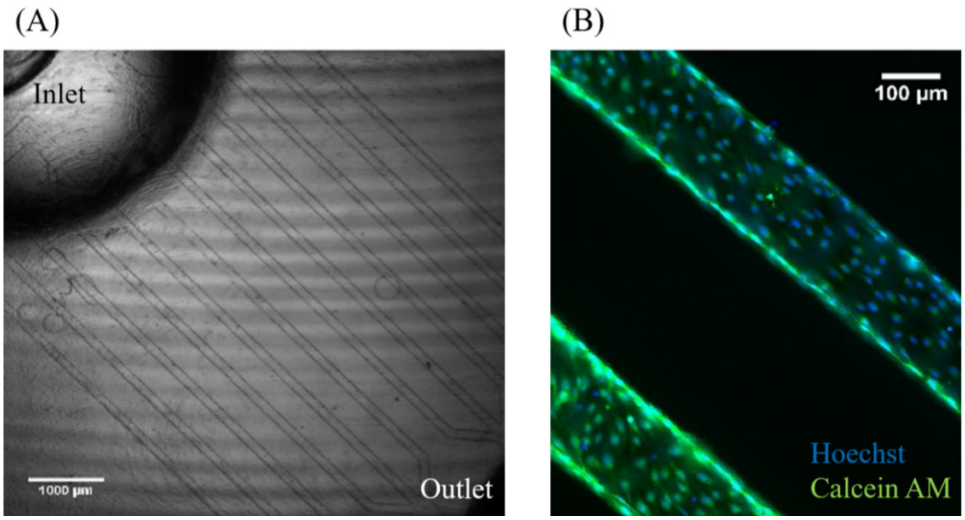

Figure 2. Condition of an *in vitro* microvessel after 4 days of culture. (A) In well-formed vessel channels, the HUVECs aligned nicely at the vessel wall. (B) Calcein AM staining showed that the HUVECS attached to the vessel channels were still viable after 4 days of culture. Cell nuclei were stained with Hoechst.

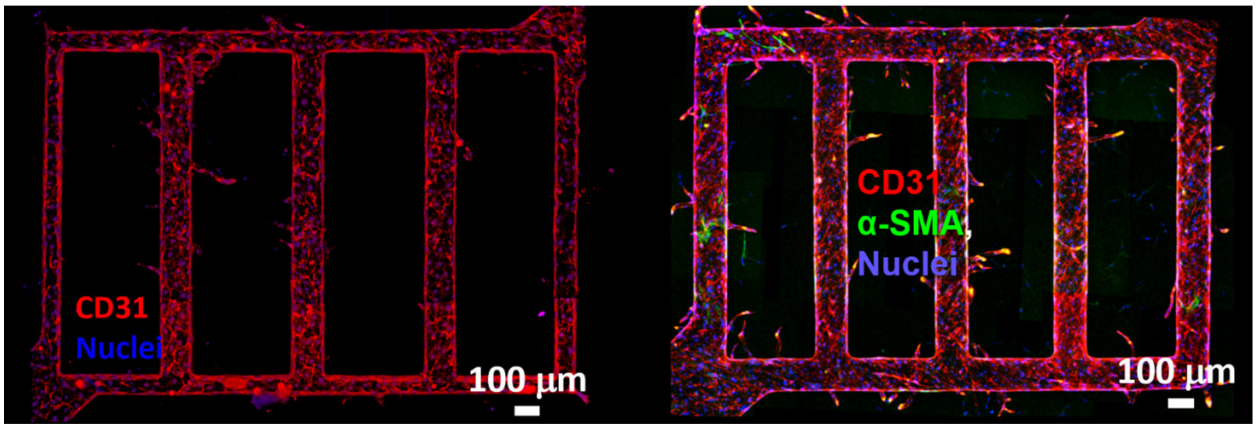

Figure 3. Left: Vessel sprouting (angiogenesis) into the collagen space under influence of proangiogenic stimuli in our *in vitro* microvessel model. Right: Co-culturing endothelial cells with perivascular cells (pericytes) stabilizes the endothelialized microvessels; promotion of angiogenesis is observed. CD31 (Red) is an endothelial-cell-specific marker. α-smooth muscle actin (α-SMC) is a differentiation marker for smooth muscle cells, and it is present in pericytes.

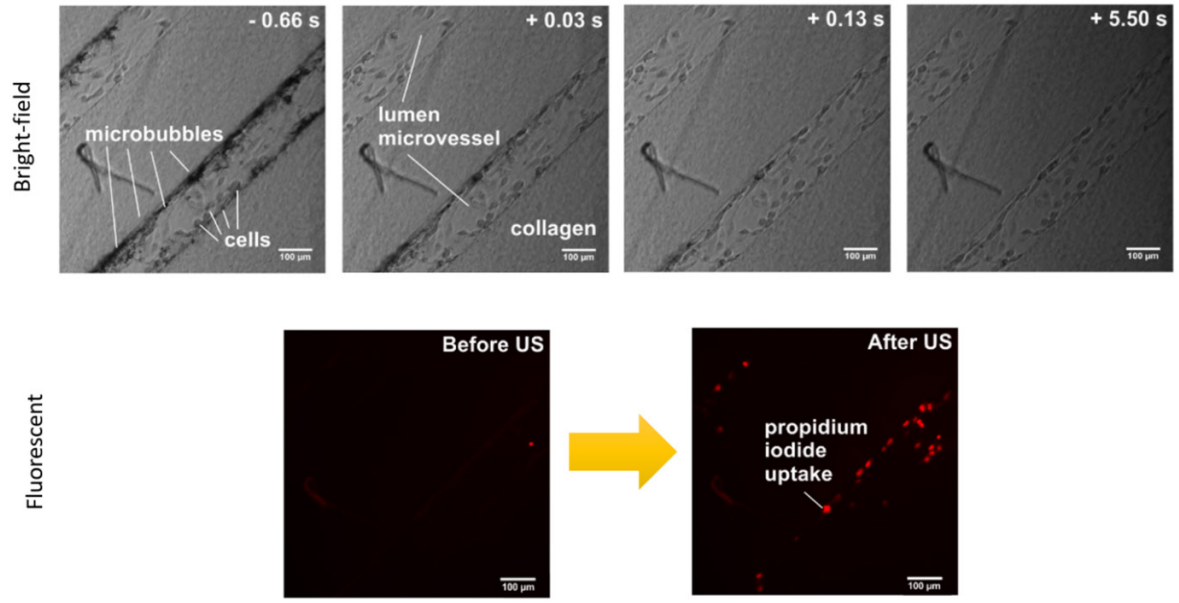

Figure 4. Bright-field (top row) and fluorescent (bottom row) images taken before and after the exposure of an *in vitro* microvessel to the ultrasound. By comparing the bright-field images taken before (-0.66s) and after (+0.03s and onward) ultrasound exposure, we can clearly see that the microbubbles are destroyed by ultrasound. PI uptake significantly increased in regions which microbubbles accumulated before ultrasound exposure.

Discussion and Conclusion

Endothelialized 3D microvascular network is an excellent model for the study of sonoporation. We have successfully fabricated endothelialized *in vitro* microvessels and were able to induce sonoporation under flow conditions. In regards to microbubble perfusion, it is worth noting that microbubbles only adhered to some regions of the vessels. These observations were made with both custom-made microbubbles and commercial microbubbles, suggesting that these result from flow variations instead of difference in microbubble properties.

While we have only used microvessels with simple geometries (parallel channels) so far, it is possible to create microvessels with more complex geometries that better mimic the human vascular network. By perfusing the microvessels with vasculogenic medium to mimic the tumor microenvironment or by co-culturing the endothelial cells with pericytes, endothelial sprouting can be induced (Figure 3).

In the future, in addition to endothelialized microvessels, we would work on incorporating tumor cells into the model to study the effect of cytotoxic and antiangiogenic drugs during sonoporation.

References

1. *Lentacker I, De Cock I, Deckers R, De Smedt SC, Moonen CT, Understanding ultrasound induced sonoporation: definitions and underlying mechanisms, Adv. Drug Deliv. Rev, 72 (2016), 49-64.*
2. *Zheng Y, Chen J, Craven M, Choi NW, Totorica S, Diaz-Santana A, Kermani P, Hempstead B, Fischbach-Teschl C, López JA, Stroock AD, In vitro microvessels for the study of angiogenesis and thrombosis, Proc. Natl. Acad. Sci. USA, 109 (2012) 9342-7.*

Combining Ultrasound Molecular Imaging with Modulated Acoustic Radiation Force for Visualization of Inflammation in the Mouse Abdominal Aorta

Shiying Wang[1], Elizabeth B Herbst[1], Sunil Unnikrishnan[1], Alexander L. Klibanov[1,2], F. William Mauldin Jr.[1], John A. Hossack[1]

[1]Department of Biomedical Engineering
[2]Division of Cardiovascular Medicine, University of Virginia, Charlottesville, VA 22908, USA

Introduction

The current standard of care for diagnosing carotid atherosclerosis relies on measurements of luminal stenosis, which is an inadequate predictor of patient stroke risk. In this study, we propose a novel method of *in vivo* ultrasound imaging which utilizes modulated acoustic radiation force (ARF) to translate molecularly targeted microbubbles to inflammatory markers expressed on the endothelium of the mouse abdominal aorta. By using a molecular-based approach, we are able to enhance imaging sensitivity and allow for quantitative measurements of disease progression.

Methods

Abdominal inflammation was modeled by treating mice ($M_{Inflammation}$) with intraperitoneal injections of tumor necrosis factor-α 2.5 hours prior to imaging with microbubbles targeted to P-selectin antibody ($MB_{P\text{-}selectin}$). Diet-induced obesity was modeled by feeding mice (M_{DIO}) a lard-based high-fat diet at 6-30 weeks of age and imaging with microbubbles targeted to VCAM-1 ($MB_{VCAM\text{-}1}$). Normal mice (M_{Normal}) were imaged using both isotype-control targeted microbubbles ($MB_{Control}$) and antibody-targeted microbubbles of each type. The complete imaging sequence consisted of 180 s of continuous imaging interspersed with 90s of ARF application. Time intensity curves of the aortic wall were collected, and microbubble adherence to the vessel wall was quantified based on residual-to-saturation ratio (RSR) (Fig. 1A).

Results

The RSR of $M_{Inflammation}$ + $MB_{P\text{-}selectin}$ trials and M_{DIO} + $MB_{VCAM\text{-}1}$ trials were 40.9% and 60%, respectively, and were significantly higher than all corresponding control trials, which had negative RSR values (Fig. 1B). Immunohistochemistry on excised $M_{Inflammation}$ and M_{DIO} abdominal aortas confirmed significant accumulation of molecular disease markers on the endothelium (Fig. 1C).

Conclusions

The application of modulated ARF during ultrasound imaging of the mouse abdominal aorta allows effective translation of P-selectin and VCAM-1 targeted microbubbles to the aortic wall. The RSR extracted from microbubble time intensity curves provides a quantitative measurement of microbubble binding to disease markers on the aortic endothelium.

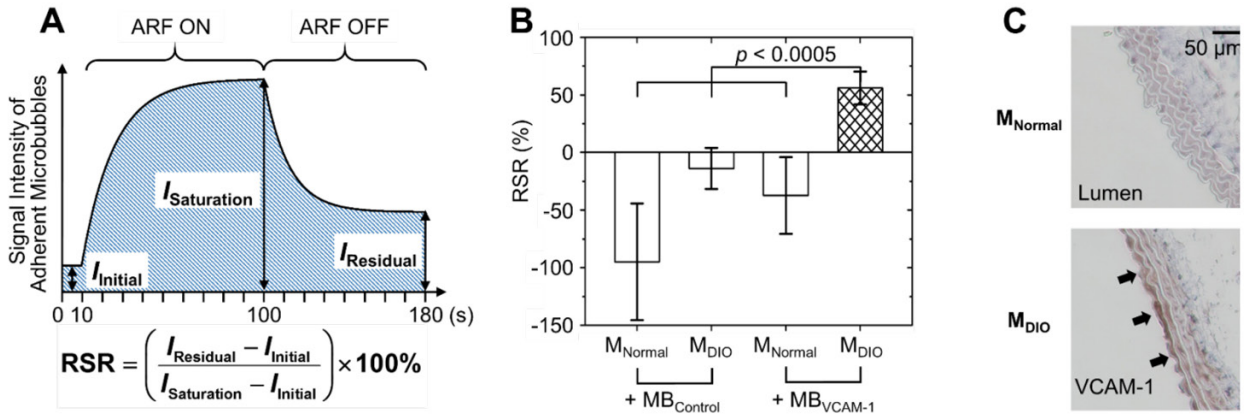

Figure 1. Measurement of residual-to-saturation ratio (RSR) using a modulated ARF imaging sequence allows for detection of VCAM-1 on the aortic endothelium. A. Diagram of the expected signal intensity of the mouse abdominal aortic wall through time. During the "ARF ON" phase, modulated ARF is used to translate targeted microbubbles to the aortic wall to promote specific binding to receptors on the endothelium. During the "ARF OFF" phase, non-adherent microbubbles flow away, leaving a residual signal of specifically adherent microbubbles. RSR is calculated based on the initial signal intensity of the aortic wall ($I_{Initial}$), the peak signal intensity near the end of the ARF sequence ($I_{Saturation}$), and the residual signal of adherent microbubbles ($I_{Residual}$). **B.** Plot of RSR values for M_{Normal} and M_{DIO} mice, administered injections of either $MB_{Control}$ or MB_{VCAM-1} microbubbles. **C.** Immunohistochemistry staining for VCAM-1 on the excised abdominal aortas of M_{Normal} and M_{DIO} mice.

Numerical study on the static response of contrast agent microbubbles

Alkmini D. Lytra & Nikos A. Pelekasis*

*Laboratory of Fluid Mechanics & Turbomachinery, Dep. of Mechanical Engineering, University of Thessaly, Volos-Greece.*pel@uth.gr*

There are two major families of coating materials that are usually employed in medical applications: polymeric and lipids. Polymeric shells are characterized by higher area dilatation modulus and shell thickness in comparison with shells covered with lipids. The latter are softer and exhibit significant deformations when subjected to forces as low as several nN. The present study presents calculations of the static deformation of a coated microbubble that is compressed by a rigid surface, in order to assist the interpretation of Atomic Force Microscopy measurements conducted to provide estimates of the shell elastic properties. A classic contact model is proposed for microbubbles covered with a polymeric shell based on the classic shell mechanics [1]. For microbubbles with a lipid shell a model that accounts for intermolecular forces is employed, by introducing an adhesive potential [2] which describes the disjoining pressure between the shell and the AFM cantilever. Thus, an additional resistance to the cantilever's advancement is introduced in order to account for the ultrathin water layer that occupies the space between the shell and cantilever, as a result of their hydrophilic nature, and resists thinning as the external pressure increases. In both models axisymmetry is assumed with respect to the vertical axes and symmetry in the equator. The resistance to gas compression is accounted for as well as the non-linearity of the constitutive law for the elastic shell [3].

The static response of a coated microbubble, employing the above models, is investigated numerically as it is compressed by a flat plate, using the finite element methodology with b-cubic splines as basis functions. Benchmark calculations verify the validity of the models and an extensive parametric analysis is carried out in order to investigate the effect of different parameters on force-deformation (f-d) curves. The results are compared against Atomic Force Microscopy measurements [4-5] and estimates of the elastic properties of the shell are obtained.

Force-deformation curves calculated for polymeric shells with the classic contact model exhibit an initial linear regime followed by a nonlinear curved downwards regime, characterized by shapes that are flat or bended in the pole region, respectively, Fig 1a. The linear regime loses stability due to excessive compression giving rise to shapes with crater formation. This behavior conforms with the classic transition from the linear, Reissner, to the nonlinear, Pogorelov, regimes in the f-d curves. Employing analytical expressions from Reissner and Pogorelov theory [1] the shell thickness and Young modulus can be estimated with excellent agreement with the experimentally obtained values [6], Fig 1b. Incorporating the effect of pre-stress in the model accurately recovers the force level at which shell buckling takes place.

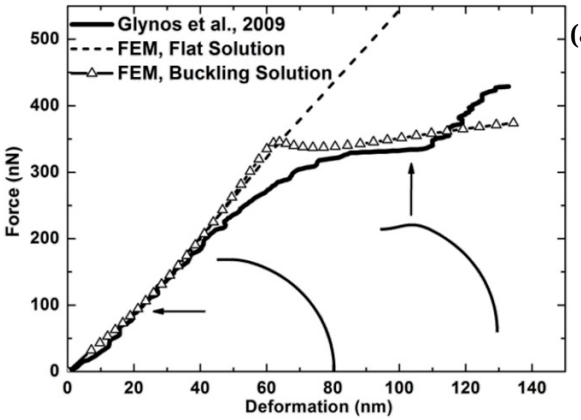

(a)

(b)

	Experimental Values [4]		Asymptotic Estimation	
D_o [μm]	E [GPa]	h [nm]	E [GPa]	h [nm]
2.6	10-16	20	8.5	25
4.1	2.5-6	31	6.1	31
3.1	6-10	23	3.4	35
4.0	2.5-6	30	4.7	30
5.5	1-3	41	1.7	47

Figure 1: **(a)** *Comparison of numerical (dashed & triangles) and experimental [1] (solid curve) results in terms of the f-d curve for microbubbles covered with polymer. Simulation parameters: initial radius R_o=2 μm, Young modulus E=4.7 GPa, shell thickness h=30 nm, surface tension γ_{bw}=0.051 N/m, pre-stress u=-1.25·10^{-3} μm, Poisson ratio v=0.42, neo-Hookean constitutive law and 400 B-cubic splines for FEM. In this case the numerical response is the intersection of the flat (dashed) and buckling (triangles) solutions.* ***(b)*** *Young modulus and shell thickness obtained via asymptotic estimates and experimental measurements.*

Using the model that accounts for the intermolecular forces, f-d curves are calculated which are directly compared against AFM measurements with lipid shells [5], Fig 2a. The two curves coincide with satisfactory agreement up to deformation of 300 nm. Shell buckling is not detected, as it was expected based on the almost linear behavior of both f-d curves; see also the shape of the microbubble in deformed configuration for selected values of deformation shown in 1b. This behavior conforms well with the Reissner response pattern. Due to the relatively small bending to dilatational stiffness ratio, $k_b / (R_0^2 \chi) << 1$ and the stabilizing effect of adhesion onto the cantilever, the Pogorelov regime is bypassed and the Reissner curve persists until relatively large forces. Repeating the calculation employing the Reissner model [7] produces almost the same response curve, Fig 2a. Coupling the linear Reissner relationship with optical measurements of the evolution of the contact length of the microbubble onto the cantilever will produce the bending resistance and area dilatation modulus of the shell. Repeating the above calculation treating isotropic surface tension as the dominant form of tension that develops on the shell, produces a quadratic f-d curve which deviates from available AFM measurements with lipid shells.

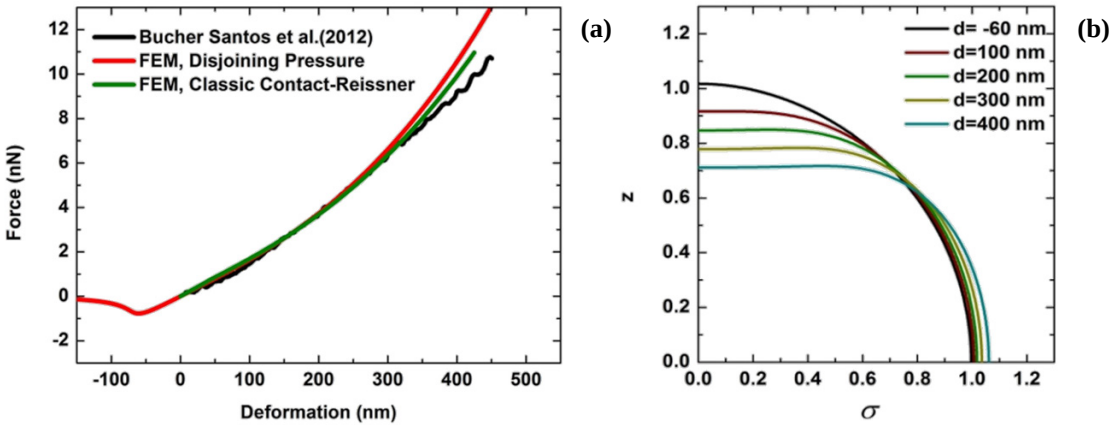

Figure 2: (a) Comparison of numerical and experimental [2] f-d curves for microbubbles covered with phospholipid monolayer and (b) Shape of the microbubble in deformed configuration for selected values of deformation (d), The axes (σ,z) are dimensionlized with the initial radius R_o. to The simulation parameters are set to: R_o=1.5 μm, area dilatation modulus χ=0.05 N/m, bending stiffness $k_b=3\cdot10^{-16}$ Nm, γ_{bw}=0, u=0, ν=0.5, Mooney-Rivlin law, adhesive potential parameters: $W_o=10^{-4}$ N/m, δ_A=50 nm and 400 B-cubic splines.

Acknowledgments

This work was performed in the framework of the operational program: «Education and lifelong learning» - «Aristeia I».

References

1. Landau, L.D., et al., Theory of Elasticity. 1986: Butterworth-Heinemann.
2. Blount, M.J., M.J. Miksis, and S.H. Davis, Proc. R Soc. A, 2013. 469(2153).
3. Barthes-Biesel, D., A. Diaz, and E. Dhenin, JFM, 2002. 460: p. 211-222.
4. Glynos, E., et al., Langmuir, 2009. 25(13): p. 7514-7522.
5. Buchner Santos, E., et al., Langmuir, 2012. 28(13): p. 5753-5760.
6. Lytra, A., Pelekasis, N., Sboros, V. Glynos, E. and Koutsos, V., Procedia IUTAM, 2015. 16: p. 123-133.
7. Updike, D. P. and Kalnins, J. Appl. Mech., 1970, Vol. 37, TRANS. ASME, Vol. 92, Series E, 635-640.

Subwavelength far-field ultrasound targeted drug-delivery

Vincent Hingot, Marine Bézagu, Claudia Errico, Yann Desailly, Romain Bocheux, Mickael Tanter, Olivier Couture

Institut Langevin, CNRS, INSERM, ESPCI Paris, PSL Research University, 17 rue Moreau, 75012, Paris

Although the diffraction-limit of resolution for ultrasound imaging has been bypassed in-vivo with the localization of microbubbles [*Errico et al, Nature 2015*], the precision of therapeutic ultrasound remains bound to the half-wavelength limit. In therapy, removing the compromise between penetration and resolution could improve the accuracy of treatment in depth or beyond the skull. In this study, we demonstrate a strategy for subwavelength drug-delivery which relies on the abrupt release threshold of monodisperse droplets along with ultrafast monitoring of their release [*Hingot et al, APL 2016*].

Monodisperse droplets are produced with a highly-parallelized microfluidic glass system to obtain a uniform size of 3.3 μm (polydispersity 9%). The inner matrix of the composite droplets, made of perfluorohexane, vaporizes when the pressure reaches a critical level, which releases the aqueous nanodroplets it contains [Couture et al. 2011, Couture et al, 2012]. In this experiment, we loaded fluorescein in the nanoemulsion, but it can be replaced by other active molecules or even serve as a chemical micro-reactor [*Bezagu et al, JACS 2014*].

We triggered the release of 3.3 μm fluorescein loaded composite droplets at 5 MHz (λ=300 μm) in a cell culture plate with an ultrasound probe connected to a programmable ultrafast ultrasound scanner. A single pulse lasting 4 µs with a peak-negative pressure of 2.6 MPa was shown to trigger the release of the droplets. By increasing gradually the pressure in this range, the release of the droplets could be confined in an area as small as 70 μm (λ/4.3) as measured optically with a fluorescence microscope (x8). When two spots were released side-by-side, they could also be distinguished at a distance of 70 μm (figure 1).

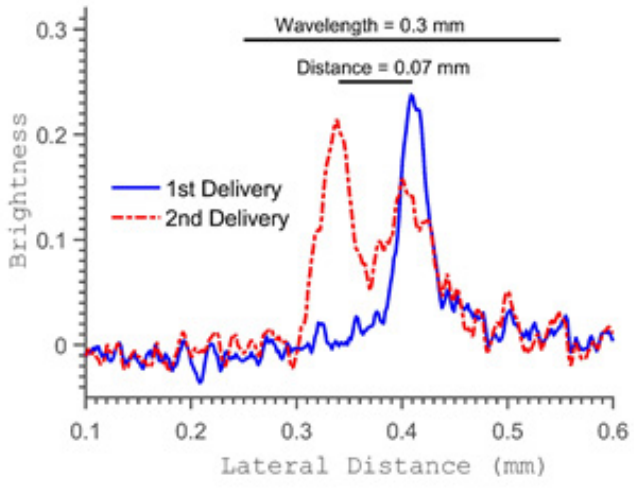

Two release spots distant of λ/4.2

We also demonstrated that the release of droplets can be followed acoustically. The acquisition of 100 ultrafast images within 15 ms before and after the release pulse can highlight the conversion of the droplets to gas. Moreover, the position of the droplet's release can be super-localized and determined with a resolution better than λ/2.

As composite droplets carry large payloads and their release last only 4 μs, this proof-of-concept let us envision the possibility to treat large lesions with a very sharp resolution without compromising on the penetration depth of the ultrasound wave. Moreover, subwavelength monitoring of the release can be done with the same probe.

Multiparametric approach for Dynamic Contrast-Enhanced Ultrasound imaging of prostate cancer

R.R. Wildeboer[1], A.W. Postema[2], L. Demi[1], M.P.J. Kuenen[3], H. Wijkstra[1,2], M. Mischi[1]

[1] Department of Electrical Engineering, Eindhoven University of Technology, the Netherlands
[2] Department of Urology, Academic Medical Center, University of Amsterdam, the Netherlands
[3] Philips Research, Eindhoven, the Netherlands

Introduction

Prostate cancer (PCa) is the most commonly diagnosed type of non-cutaneous cancer in American men [1]. A sufficiently reliable PCa imaging method is currently not available, leaving systematic biopsy as the guideline-recommended technique for PCa diagnosis [2]. Dynamic Contrast-Enhanced Ultrasound (DCE-US) is currently being studied for the characterization of prostatic tissue, since it might prove able to reveal the vascular changes associated with (PCa) angiogenesis [3]. The effect of PCa on blood flow, however, is ambiguous [4]; assessment of the contrast agent kinetics that is more objective than the visual inspection of the contrast video is therefore required.

In recent years, parametric analysis of DCE-US recordings has shown promising results in distinguishing benign and malignant tissue. The pixel-specific evolution of contrast intensity over time, referred to as the time-intensity curve (TIC), can be used to extract valuable heuristic parameters: the peak intensity (PI), the peak time (PT), the appearance time (AT, where the TIC reaches 5% of the PT), the wash-in time (WIT, from the AT to the point where the TIC reaches 95% of the PI), and the full-width half maximum (FWHM). Analysis of the TIC by fitting the data by a local density random walk model also allows for the extraction of physics parameters such as the mean transit time (μ), the skewness parameter (κ), and the ratio between the diffusive and convective time ($\lambda = \mu\kappa$) [5]. Lastly, the TIC similarity between each pixel and its neighbours can be quantified by the spectral coherence (ρ) or spatiotemporal correlation (r), providing a measure of contrast dispersion [6].

The mentioned parameters can be viewed as related to dispersion or perfusion. Therefore, we hypothesize that they exhibit complementary information. A combination of parameters might thus improve the accuracy of PCa localization in DCE-US images. We tested three supervised machine learning strategies to combine individual parameters in a multiparametric approach.

Materials & Methods

At the Academic Medical Center, University of Amsterdam, DCE-US recordings were performed in 19 patients that were referred for radical prostatectomy. The procedure was carried out using a 2.4 mL SonoVue® (Bracco, Milan) bolus that was intravenously injected and imaged with an iU22 ultrasound scanner (Philips, Bothell; equipped with a C10-3v or C8-4v probe). Histopathological analysis allowed us to draw ~0.5-cm^2 regions of interest (ROIs) on the B-mode images, depicting 43 benign and 42 malignant areas on 45 DCE-US images in total. From the pixels in these ROIs, all parameters mentioned in the introduction were extracted following the methods in [5, 6]. Subsequently, these parameters were individually evaluated using the optimum threshold based on their Receiver Operating Characteristics (ROC) curve.

The accuracy of the multiparametric classification was evaluated in each prostate using the other prostates as a training set following a leave-one-out approach. Values were normalized to their 90th

percentile. Due to the ease of its implementation, the *k*-Nearest Neighbour (*k*-NN) approach is often used as the benchmark for other machine learning approaches [7]. This algorithm classifies each pixel in the test set by assessing the most represented class in the *k* pixels with the shortest distance in multiparametric space (k = 5, Euclidean distance). Furthermore, we evaluated a Support Vector Machine (SVM) algorithm that defines a hyperplane separating benign and malignant pixels in the training set [7]. Subsequently, each pixel in the test set is classified depending on its location with respect to this decision boundary. A nonlinear hyperplane based on a radial basis function (i.e., Gaussian) was adopted and the pixels in the training set were downsampled by a factor 30 to reduce computation time. In addition, a Gaussian Mixture Model (GMM) approach was performed [8]. For this, the same-class pixels are described by Gaussian probability distributions in multiparametric space, allowing us to classify each test pixel as the class for which it has the highest probability (p_A). Moreover, we defined a confidence level of the classification based on the ratio of the two probabilities (p_A and p_B) via $P = 2p_A / (p_A+p_B) - 1$. The analyses were performed in Matlab® (MathWorks, Natick, MA).

	ROC: single parameters			*k*-NN		SVM		GMM	
Parameters:	*r*	*WIT*	*μ*	*κ, λ, r*		*AT, PT, μ, r*		*PT, κ, μ, r*	
Accuracy (%)	73	72	72	**78**	*76 (65–91)*	**81**	*81 (68–97)*	**81**	*81 (68–98)*
Sensitivity (%)	71	75	74	**73**	*74 (54–96)*	**74**	*84 (47–98)*	**79**	*87 (45–99)*
Specificity (%)	75	68	70	**79**	*79 (63–93)*	**86**	*90 (69–100)*	**80**	*84 (55–100)*

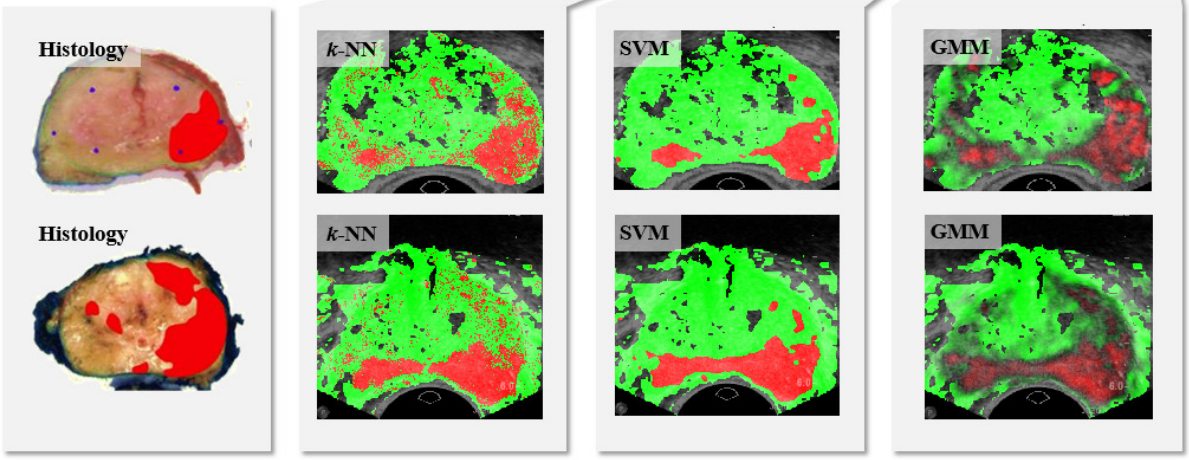

FIG 1. *Performance of the best-performing single parameters as well as the best-performing multiparametric sets using the three machine learning approaches. The* **mean** *of the multiparametric sets as well as the median (10%–90% range) are reported. Below the table, the multiparametric maps of overlaying two imaging planes are shown alongside histopathology. Suspicious regions are shown in red, whereas non-suspicious areas are depicted in green. The transparency of the GMM images scales with the confidence level.*

Results

For each classification algorithm, the multiparametric set consisting of one to four parameters with the highest average accuracy over all prostates was selected. The table in **Fig. 1** reports the classifier performance as well as the best performing single parameters from similarity analysis, curve assessment, and model-based analysis, respectively. The multiparametric results of the *k*-NN algorithm are an improvement as well as those of the SVM and, in particular, the GMM, which outperforms the single parameters over all performance measures.

In **Fig. 1**, full-plane multiparametric maps are shown alongside the histopathology to give an impression of the classifiers' results. Generally, *k*-NN algorithms yield images in which classes are somewhat scattered instead of delineated in specific malignant and benign areas. Furthermore, the GMM algorithm allows the definition of a confidence level that enables us to assess the likelihood of misclassification. Exclusion of low-confidence pixels was shown to result in an increased accuracy.

Discussion and Conclusion

In this work, we evaluated the performance of multiparametric DCE-US for the localization of PCa using several machine learning approaches. Due to the underlying design of the *k*-NN, SVM, and GMM algorithms and the differences in parameter distributions, each method yields a different best-performing parameter set. However, all approaches demonstrate that a combination of dispersion and perfusion related parameters mostly improves the accuracy of classification, that is, all of them select both r and μ or λ. In comparison, the SVM and the GMM seem more suitable for this technique than the *k*-NN algorithm.

Validation in an extended patient group and further optimization of the classification algorithms are recommended. Nevertheless, the results obtained by multiparametric classification of DCE-US are promising and suggest that this technique might become useful in targeted biopsy or the planning of focal therapy.

Acknowledgements

This work was performed in the framework of the IMPULS2-program within the Eindhoven University of Technology in collaboration with Philips. It was also supported by an unrestricted grant from the Dutch Cancer Society (#UVA2013-5941) and the European Research Council Starting Grant (#280209).

References

1. *American Cancer Society (2015) Cancer Facts and Figures 2015. Am Cancer Soc.*
2. *Heidenreich A, Bastian PJ, Bellmunt J, et al. (2014) EAU Guidelines on Prostate Cancer. Part 1: Screening, Diagnosis, and Local Treatment with Curative Intent—Update 2013. Eur Urol 65:124–137.*
3. *Cosgrove D (2003) Angiogenesis imaging–ultrasound. Br J Radiol 76:S43–S49.*
4. *Carmeliet P, Jain RK (2000) Angiogenesis in cancer and other diseases. Nature 407:249–257.*
5. *Kuenen MPJ, Mischi M, Wijkstra H (2011) Contrast-ultrasound diffusion imaging for localization of prostate cancer. IEEE Trans Med Imaging 30:1493–1502.*
6. *Kuenen MPJ, Saidov T a, Wijkstra H, et al. (2013) Spatiotemporal correlation of ultrasound contrast agent dilution curves for angiogenesis localization by dispersion imaging. IEEE Trans Ultrason Ferroelectr Freq Control 60:2665–9.*
7. *Nattkemper TW, Arnrich B, Lichte O, et al. (2005) Evaluation of radiological features for breast tumour classification in clinical screening with machine learning methods. Artif Intell Med 34:129–139.*
8. *Acharya R, Ng EYK, Chang YH, et al. (2008) Computer-based identification of breast cancer using digitized mammograms. J Med Syst 32:499–507.*

Optical Flow tracing and Particle Image Velocimetry of micro-contrast agents in micro-ultrasound acquisitions: new method for tumor's rheological and microenvironment evaluation

Pierangela Giustetto[1], Dieter Fuchs[2]

[1]Freedom Waves srl – I3P Politecnico di Torino, Turin - Italy
[2] Fujifilm VisualSonics, Joop Geesinkweg 140, Amsterdam, The Netherlands.

Introduction

Studies of tumor angiogenesis, vascular function and microenvironment are being pursued using multiple approaches. For example, histological and molecular methods readily provide quantitative analyses at tissue, cellular, sub-cellular and molecular levels in both preclinical models and in clinical studies. However, these techniques are not suitable for dynamic or functional studies and are highly invasive. On the other hand, imaging techniques provide non-invasive or minimally invasive dynamic measurements of physiological functions in real-time.

Early evidence of vascular phase is very important into the study of tumor growth, because microcirculation plays an important role in the growth, metastasis, detection, and treatment of tumors.

In addition to the physiological and biochemical changes, tumors generate physical forces during growth and progression; these physical forces can compress blood and lymphatic vessels, reducing perfusion rates and creating hypoxia area.

When exerted directly on cancer cells, they can increase their invasive and metastatic potential. Tumor vessels - while provides energy and furnishes nourishment to the tumor - are usually leaky and tortuous, which further decreases tissues perfusion. Hypo-perfusion and hypoxia contribute to immune-evasion, promote malignant progression and metastasis diffusion, and reduce the efficacy of cancer therapies.

In parallel, vessel leakiness together with vessel compression cause a uniformly elevated interstitial fluid pressure that hinders delivery of blood-borne therapeutic agents, lowering the efficacy of chemo- and nano-therapies. Moreover, shear stresses exerted by flowing blood and interstitial fluid modulate the behavior of cancer and a variety of host cells. Knowing these physical forces can improve therapeutic outcomes in many cancers.

The aim of our work is to integrate the imaging methods, as micro-US and PA, with molecular modeling, drug design and post processing with Optical Flow (OF) method to understand the effects and the action mechanisms of diagnostic, therapeutic and theragnostic agents on cells, tissues and microenvironment of cancer.

Material & method

The transport of mass, momentum, and energy in fluid flows is ultimately determined by spatiotemporal distributions of the fluid velocity field. Consequently, a prerequisite for understanding, predicting, and controlling fluid flows is the capability to measure the velocity field with adequate spatial and temporal resolution. Among modern airflow measurement methods, Particle Image Velocimetry (PIV) and Particle Tracking Velocimetry (PTV), as visualized and non-instructive

measurement techniques, are playing more important role. The Particle Image Velocimetry is undoubtedly one of the most important technique in Fluid-dynamics since it allows to obtain a direct and instantaneous visualization of the flow field in a non-intrusive way. This innovative technique spreads in a wide number of research fields, from aerodynamics to medicine, from biology to turbulence researches, from aerodynamics to combustion processes.

The term Particle Image Velocimetry (PIV), in the technical world, is used to describe a powerful, automated flow visualization method which quantifies the instantaneous flow velocity field in two dimensions. PIV gives valuable information on how velocity field changes at a specific measurement plane, at regular time intervals, selected by the operator.

All exams were performed with VEVOLAZR system (Fujifilm VisualSonics Inc.) and Integrated US transducer LZ-250 which operates between 1 – 24 MHz, with frame rate of 18 fps; fifteen Balb/C bearing to subcutaneous syngeneic breast cancer (TS/A) were recruited.

We analyzed several aspects of cancer rheology behavior, with the impact of MM1 micro-bubble bolus (Vevo MicroMarker, Untargeted MM1 - with a diameter ranging from 2.3 to 2.9 μm - injected in the tail vein); the acquisitions modality was evaluated with nonlinear contrast agent (NLCA) acquisitions (fig.1a - 1b). The micro-ultrasound contrast agent monitoring is lasted 30 minutes after injection.

Results

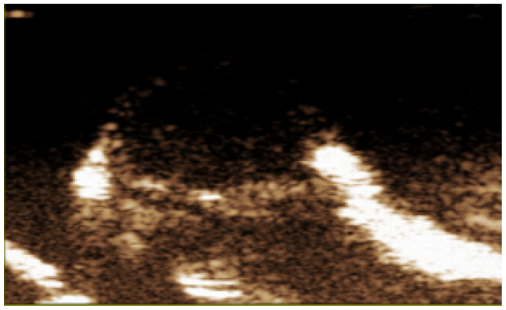

Fig. 1a – 2D tumor image before MM1 injection – non linear contrast mode

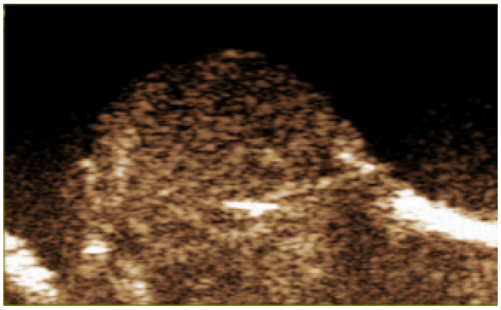

Fig. 1b – 2D tumor image after MM1 injection – non linear contrast mode

PIV involves two processes, i.e. capturing the image (with 2D slice-by-slice scanning approach) for the visualization and the images analysis in order obtain 2D and 3D parameters values, as vector flow, velocity (with the vector components), vorticity, shear rate and strain rate data.

The vector plot shows velocity vectors every fourth column, and the background color contour map corresponds to velocity magnitude (fig. 2a)

An instantaneous echo particle image velocimetry vector field is shown in fig.2b, and in fig.2c streamline are represented; a streamline is a curve parallel to the velocity vector. In fully developed flow, streamlines coincide with the paths of the fluid particles.

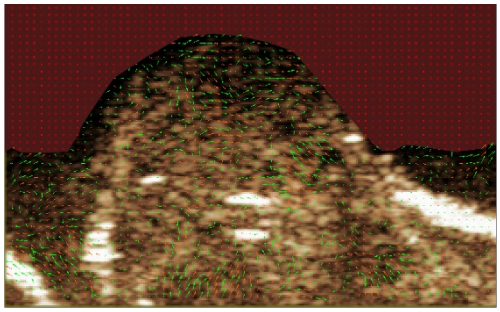

Fig. 2b – 2D tumor image before MM1 injection – non-linear contrast mode

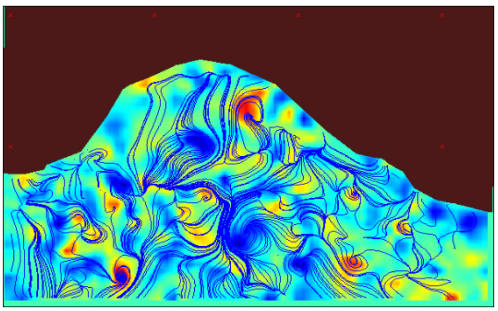

Fig. 2c – 2D tumor image – PIV velocity map with streamlines representation

Sub-volumes with distinct property's inside tumors can now be identified with OF analysis (fig. 3), showing velocities magnitude with its components, shear rate, viscosity, vorticity, strain rate (fig. 4-5) and divergence numerical quantification. In the figure, the different strain rate values and trend in different points of tumor vector map are showed; vessel bifurcation and bending as well as diameter reduction also produce local vortices with increased mass transfer rates and are therefore considered as potential docking points for circulating cancer cells.

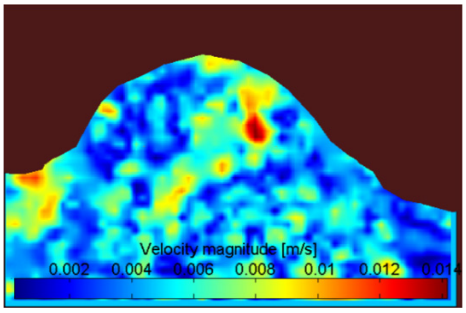

Fig. 2a – PIV velocity magnitude - velocity value vs. color map relation

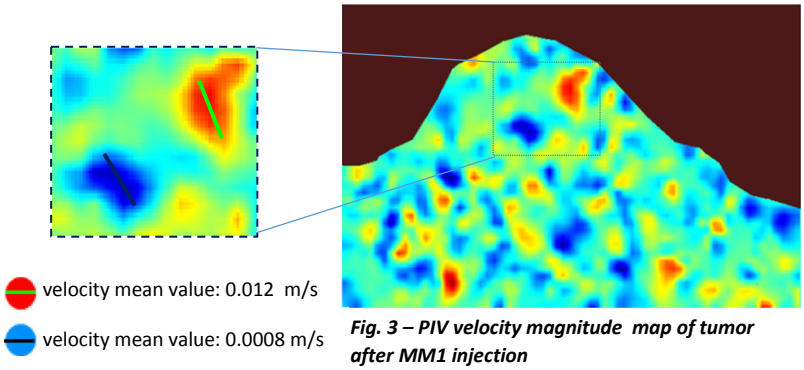

Fig. 3 – PIV velocity magnitude map of tumor after MM1 injection

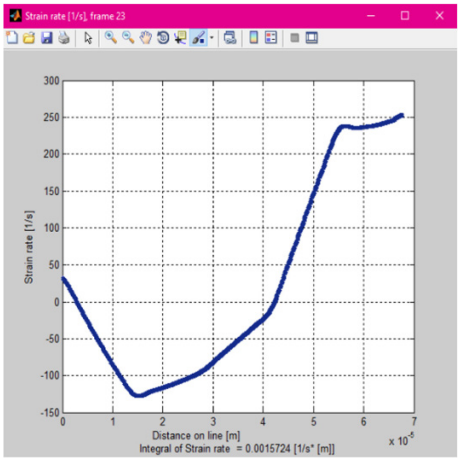

Fig. 4 – Strain rate value trend in high velocity magnitude area

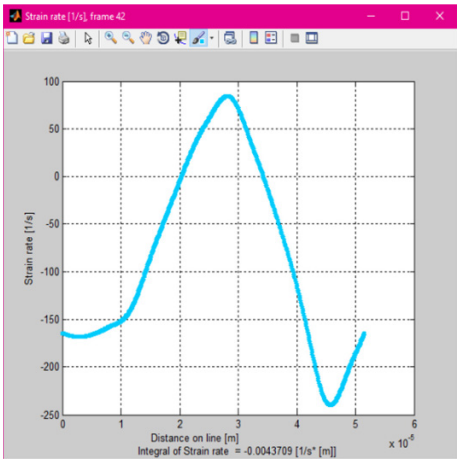

Fig. 5 – Strain rate value trend in low velocity magnitude area

All elaborations were performed with Particle Image Velocimetry in MATLAB platform; code adaptations are introduced to improve the accuracy and applicability of ultrasound PIV.

After PIV elaboration, 3D volume reconstruction with Mathematica 10 code was obtained; we wrote this software section which could evaluate the tridimensional data reconstruction (fig. 6) and assess the histogram components.

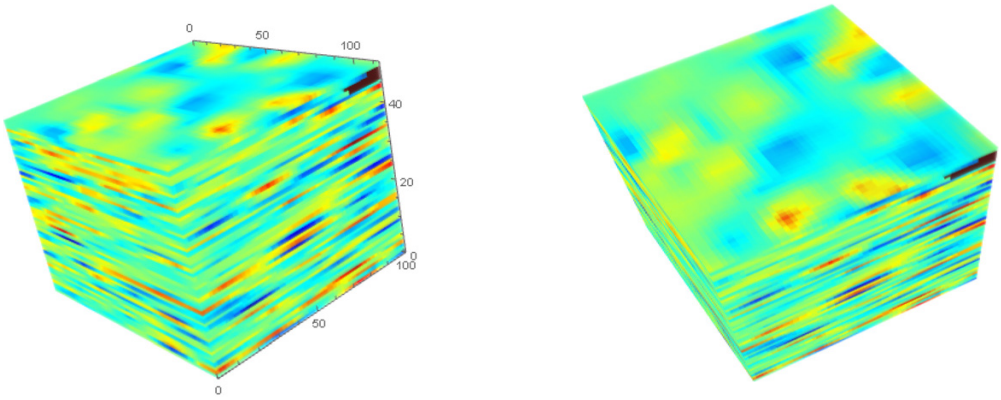

Fig. 6 – 3D PIV map reconstruction (Mathematica 10 software)

In order to obtain a quantification of the rheology parameters correlated with PIV color map, a dominant color count was performed with Mathematica 10 software on 3D reconstruction.

In this case , we show the values obtained for volume of fig. 6.

3D dominant color count :

{{■,13522},{■,17900},{■,26342},{■,30161},{■,38244},{■,63541},{■,84909},
{■,87328},{■,99585},{■,109118}}

{■,13522} low velocity into the 3D PIV map reconstruction (fig.6)

{■,38244} high velocity value into the 3D PIV map reconstruction (fig.6)

3D dominant color count graphic representation (fig. 7):

```
BarChart[Apply[Labeled, R[%41, 2], {1}]]
```

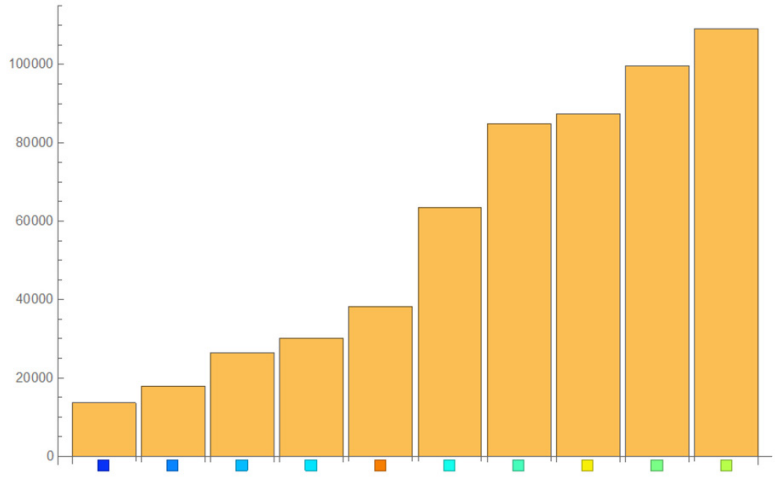

Fig.7 – Dominant color count histogram

Conclusion

Multi-parametric imaging has many potential clinical roles; it's useful for pharmaceutical drug development and for predicting therapeutic efficacy.

For this reason, the goal of our research project is to develop a volumetric strategy for real-time monitoring and characterization of tumor blood flow using microbubble contrast agents and ultrasound (US) imaging for preclinical and clinical use, improving sensitivity and resolution of imaging equipment in multimodal multiscale imaging.

This method gets a complete information on rheological phenomena who are involved in the throughout the tumor during diagnostic and drug administration processing or follow-up controls.

References

1. *Wang Hongwei, Huang Zhan*, Gong JianXiong Hongliang ;The Optical Flow Method Research of Particle Image Velocimetry - Procedia Engineering 99 (2015) 918 – 924 ScienceDirect; doi:10.1016/j.proeng.2014.12.622*
2. *Dirk Michaelis, Bernhard Wieneke; Comparison between Tomographic PIV and Stereo PIV -*
3. *14th Int Symp on Applications of Laser Techniques to Fluid Mechanics, Lisbon, Portugal, 07-10 July, 2008*
4. *A.R. Priesand T.W. Secomb ; Rheology of the microcirculation -Clinical Hemorheology and Microcirculation 29 (2003) 143–148 IOS Press*
5. *J. Che, E. Sollier, D.E. Go, N. Kummer, M. Rettig, J. Goldman, N. Nickols, S. McCloskey, R.P. Kulkarni, and Dino Di Carlo; Microfluidic vortex technology for pure circulatingtumor cell concentration from patient blood – 17th International Conference on Miniaturized Systems for Chemistry and Life Sciences 27-31 October 2013, Freiburg, Germany*
6. *Carl-Henrik Heldin*, Kristofer Rubin , Kristian Pietras and Arne Östman ; High interstitial fluid pressure — an obstacle in cancer therapy - October 2004, Volume 4 - Nature Reviews Cancer*
7. *Needles A, Arditi M, Rognin NG, Mehi J, Coulthard T, Bilan-Tracey C, Gaud E, Frinking P, Hirson D, Foster FS.; Nonlinear contrast imaging with an array-based micro-ultrasound system. Ultrasound Med Biol. 2010 Dec;36(12):2097-106. doi: 10.1016/j.ultrasmedbio.2010.08.012.*

Experimental study of single bubble fission threshold near a solid wall

T. Nagasawa, N. Sugita and T. Sugiura

Department of Mechanical Engineering, Keio University, Japan

Background

Under ultrasound irradiation, microbubbles scatter superharmonic or subharmonic signals. By receiving these nonlinear signals, encapsulated microbubbles can be used as ultrasound contrast agents for medical imaging and drug delivery for ultrasound therapy. High-speed observations showed that when encapsulated microbubbles were subjected to high-amplitude ultrasound, the bubbles split into smaller bubbles [1]. Characterization of bubble fragmentation provides important insights for ultrasound applications. In this study, we observed collapsing of a free (not encapsulated) single bubble into many fission fragments by a high-speed camera and found a threshold radius of bubble fission near a solid wall in three different liquids.

Material and Methods

A rectangular acrylic vessel (inside dimension: 50×50×100 mm, thickness: 5 mm) filled with liquid of 90 mm height is fixed on a vibration generator (EMIC, 513-BS/Z08). A vacuum pump (DAP-6D, ULVAC KIKO) is connected to the vessel through a valve in order to reduce the hydrostatic pressure in the vessel to a value near a vapor pressure. This allows large pressure amplitude to be developed in the liquid at low driving amplitude and frequency of hundreds of Hz. The recording system consists of a high-speed video camera (Photron, FASTCAM SA-5), a distortion-less macro lens and a LED backlight. A sub-millimeter sized gas bubble as a cavitation nucleus is injected by a needle through a silicon plug of 5 mm diameter located at 30 mm above the vessel bottom and 25 mm away from the side wall. As the driving acceleration is exerted on the liquid vessel, pressure gradient is generated in the vertical direction inside the vessel, and the cavitation nucleus splits into many fission fragments and forms a bubble cluster. The liquids used in our experiments are water, 2-propanol and silicone-oil.

Results

Image sequences of a typical collapsing bubble are shown in Fig. 1, respectively, for (a): inside water, (b): 2-propanol and (c): silicone oil. The bubble departs from the silicone plug and violently collapses as a result of large amplitude oscillation, producing a number of fission fragments which coalescence again during the next expansion phase. The driving frequencies are 300 and 600 Hz, and the pressure amplitude is approxi- mately 4 kPa at the center of the bubble. We counted the number of fission fragments whose radii are over 0.1 mm after four driving periods from the beginning of oscillation as shown in Fig. 1 (d). Fig. 2 shows relations of the maximum bubble radius, R_{max}, and the number of fission fragments, N, after four driving periods. Now we define the threshold pressure, p_c, as the ratio of the static pressure at the bubble position minus the vapor pressure, given by $p_0 - p_V$, to the reference dynamic pressure at the bubble interface :

$$p_c = \frac{p_0 - p_V}{0.5\rho_L(R_{max}\omega)^2},$$

and R_{max} is normalized by the critical bubble radius, R_M, which is the radius corresponding to $p_c = 1$. It can be found that if the reference dynamic pressure exceeds the static pressure ($p_c < 1$), corresponding to $R_{max}/R_M > 1$, a single bubble splits into many fragments.

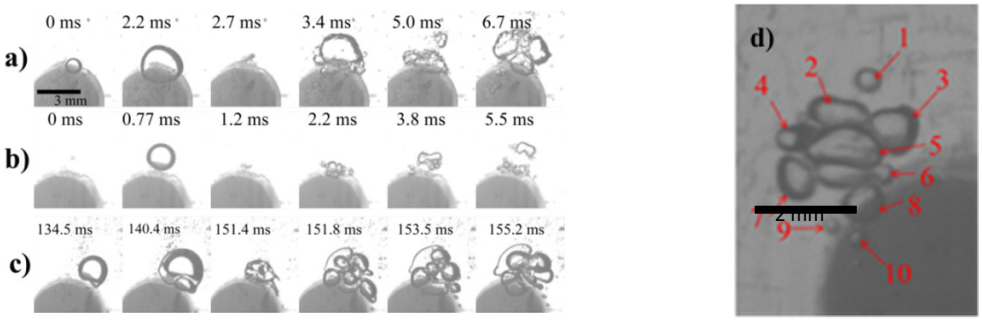

Figure 1: The recorded image sequences of a single collapsing bubble splitting into many fission fragments inside (a) water, (b) 2-propanol and (c) silicone-oil. The driving frequencies are 300 and 600 Hz, and the pressure amplitude is approximately 4 kPa at the position of the bubble. The frame rate of the camera is set to 10,000 fps. Ten fission fragments larger than 0.1 mm in radius are found in (d).

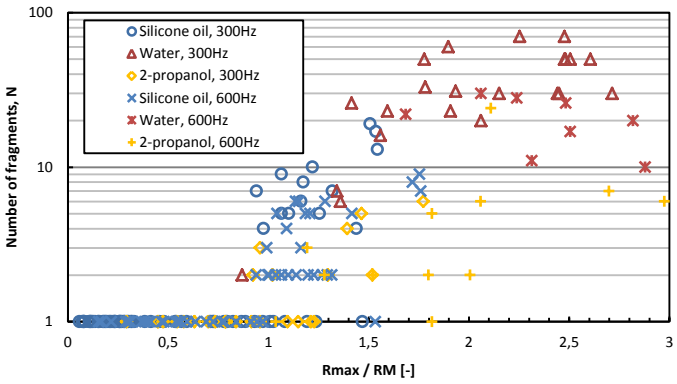

Figure 2: Relationship between the maximum bubble radius and the number of fission fragments in three different liquids. Driving frequencies are 300 Hz and 600 Hz. The maximum bubble radius, R_{max}, is normalized by the critical bubble radius, R_M. *N*=1 corresponds to no fission. Bubble fission occurs if R_{max} exceeds R_M.

Reference

1. *M. Postema, A. Bouakaz, Chein Ting Chin, N. de Jong, "Optically observed microbubble coalescence and collapse", IEEE International Ultrasonics Symposium Proceedings, 2002; 1949-1952.*

Bubble acoustic stability in high frame rate cardiac imaging using diverging waves

M. Toulemonde[1], R J. Eckersley[2], M.X. Tang[1]

[1]Department of Bioengineering, Imperial College London, London, SW7 2BP, UK
[2]Biomedical Engineering Department, Division of Imaging Sciences, Kings College London, London, SE1 7EH, UK
mengxing.tang@imperial.ac.uk

Introduction

High-frame rate (HFR) ultrasound imaging has recently shown its potential for various clinical applications. Different approaches have been proposed in order to improve the frame rate for cardiac acquisition: multi-line acquisition, multi-line transmission and diverging wave transmission. The benefit of imaging with diverging waves has been shown for 3D cardiac Doppler [1] and cardiac elastography [2]. The first combination of HFR cardiac imaging using pulse inversion (PI) and diverging waves for contrast enhanced ultrasound (CEUS), named HFR CEUS, for *in-vivo* myocardium perfusion experiments was shown recently [3]. The contrast between the heart chamber full of ultrasound contrast agents and the myocardium was improved by a factor of 2 compared to standard focused transmission, even with a peak negative pressure for HFR CEUS that was 4 times lower than focused transmission.

In HFR CEUS, microbubbles are exposed to much more frequent ultrasound excitation than that of the focused approach, potentially causing more bubble destruction. This may affect myocardium perfusion quantification. The destruction of ultrasound contrast agents and contrast improvement was previously evaluated for HFR plane wave versus focused transmission at high clinical frequencies. In [4-5], plane wave transmission was evaluated for B-Mode images and CPS transmission. In [6] plane wave and focus amplitude modulation transmissions have been evaluated for different PNP (70 – 110 – 140 kPa). It was shown that plane wave transmission resulted in less destruction of UCAs compared to focused transmission as well as better contrast. However, plane wave transmission was at high clinical frequency (3.5 MHz and 7.5 MHz) and the destruction was only evaluated at a few centimetres (2.5 cm). We are not aware of any study of the acoustic stability of microbubbles for cardiac HFR CEUS applications.

The aim of this study is to investigate the acoustic stability of bubbles in cardiac HFR CEUS using PI diverging waves where the transmission frequency is low and a larger proportion of the bubble population is resonant.

Method

HFR CEUS diverging transmission was evaluated against standard CEUS focused transmission using a Verasonics research system (Vantage 128) with a P4-1 phased-array probe having 96 active elements. In order to obtain a diverging wave, a virtual point source was created behind the probe creating a diverging beam which enlarge the region illuminated (Figure 1) [7]. Similar to plane wave imaging, a single diverging wave has a low contrast and resolution. So a coherent diverging compounded image is obtained by varying the position (steering) of the virtual point source and by coherently averaging the echoes of the diverging transmissions. Moreover, for each steering angle, two successive pulses of opposite phase were transmitted and combined in post-processing to form the PI image. The transmission parameters are show in Table I. Several values of mechanical index

(MI) were used. In the case of diverging transmission, the MI is obtained by using the spatial peak acoustic pressure close to the probe while for the focus, it is at the focal depth set at 80 mm (Figure 1).

A water tank filled with 5 L of water with 0.125 ml of Sonovue ultrasound contrast agent was used. The solution was diluted 1/40000 times and mixed by a magnetic stirrer. The stirring was stopped 50s before each acquisition in order to avoid flow during measurements and then restarted after the acquisition.

The acoustic stability of bubbles was evaluated by the disruption ratio as a function of MI and at several depths (Figure 2.a). The squares in Figure 2.a show the different regions-of-interest (ROIs) 20 x 30 mm (depth x lateral). The disruption ratio at any time point for an ROI is calculated by normalising the intensity of the microbubbles in the ROI at that time point against that at time zero [5]. The resolution is also evaluated by estimating the full width at half maximum in both the lateral and axial directions of the cross-correlation in the previous ROIs [8].

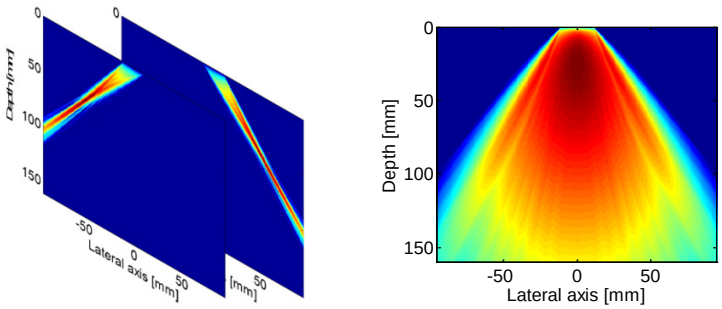

(a) (b)

Figure 1: Log compressed pressure field with a 20 dB dynamic simulated by the Verasonics Platform for (a) focalization and (b) diverging transmissions [7].

	HFR CEUS	CEUS
Frequency (Cycles)	1.25 MHz (3)	1.25 MHz (3)
Angle range	60	90
Number of angles/lines	7 (x2 PI)	82 (x2 PI)
Focus	---	80 mm
Frames	800	80
PRF	5900 Hz	5900 Hz
Frame rate	350 Hz	30 Hz
MI	0.01 / 0.025 / 0.05 / 0.1 / 0.15 / 0.2 / 0.25	0.05 / 0.10 / 0.15 / 0.2 / 0.25

Table 1: Transmission parameters used during in-vitro experiments.

Results

Figure 2.b and Figure 3 show three frames of CEUS and HFR CEUS at 0.0, 0.5 and 2.0 seconds for two MIs, 0.05 and 0.20, respectively. With 0.05 MI, for both transmission, there is visually little disruption of microbubbles. While at 0.2 MI, there are already some image intensity changes at 0.5s for HFR CEUS and apparent disruption for both techniques at 2.0s.

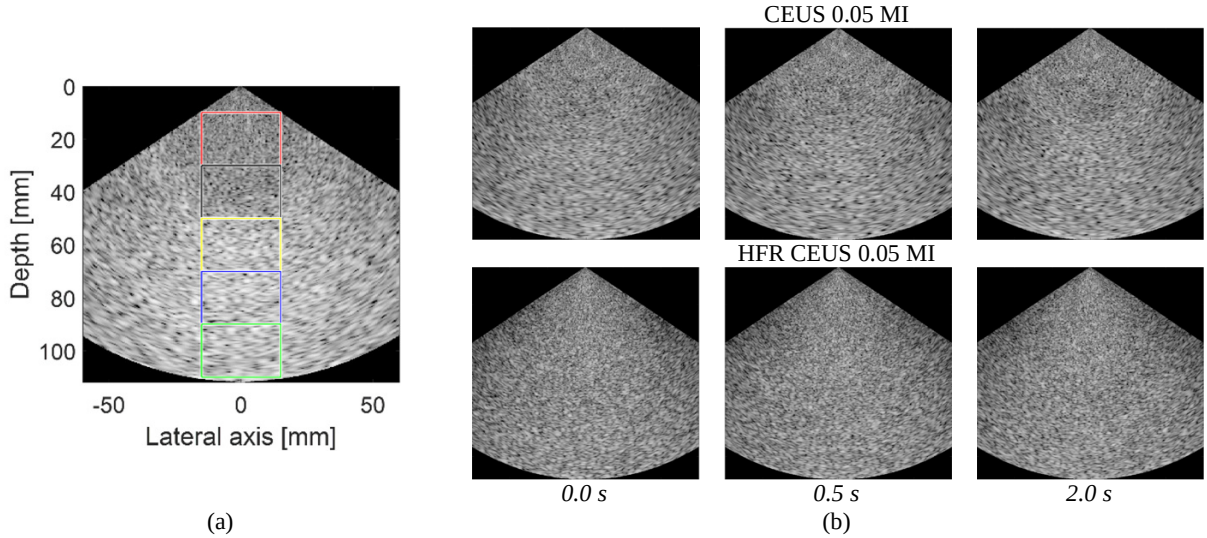

Figure 2: (a) Region-of-interest (ROI) where is evaluated the disruption ratio. The squares are 20 x 30 mm (depth x lateral). (b) CEUS and HFR CEUS frames at 0.0, 0.5 and 2.0 s for 0.05 MI. The frames are normalized by the maximum intensity frame of the full sequence and displayed with a dynamic range of 50 dB.

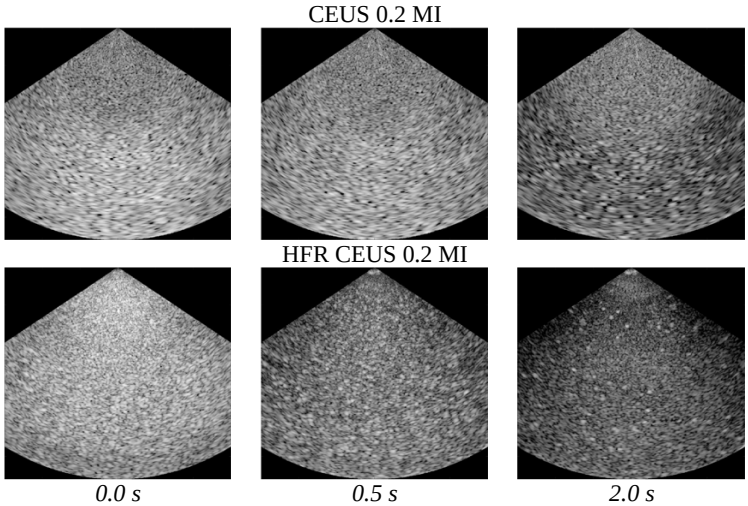

Figure 3: CEUS and HFR CEUS frames at 0.0, 0.5 and 2.0 s for 0.2 MI. The frames are normalized by the maximum intensity frame of the full sequence and displayed with a dynamic range of 50 dB.

Figure 4 gives the disruption of microbubbles as a function of MI at 20 and 80 mm after 0.5 s. For both positions, the disruption of microbubbles increases with the MI. The disruption of microbubbles close to the probe is more significant for HFR CEUS for MIs superior to 0.1. However, at 80 mm, the disruption of both transmission types is similar below 0.15 MI.

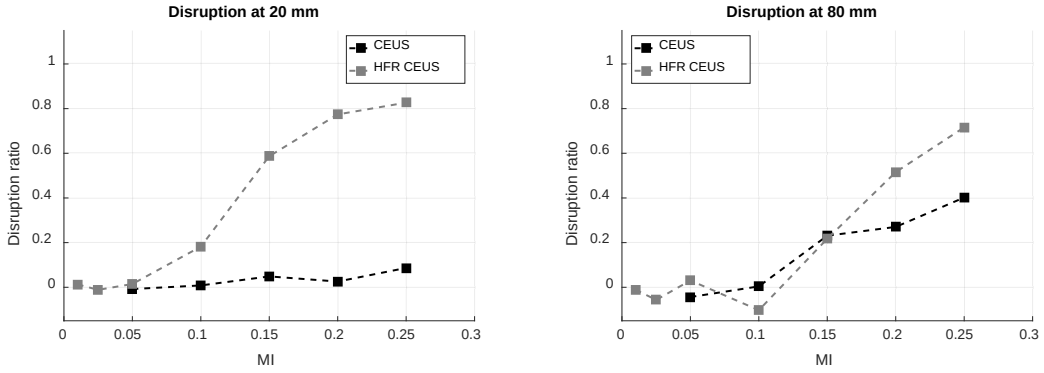

(a) (b)

Figure 4: Disruption ratio as a function of MI at 0.5s at (a) 20 mm and (b) 80 mm depth.

Figure 5 shows the disruption of microbubbles as a function of depth for the same MI at 0.5 s. Close to the probe there is no microbubble destruction with 0.05 MI for both transmission types, while there is limited disruption at 0.1 MI with HFR CEUS. At larger depths, both transmission types generate no disruption.

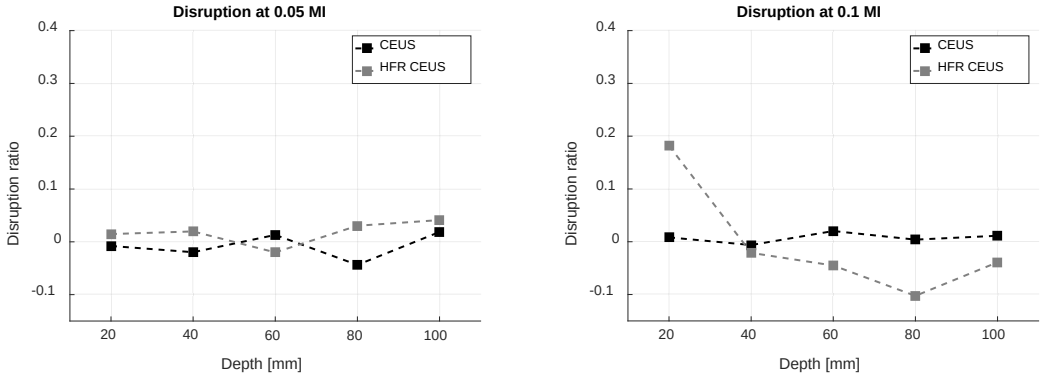

(a) (b)

Figure 5: Disruption ratio as a function of depth at 0.5s with (a) 0.05 and (b) 0.1 MI.

The lateral and axial resolutions obtained for both transmission types are given in Table 2. The resolutions have been calculated at 0.0 s with the same 0.05 and 0.1 MI. The axial resolution is similar for both while the lateral resolution is better for HFR CEUS, by up to 100% improvement at 10 cm depth.

		Depth	**20 mm**	**40 mm**	**60 mm**	**80 mm**	**100 mm**
CEUS	0.05 MI	Lateral (mm)	0.72	1.44	1.92	2.64	3.11
		Axial (mm)	*0.76*	*0.76*	*0.68*	*0.80*	*0.80*
HFR CEUS		Lateral (mm)	0.72	0.96	1.20	1.68	1.92
		Axial (mm)	*0.80*	*0.80*	*0.84*	*0.84*	*0.76*
CEUS	0.1 MI	Lateral (mm)	0.72	1.20	1.92	2.64	3.36
		Axial (mm)	*0.72*	*0.80*	*0.92*	*0.84*	*0.84*
HFR CEUS		Lateral (mm)	0.72	0.96	1.20	1.44	1.68
		Axial (mm)	*0.80*	*0.84*	*0.84*	*0.76*	*0.72*

Table 2: Lateral and axial resolution as a function of depth at 0.0 s with 0.05 and 0.1 MI.

Discussion and Conclusion

This work presents the acoustic stability of bubbles for cardiac applications using high-frame-rate (HFR) pulse inversion (PI) diverging waves and standard contrast enhance ultrasound (CEUS) transmission. It can be seen that how HFR cardiac CEUS affects bubble destruction differently from standard CEUS is spatially and MI dependent. At a low MI of 0.05 no disruption was observed for either approach. As the MI increases to 0.1, limited destruction was observed close to the probe for HFR cardiac CEUS (Figure 4.a). As MI increases further both approaches show significant bubble destructions over large areas.

Even at very low MI, where no bubble destruction was observed, HFR cardiac CEUS is shown to be able to produce significant improvement in image resolution in deep tissues, up to 100% at 10 cm, thanks to the coherent compounding (Table 2). Our recent work has also demonstrated a significant improvement in image contrast for HFR CEUS using very low MIs, comparing to standard CEUS at higher MIs [3].

In conclusion, our preliminary work shows that it is possible to substantially improve image resolution and contrast without significant microbubble destruction using HFR cardiac CEUS.

Acknowledgement

This work is funded by the UK Engineering and Physical Sciences Research Council (EPSRC) grant EP/M011933/1 and grant EP/M010961/1.

References

1. *J. Provost, C. Papadacci, J. E. Arango, M. Imbault, M. Fink, J-L. Gennisson, M. Tanter, and M. Pernot, "3D ultrafast ultrasound imaging in vivo", Physics in Medicine & Biology, vol. 59, pp. 1 – 13, 2014*
2. *M. Correia, J. Provost, S. Chatelin, I. Villemain, M. Tanter, and M. Pernot, "Ultrafast Harmonic Coherent Compound (UHCC) Imaging for High Frame Rate Echocardiography and Shear-Wave Elastography", IEEE Trans. on UFFC, vol. 63, no. 3, pp. 420-431, 2016.*
3. *M. Toulemonde, Y. Lin, S. Lin, M. Butler, R. Eckersley, W C. Duncan, V. Sboros, and M.X. Tang, "Cardiac imaging with high frame rate contrast enhanced ultrasound: in-vivo demonstration", IEEE IUS, Tours, 2016.*
4. *J. Viti, H. J. Vos, N. Jong, F. Guidi, and P. Tortoli, "Detection of Contrast Agents: Plane Wave Versus Focused Transmission", IEEE Trans. on UFFC, vol. 63, no. 2, pp. 203-211, 2016.*
5. *O. Couture, S. Bannouf, G. Montaldo, J. F. Aubry, M. Fink, and M. Tanter, "Ultrafast Imaging of Ultrasound Contrast Agents", Ultrasound in Medicine & Biology , vol. 35, no. 11, pp. 1908-1916, 2009.*
6. *O. Couture, M. Fink, and M. Tanter, "Ultrasound contrast plane wave imaging", IEEE Trans. on UFFC, vol. 59, no. 12, pp. 2676-2683, 2012.*
7. *M. Toulemonde, V. Papadopoulou, and M.X. Tang, "A Contrast Enhanced Ultrasound imaging system with diverging waves for cardiac imaging – initial evaluation on a beating phantom", The 21st European Symposium on Ultrasound Contrast Imaging, Rotterdam, 2016.*
8. *R. F. Wagner, S.W. Smith, J. M. Sandrik, and H. Lopez, "Statistics of Speckle in Ultrasound B-Scans", IEEE Trans. on Sonic and Ultrasonics, vol. 30, no. 3, 1983.*

Microbubble Size Effects on Plane-Wave B-Mode Imaging: Initial Results

Francesco Guidi[1], Mark Borden[2] and Piero Tortoli[1]

[1] Electronics and Telecomm. Dept, Università di Firenze, Firenze, ITALY
[2] Mechanical Engineering, University of Colorado, Boulder, USA

Plane-wave imaging has emerged as an exciting new tool for ultrasound applications employing microbubbles, such as contrast-enhanced imaging and super-resolution imaging. At the same time, microbubble formulation techniques have advanced to the point where the mean diameter can now be selected with a relatively narrow size distribution. This poster will present results from our recent collaborative work at the nexus of these two technological developments.

Our initial hypothesis was that larger microbubbles are more stable against ultrasound-induced destruction than smaller microbubbles. We therefore expect different imaging behaviour as we vary ultrasound pressure and pulse repetition frequency (PRF). For example, over a pressure range between destruction thresholds, the echo intensity of larger microbubbles should increase with pressure, while the opposite is expected for smaller microbubbles. Such a parametric study on microbubble ensembles is facilitated by the plane-wave imaging mode, where uniform insonation conditions ensure that all microbubbles are hit by nearly identical ultrasound pulses even if they move in a wide field-of-view.

To test our hypothesis, we investigated size-selected, lipid-coated microbubbles of 1-2 µm and 6-8 µm diameter, i.e., with non-overlapping size distributions. The microbubbles were diluted 1:2000 by volume in deionized water and flowed at 30 mL/min through a 6.0-mm diameter peripheral vascular flow phantom. The microbubbles were imaged along the tube axis with the ULA-OP system operating at 3.5 MHz in plane-wave pulse-echo mode. The ultrasound pressure was varied by changing the transducer voltage from 20% to 100%, and the PRF was varied 1 to 6 kHz.

Our preliminary results showed that the microbubble-to-tissue echo ratio increases with ultrasound pressure for 6-8 µm microbubbles, while it decreases for 1-2 µm bubbles, which supports our hypothesis (Fig. 1). Results will also be presented to show effects of microbubble size, acoustic pressure and PRF on echo intensity and related spectra at different points of the field-of-view.

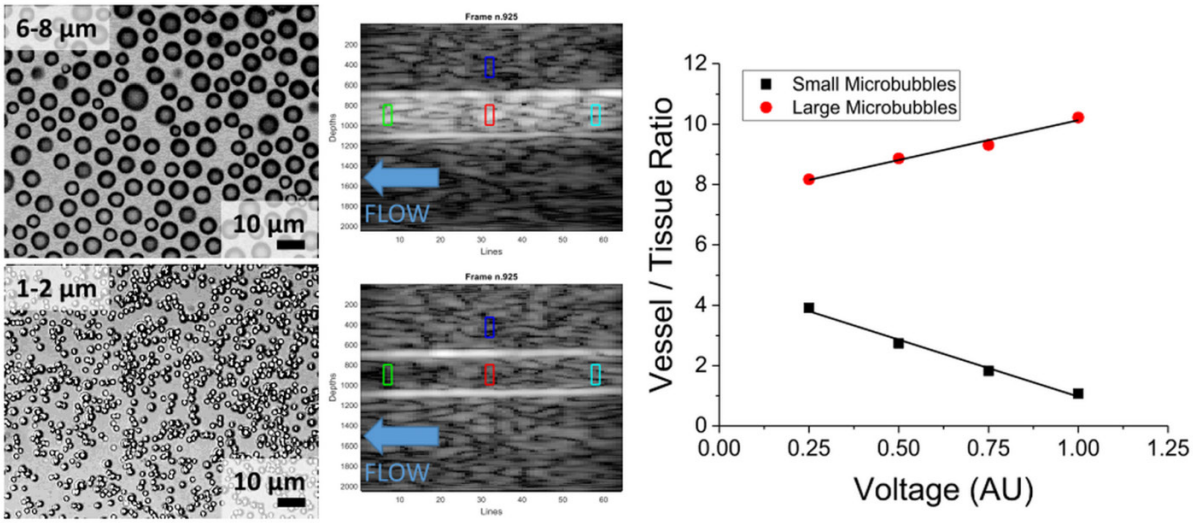

Figure 1. (Left) Microscope images of large (top) and small (bottom) microbubbles. Size distribution range is shown in the upper-left corner, and a 10-µm scale bar is shown in the bottom-right corner. (Middle) B-mode images at the high acoustic pressure. Images are scaled to maximum intensity. Shown are the direction of flow and various regions of interest. (Right) Plot of vessel-to-tissue echo ratio versus pressure (voltage). Echo intensity was determined within the center regions-of-interest and averaged over the 1000 frame acquisition. Note that the ratio increases for large microbubbles and decreases for small microbubbles.

Using Nanoscale Phase-Shift Droplets for Indicator Dilution Measurement of Flow

Zachary Zajac[1,2], Paul Sheeran[1,2], Charles Tremblay-Darveau[1,2], Kimoon Yoo[1], Ross Williams[1] and Peter N. Burns[1,2]

[1]Sunnybrook Health Sciences Centre, Toronto, Ontario, Canada
[2]Department of Medical Biophysics, University of Toronto, Toronto, Ontario, Canada

Introduction

Hepatic tumours are known to cause an increase in the proportion of blood entering the liver from the hepatic artery relative to the total blood flow[1], a quantity known as hepatic perfusion index (HPI). This phenomenon may allow for a method to infer the presence of liver metastases without necessarily imaging lesions[2]. The microbubble disruption-replenishment method can measure the local blood flow rate by metering the rate of contrast replenishment in a target region following non-invasive destruction of microbubbles by a high intensity pulse. However, the use of such a negative bolus requires complete mixing of contrast and a steady state, so is usually achieved by infusion. This makes it an unsuitable method to measure HPI as the contrast will be in both the hepatic portal vein as well as the hepatic artery. The vessels are adjacent to each other, so disrupting bubbles in only one of them is not realistic. The development of phase-shift agents that can be activated locally to convert to microbubbles[3] provides an opportunity to create a highly localized positive bolus. This may allow for the measurement of HPI though indicator dilution methods by creating contrast which is specific to the hepatic artery, where a bolus of intravenous origin arrives several seconds before appearing in the portal vein. For the application of droplets in indicator dilution measurements, they must (1) be shown to be free-flowing intravascular agents after activation, (2) provide steady microbubble enhancement over the measurement period and (3) show a linear relationship between the measured contrast enhancement and the concentration of microbubbles produced from droplet vaporization. Previous studies have developed and characterized sub-micron phase-shift agents that produce free-flowing microbubbles following activation[4]. In this study, we use a programmable ultrasound platform to measure contrast enhancement properties resulting from activated droplets in a vessel flow phantom with the goal of evaluating this unique agent's suitability for indicator dilution measurement of flow by means of selective excitation.

Materials and Methods

Sub-micron droplets were prepared through the condensation of microbubbles previously described[5] consisting of a decafluorobutane (DFB) core and DBPC/DPPE-PEG5000 lipid shell mixture. Droplets were added to a reservoir of gas-equilibrated de-ionized water at 37C and then passed through an agar vessel phantom (0.66 mm diameter) at flow rates near 50 mL/min and droplet sample concentrations between 0.0025% and 0.18% in DI water. A Verasonics Vantage 128 was used to both image and activate droplets with an L7-4 transducer through custom imaging scripts. The low mechanical index imaging sequence consisted of pulse inversion with angular compounding at a frame rate of 100 Hz, while activation was accomplished with 4 high mechanical-index focused pulses at frame rate 80 Hz, with the focus adjusted to lie within the lumen of the vessel. Video sequences before and after activation were stored and analyzed offline to characterize contrast enhancement as a function of droplet concentration and time after activation. The mean intensity inside an ROI surrounding the microbubble bolus was calculated for 10 separate vaporization events at increasing concentrations.

This experiment was repeated for 3 different samples, and results were normalized to the maximum intensity reached per trial.

Results and Discussion

Droplet vaporization under flow conditions allowed for direct visualization of the parabolic flow profile as microbubbles spread by flow convection (figure 1). From the laminar profile in this example, we can calculate an average flow velocity of 2.24 cm/s, allowing for a calculation of flow rate within 8% of the value measured with an external flow meter. This provides a measurement of flow to which indicator dilution derived values can be compared using the same bolus. Contrast enhancement on the order of 15 to 20 dB was observed after activation, consistent with previous studies of nanoscale phase-shift agents[5]. A linear relationship between droplet concentration and intensity of the ensuing microbubble bolus is maintained at concentrations as much as 6 times higher than is typically found for conventional microbubble contrast agents[6] (figure 2). Preliminary results indicate that the bubbles produced from nanoscale phase-shift agents dissolve significantly over the course of 20 seconds, which may limit their use for indicator dilution methods. Thus, refinements of the current droplet formulation may be needed. Next steps are to optimize droplet size and encapsulation material in order to improve stability of the resulting microbubbles.

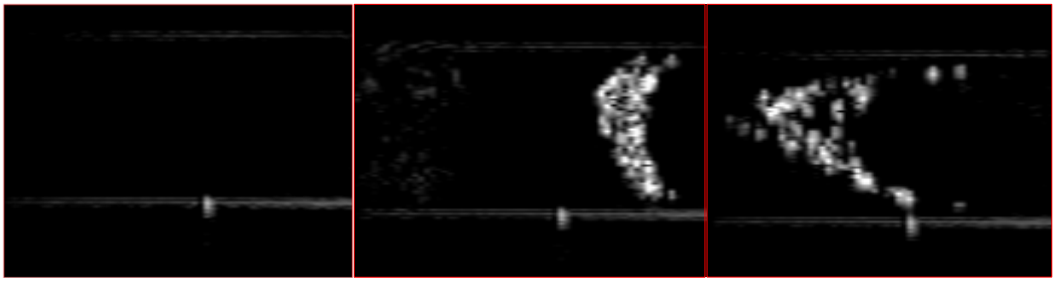

Figure 1 - Activation of DFB - DBPC/DPPE-PEG5000 phase-change contrast agents within wall-less flow phantom using a pulse-inversion contrast scheme. Flow though phantom is from right to left.

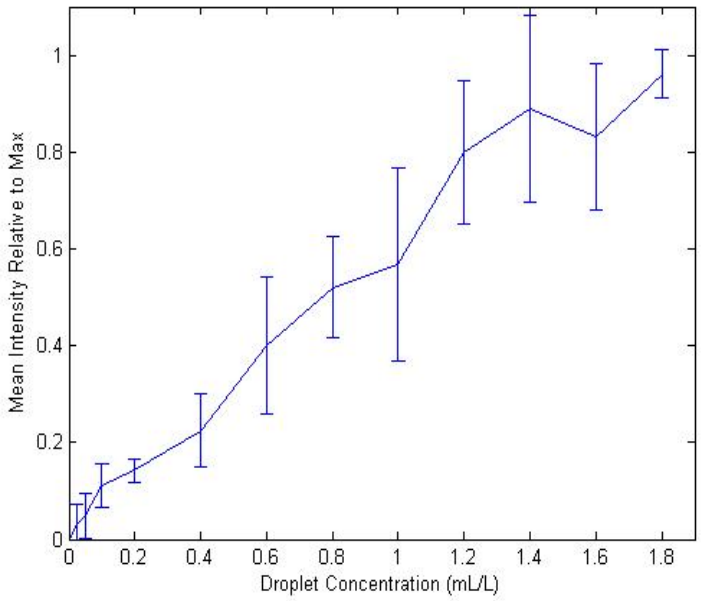

Figure 2 - Mean intensity within ROI drawn around bolus of microbubbles vs concentration of DFB - DBPC/DPPE-PEG5000 droplets using B-mode imaging.

Conclusions

Phase-shift contrast agents present an opportunity to visualize flow patterns through the tracking of a locally created bolus. This study presents evidence for a linear relationship between the concentration of droplets and the intensity of the microbubble bolus created after its vaporization within a tested regime. Further experiments utilizing indicator dilution methods should aim for droplet concentrations which lie within this linear regime. Future work is aimed at improving microbubble stability over time, as a requirement of indicator dilution is the conservation of the contrast indicator. Future work will also test *in-vivo* activations of target vessels.

References

1. *Leen, E. The detection of occult liver metastases of colorectal carcinoma. Journal of Hepatobiliary Pancreat Surgery. Vol 1, pp7-15. 1999.*
2. *Leen et al. Detection of hepatic metastases using duplex/color Doppler sonography. Annals of Surgery. Vol 214, pp599-604. 1991.*
3. *Sheeran. P, Dayton. P. Phase-Change Contrast Agents for Imaging and Therapy. Current Pharmaceutical Design. Vol 18, pp. 2152-2165, 2012.*
4. *Sheeran et al. Image-Guided Ultrasound Characterization of Volatile Sub-Micron Phase-Shift Droplets in the 20-40 MHz Frequency Range. Ultrasound in Medicine & Biology. Vol 42, pp 795-807. 2016.*
5. *Sheeran et al. More Than Bubbles: Creating Phase-Shift Droplets from Commercially Available Ultrasound Contrast Agents. Ultrasound in Medicine & Biology, 2016.*
6. *Hudson, John (2011). Quantification of Blood Flow Using Ultrasound Contrast Agents (Doctoral Dissertation). Retrieved from TSpace Repository.*

The role of polymers and core fluorescent staining of polysaccharide-based nanodroplets on their acoustic contrast properties

Sara Zullino,[1,2] Monica Argenziano,[3] Roberta Cavalli,[3] Caterina Guiot,[1] Klazina Kooiman[2] and Nico de Jong[2,4]

[1]Department of Neuroscience, University of Turin, Turin, Italy
[2]Department of Biomedical Engineering, Thorax Center, Erasmus MC, Rotterdam, the Netherlands
[3]Department of Drug Science and Technology, University of Turin, Turin, Italy
[4]Laboratory of Acoustical Wavefield Imaging, Faculty of Applied Sciences, Delft University of Technology, Delft, the Netherlands

Background

In recent years, submicron phase-change contrast agents, briefly named nanodroplets (NDs), have proven to be a viable alternative to microbubbles for ultrasound-based applications as they can extravasate through the leaky vasculature of the tumor via the enhanced permeability and retention (EPR) effect [1].

Superheated liquid NDs are phase-transitioned into gas microbubbles by means of ultrasound (US). This phenomenon, termed acoustic droplet vaporization, is a potential method of designing a contrast agent that can exploit the EPR effect and provide imaging contrast in tumor extravascular space [2].

In this study, a clinical echomachine was used to evaluate the phase-change and scatter intensity at a fixed frequency. Different nanodroplet formulations were compared to test the effect of the polymeric shell composition and of the core staining on the acoustical behavior of these potential phase change contrast agents.

Materials and Methods

Blank nanodroplets were prepared according to a multi-step protocol [3]. A pre-emulsion was obtained adding an ethanolic solution containing Epikuron®200 (3% w/v) to perfluoropentane (PFP) under magnetic stirring for A formulation. For B and C formulations, palmitic acid (0.5% w/v and 1% w/v, respectively) was also added.

After the addition of ultrapure water, the system was homogenized using a Ultra-Turrax SG215 homogenizer (IKA, Staufen, Germany). To obtain the polymeric NDs, 2% w/v dextran sulfate aqueous solution (for dextran-shelled NDs) or 2.7% chitosan solution (for chitosan-shelled NDs) was added drop-wise under magnetic stirring.

Double labelled ND formulations of different sizes (samples A, B, C) were prepared using Rhodamine 6G (Rh6G) dissolved in the PFP core and dextran-FITC or chitosan-FITC for the shell.

Based on sample C, three additional types of formulations were prepared: blank dextran-shelled NDs (C1); fluorescent dextran-shelled NDs (C2, double labelled using Red Nile (RN) in the core and dextran-FITC for the shell); fluorescent dextran-shelled NDs (double labelled using Rh6G in the core and dextran-FITC for the shell).

Each formulation was stored at 4 °C.

Average diameter and polydispersity index (PDI) of nanodroplets were determined by dynamic light scattering (DLS) using a 90Plus Nanoparticle Size Analyzer (Brookhaven, NY, USA). PDI is a dimensionless measure of the broadness of the

size distribution calculated from the cumulants analysis, a method of analyzing the autocorrelation function generated by a DLS experiment. PDI values greater than 0.7 indicate a very broad distribution of particle sizes.

The analysis were carried out at a scattering angle of 90° and a temperature of 25°C. First, 2.5 ml of filtered water were placed in the cuvette, then 250 µl of the sample were added. Each measured value was the average over ten readouts.

For the acoustic characterization of the nanodroplets, a tank was filled with 1500 ml of demi water (Fig. 1). At the bottom of the tank an acoustic absorbing pad was placed. On this pad the tissue mimicking phantom (TMP) was located. A right stand and clamp held the linear array transducer (LA523, Esaote, Italy) which was coupled to clinical ultrasound echomachine (MyLab™25Gold, Esaote, Italy).

A volume of 150 µl of ND was pipetted into the water tank for a final ND concentration of 10^8 ND/ml. The suspension was continuously mixed by magnetic stirring.

The B-mode recordings consisted of 10 s movies taken at a frame rate of 21 Hz, for a total frame number of 213, in which the mechanical index (MI) was increased from 0.4 to 1.1. The central frequency of the transmitted pulse was 7.5 MHz.

Post-capture video analysis was carried out via a code written in MATLAB (Mathworks, Inc.). Each frame was converted to grayscale. For a given video, at a fixed position, two regions of interest (ROI) were selected in both the TMP and the nanodroplet suspension. The respective mean pixel intensities of the two ROIs were averaged over all the 213 frames.

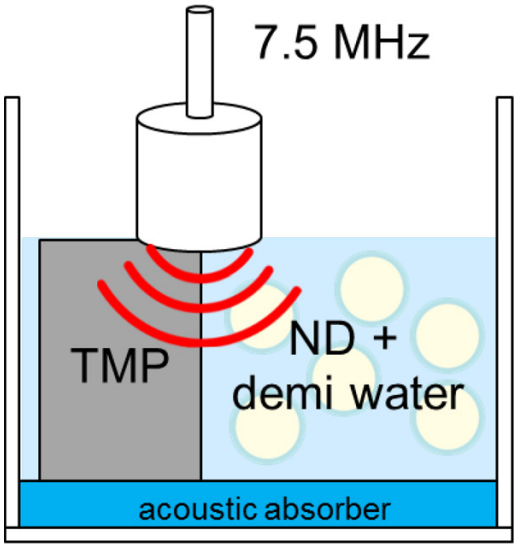

Figure 1: Schematic of set-up used for the experiments. A clinical ultrasound system insonified a tissue mimicking phantom (TMP) and the nanodroplet (ND) suspensions.

Results

Table 1 reports the size and PDI values of the nanodroplet formulations.

Blank formulations		
Sample	**Average size (nm) ± SD**	**PDI**
DEX B	333.9 ± 31.6	0.293
CHI C	425.9 ± 66.6	0.058
Rh6G fluorescent formulations		
DEX A	128.9 ± 2.1	0.220
DEX B	307.3 ± 9.3	0.249
DEX C	424.3 ± 29.1	0.264
CHI B	312.4 ± 21.5	0.254
CHI C	416.3 ± 15.4	0.263
Formulation type C		
DEX C1 blank	408.5 ± 23.6	0.231
DEX C2 NR	417.6 ± 40.6	0.270
DEX C3 Rh6G	423.2 ± 34.5	0.265

Table 1: Average size and polydispersity index (PDI) of the nanodroplets (NDs).

The recorded B-mode movies consisted of 800×652 pixels. The TMP is positioned to the right of the image and the nanodroplets were injected into the left side (Fig. 2).

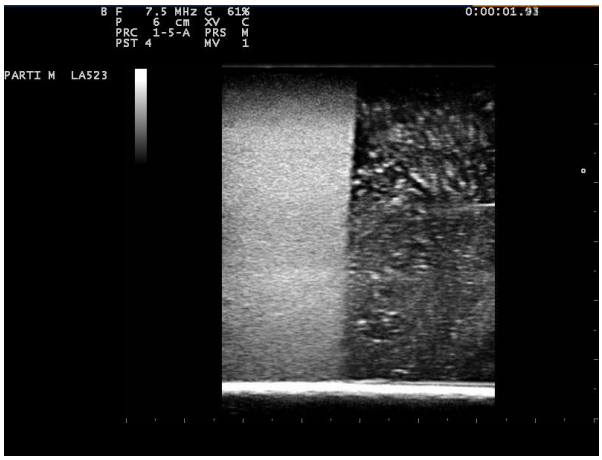

Figure 2: B-mode image recorded at MI of 0.4. Tissue mimicking phantom (TMP) and C2 type nanodroplets (NDs) are shown.

A ROI of 100×100 pixels was selected in the TMP and nanodroplet suspension across the focal region.

For all the MI considered, the mean pixel intensity of the ND suspension was divided by the mean pixel intensity of the TMP at each frame.

Fig. 3 shows the normalized mean pixel intensities as a function of the MI for two nanodroplet formulations grouped according to the shell polymeric composition.

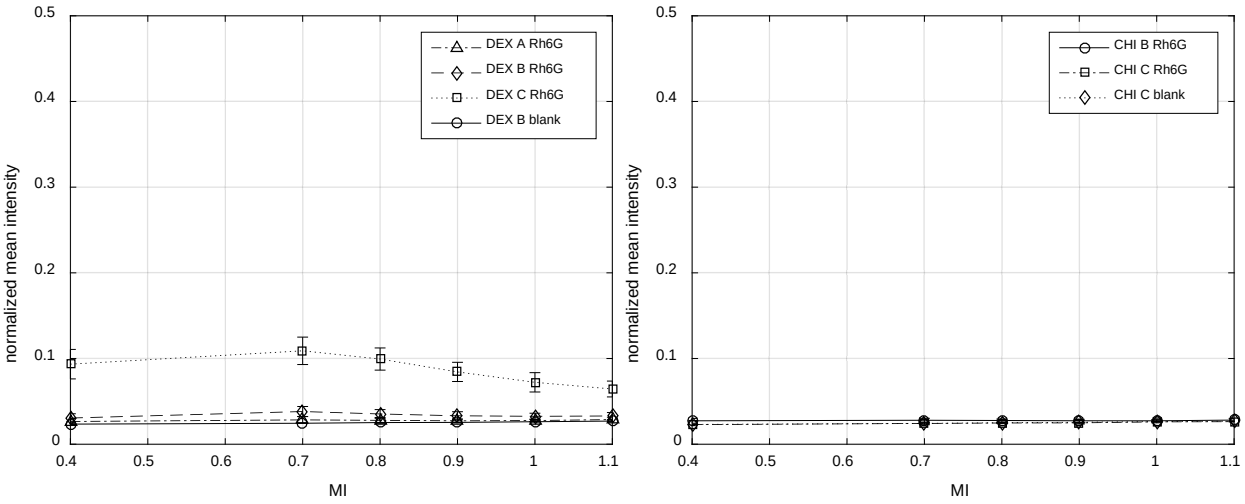

Figure 3: Normalized mean pixel intensities for dextran-shelled nanodroplets (left panel) and chitosan-shelled nanodroplets (right panel) as a function of the mechanical index (MI) at a frequency of 7.5 MHz

Dextran shelled nanodroplets show an enhanced echogenicity compared to the chitosan shelled ones.

The presence of Rh6G staining seems to promote the phase transition as respect to the blank formulation. The larger nanodroplet considered (DEX C Rh6G) presents a noticeable acoustic response.

In Fig. 4, the acoustic responses for the largest dextran-shelled nanodroplets (type C) are shown to compare the blank formulation to the fluorescent ones. Two different dyes are considered. The dextran-shelled nanodroplets labelled with NR (DEX C2 NR) shows a high echogenicity with respect to the nanodroplets labelled with Rh6G (DEX C3 Rh6G). In both cases, the scattering intensity is higher than the intensity of the blank formulation (DEX C1 blank).

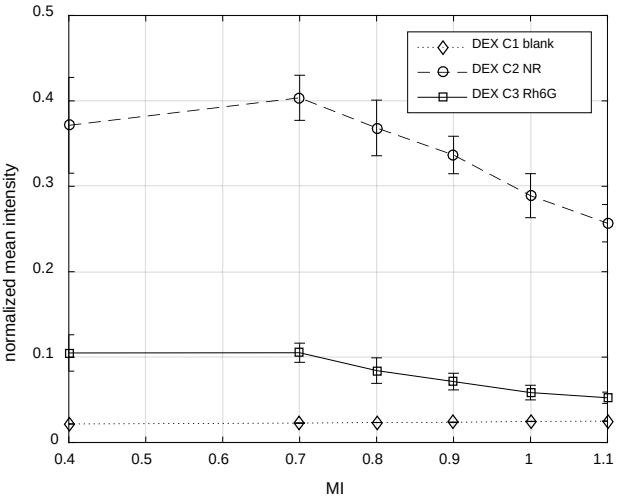

Figure 4: Normalized mean pixel intensities for dextran-shelled nanodroplets as a function of the mechanical index (MI) at a frequency of 7.5 MHz. Blank and two different fluorescent formulations are compared.

Discussion and Conclusion

Polymer-shelled nanodroplets (NDs) containing a volatile liquid PFP core have been studied as contrast agents due to their potential ability to turn into microbubbles upon ultrasounds.

This study reveals that the dextran-shelled nanodroplets are more easily vaporized than the chitosan-shelled ones and that the larger sizes shows enhanced contrast.

For the chitosan-shelled nanodroplets, the presence of the Rh6G seems not to affect echogenicity.

Nanodroplet scattering intensity varies with a factor of 4 depending on the dye.

The dependence of acoustic response on coating properties and core staining will help to fine-tune the formulation, behavior, and vaporization dynamics of acoustically-responsive nanodroplets.

References

1. *Sheeran et al., Curr Pharm Des. 18(15): 2152-65 (2012).*
2. *Sheeran et al., Ultrasound in Med Biol. 37: 1518-30 (2011).*
3. *Cavalli et al., Int J Pharm. 378(1-2), 215-217 (2009).*

Spectral Imaging of Lipid Packing in Microbubbles

Richard J. Browning[1¶], Dario Carugo[1,2¶], Shamit Shrivastava[1], Paul Rademeyer[1], Erdinc Sezgin[3], Jorge Bernardino de la Serna[3], Christian Eggeling[3] and Eleanor Stride[1]

1 Institute of Biomedical Engineering, University of Oxford, Oxford UK
2 Faculty of Engineering and the Environment, University of Southampton, Southampton UK
3 Weatherall Institute of Molecular Medicine, University of Oxford, Oxford UK
Email: richard.browning@eng.ox.ac.uk

Microbubbles (MBs) are microscale acoustically active gas filled particles in clinical use as ultrasound (US) contrast agents and under investigation for other applications such as drug delivery and ablation enhancers [1]. To prevent rapid dissolution, they are coated with a lipid, protein or polymer shell, which also allows functionalisation of the MB. The shell influences the acoustic response, stability and behaviour of the MB, however previous methods to study these relationships have been low-throughput, used less relevant MBs formulations or are based on models for which validity is unknown [2,3]. Spectral imaging of C-Laurdan reveals the hydration of a lipid membrane. It is established that penetration of water molecules into the lipid membrane is a result of changes in lipid packing and has been used to probe cells, GUVs and liposomes [4]. Here, we investigate the potential of spectral imaging for characterising lipid shelled MB.

Five types of MBs were chosen for characterisation; 3 research and 2 clinically relevant formulations (Table 1). All MBs were initially prepared as a lipid film by solvent evaporation and rehydrated prior to air-interface sonication using water (DSPC, DPPC), phosphate buffered saline (DSEPC) or a water, propylene glycol and glycerol mixture (Definity-like). All MBs were washed once by centrifugation to reduce background lipid content then incubated with C-Laurdan. After 30 minutes, stained MBs were imaged using a confocal fluorescence microscope at a range of spectral wavelengths. This was repeated three times per formulation with fresh lipid films, with ~1400 MB per formulation.

C-Laurdan has peak wavelength maxima at 440 nm or 490 nm in gel-like or fluid-like membranes respectively. Using a custom MATLAB (Mathworks) script, the confocal images were processed to extract the intensities at the two wavelengths of the MB shell. By using the generalised polarisation (GP) ratio on each pixel of the MB shell – $GP = (I_{440} - I_{490}) / (I_{440} + I_{490})$ – a mean GP value per MB can be calculated. Overall median GP values for formulations were then calculated from GP/MB.

In addition, further characterisation was performed to determine dependencies. Environmental stability of the formulations was examined as changes in population statistics over 40 minutes as measured by brightfield microscopy [5]. Single MB acoustic behaviour was investigated using an optical microfluidic system [6].

Median GP values were significantly different between all formulations tested (Figure 1 – Definity-like MB are still under investigation), however the magnitude of the differences was small. GP values were related to carbon chain length, with MB containing longer chain lengths having higher GP values, and thus better lipid packing. DSEPC had the highest GP value, potentially due the neutralisation of charge repulsion at the phosphate level improving packing. Stability may also be related to GP, likely due to chain length [7], with DPPC showing the highest change in concentration and size over 40 minutes, although this trend was not matched by SonoVue. GP values did not appear to be associated with MB size at the clinical range (1-10 μm), nor single MB acoustic response, which was similar across all formulations.

Spectral imaging allows high throughput investigation of MB shell properties in comparison to previous techniques. Further GP work is underway to determine changes in GP during acoustic activation for bulk MB suspensions and single MBs.

References

1. *S. Sirsi & M.A. Borden, Bubble Sci Eng Technol, 1:3 (2010)*
2. *N.A. Hosny et al., PNAS, 110:9225 (2013)*
3. *K. Kooiman et al., 2010 IEEE IUS Proceedings, 900 (2010)*
4. *L.A. Bagatolli, Chem Phys Lipids, 122:137 (2003)*
5. *C.A. Sennoga et al., Ultrasound Med Biol, 36:2093 (2010)*
6. *P. Rademeyer et al., Lab Chip, 15:417 (2015)*
7. *M.A. Borden & M.L. Longo, Langmuir, 18:9225 (2002)*

Table 1: Five microbubble formulations under investigation. Average population statistics are given as measured by light microscopy. (Abbreviations: DSPC: 1,2-disteroyl-sn-glycero-3-phosphocholine; DSEPC: 1,2-distearoyl-sn-glycero-3-ethylphosphocholine; DPPC: 1,2-dipalmitoyl-sn-glycero-3-phosphocholine; DPPG: 1,2-dipalmitoyl-sn-glycero-3-phospho-(1'-rac-glycerol); DPPA: 1,2-dipalmitoyl-sn-glycero-3-phosphate; PA: palmitic acid; Macrogol 4000: polyethylene glycol, molecular weight 4000; PEG40S: polyethylene glycol (40 units) stearate; DSPE-mPEG5000: 1,2-distearoyl-sn-glycero-3-phosphoethanolamine-N-[methoxy(polyethylene glycol)-5000].)

Short name	Lipids	Molar Ratio	MB conc. ($x10^8$ MB/mL)	Mean dia. (± stdev)
DSPC	DSPC : PEG40S	9 : 1	22.4	1.57 ±1.09
DSEPC	DSPC : DSEPC : PEG40S	19.3 : 9 : 1	17.9	1.15 ±0.55
DPPC	DPPC : PEG40S	9 : 1	24.8	1.52 ±0.79
SonoVue®	DSPC : DPPG : PA : Macrogol 4000	Unknown	2.51	1.67 ±1.13
Definity-like	DPPC : DPPA : DSPE-mPEG5000	8:1:1	8.02	1.29 ±0.77

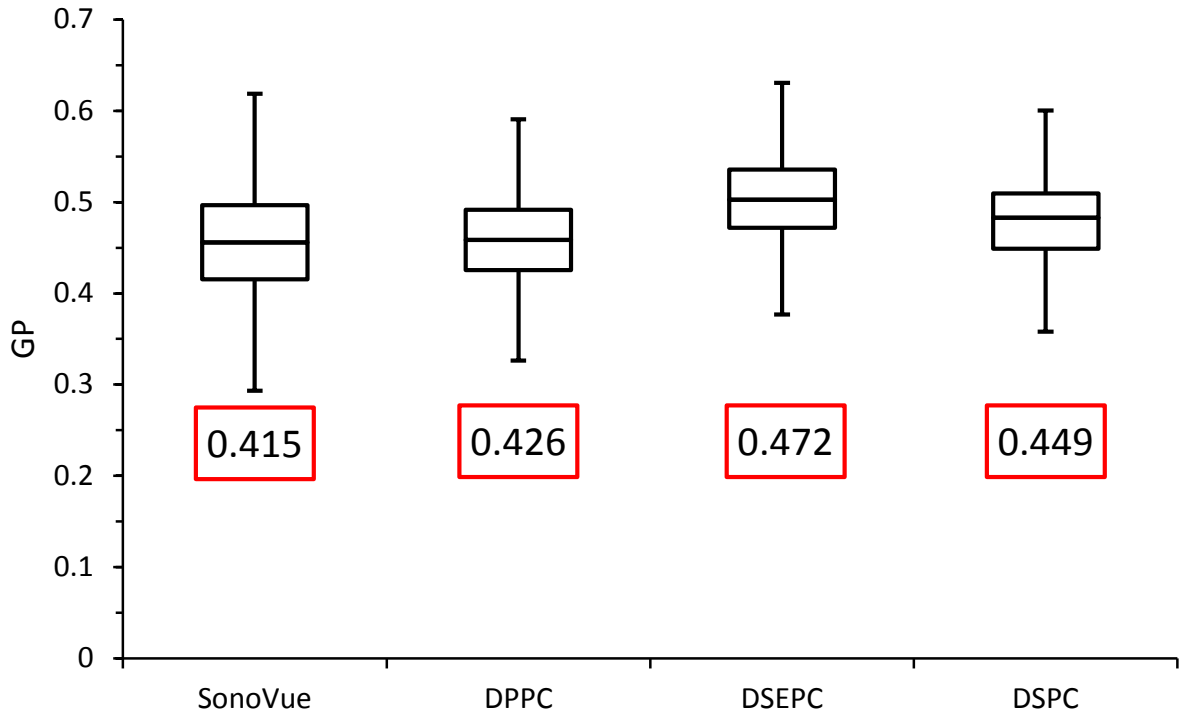

Figure 1: GP values for the four MB formulations. Spectral imaging was performed on ~1000-2000 MB per formulation. Median GP values per formulation are shown in the box plot (box is Q1-Q3 range, central line is median, whiskers are 1.5x interquartile range).

Laser-activated polymeric microcapsules for multimodal contrast imaging and therapy

Guillaume Lajoinie[1], Mirjam Visscher[1], Emilie Blazejewski[2], Audrey Lathuile[2], Gert Veldhuis[2], and Michel Versluis[1,✉]

[1]Physics of Fluids group, MIRA Institute for Biomedical Technology and Technical Medicine, MESA+ Institute for Nanotechnology, University of Twente, Enschede, The Netherlands
[2] Nanomi BV, Oldenzaal, The Netherlands
✉ m.versluis@utwente.nl

Design and novel formulations

Polymeric microcapsules are currently being investigated for multiple applications in the fields of biomedical imaging and therapy as they can serve simultaneously as highly stabilizing shells and as drug carriers. Furthermore, the shell of a microcapsule can be functionalized to adhere to specific cells and the polymer loaded with light responsive and magnetic nanoparticles that allow for alternative and non-invasive actuation. Here we investigate formulations to produce monodisperse, micro-sized, light absorbing and biocompatible oil-loaded polymeric microcapsules using a high-throughput sieve emulsion process. The effect of the oil, polymer, polymer molecular weight, and dye concentration is investigated in terms of particle morphology and stability.

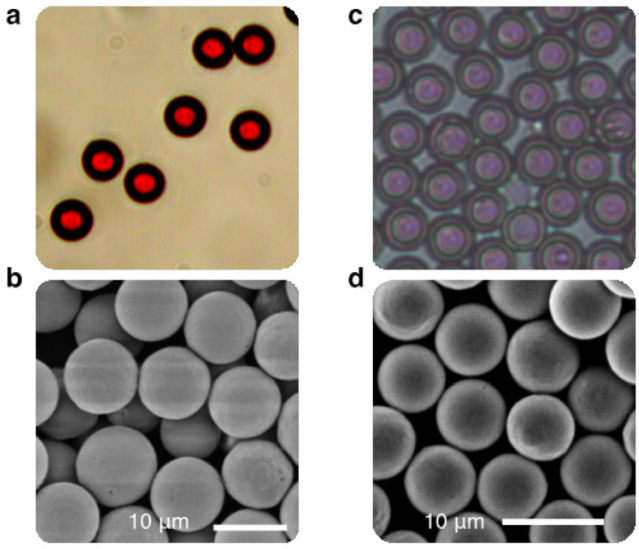

Three phase theory and single capsule behavior

Precision control of vaporization, both in space and time, can be achieved through the use of polymeric light absorbing microcapsules. Above the required energy threshold microcapsules containing a high-boiling point oil can vaporize the surrounding water upon irradiation by a laser beam. This leads to the creation of a vapor bubble that emits a strong acoustic signature and al lows for detecting individually activated particles. Here we compare the same type of laser-activated

particles to another one consisting of a low melting point polymer and a low-boiling point oil. The use of such oil reduces the energy required to achieve cavitation as the water no longer needs to be vaporized. We compared the experimental result of ultra high-speed observations of the cavitation events to a three-phase model that accounts for the partial vaporization of both fluids. The convincing agreement will open new possibilities for the optimization of such optically driven systems.

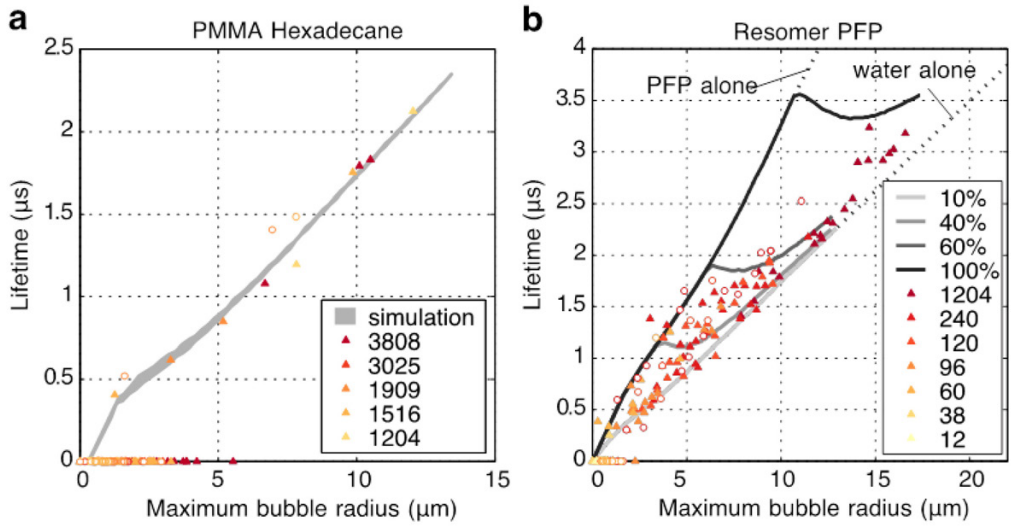

Multimodal imaging: ultrasound and photoacoustics

Upon pulsed laser irradiation, polymeric microparticles that contain a dye and an oil droplet can create a cavitation bubble and subsequently emit a strong acoustic wave. Depending on the choice made for the oil, these capsules can also create a stable bubble. Here we investigate the applicability of such particles for multimodal imaging with photoacoustics and ultrasound and study the influence of the parameters, both those of the suspension (concentration, particle type, dye load) and the local environment (temperature).

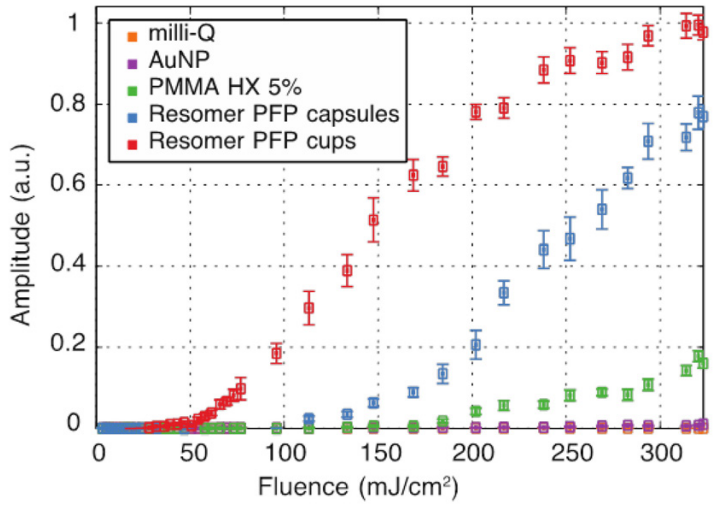

Fluorocarbon Gases Can Help Incorporate Drugs, Biomarkers and Nanoparticles in the Microbubble Shell

Marie Pierre Krafft

University of Strasbourg, CNRS, Institut Charles Sadron. F-67000 Strasbourg, France
krafft@unistra.fr

Most phospholipid-based microbubble (MB) contrast agents for diagnosis of ventricular dysfunction involve a fluorocarbon (*F*C, *e.g.* C_3F_8, C_4F_{10}, C_5F_{12}, C_6F_{14}) in their internal core. The properties of *F*Cs that are exploited include extremely low water solubility combined with high vapour pressure, low surface tension and biological inertness. We have established that *F*Cs also provide unexpected co-surfactant properties to phospholipids (PLs) and a highly effective capability to promote the recognition and adsorption of a range of compounds (phospholipids, surfactants, proteins, polymers, fluorinated therapeutics) and nanoparticles at the air/water interface and can allow their immobilization in the interfacial layer. We propose that this *F*C-driven immobilization concept offers new potential in MB-mediated drug delivery and ultrasound imaging, and for the design of bubble-based lung surfactant substitutes.

The kinetics of adsorption of PLs at the air/water interface are substantially accelerated and their interfacial tensions at equilibrium (σ_{eq}) are strongly decreased by an *F*C gas.[1] The *F*C gas modifies the competitive adsorption of PLs vs. serum albumin at the interface, reversing its "normal" outcome, a key issue in the design of lung surfactant substitutes.[2] The *F*C gas profoundly modifies the formation, stability and behaviour of monolayers of protein hydrophobin HFBII at the air/water interface, leading to stable HFBII MBs.[3] The *F*C gas accelerates the adsorption of water-soluble block copolymer Pluronic F-68 and decreases σ_{eq}. Consequently, stable MBs can be prepared from Pluronic F-68 alone when the *F*C gas is present.[4] Attractive fluorine-fluorine interactions arise between a *F*C gas and C_nF_{2n+1}-tagged compounds across a PL monolayer, allowing selective recruitment and immobilisation of the fluorinated compound into the PL layer.[5] This new molecular recognition phenomenon allows preparation of MBs loaded with a C_2F_5-labelled hypoxia biomarker (also a probe for ^{18}F-PET when radio-labelled). The adsorption and structural organization of nanodiamonds and magnetite nanoparticles on MBs can also be controlled with *F*C gases.

References

1. *a) P.N. Nguyen, T.T.T. Dang, G. Waton, T. Vandamme, M.P. Krafft, ChemPhysChem* ***2011****, 12, 2646; b) C. Szijjarto, S. Rossi, M.P. Krafft, Langmuir* ***2012****, 28, 1182.*
2. *a) P.N. Nguyen, G. Waton, T. Vandamme, M.P. Krafft, Angew. Chem. Int. Ed.* ***2013****, 52, 6404; b) P.N. Nguyen, G. Waton, T. Vandamme, M.P. Krafft, Soft Matter* ***2013****, 9, 9972.*
3. *L. Gazzera, R. Milani, L. Pirrie, M. Schmutz, C. Blanck, G. Resnati, P. Metrangolo, M.P. Krafft, Angew. Chem. Int. Ed.* ***2016****, 55, 10263.*
4. *Y. Ando, H. Tabata, M. Sanchez, A. Cagna, D. Koyama, M.P. Krafft, Langmuir* ***2016****, DOI: 10.1021/acs.langmuir.6b01883.*
5. *G. Yang, M. O'Duill, V. Gouverneur, M.P. Krafft, Angew. Chem. Int. Ed.* ***2015****, 54, 8402.*

Molecular engineering and nonlinear imaging of nanoscale acoustic biomolecules

David Maresca,[1] Anupama Lakshmanan,[2] Audrey Lee-Gosselin,[1] Johan M. Melis,[2] Yu Li Ni,[1] Raymond W. Bourdeau,[1] Dennis M. Kochmann[3] and Mikhail G. Shapiro[1]

[1]Division of Chemistry and Chemical Engineering, [2]Division of Biology and Biological Engineering, [3]Division of Engineering and Applied Science, California Institute of Technology, Pasadena, California, 91125, USA

Gas vesicles – genetically encoded protein nanostructures isolated from buoyant photosynthetic microbes – have recently been identified as nanoscale reporters for ultrasound [1]. Their unique physical properties give gas vesicles significant advantages over conventional microbubble contrast agents, including nanoscale dimensions and inherent physical stability. Furthermore, as a genetically encoded material, gas vesicles present the possibility that the nanoscale mechanical, acoustic, and targeting properties of an imaging agent can be engineered at the level of its constituent proteins. In a recent study [2], we demonstrated that genetic engineering of gas vesicles results in nanostructures with new mechanical properties that enable multiplexed and harmonic imaging.

Anabaena flos-aquae gas vesicles (Ana GVs) are cone-tipped cylindrical structures with a diameter of approximately 140 nm and length of 200−800 nm (**Fig 1a,b**). These structures are encoded by a cluster of nine different genes, including the two primary structural proteins, gas vesicle protein A (GvpA) and gas vesicle protein C (GvpC). To enable modular molecular engineering of Ana GVs, we established a platform in which genetically engineered GvpC variants are recombinantly expressed in Escherichia coli and subsequently added to Ana GVs that have been purified from A. f los-aquae and stripped of their native GvpC proteins (**Fig 1d**). We produced genetically engineered variants of Ana GvpC containing N- or C-terminal hexahistidine sequences in E. coli. The addition of recombinant GvpC in the presence of stripped Ana GVs resulted in Ana GVs with a new, engineered GvpC layer (**Fig 1d**).

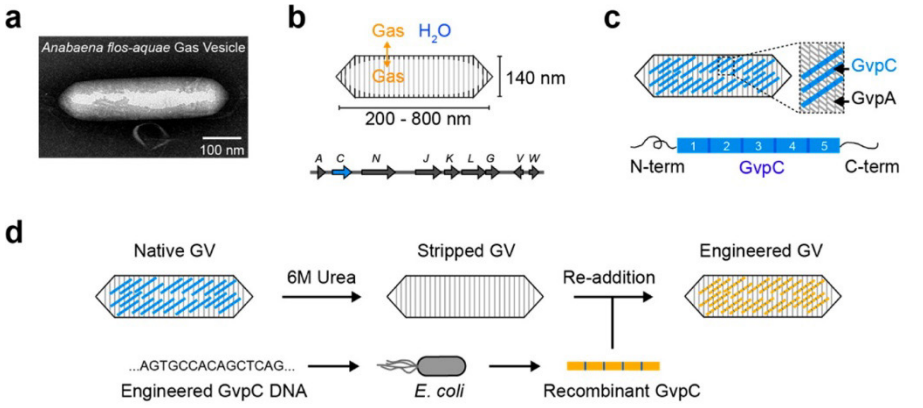

Fig 1. *Molecular engineering platform for acoustic protein nanostructures. (a) TEM image of a single Ana GV. (b) Schematic illustration of Ana GV (top) and the gene cluster encoding GvpA, GvpC, and several other essential proteins. (c) GvpA and GvpC are the two major structural constituents of GVs, with GvpA ribs (gray) forming the primary GV shell and the outer scaffold protein GvpC (blue) conferring structural integrity. Each GvpC molecule has five 33-amino acid repeats flanked by N- and C-terminal regions. (d) Paradigm for modular genetic engineering of Ana GVs. Native GVs are treated with 6 M urea to produce stripped Ana GVs without native GvpC (blue). Genetically engineered GvpC is recombinantly expressed in Escherichia coli (orange) and added to the stripped Ana GVs during dialysis to create engineered GVs with a modified GvpC layer.*

To determine whether genetic tuning could enable enhanced multiplexing, we engineered three Ana GV variants with distinct mechanical properties. ΔGvpC comprises GVs completely lacking the outer GvpC layer; ΔN&C contains a truncated form of GvpC without its N- and C-terminal regions; $GvpC_{WT}$ has an engineered GvpC protein that closely resembles the wild-type sequence (**Fig 2a**). We assessed the hydrostatic collapse behavior of these nanostructures using pressurized absorbance spectroscopy, in which the optical density of GVs (which scatter 500 nm light when intact) is measured under increasing hydrostatic pressure. This provides a rapid assessment of GV mechanics and allows comparisons to literature.6 Our three variants spanned a dynamic range of 380 kPa (**Fig 2b**). ΔGvpC had the lowest collapse pressure midpoint at 195.3 ± 0.3 kPa, the ΔN&C variant showed an intermediate value of 374.3 ± 1 kPa, and GvpCWT had the highest value of 569.9 ± 4 kPa.

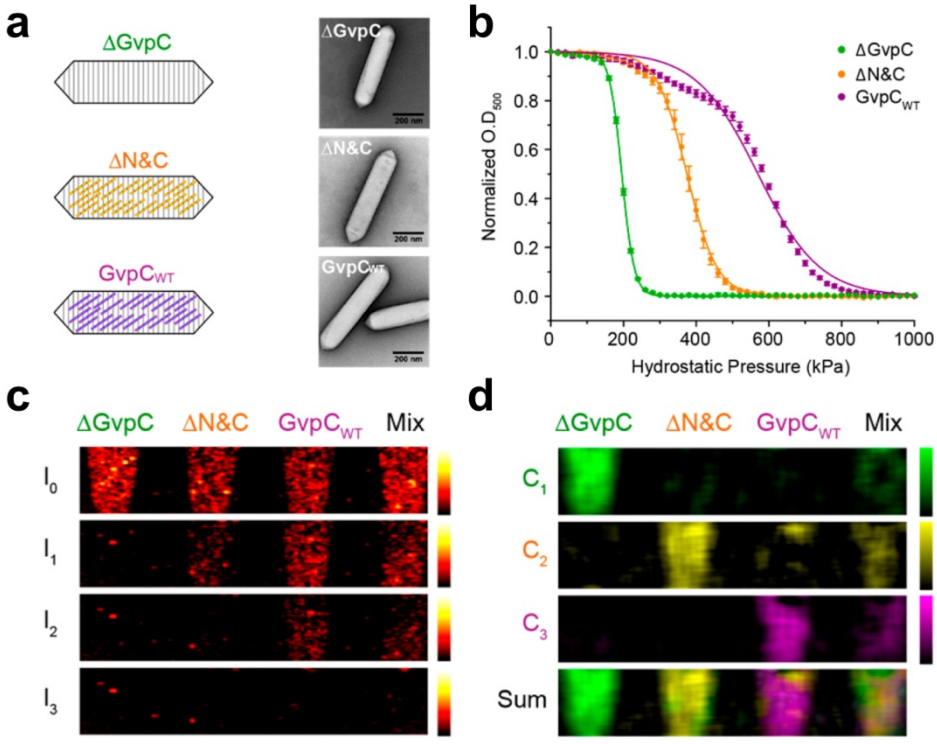

Fig 2. *GvpC engineering enables tuning of GV collapse pressure for acoustic multiplexing. (a) Schematic illustration of the three engineered GV variants used for acoustic multiplexing. ΔGvpC, ΔN&C, and GvpCWT variants are represented by green, orange, and purple colors, respectively. Accompanying TEM images show the conservation of GV shape among the three variants (scale bars are 200 nm). (b) Optical density measurements of engineered Ana GVs as a function of hydrostatic pressure (N = 7 independent preparations, error bars are SEM). (c) Ultrasound images of an agarose phantom containing wells with ΔGvpC, ΔN&C, GvpCWT and a mixture of the three variants (all GVs at final OD 1.0 in PBS), acquired at 6.25 MHz. I0, before collapse; I1, after collapse at 630 kPa I2: after collapse at 790 kPa I3: after collapse at 1230 kPa. (d) Spectrally unmixed images processed from the raw ultrasound data in (f). The bottom panel shows an overlay of the three unmixed channels C1, C2, and C3.*

We hypothesized that altering Ana GV shell mechanics by engineering GvpC could yield Ana GVs that produce harmonic signals under ultrasound exposure via threshold-dependent shell buckling, and that an amplitude modulation (AM) imaging strategy could be used to identify GV-specific signals based on this threshold behavior. In a recent study [3], we establish AM as a highly effective strategy for the selective imaging of ΔGvpC GV nanostructures, now referred to as harmonic GVs (hGVs) in the rest of the text. Through the combination of finite element mechanical modeling and experiments, we found that hGVs buckle and produce strongly nonlinear acoustic signals when exposed to ultrasound above a specific pressure threshold of around 400 kPa (**Fig 3a, b**). An AM pulse sequence taking advantage of this behavior, with full- and half-amplitude pulses above and below threshold, respectively, was highly effective at distinguishing hGVs from linear GVs.

In one approach, we demonstrate the utility of this nonlinear imaging approach in applications of GVs as targeted or genetically encoded cellular imaging agents, we nanoinjected hGVs into individual oocytes of the frog Xenopus laevis (50 nL per cell at 1.8 nM). We arranged GV-labeled cells and unlabeled controls on the surface of an agarose phantom, and scanned them with B-mode and AM mode ultrasound. While in B-mode it was challenging to distinguish labeled oocytes based on their echogenicity (**Fig 3c**), the AM sequence readily identified oocytes that contained the imaging agent (**Fig 3d**), suggesting that nonlinear imaging will enhance the visualization of GVs in the cellular context.

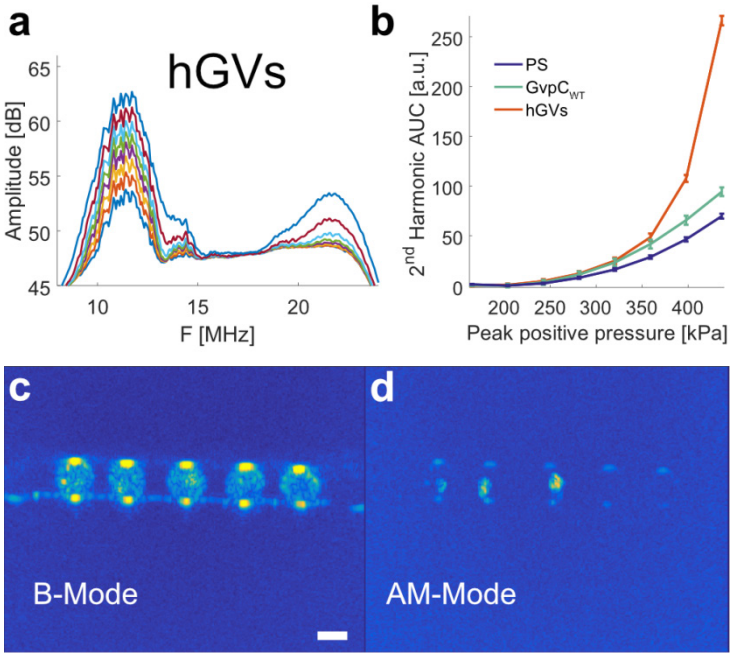

Fig 3. *(a) Experimental spectra of backscattered signals from hGVs for peak positive pressures ranging from 165 to 437 kPa. (b) Second harmonic area under the curve integrated between 19 MHz to 24 MHz as a function of pressure (N=5 samples; error bars represent standard error of the mean). Polystyrene beads are labelled in blue, wtGVs in green and hGVs in orange. (c) In cellulo nonlinear imaging of harmonic GVs at 18 MHz in Xenopus laevis oocytes. B-Mode imaging of 5 oocytes. The first three oocytes on the left were injected with hGVs (50 nL, 1.8 nM). (d) Corresponding amplitude modulation (AM) image. Scale bars represent 1 mm.*

Acknowledgements

This research was supported by the National Institutes of Health (R01-EB018975). D.M. is supported by the Human Frontiers Science Program Cross-Disciplinary Postdoctoral Fellowship (Award No. LT000637/2016). A.L. is supported by the NSF graduate research fellowship (award number 1144469). Research in the Shapiro laboratory is also supported by the Heritage Medical Research Institute, Burroughs Wellcome Career Award at the Scientific Interface, the Pew Scholarship in the Biomedical Sciences and the Packard Fellowship for Science and Engineering.

References

1. *M. G. Shapiro, P. W. Goodwill, A. Neogy, M. Yin, F. S. Foster, D. V. Schaffer, and S. M. Conolly, Nature nanotechnology 9 (4), 311 (2014)*
2. *A. Lakshmanan, A. Farhadi, S. P. Nety, A. Lee-Gosselin, R. W. Bourdeau, D. Maresca, and M. G. Shapiro, ACS nano 10 (8), 7314 (2016)*
3. *D. Maresca, A. Lakshmanan, A. Lee-Gosselin, J. M. Melis, Y.-L. Ni, R. W. Bourdeau, D. M. Kochman, and M. G. Shapiro, Nonlinear Ultrasound Imaging of Nanoscale Acoustic Biomolecules, submitted*

Optically and acoustically triggerable sub-micron phase-change contrast agents for enhanced photoacoustic and ultrasound imaging

Shengtao Lin,[1] Anant Shah,[2] Javier Hernández-Gil,[3] Antonio Stanziola,[1] Bethany I. Harriss,[3]
Terry O. Matsunaga,[4] Nicholas Long,[3] Jeffrey Bamber,[2] Meng-Xing Tang[1*]

[1]Department of Bioengineering, Imperial College London, London, UK
[2]Joint Department of Physics and Cancer Imaging Centre, The Institute of Cancer Research and The Royal Marsden NHS Foundation Trust , London, England, UK
[3]Department of Chemistry, Imperial College London, London, UK
[4]Department of Medical Imaging, University of Arizona, Tucson, Arizona, USA
**mengxing.tang@imperial.ac.uk*

In this study we demonstrate a versatile phase-change sub-micron contrast agent (Figure.1) that can provide three modes of contrast enhancement: 1) photoacoustic imaging contrast, 2) ultrasound contrast with optical activation, and 3) ultrasound contrast with acoustic activation. Such a contrast agent, which we call a 'Cy-droplet', comprises of a highly volatile perfluorocarbon (decafluorobutane, C_4F_{10}) and a near infrared optically absorbing dye (Cyanine7.5). It is prepared via a 'microbubble condensation' method [1]. The phase transition of Cy-droplets can be optically triggered by a pulsed laser illumination generating an optoacoustic signal, or acoustically activated upon external acoustic energy deposition with clinically acceptable ultrasound exposure parameters. Both *in vitro* experiments on phantoms and *in vivo* experiments have been conducted and results show that activation of the Cy-droplets using either approach forms acoustically detectable gas bubbles, which could potentially offer extravascular ultrasound contrast enhancement due to their sub-micron initial size. Such versatility of acoustic and optical 'triggerability' can potentially improve multi-modality imaging, molecularly targeted imaging and controlled drug release in the diagnosis and treatment of cancer and other diseases.

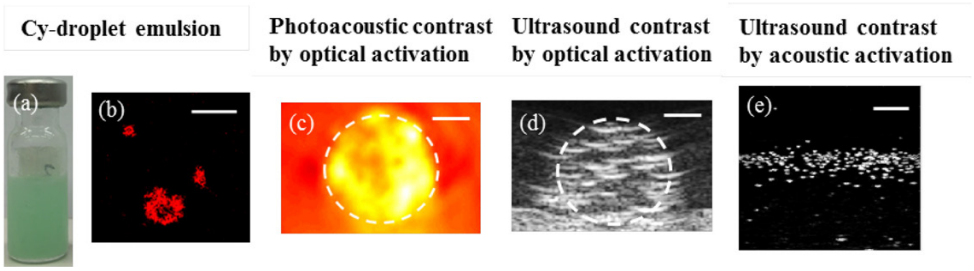

Figure 1. (a) Cy-droplet emulsion in a 2-mL glass vial. (b) Confocal fluorescence of Cy-droplets. 'Large ones' (size outliers) were demonstrated for the purpose of visualisation of the location of fluorescent lipid. Scale bar 10 µm. (c) Photoacoustic contrast induced by optical activation of Cy-droplets embedded in a phantom using a MSOT system (inVision 256-TF, iThera Medical). Scale bar 5 mm. (d) Ultrasound contrast generated after optical activation of Cy-droplets embedded in a phantom. Scale bar 5 mm. (e) Ultrasound contrast produced after acoustic activation of Cy-droplets dispersed in a 37°C water tank. It was conducted using a programmable ultrasound research platform (Vantage 128, Verasonics). Scale bar 5 mm.

Reference

1. *Matsunaga, T.O., P.S. Sheeran, S. Luois, J.E. Streeter, L.B. Mullin, B. Banerjee, et al., Phase-change nanoparticles using highly volatile perfluorocarbons: toward a platform for extravascular ultrasound imaging. Theranostics, 2012. 2(12): p. 1185-98.*

Acknowledgement

The authors acknowledge Dr Eleni Bazigou for the help with confocal microscopy. S. Lin acknowledges Imperial-CSC scholarship. The authors acknowledge Prof. David Cosgrove, Dr Robert Eckersley, Dr Dan Elson, Dr Ji Qi for the fruitful discussion. This work was supported by the National Institutes of Health Grant# CA185684 (T.O.M). We acknowledge support from the Engineering and Physical Sciences Research Council and the Cancer Research UK grant to the Imaging Centre at the Institute of Cancer Research. Special acknowledgement is given to the Ultrasound Laboratory for Imaging and Sensing (ULIS) Group, Imperial College London.

In-house produced microbubbles for high-frequency contrast enhanced ultrasound imaging

Verya Daeichin[1], Tom van Rooij[1], Ilya Skachkov[1], Bulent Ergin[2], Patricia A.C. Specht[3], Alexandre Lima[4], Can Ince[2,4], Johan G. Bosch[1], Antonius F.W. van der Steen[1], Nico de Jong[1], Klazina Kooiman[1].

[1]Dept. of Biomedical Engineering, Thoraxcenter, Erasmus MC, Rotterdam, the Netherlands; [2]Dept. of Translational Physiology, Academic Medical Center, Amsterdam, the Netherlands; [3]Laboratory of Experimental Anesthesiology, Erasmus MC; [4] Department of Intensive Care Adults, Erasmus MC.

Background

Although high-frequency ultrasound imaging is gaining attention in various applications [1], hardly any ultrasound contrast agents (UCAs) dedicated to such frequencies (>15 MHz) are available for contrast-enhanced ultrasound imaging (CEUS). Moreover, of the limited commercially available UCAs for high-frequency CEUS (hfCEUS) the composition of most of them is unknown, while shell properties have been shown to be an important factor for their performance [2,3]. The aim of our study was to produce UCAs in-house with high nonlinear response for hfCEUS.

Methods

Twelve different UCA formulations, type A-L, were either made by probe sonication at 20 kHz (A-C and G-I formulation) or mechanical agitation (D-F and J-L formulation) using a Vial Shaker. The main coating lipid was either DSPC (A-F formulation) or DPPC (G-L formulation) (59.4 for the sonication UCAs or 92.4 mol% for the mechanical agitation UCAs) with the addition of DSPE-PEG2000 (4.9 or 7.6 mol%); for the UCAs made by sonication PEG40-stearate (35.7 mol%) was also added. The gas core consisted of C_4F_{10}. The performance of the in-house produced UCAs was compared to Target-Ready MicroMarker (FujiFilm VisualSonics Inc.) using the Vevo 2100 high frequency preclinical scanner (FujiFilm VisualSonics Inc.). For the *in vitro* studies, non-linear hfCEUS (transmit frequency 30 MHz, subharmonic pulse inversion, MS250 probe, 10 % power) was used. A selection of the in-house produced UCA formulation was also evaluated *in vivo* in pigs where the kidney had been surgically exposed (n=7). The *in vivo* studies were performed with the MS250 transducer, transmit frequency 18 MHz, 10% power, ~400 kPa (MI < 0.1), 10 frames per second recording.

Results

Mechanical agitation resulted in UCAs with smaller microbubbles (number weighted mean diameter ~1 μm) than sonication (number weighted mean diameter ~2 μm). UCA formulations with similar size distributions but different main lipid component, showed that the DPPC-based UCA formulations had higher nonlinear responses at both the fundamental and subharmonic frequencies *in vitro*. In addition, UCA formulations F (DSPC-based) and L (DPPC-based) that were made by mechanical agitation performed similar *in vitro* to the commercially available Target-Ready MicroMarker (FUJIFILM VisualSonics Inc.). Of the formulations that were studied *in vitro* for their subharmonic and nonlinear fundamental response, the two best performing UCA formulations were selected for *in vivo* hfCEUS studies: F and L. UCA formulation F also performed similar to Target-Ready MicroMarker *in vivo* in

pigs with similar mean contrast intensity within the kidney, but formulation L did not as shown in Fig. 1. This is likely due to the lower stability of formulation L *in vivo*.

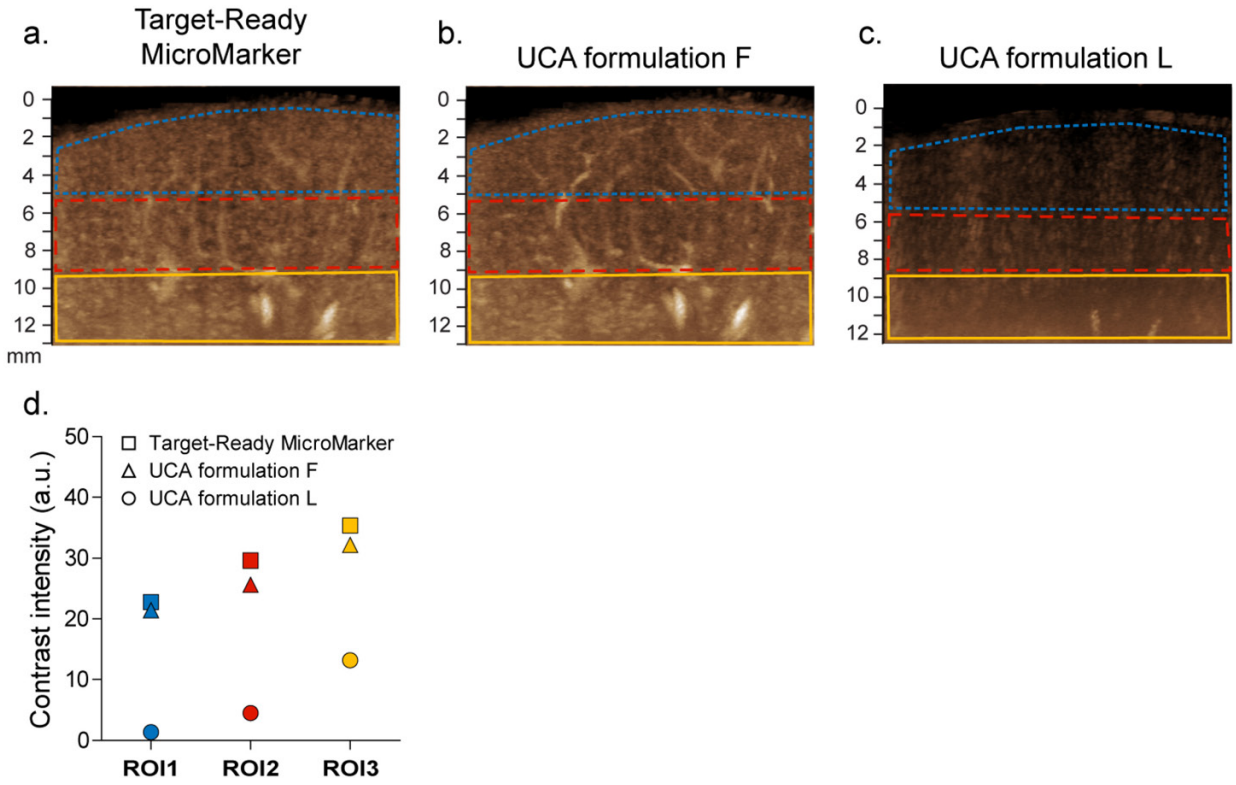

Figure 1: *In vivo* high-frequency non-linear contrast enhanced ultrasound imaging (18 MHz) of exposed pig kidney. a-c: maximum intensity projection for 1 mL bolus injection of UCA. Blue, red, and yellow lines indicate regions of interests (ROI). d: Contrast intensity in the ROIs during the peak enhancement of the shown echograms in a-c.

Conclusion

Our results suggest that our UCA formulation F performs equally well as Target-Ready MicroMarker in hfCEUS imaging. Formulation F was produced by mechanical agitation and had a shell composition of 92.4% DSPC, 7.6% DSPE-PEG2000 encapsulating a C_4F_{10} gas core.

Acknowledgements

Funding from the Center for Translational Molecular Medicine and the Netherlands Heart Foundation (PARISk), the Dutch Kidney Foundation (Innovation Grant 14O11), and NanoNextNL, a micro and nanotechnology consortium of the Government of the Netherlands and 130 partners, is gratefully acknowledged.

References

1. *Foster et al., Interface Focus 2011; 1: p. 576*
2. *van Rooij et al., Ultrasound Med Biol 2015; 41: p. 1432*
3. *Helfield et al., Ultrasound Med Biol 2012; 38: p. 846*

Coherence-based flow and perfusion segmentation using fast contrast imaging, and generalization to 3D

Charles Tremblay-Darveau[1], Paul S. Sheeran[1], Avinoam Bar-Zion[2], Ross Williams[1], Laurent Milot[1], Thanasis Loupas[3], Matthew Bruce[4] and Peter N. Burns [1,5]

[1] *Sunnybrook Health Sciences Centre, Toronto, Canada*
[2] *Technion-Israel Institute of Technology, Haifa, Israel*
[3] *Supersonic Imagine, Aix-en-Provence, France*
[4] *University of Washington, Seattle, USA*
[5] *Department of Medical Biophysics, University of Toronto, Toronto, Canada*

Introduction

The advent of plane-wave ultrasound has triggered a veritable paradigm shift in Doppler ultrasound. The ability to acquire Doppler ensembles two orders of magnitude longer than conventional line-by-line imaging has enabled the duplexing of Doppler and bubble-specific contrast-enhanced imaging without sacrificing flow sensitivity or tissue motion rejection. The use of long Doppler ensembles also averages the zero-lag autocorrelation R(0), which smoothes ultrasound speckle and background noise fluctuations. This improves visualization of blood vessels on power Doppler, but does not directly decrease the mean noise background. The ability to detect weak flow signals is then limited by inhomogeneities of the noise background caused by to, for example, the dynamic received beamforming aperture. One way to further improve contrast power Doppler is to exploit the concept that ultrasound noise is uncorrelated from pulse-to-pulse, while flow signals remain correlated for much longer. We demonstrate here that the SNR of power Doppler estimates can be increased simply by using the higher lags of the autocorrelation function (e.g., R(1), R(2),...) of the Doppler signal instead of the signal power (R(0)). As signal coherence is inversely proportional to velocity, we also assess how signal coherence can discriminate capillary from conduit flow through the use of much higher imaging lags (e.g. R(50)). Finally, we show that these concepts can be readily extended to 3D imaging.

Method

Coherence detection occurs at the envelope detection stage of echo processing. The autocorrelation R of a Doppler signal s with ensemble N is defined as $R(\tau) = \frac{1}{N}\sum_{k=1}^{N} s(k)s^*(k-\tau)$, for an imaging lag τ. Under such a formalism, conventional power Doppler is equivalent to estimating R(0). Since thermal noise is incoherent from pulse-to-pulse, its autocorrelation function self-averages proportionally to $1/\sqrt{N}$, resulting in the much-quoted reduction of the noise background. Conversely, only minimal signal loss should be observed for low lag values (e.g. 1 or 2) as long as the signal is not severely aliased. We implement this on a 4.5MHz centre-frequency planewave system (Verasonics Inc) operating in amplitude modulation Doppler (AMD) mode. Scanning was performed on a VX2 carcinoma in a rabbit.

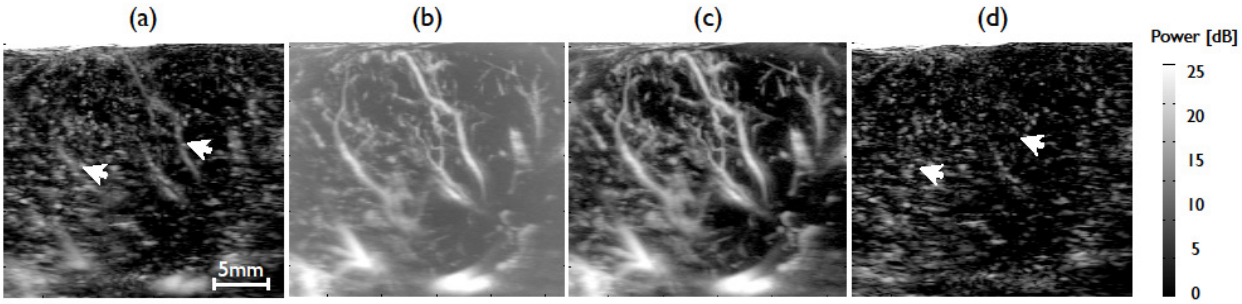

Figure 1: Vessel and perfusion segmentation using signal coherence in a VX-2 tumour perfused by microbubbles. (a) Contrast-enhanced (AM) images highlighting all blood. (b) Nonlinear power Doppler using conventional R(0) power detection segmenting flow. (c) Nonlinear power Doppler with suggested |R(1)| detection improving SNR by ~12 dB. (d) Long lag |R(50)| contrast power detection highlighting perfusion-only.

Results and discussion

Short lag imaging: the bubble whisperer

Figure 1 shows the nonlinear power Doppler image of an intramuscular VX-2 tumour perfused by Definity microbubbles for (b) conventional R(0) power detection and (c) the |R(1)| short lag estimate. Both images reveal similar vascular structures, but the noise background of the |R(1)| is 12 dB lower than the R(0) estimate. Short lag coherent imaging enables the detection of very weak signals that are otherwise buried within the noise background. It has been demonstrated in previous work that ultra-low pressure imaging (as little as 10kPa peak negative pressure, see Figure 2) is helpful in preserving microbubble contrast [1] and improving contrast-to-tissue ratio (CTR) [2], but may be unpractical on clinical platforms due to SNR limitations. The proposed algorithm should relax SNR limitations, and could translate into an improved CTR.

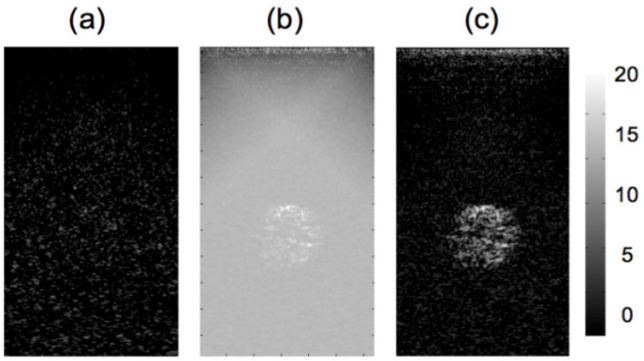

Figure 2. Detecting microbubble contrast agents using ultra-low acoustic pressures. The faint nonlinear echo (detected using amplitude modulation) of Definity microbubbles subjected to a derated pressure of 10kPa is detected with short range coherence imaging and no wall-filter. (a) Single frame image R(0) (log- compressed) only detecting noise, (b) Log-compressed accumulated signal power (R(0)) over 500 frames showing a faint vessel and (c) Log-compressed short range coherence R(1) estimated using 500 frames clearly highlighting a bubble filled region from the surrounding noise.

Long lag imaging: segmenting fast and slow flow

Signal coherence can be targeted to separate flows of different velocities since the decorrelation rate increases with respect to blood velocity. Quasi-stationary signal in capillaries remains correlated for hundreds of pulses, while flow fully decorrelates in tens of pulses. Figure 1d shows the |R(50)| long lag coherence estimated from the nonlinear microbubble echo, which highlights only very slow moving perfusion. The proposed technique does not require more calculation than standard envelope detection.

Extending to 3D volumetric acquisitions

The presented technique can also be readily extended to 3D imaging. Volumetric data were acquired by translating a L12-5 linear array connected to a Vantage 128 (Verasonics) with a stepper-motor system. A Doppler ensemble of 100 was acquired for each plane using an AMD transmit scheme. Figure 3 shows the contrast-enhanced microbubble data, the slow signal perfusion-only and the rendered 3D conduit flow perfusion. The acquisition took 30 seconds due to the step-motor approach, but could be greatly accelerated to approximately 1 second if implemented on a 2D matrix array transducer. Blood vessels were rendered in 3D using the lowest principal curvature of the |R(1)| nonlinear power Doppler volume (Figure 3c). Such analysis is analogous to that used in X-ray and MR angiography [3], and has been demonstrated by our group to work well for CEUS-Doppler angiograms acquired with long Doppler ensembles. The method successfully resolves 3D vessels structures, even for relatively short Doppler acquisitions.

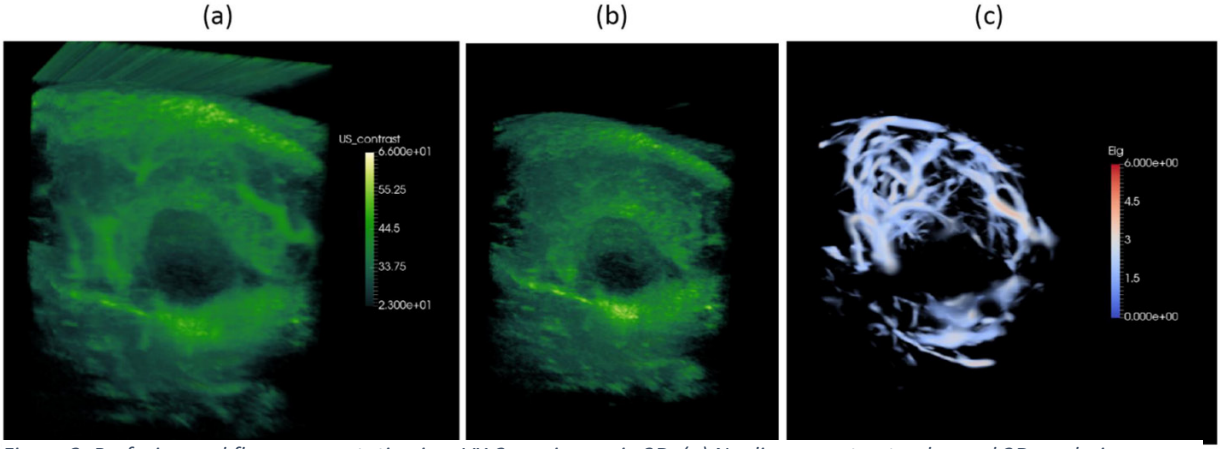

Figure 3: Perfusion and flow segmentation in a VX-2 carcinoma in 3D. (a) Nonlinear contrast-enhanced 3D rendering showing highlighting all blood. A necrotic zone is visible at the middle of the tumour. (b) Quasi-stationary perfusion-only estimated from higher imaging lags. Note that the large vessels visible in (a) are absent in (b). (c) Fast flow 3D rendering extracted from the principal curvature information. 3D rendering was performed in VTK-based Paraview software.

Conclusions

Coherence-based power detection surpasses conventional zero-lag autocorrelation through a significant reduction of the background noise, and enables perfusion background segmentation. The method does not require additional acoustic transmits compared to CEUS-Doppler and could be readily included in the Maximum Intensity Projection (MIP) processing pathways in most clinical scanners. These concepts, readily extensible to volumetric acquisitions, may help realise 3D real-time flow and perfusion detection in vivo.

References

1. *Tremblay-Darveau et al. (2014). IEEE Trans. UFFC, 61(12), 1988–2000.*
2. *Tremblay-Darveau et al. (2014). IEEE Ultrason. Symp., 1742–1745.*
3. *Frangi et al. (1998) Med Image Comput Comput Assist Interv, 130–137.*

Super-resolution imaging with ultrafast ultrasound localization microscopy (uULM)

Olivier Couture

Institut Langevin (CNRS, INSERM, ESPCI), 17 rue Moreau, Paris. olivier.couture@espci.fr

In ultrasound imaging, the trade-off between penetration and resolution was deemed incompressible until recently. Due to diffraction, the echoes from scatterers, such as microbubbles flowing in large concentrations in blood vessels, are undistinguishable from each other's. In optics, this limit was bypassed using localization microscopy techniques, such as FPALM. It exploits the blinking of individual sources on thousands of images to separate fluorophores and determine their actual location with a resolution better than wavelength/10 [Betzig et al., Science, 2006].

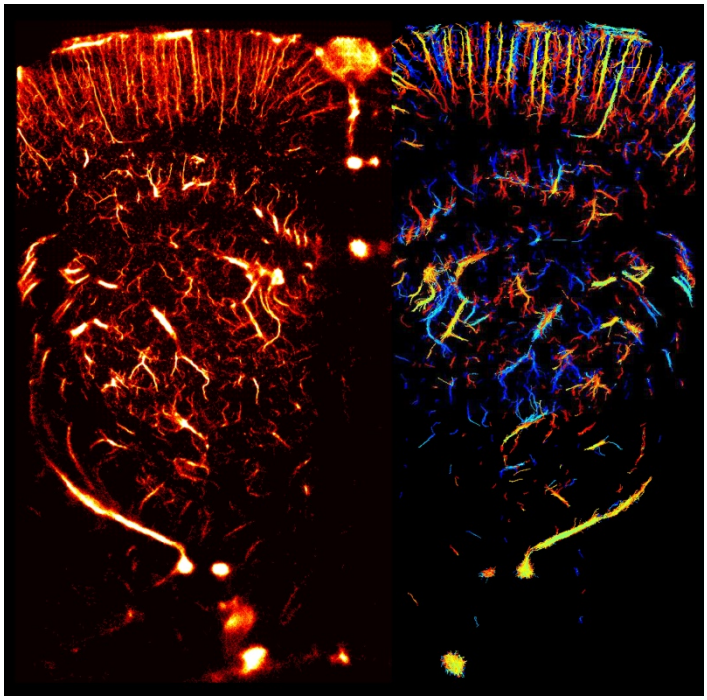

uULM of the rat brain L: bubble density , R: velocity map [Errico et al. Nature, 2015]

We have shown that such phenomenon can also be obtained in ultrasound imaging by observing large concentrations of microbubbles at ultrafast frame rates. This lead us to introduce the concept of ultrafast ultrasound localization microscopy [uULM, Couture et al. Patent 2010, Couture et al. IEEE IUS Orlando 2011], which allows super-resolution imaging by reconstructing the precise position of individual microbubbles flowing into microvessels. We initially tested ULM in 3D in a microvessel phantom [Desailly et al. APL, 2013], before moving to the rat brain [Errico et al. Nature, 2015]. This technique has recently been applied by Dayton's group to map angiogenesis in a tumor model and assess its tortuosity [Lin et al. 2016].

Other approaches for ultrasound super-resolution have since been proposed. Microbubble Accumulation Super Resolution, which relies on low dilution of microbubbles observed at conventional frame rates has been applied both in-vitro [O'Reilly et al, Medical Physics 2013; Viessmann et al., PMB, 2013] and in-vivo [Siepmann et al., IEEE IUS 2011, Christensen-Jeffries et al., IEEE UFFC, 2015]. More recently, Super-Resolution Acoustical Fluctuation Imaging, which relies on the higher-order statistics of the echoes temporal fluctuation, has been demonstrated by Bar-Zion et al. [ArXiv 2016].

In general, the position of individual microbubbles can be determined with a resolution defined by the signal to noise ratio and the geometry of the system [Desailly et al., PMB, 2015]. The maximum resolution attainable with current programmable scanners was predicted to be 5 microns at 15 MHz, or wavelength/20. In uULM, this was confirmed in-vivo by injecting boluses of microbubbles in rat brain and performing ultrafast imaging coronally (500 fps) for 150 seconds. The resulting map of microbubble positions was reconstructed with a resolution of $\lambda/12$ (8 μm), down to 12 mm in depth.

Ultrasound localization microscopy brings new parameters in the trade-off between penetration and resolution, such as the concentration of microbubbles, frame rate, signal-to-noise ratio and acquisition time. This approach allows us to map vessels that are not visible by other imaging modalities in-depth. However, it remains limited by micrometric motion which can drastically affect image quality. Subwavelength image registration has been proposed to solve this issue [Hingot et al., submitted, 2016a]. Data overload, challenging probe design and electronics, currently restrict the use of 3D uULM, which is a *conditio sine qua non* for the mapping of complex microvasculature. Finally, we consider that ultrasound therapy should also benefit from the evolution toward a subwavelength precision, which was recently demonstrated for drug-delivery [Hingot et al., APL, 2016b].

Subwavelength motion-correction for ultrafast Ultrasound Localization Microscopy

Vincent Hingot, Claudia Errico, Mickael Tanter*, Olivier Couture*
****These authors have contributed equally***

Institut Langevin, CNRS, INSERM, ESPCI Paris, PSL Research University, 17 rue Moreau, 75012, Paris.

Introduced recently [Couture et al., 2011], ultrasound super-resolution techniques [Viessmann et al. 2013, O'Reilly et al. 2013] such as ultrafast Ultrasound Localization Microscopy (uULM) [Desailly et al., 2013] bypasses the diffraction-limit and surpasses the conventional resolution by an order of magnitude. We previously exploited uULM to achieve resolution of 8 µm over a depth of 12 mm in the rat brain vasculature [*Errico et al, Nature 2015*]. However, at this resolution scale, the sensitivity to motion, even small ones, becomes particularly problematic. Our previous solution was to restrain the rat's head in a stereotaxic frame. But for most applications of uULM, for example in the vigil rat's brain, in soft tissues (heart, pancreas, etc.), or for imaging in humans, a tight physical restraint cannot be implemented. Here, we introduce a first-order correction for rigid motion. This phase-correlation method represents a first proof of concept in generalizing super-resolution to moving organs.

Experiments were performed by placing a 15 MHz 128 element transducer over a rat head without tight constraint. Ultrafast acquisitions were performed at 500fps by blocks of 400ms for 3 minutes after the injection of a bolus of contrast agents. A spatiotemporal clutter filter based on Singular Value Decomposition (SVD) of raw data was first used to extract tissue dominated images. Between two translated images $I_1(x, z)$ and $I_2(x, z) = I_1(\mathrm{x}+\Delta x, z+\Delta z)$, we can write the cross correlation (1).

$$\frac{\mathcal{F}(I_1)\circ\mathcal{F}(I_2)^*}{|\mathcal{F}(I_1)\circ\mathcal{F}(I_2)|} = e^{j\varphi(\Delta x,\Delta z)} \quad (1)$$

The inverse Fourier transform of (1) is a Dirac peak in $\Delta x, \Delta z$ where $\Delta x, \Delta z$ is the displacement between the two frames. Comparison with a reference image allowed us to associate a displacement to every image. SVD filter was then used on the raw data to extract flowing bubbles. The bubbles were localized and their positions were corrected accordingly. The positions were accumulated to form the corrected uULM image. As shown in figure 1, this approach can help the registration of the bubble passage in vessels much smaller than the wavelength.

Combined with ultrafast imaging, phase correlation can correct rapid rigid and can be of great help for organs such as the brain. The corrected motion can be much finer than the wavelength. However, it is limited to in plane motions and deformations can only be corrected to a certain extent by using phase correlation to subsets of the image to determine local motions. A more general approach, in 3D, should allow the correction of subwavelength motion for all applications of super-resolution ultrasound imaging.

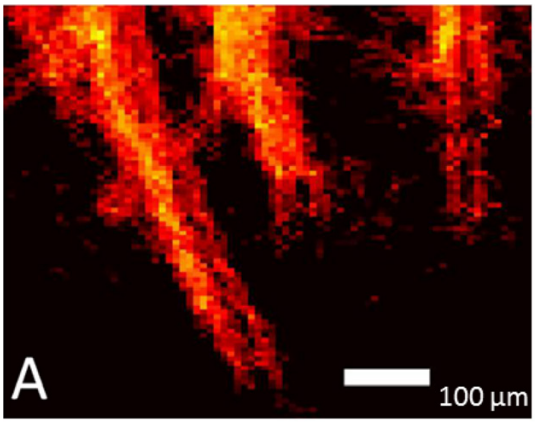

Fig.1.A. Uncorrected image of a 60 µm vessel

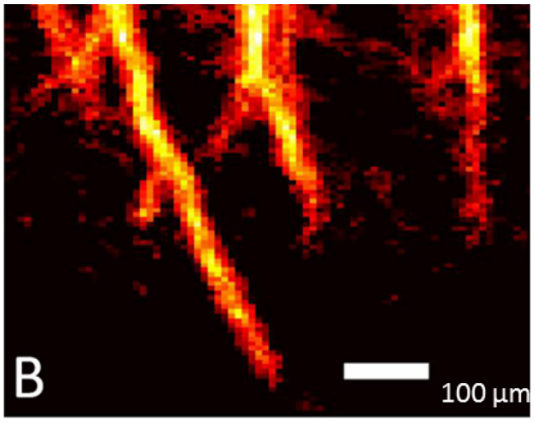

Fig.1.B. Same vessel after motion correction

Sparsity-based Ultrasound Super-resolution Imaging

Avinoam Bar-Zion[1], Oren Solomon[2], Charles Tremblay-Darveau[3], Dan Adam[1] and Yonina C. Eldar[2]

[1] Department of Biomedical Engineering, Technion - Israel Institute of Technology, Haifa, Israel.
[2] Department of Electrical Engineering, Technion - Israel Institute of Technology, Haifa, Israel.
[3] Physical Sciences, Sunnybrook Research Institute, Toronto, Ontario, Canada.

Background

Inspired by super-localization methods in fluorescence microscopy, several methods for achieving super-localization in contrast-enhanced ultrasound (CEUS) imaging were presented in the last few years [1], [2], [3]. These methods enable the depiction of blood vessel structure and the flow within them, deep within the body, with unprecedented spatial resolution. However, all CEUS super-localization methods are currently limited by long acquisition times, impeding their application for clinical imaging. Recently, a statistical post-processing method named super-resolution fluctuation imaging (SOFI) [4] was applied to CEUS data and produced enhanced spatial resolution with very short acquisition times, using high ultrasound contrast agent concentrations [5]. In this work, we combine statistical tools with additional structural priors in the form of sparsity, to further improve the obtained resolution gain while maintaining high temporal resolution. The overall method is called Sparsity-based Ultrasound Super-resolution Imaging (SUShI).

Methods

First, the microbubble related signal in each acquired cine-loop was separated from the tissue clutter using a high-pass Doppler filter. The point spread function (PSF) of the system was estimated from the data: patches containing single microbubbles in each frame were detected, automatically aligned, and principal component analysis (PCA) was applied to the resulting image patch stack, to reject local noises. Next, the autocorrelation of the time series in each pixel was calculated for a specific prechosen time-lag. A dictionary was constructed based on the estimated PSF, and the underlying structure of the vasculature was reconstructed solving a sparse representation problem. Two New-Zealand white rabbit models were used to validate the proposed method: normal blood vessels of different scales were imaged in the kidney of healthy rabbits while tumor vasculature was imaged using a VX2 hind-limb model. Plane wave scans were acquired at a PRF of 5kHz using a the Verasonics Vantage scanner with a linear probe and a 4.5 MHz carrier frequency. Bolus injections of Definity were used with a clinically recommended concentration of 10μL/kg.

Results and discussion

The high ultrasound contrast agents concentration enabled short acquisition times: 90 msec and 600 msec for the kidney and tumor scans, respectively. The highly-detailed estimated PSF presented unsymmetrical axial profile and lateral side lobes. Using this estimation, the vasculature was reconstructed on a sub-pixel grid. The proposed method resulted in super-resolution images presenting small vessels and bifurcations (Fig. 1). Near the bifurcation, vessels that could not be resolved in the original temporal mean image were separated (Fig. 1 right-bottom picture, and graph Fig. 2a). The full-width-half-max (FWHM) measured in a lateral cross section through a small vessel is 149 μm (Fig. 2c) compared to 601 μm in the temporal mean image.

Conclusion

The proposed method enabled fast super-resolution scans with improvement in spatial resolution by a factor of 4. The incorporation of priors regarding the PSF and the structure of the underlying vasculature produced improved results compared to those of CEUS SOFI [5]. The reported results present a new trade-off between spatial and temporal resolution with acquisition times of tens of hundreds of milliseconds compared to tens or hundreds of seconds using super-localization methods [1], [3]. These short acquisition times can enable local hemodynamic monitoring and imaging of internal organs that are affected by respiratory motion.

References

1. *C. Errico, J. Pierre, S. Pezet, Y. Desailly, Z. Lenkei, O. Couture, and M. Tanter, "deep super-resolution vascular imaging," Nature, vol. 527, no. 7579, pp. 499–502, 2015.*
2. *M. A. O. Reilly and K. Hynynen, "A super-resolution ultrasound method for brain vascular mapping A super-resolution ultrasound method for brain vascular mapping," vol. 110701, no. 2013, 2016.*
3. *K. Christensen-jeffries, S. Member, R. J. Browning, M. Tang, C. Dunsby, R. J. Eckersley, and S. Member, "In Vivo Acoustic Super-Resolution and Super-Resolved Velocity Mapping Using Microbubbles," vol. 34, no. 2, pp. 433–440, 2015.*
4. *T. Dertinger, R. Colyer, G. Iyer, S. Weiss, and J. Enderlein, "Fast, background-free, 3D super-resolution optical fluctuation imaging (SOFI).," Proc. Natl. Acad. Sci. U. S. A., vol. 106, no. 52, pp. 22287–92, 2009.*
5. *A. Bar-Zion, C. Tremblay-Darveau, O. Solomon, D. Adam, and Y. Eldar, "Fast Vascular Ultrasound Imaging with Enhanced Spatial Resolution and Background Rejection," IEEE Trans. Med. Imaging, vol. 7, pp. 1–12, 2016.*

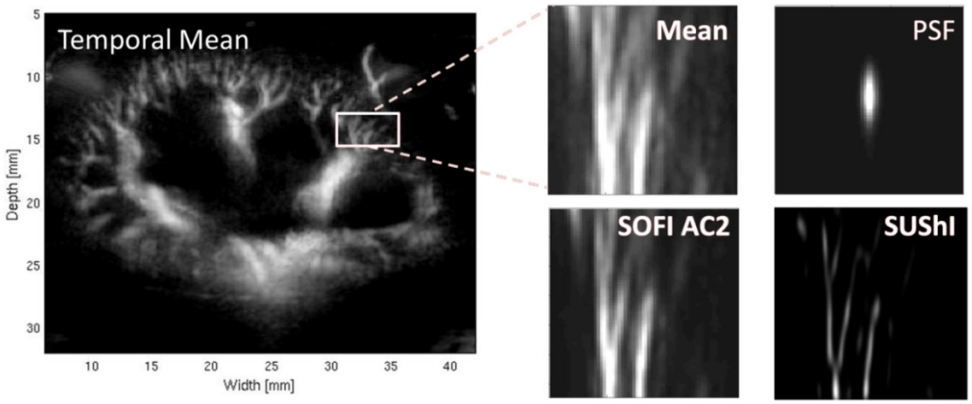

Fig. 1: Kidney model: comparison between different imaging methods

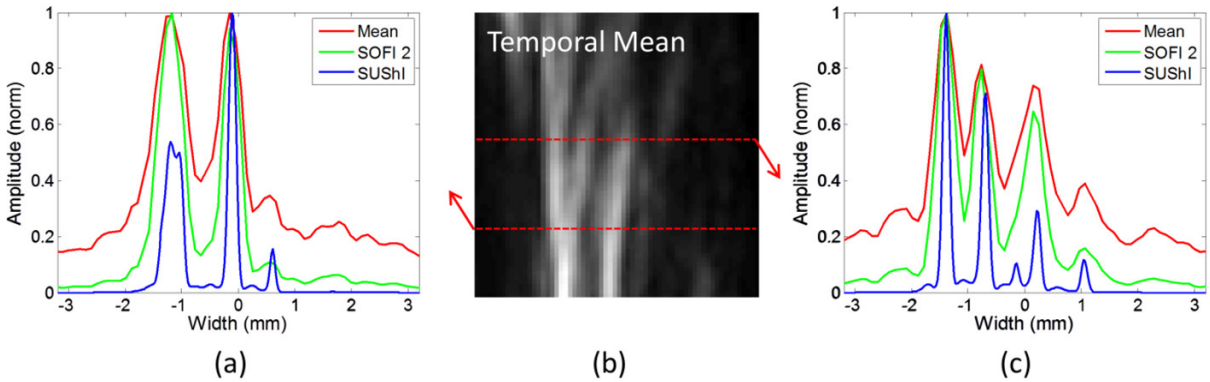

Fig. 2: Cross sections through small kidney vessels

Microbubble Super-Localisation in Human Lower Limb Microvasculature with Motion Correction

Sevan Harput[1], Kirsten Christensen-Jeffries[2], Yuanwei Li[1], Jemma Brown[2], Paul Aljabar[2], Robert J. Eckersley[2*], Christopher Dunsby[3*] and Meng-Xing Tang[1*]

[1]Department of Bioengineering, Imperial College London, London, SW7 2BP, UK
[2]Biomedical Engineering Department, Division of Imaging Sciences, Kings College London, London, SE1 7EH, UK
[3]Department of Physics and Centre for Pathology, Imperial College London, London, SW7 2AZ, UK
**These authors contributed equally to this work*

Email: S.Harput@imperial.ac.uk, Mengxing.Tang@imperial.ac.uk

Background and Objective

Motion correction is crucial for ultrasound modalities taking advantage of the use of multiple frames such as pulse inversion and compounded plane wave imaging and also for applications such as flow imaging and super-resolution imaging. In super-resolution imaging, acquisition of precise and accurate information through hundreds of frames is necessary to create a high resolution map of the microvasculature [1-2]. In flow imaging the same MB must be followed for several frames to achieve flow velocity information. Although the algorithms used in these applications are successful for in-vitro and well controlled in-vivo experiments, adaptation to clinical ultrasound imaging is still a big challenge due to the effect of motion on ultrasound speckle patterns [3].

In this study, before compensating for motion, we analysed the factors that are generating motion. For human lower limb imaging there are three main causes of motion: that the ultrasound probe is held by the practitioner and so may move relative to the patient; pulsations of arterioles and venules; and twitching of muscles. These motion sources create rigid and non-rigid tissue deformations. For this reason, a two stage motion estimation was performed on every B-mode frame by using intensity-based registration methods to find a transformation field. Transformation fields were applied on the contrast mode images acquired by a commercial ultrasound scanner to correct for motion and improve the microbubble localisation accuracy.

Methodology

Rigid intensity-based registration registration methods can compensate for ultrasound probe movements, but they are not the ideal method for tissue motion correction in diagnostic ultrasound imaging. On the other hand, non-parametric non-rigid registration methods are not necessarily required for ultrasound imaging because the tissue motion is locally connected. Registration methods based on parametric non-rigid transformations give a good trade-off between smoothness and computation time by the choice of regularization parameter and thus chosen for tissue motion estimation.

In this study, a rigid motion correction was applied first to minimize the global motion generated by the hand-held probe. The second stage was based on free-form deformations with non-rigid registration [4]. First stage corrects for the global rigid motion and provides a better starting point for the second non-rigid registration stage, allowing it to achieve a smaller error with less number of iterations. Sum of square differences was chosen as the similarity metric and the regularization parameter had a penalty of 10^{-5}.

Experimental Setup

Contrast enhanced ultrasound imaging was performed in the tibialis anterior muscle using a Philips iU22 clinical ultrasound scanner with a 3-9 MHz linear array transducer. A 45 second acquisition of B-mode and Contrast mode images were recorded at a frame rate of 13 Hz. A low mechanical index of 0.06 was used to avoid the destruction of diluted Sonove microbubbles using a 20 ml saline solution.

Results and Discussion

The maximum intensity projection (MIP) for all acquired contrast mode frames are plotted in Fig. 1(top) with and without motion correction. MIP images represent the maximum intensity values recorded for each vascular structure with the B-mode image resolution, where the wavelength is 0.25 mm for the full bandwidth of the probe. In Fig. 1(bottom), all localised microbubble events are visualised after filtering and noise thresholding with and without motion correction.

To compare the differences before and after super localisation and motion correction, a vessel located at a depth of 18 mm and a lateral location of 8 mm was selected. A lateral section of this vessel is plotted in Fig. 2 for all scenarios presented in Fig.1. The full-width at half-maximum (FWHM) was measured as 0.6 mm and 0.45 mm for the MIP without and with motion correction, respectively. For the super-localised microbubbles the FWHM of the same vessel was 0.1 mm for both cases, however without motion correction the selected vessel has an artificial shadow which is 0.25 mm apart from the main.

Conclusions

Tissue motion correction is an ongoing challenge for all diagnostic ultrasound applications. Correlation based techniques and rigid transformations usually fail to compensate for localised motion. Therefore, sub-pixel motion estimation and non-rigid motion correction methods are required to visualise microvascular structures and flow beyond the diffraction limit through localisation of spatially isolated microbubbles.

Although the motion correction was performed on B-mode images acquired by a commercial scanner, the application of the proposed motion correction scheme is not limited to image data and the use of phase information in RF data will improve the sub-wavelength motion estimation accuracy.

Acknowledgements

The authors gratefully acknowledge funding from the Engineering and Physical Sciences Research Council (UK) via grant no. EP/N015487/1 and EP/N014855/1.

References

1. *O. M. Viessmann, R. J. Eckersley, K. Christensen-Jeffries, M. X. Tang, and C. Dunsby, "Acoustic super-resolution with ultrasound and microbubbles.," Phys. Med. Biol., vol. 58, no. 18, pp. 6447–58, Sep. 2013.*
2. *K. Christensen-Jeffries, R. J. Browning, M.-X. Tang, C. Dunsby, and R. J. Eckersley, "In Vivo Acoustic Super-Resolution and Super-Resolved Velocity Mapping Using Microbubbles," IEEE Trans. Med. Imaging, 2015.*
3. *Renaud Morin, Adrian Basarab, Stephanie Bidon, and Denis Kouame, "Motion Estimation-Based Image Enhancement in Ultrasound Imaging", Ultrasonics, Elsevier, 2015, 60, pp. 19-26.*
4. *D. Rueckert et al. "Nonrigid Registration Using Free-Form Deformations: Application to Breast MR Images", IEEE Trans Med Imaging, 1999.*
5. *M. Bro-nielsen and C. Gramkow. "Fast Fluid Registration of Medical Images", Visualization in Biomedical Computing, 1996.*

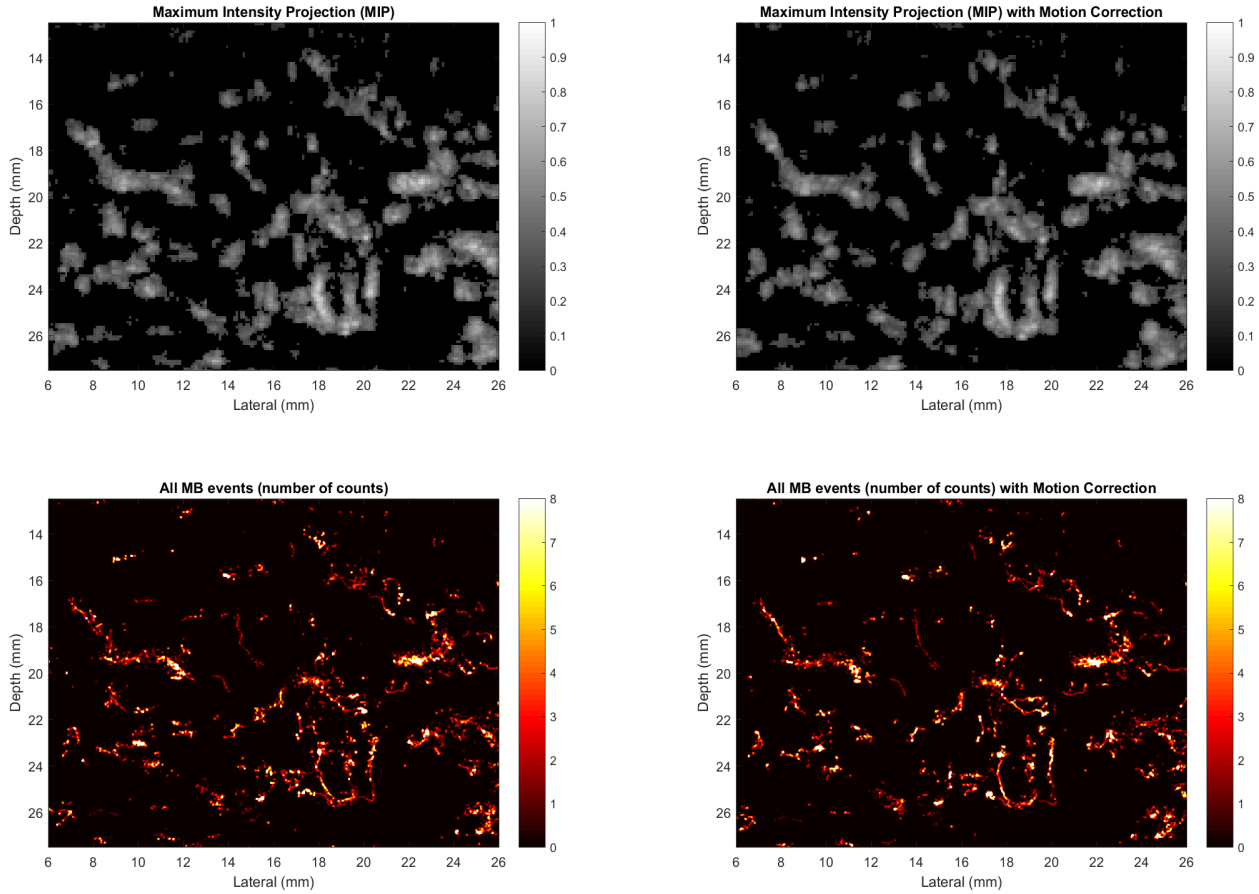

Fig. 1. (Top-left) Maximum intensity projection of contrast enhanced ultrasound of human tibialis anterior muscle without motion correction and (Top-right) with motion correction. The colour bar corresponds to normalised intensity. (Bottom-left) All localised microbubble events are visualised without motion corrections and (Bottom-right) with motion correction. The colour bar corresponds to number of localisations.

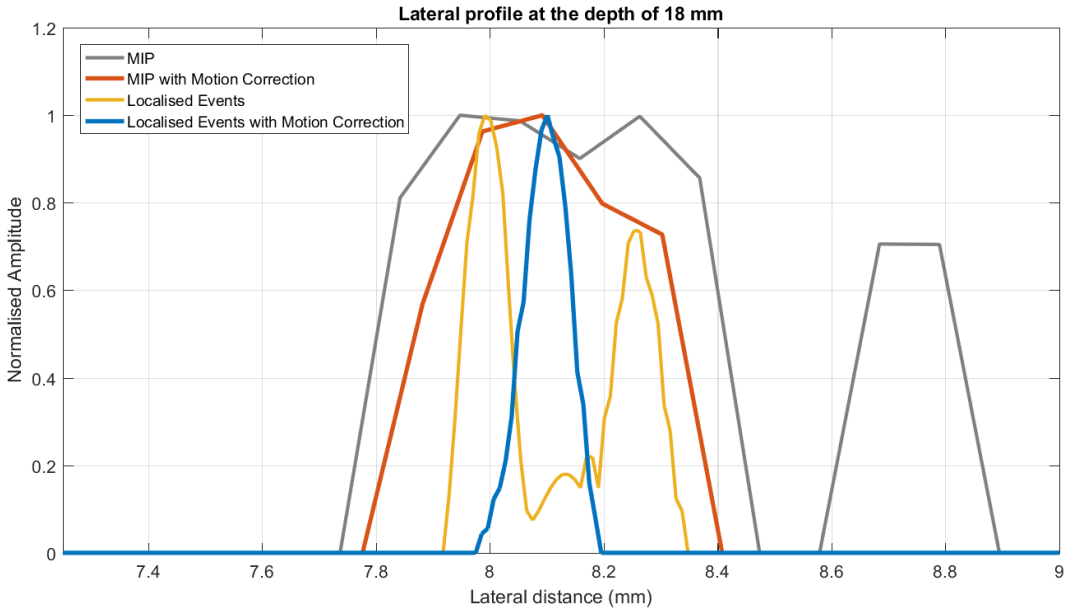

Fig. 2. Lateral profile at a depth of 18 mm was selected to compare the maximum intensity projection images and super-localised microbubbles with and without motion correction.

Contrast Enhanced Ultrasound of Liver Lesions: A Children's Cancer Center Experience

Beth McCarville, MD, Jamie Coleman, MD,

Background

Focal liver lesions (FLLs) occur in about 17% of children after cancer therapy, are potentially metastatic and often lead to additional imaging and patient/parent anxiety. The contrast enhanced ultrasound (CEUS) features of FLLs in adults are well described but CEUS has not been widely accepted in pediatrics in the United States. In 2016 the US Food and Drug Administration approved the first ultrasound contrast agent for use in assessing liver lesions in both adults and children. This has led to an increased interest and awareness of the potential role of CEUS to evaluate the liver in children. Our research has shown that CEUS is safe in children and in mid-2013 we began using it clinically. The most common indication has been to assess FLLs. We seek to share our experience in an effort to promote CEUS in children.

Methods

After IRB approval, two radiologists retrospectively reviewed imaging (including CEUS) of 25 patients who had been treated for cancer or referred to our institution to rule out cancer and had FLLs. We recorded age at CEUS, time-point FLL discovered relative to cancer therapy, modality/study type that detected FLL, number of FLLs/patient, interpretation of CEUS (adenoma, focal nodular hyperplasia [FNH], metastasis, etc.), reaction to ultrasound contrast agent, biopsy results, clinical follow-up, demographics and primary diagnosis.

Results

There were 10 males, 15 females, average age at CEUS=15.5 yr (range, 3 mo -25 yr), primary diagnoses; leukemia (n=5), medulloblastoma (n=3), rhabdomyosarcoma (n=3), Ewing sarcoma, chondrosarcoma, Wilms tumor, neuroblastoma (n=2 each) and hemangiopericytoma, low-grade mesenchymal tumor, desmoplastic small round cell tumor, carcinoid, hepatocellular carcinoma (HCC), hemangioma (n=1 each). Lesions were discovered on abdomen CT (n=9), abdomen ultrasound (n =4), MRI for liver iron measurement (n=3), chest CT (n=3), spine MRI (n=2), bone density CT (n=2) and abdomen MRI (n=2). There were 2 newly diagnosed primary liver tumors; 1 infantile hemangioma, 1 HCC. In the remaining 23 subjects FLLs were discovered, on average, 5 yr after completion of therapy (range, 0 – 17 yr). Two subjects had too numerous to count FLLs, the remaining 23 had an average of 2.5 FLLs/subject (range, 1- 8). On CEUS 21 of the 25 subjects (84%) had lesions with benign features interpreted as; FNH (n=11), adenoma (n=5), FNH vs adenoma (n=3) and perfusion defect, regenerative nodule and infantile hemangioma (n=1 each). Four had lesions suspicious for metastatic disease (n=2), or HCC (n=2). Biopsies performed in 2 of these 4 showed HCC and granuloma. The lesion in the subject with granuloma continued to grow on follow-up imaging. Rebiopsy of this lesion proved metastatic disease. One lesion suspected to be HCC was resected and found to be FNH. The final subject subsequently developed a local recurrence and is being followed. No subject had an adverse reaction to ultrasound contrast agent.

Conclusions

CEUS is safe in this patient population. CEUS accurately characterizes FLLs as benign or malignant without exposing the patient to radiation or sedation, and provides immediate feedback to the patient/parent. When CEUS is equivocal or does not match clinical findings, we recommend MRI for additional lesion characterization, before biopsy or resection.

Microbubble-cell interactions: Mechanistic insight into the biophysics of sonoporation

Brandon Helfield[1], Xucai Chen[1], Simon C. Watkins[2], Flordeliza S. Villanueva[1]

[1]Center for Ultrasound Molecular Imaging and Therapeutics, University of Pittsburgh, PA, USA
[2]Center for Biologic Imaging, Department of Cell Biology, University of Pittsburgh, PA, USA

Background

Ultrasound-stimulated microbubbles are emerging as novel target-specific non-viral gene delivery vectors for the treatment of disease for which gene targets have been identified, *e.g.* to deliver VEGF plasmid DNA to promote arteriogenesis. The nature of the microbubble-target cell interactions that facilitate nucleic acid delivery across cell membranes and into cells outside the vasculature, and hence strategies to optimize the efficiency of this platform, remain poorly understood. The objective of this work is to gain mechanistic insight into microbubble-cell interactions over the intrinsic timescales associated with the biophysics of sonoporation, linking bubble cavitation physics with cellular permeability and membrane repair response.

Methods

Individual phospholipid coated microbubbles were examined adjacent to cultured human umbilical vein endothelial cells (HUVECs) at 37°C. Propidium iodide (PI) was diluted into the media pre-exposure as a drug surrogate and a marker for sonoporation. For a subset of microbubble-cell pairs (n=351), a simultaneous ultrafast bright-field (16 Mfps; UPMC-Cam) and standard epi-fluorescence (15 fps) imaging system was employed in order to couple microbubble cavitation physics (~**µs** timescale) with cell membrane permeability dynamics (~**ms** timescale). Individual microbubble-cell pairs were exposed to a single ultrasound pulse at 0.5, 1, or 2 MHz, with a pulse duration of 4, 8 or 16 µs and ultrasound pressures between 0.1-0.8 MPa. We next examined the resulting effects on cellular biophysics (~**seconds to minutes** timescale) via 3D live-cell confocal microscopy during sonoporation events (single 8 cycle pulse, 1 MHz, 0.1-0.8 MPa), with visualization of the plasma membrane and Ca^{2+} signaling events (n=12), both known factors involved in cell wound/poration repair.

Results

The maximum absolute microbubble expansion and associated shear stress were strong threshold indicators of sonoporation. For an 8 µs pulse, the oscillation (shear stress) threshold above which HUVECs perforate was 3.9, 2.6, and 1.4 µm (7.8, 14.5, 22.7 kPa) at 0.5, 1 and 2 MHz respectively. At a given ultrasound frequency, increases in pulse duration decreased the required excursion and shear stress. Real-time confocal microscopy highlights that microbubbles exposed to a single 8 µs pulse can generate large, heterogeneous pore patterns that may re-seal out-of-plane, as measured by PI cessation despite persistent evidence of cell perforation (Fig. 1). Sonoporation also affects intercellular Ca^{2+} concentrations in both sonoporated (PI+) and adjacent, yet non-treated (PI-) cells. Maximum relative Ca^{2+} concentrations in non-treated cells was found to decrease with increasing proximity from the pore site (p<0.003).

Conclusions

Local large-magnitude (~kPa), short-duration (~μs) shear stresses generated by ultrasound-stimulated microbubbles in close proximity to HUVECs induces sonoporation in a threshold-dependent manner, requiring larger shear magnitudes with increasing frequency and decreasing pulse length. Once achieved, sonoporation induces membrane perforations that repair and close via apical-to-basal membrane resealing, occurring over minutes. Further, sonoporation affects Ca^{2+} signaling in both treated and neighboring, untreated cells, suggesting its potential role as an important secondary messenger in the remote effects of intravascular sonoporation. This data contributes towards the substantiation of the merit of this approach as a viable, non-viral delivery platform by linking the salient ultrasound-triggered cavitation physics with the resulting effects of sonoporation on aspects of cellular function.

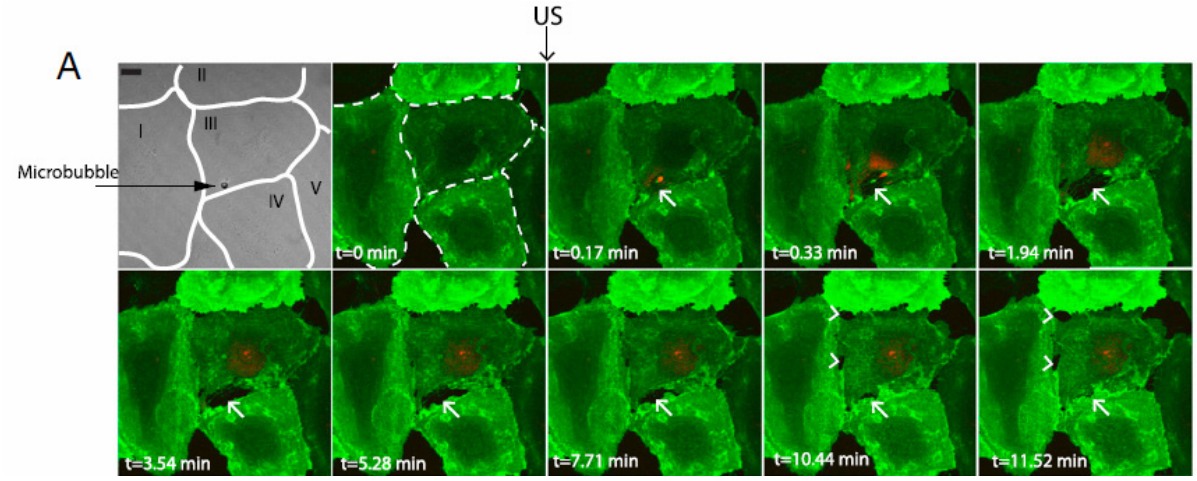

Figure 1: Bright-field image of a microbubble adjacent to a confluent endothelial cell, delineated by a white border (left panel). Subsequent panels depict images of the cell membrane, labeled green. Pre-ultrasound exposure (t=0 s), the cell membrane is uniform. After exposure (8 microseconds in duration), a membrane breach is visible (white arrow) and the entry of surrogate drug is apparent (propidium iodide – red). This pore persists for ~ 12 minutes however it reseals along its lateral surface area, as marked by a cessation in surrogate drug uptake. Gaps between otherwise confluent cells are generated (white arrowheads) < 10 minutes post-US and can last up to 30 minutes. Scale bar is 10 μm. Figure adapted from Helfield et al., PNAS, 113(36), 9983-9988, 2016.

Ultrasound mediated intracellular streaming

Valerio Pereno[a], Fabio Bianchi[b], Junjun Lei[c], Dario Carugo[c], and Eleanor Stride[a]

a Biomedical Ultrasonics, Biotherapy and Biopharmaceuticals Laboratory (BUBBL), University of Oxford.
b Tissue Engineering and Bioprocessing Group, University of Oxford
c Mechatronics and Bioengineering Science research groups, University of Southampton

Studies on the bioeffects of ultrasound and microbubbles have focused mainly on bulk tissue, individual cells, and biological membranes. Relatively little is known about the physical effects and dynamics of intracellular components. Mechanisms such as acoustic forces, cavitation, and streaming have been widely observed *in vitro* and *in vivo*, but the extent to which these phenomena affect the intracellular milieu is still an open question.

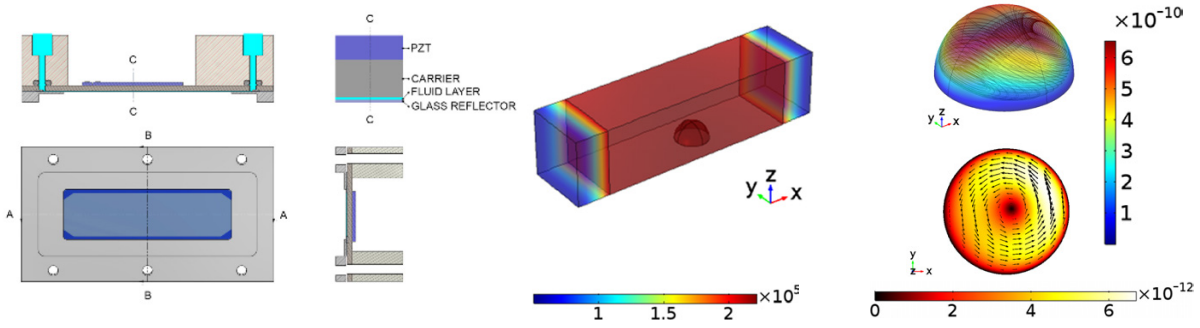

Figure 1 — *(left)* Thin-reflector resonator for exposure of giant unilamellar vesicles (GUVs) and cells to ultrasound and microbubbles*; (centre)* Colour-map of the acoustic field on fixated vesicle used in simulations. Units are expresses as Pa*; (right)* simulated fluid flow maps resulting from ultrasound exposure in fixated GUVs. Units are expressed as m/s.

The aim of this study was to observe and quantify the *intracellular* dynamics produced by exposure to ultrasound (1 MHz, 150 kPa, 60 s CW) and microbubbles (DSPC-PEG40S 9:1 molar ratio). A custom acoustofluidic chamber was designed and built to enable simultaneous ultrasound exposure and microscopic observation (Figure 1 - *left*). Particle tracking on latex flow tracers and intracellular lipid vesicles was performed by post-processing the time-series with the ImageJ® Fiji Trackmate plugin (Figure 2 - *bottom left*).

The first step consisted of modelling and numerically solving attenuation-driven streaming equations to yield flow patterns within a hemi-sphere inside a fluid channel (Figure 1 – *right*). Second, the motion of tracer beads within the lumen of giant unilamellar vesicles (GUVs), employed as cell models, was quantified experimentally (Figure 2 – *bottom*). Third, the dynamics of fluorescently labelled organelles was determined in adenocarcinomic human alveolar basal epithelial cells.

The experimental observations demonstrate the evolution of rotational internal streaming in lipid vesicles upon ultrasound exposure both with and without the presence of microbubbles. Results show significant increases in bead velocity in GUVs for increasing acoustic pressures, consistently with numerical simulations (Figure 2 – *top*). Intracellular lipid vesicles (Figure 2 – *bottom*) and mitochondrial dynamics were also quantified, with indication of altered trafficking velocity and displacement patterns in the presence of microbubbles.

Changes in flow and organelle trafficking patterns within cells have been shown to affect signaling pathways, transport phenomena, and mechanotransduction – potentially revealing previously unexplored bioeffects.

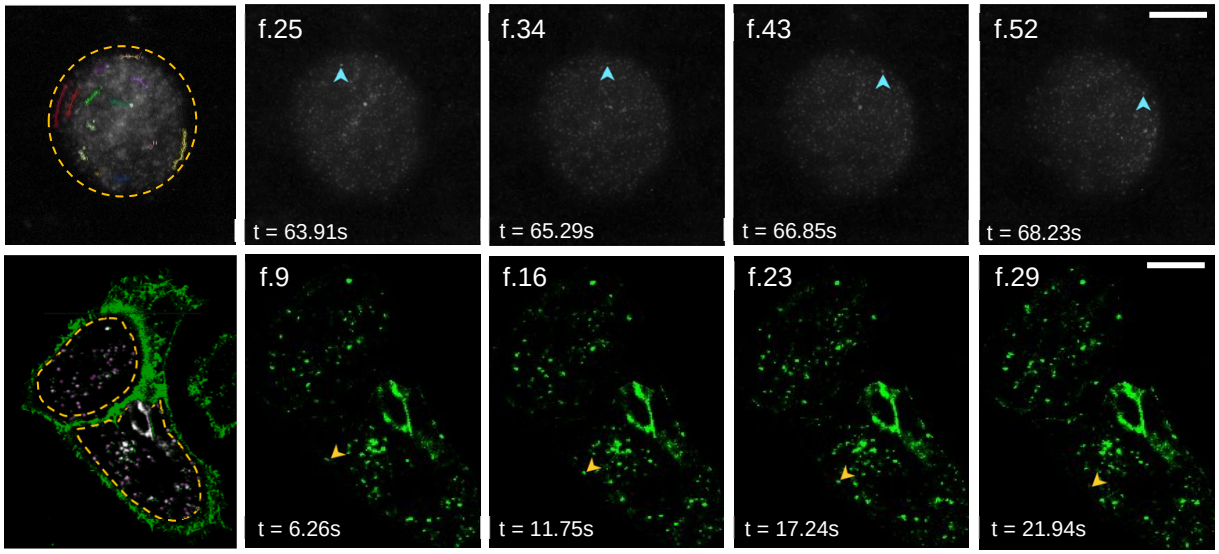

Figure 2 – *(top)* Latex beads streaming within the lumen of a GUV. Cyan chevron indicates movement of single beads in successive frames. Scale bar = 10μm. *(bottom)* Particle tracking of lipid vesicles within region of interest in the cellular lumen. Scale bar = 15μm.

High-speed Observation of Bubble-cell Interaction in an in Vivo-like Situation

Nobuki KUDO, Akane ISONO

Graduate School of Information Science and Technology, Hokkaido University
N14W9, Kita-ku, Sapporo 060-0814, Japan

Introduction

The mechanisms of sonoporation have not been fully elucidated yet; however, it is widely accepted that microbubbles oscillating adjacent to cells play an important role in the induction of membrane damage. Dynamics of microbubbles has strong dependence not only on exposure parameters of ultrasound but also on surrounding conditions of the bubbles. We previously carried out sonoporation experiments using monolayer cells cultured on scaffolds with different degree of stiffness and showed that sonoporation efficiency had strong dependence on the stiffness of the scaffold on which the cells were cultivated. In this study, high-speed observation of bubble-cell interaction was carried out to elucidate the mechanisms by which the surrounding conditions affect sonoporation efficiency.

Materials and methods

Two types of high-speed cameras, Ultranac (Nac Image Technology) and HPV-X2 (Shimadzu), were used for observations. Ultranac uses an image converter tube and can take 24 frames at a maximum framing rate of 20 Mfps, and HPV-X2 uses a CMOS burst image sensor and can take 256 frames at a maximum framing rate of 10 Mfps. A newly designed chamber was used for observation of the interaction from a lateral direction, enabling visualization of translational movements of bubbles beside a scaffold and of bubble-cell interaction without hiding the interacting point by the oscillating bubble itself.

Results and discussion

It was observed that a bubble on a soft scaffold surface moves translationally in a direction separating from the surface, whereas a bubble on a hard scaffold surface remains on the surface. Adhesion of a bubble to the top of a cell caused a considerable decrease in bubble oscillation amplitude, but membrane damage was confirmed in all of the observed cells with attached bubbles, indicating the importance of taking into account the conditions surrounding a bubble in order to understand the mechanisms of in vivo sonoporation.

Conclusion

Many studies have been carried out to understand the mechanisms of sonoporation, and it has been shown that microbubbles induce a sonoporation effect by various mechanisms. Our study indicates the importance of high-speed observations in in vivo-like situations to determine dominant mechanisms and important parameters for efficient sonoporation in vivo.

Ultrastructural modifications of cell membranes induced by sonoporation

Jean-Michel Escoffre, Aya Zeghimi, Ayache Bouakaz

Inserm UMR 930, Université François-Rabelais de Tours, Tours, France

Rationale and aim

Sonoporation is a physical method that has been successfully used to deliver drugs into living cells both *in-vitro* and *in-vivo* for experimental and therapeutic purposes [1]. Despite numerous studies on this topic, often reporting successful outcomes, very little is known about the mechanisms involved in the hypothesized membrane permeabilization processes. In this study, electron microscopy was used to investigate the ultra-structural modifications of cell membranes, induced by sonoporation [2].

Material & Methods

Glioblastoma U-87 MG cells were seeded on 18 mm diameter cover slips placed in 24 well plates. Three experimental groups were defined: (*i*) control (*i.e.*, untreated), (*ii*) US alone (*i.e.*, without MBs) and (*iii*) US+MB (*i.e.*, sonoporation). SYTOX-Green (marker of membrane permeabilization) and/or BR-14 microbubbles were added immediately before ultrasound application to give a final concentration of 1 μM SYTOX-Green and a microbubble-to-cell ratio of 5. A 1 MHz single-element focused transducer with a diameter of 15 mm and focused at 25 mm was immersed into each well of 24-well plates. Various exposure conditions were investigated by varying, either the duty cycle (10%, 20% and 40%), the acoustic intensity (0.5 - 2 W/cm^2), or the total exposure time (10 or 60 seconds) (Table 1). Both the permeabilization level and efficiency were assessed by flow cytometry, at different time points (*i.e.*, 0, 5, 10, 15, 30, 60 min) after sonoporation. The cell suspension was washed and then stained with propidium iodide in order to quantify the cell mortality.

Ultrastructural modifications of cell plasma membrane were assessed by scanning electron microscopy (SEM). The number of transient permeant structures was determined for each image (10 images/cell; N>30 cells/experimental condition).

Conditions	Intensity (W/cm²)	Duty Cycle (%)	Exposure time (s)	Microbubbles
A	-	-	-	-
B	1	20	60	-
C	0.5	20	60	+
D	1	20	60	+
E	1	20	10	+
F	1	10	60	+
G	2	50	60	+

Table 1. Experimental groups and applied ultrasound settings.

Results

To directly monitor membrane modifications induced by sonoporation, U-87 MG cells were exposed to different US conditions (Table 1) in the presence of SYTOX-Green, either with (Condition A, C-G)

or without BR14 microbubbles (Condition B). The US exposure of cells in the absence of MBs (Condition B) was characterized by 28 ± 1% of permeabilized cells as compared to 59 ± 2% cells ($p < 0.05$) for US combined with MBs (Condition D, Fig. 1A). Significantly, sonoporation exhibited a 8-fold increase in cell permeabilization efficiency compared to US alone ($p < 0.001$) (Fig. 1B).

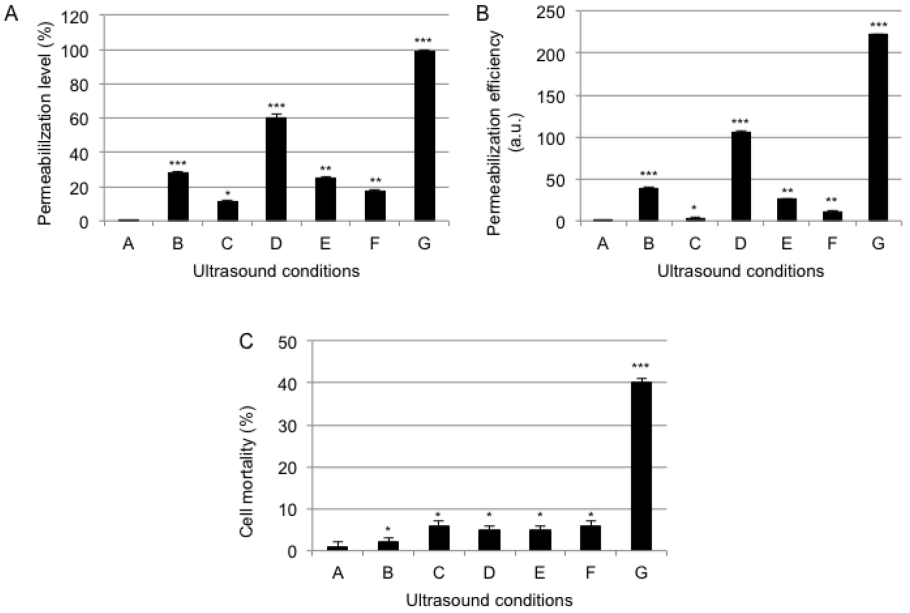

Figure 1: Effect of sonoporation using various ultrasound excitation parameters on the cell permeabilization and viability.

Under these acoustic parameters, the presence of MBs significantly affected the cell viability ($p < 0.05$) (Fig. 1C). In addition, the ultrasound conditions C, E and F were less efficient to permeabilize cells compared to the condition D (Fig. 1). Under the US condition G, the permeabilization level and efficiency were significantly increased compared to the condition D ($p < 0.05$). However, this condition dramatically increased the cell mortality ($p < 0.05$). Altogether, these results suggested that the acoustic parameters of the condition D were the most appropriate to get a high percentage of permeabilized and viable cells.

To visualize ultra-structural modification of cell membranes induced by sonoporation, cells were immediately fixed after sonoporation and analyzed using electron microscopy. SEM images of control (untreated) U-87 MG cells (Fig. 2A, Condition A) were characterized by a smooth surface with sparse distribution of microvilli. Compared to US alone condition (Fig. 2A, Condition B), the combination of US+MB induce the formation of dark and spherically-shaped structures in addition to scattered patches that were randomly distributed across cell membranes (Fig. 3A, Conditions C-G), suggesting a direct involvement of sonoporation in the creation of these structures.

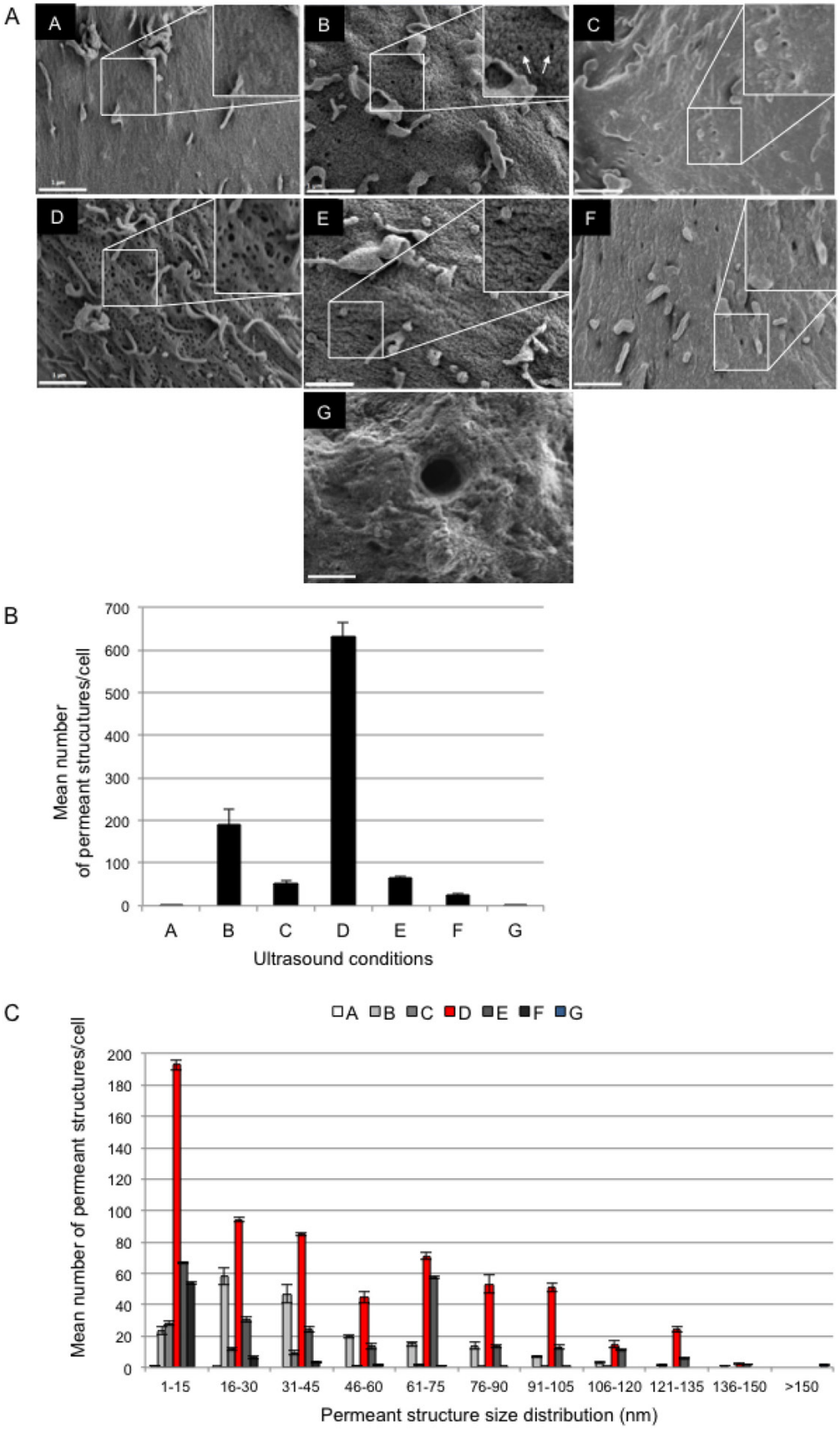

Figure 2. Ultra-structural modifications of U-87 MG cell membranes after sonoporation.

Apart from condition G, one can notice that the high permeabilization level and efficiency shown in Fig. 1B were positively associated to a high mean number of observed structures per cell (Fig. 2B).

For this reason, these structures are hereafter termed *permeant structures*. The size distribution of the observed structures was heterogeneous with a diameter ranging from a few nanometers up to 150 nm (Fig. 2C), irrespective of the US conditions tested in this study. Under the US condition G, the mean number of *permeant structures* per cells was low but the size of these structures (0.5 – 4 μm) was much higher than those induced in other US conditions (Fig. 2C). The formation of such micro-sized structures are associated with loss of cell viability as confirmed by the quantification of cell viability displayed in Fig. 1C. It was noticeable that the count of the *permeant structures* was significantly higher for sonoporation in the presence of MBs as compared to US alone ($p<0.001$; Fig. 1B).

Conclusions

In summary, microbubble-assisted US treatment led to a higher number of *permeant structures* and increased cell permeabilization level compared with US treatment alone, thus suggesting that MBs potentiated the US-mediated membrane permeabilization.

Acknowledgement

This work was supported by grants from Inserm and the European Commission FP7 Program SONODRUGS (NMP4-LA-2008-213706). The authors thank Bracco Research Geneva for supplying the microbubbles.

References

1. *Escoffre JM, Bouakaz A (Eds) Therapeutic ultrasound. Advances in Experimental Medicine and Biology, Vol 880, Springer International Publishing Switzerland 2016.*
2. *Zeghimi A, Escoffre JM, Bouakaz A (2015) Role of endocytosis in sonoporation-mediated membrane permeabilization and uptake of small molecules: a electron microscopy study. Phys. Biol., 12:066007.*

Ultrasound-mediated trans-membrane drug delivery into a monolayer of endothelial cells during high flow in vitro conditions

Syed Mohd Nooh, Rob Krams, James J. Choi

Department of Bioengineering, Imperial College London, London, UK

Background and Objectives

The treatment of atherosclerosis and other cardiovascular disease is constrained by the inability to deliver therapeutic drug across the cell membrane effectively and safely. Entire classes of drugs, such as genetic medicines (e.g., siRNA, mRNA, gene therapy), are made ineffective, because they cannot enter the cell at safe systemic doses that do not cause side effects throughout the body [1]. Over the last several decades, ultrasound-mediated trans-membrane drug delivery methods (e.g. sonoporation) have been studied in vitro to deliver drugs into cells. Through these studies, it was discovered that several mechanisms of trans-membrane drug delivery exist and that they are highly dependent on the acoustic parameters, microbubble conditions, and the cell-type used [2]. Despite promising results from these study, the advancement from single cell-bubble interactions to clinical use has not been made. This gap in development is largely because the underlying mechanism of trans-membrane drug delivery under high flow condition and for a large population of cells, remains poorly understood and poorly controlled. Our study explores the trans-membrane drug delivery efficacy of a monolayer of endothelial cells using a state-of-the-art physiologically-relevant cultivation system under different ultrasound exposure conditions and evaluate the critical question on whether safe trans-membrane drug delivery can be achieved in such a complex, physiologically relevant environment.

Methods

Human umbilical vein endothelial cells (HUVEC) were selected as our model cells since they are well described due to their extensive use in vascular biology and are similar to the arterial endothelial cells we'd like to treat in future studies (e.g., in Atherosclerosis). They were cultured as a monolayer in a flow chamber under static or pulsatile shear stress (10 dyne/cm2) and at 37°C for 3 days. A focused ultrasound transducer (0.5 MHz) sonicated the flow chamber in the presence of lipid-shelled microbubbles and during flow conditions (fluid flow rate: 17 ml/min). A centrally-inserted transducer (7.5 MHz) was used to determine the type of microbubble activity generated by passively detecting cavitation emissions during sonication [3]. After sonication, trans-membrane delivery was assessed by quantifying the intracellular uptake of propidium iodide (PI), which is a DNA-binding fluorescent dye that is normally impermeable to the cell membrane. Cell viability was assessed by Calcein-AM. A range of ultrasound parameters (pressure, pulse length and exposure duration) and microbubbles conditions were systematically evaluated to identify different trans-membrane delivery and safety profiles.

Results

The main finding of our study is that safe trans-membrane drug delivery can be produced in a clinically targetable cell type (i.e., endothelial cells) under physiologically relevant conditions (i.e.,

high fluid velocities) (Fig. 1d). This safe delivery is indicated by cells where red propidium iodide is co-localised with green calcein. A range of ultrasound parameters was explored and we were able to characterise the undergoing acoustic cavitation according to specific bio-effects: cell viability with and without transmembrane delivery, cell death and cell detachment. Trans-membrane delivery increased and cell viability decreased with pressure ranging from 50 kPa to 150 kPa, at pulse length of 500 and 1000 cycles and in the presence of microbubbles (Fig. 2). It was seen that at the highest pressure and pulse length evaluated, transmembrane delivery occurred in 9.68% ± 10.96% of cells while only 13.18 ± 7.33% maintained cell viability. At the lowest acoustic pressure and pulse length evaluated, trans-membrane delivery occurred in 1.12% ± 1.35% of cells while cell viability was 92.45% ± 9.04%.

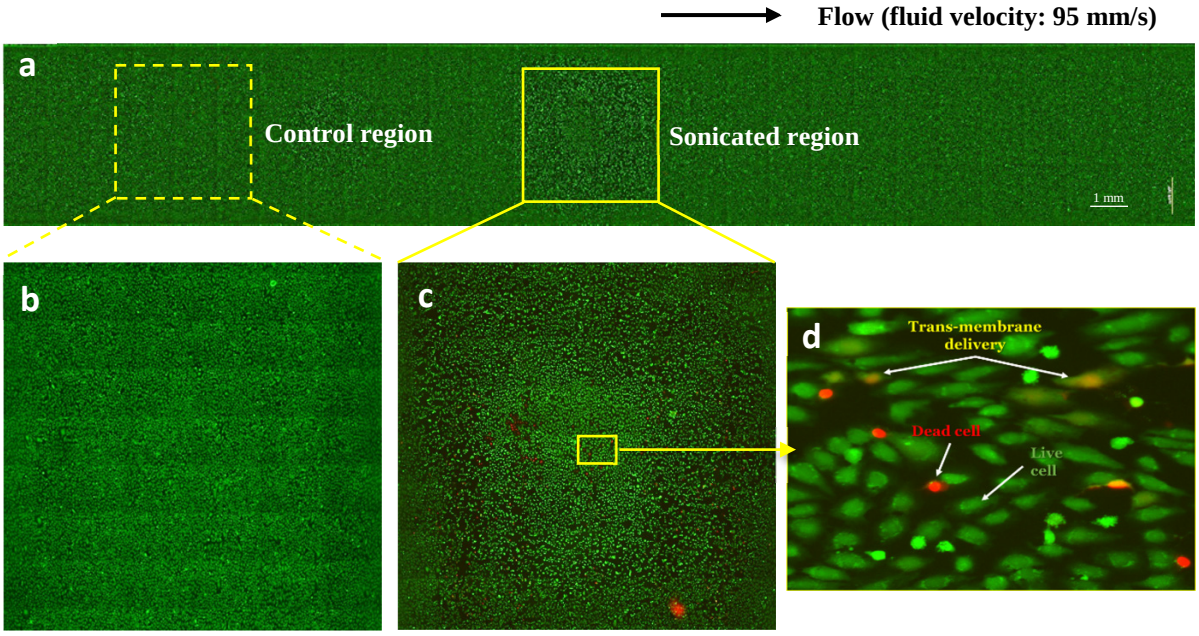

Fig.1. Trans-membrane drug delivery under flow conditions. Human umbilical vein endothelial cell (HUVEC) were stained for cell viability by calcein-AM (green cells) and transmembrane delivery by internalization of propidium iodide (red cells). (a) Microbubbles were made to flow (fluid velocity: 95 mm/s) through a collagen-treated flow chamber with a channel height of 600 µm and a volume of 150 µL. (b) The central chamber region was sonicated (solid rectangle), while (c) other region (dotted rectangle) acted as non-sonicated control region. (d) Zoomed in view at delivery region; a population of cell that exhibited a mixture of viable cells (green cell) with and without trans-membrane delivery and dead cell (red cell).

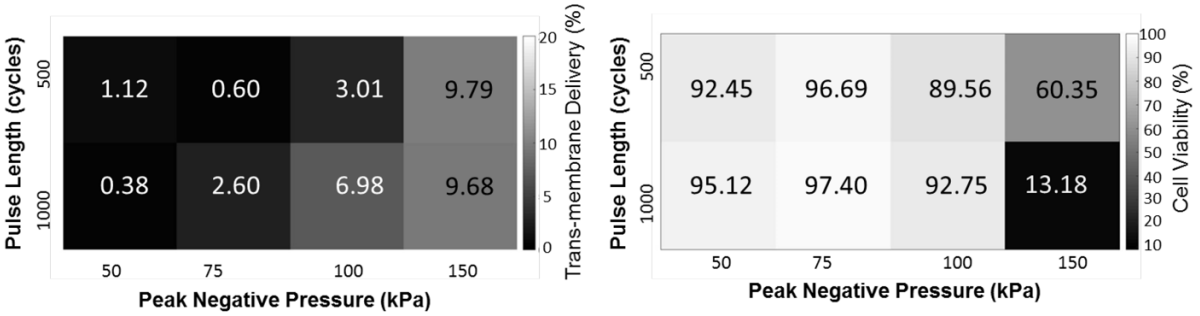

Fig.2 The effect of acoustic pressure and pulse duration on (a) Trans-membrane delivery and (b) cell viability. The percentages of trans-membrane delivery and cell viability are shown with respect to pressure at 50, 75, 100 and 150 kPa with pulse length of 500 and 1000 cycles. Exposure condition: fc=0.5 MHz, PRF=1.4 Hz, Np =500 with microbubbles at 1X clinical dose. The results shown represents the mean for at least three independent measurement.

Conclusion

This study demonstrated that safe trans-membrane drug delivery can be produced in a clinically targetable cell type (i.e., endothelial cells) and under physiologically relevant conditions (i.e., high shear stress condition). However, the trans-membrane delivery efficiency was low. This implies that there is a specific microbubble dynamic within the exposed tissue volume that can produce the desired bio-effect. In future works we will identify this specific dynamic and develop technologies to control it so that we can maximise safe drug delivery in treating atherosclerosis.

Reference

1. *E. Unger, T. Porter, J. Lindner, and P. Grayburn, "Cardiovascular drug delivery with ultrasound and microbubbles.," Adv. Drug Deliv. Rev., vol. 72, pp. 110–26, Jun. 2014.*
2. *K. Kooiman, H. J. Vos, M. Versluis, and N. De Jong, "Acoustic behavior of microbubbles and implications for drug delivery," Adv. Drug Deliv. Rev., vol. 72, pp. 28–48, 2014.*
3. *F. E. Shamout, A. N. Pouliopoulos, P. Lee, S. Bonaccorsi, L. Towhidi, R. Krams, and J. J. Choi, "Enhancement of Non-invasive Trans-membrane Drug Delivery Using Ultrasound and Microbubbles during Physiologically Relevant Flow," Ultrasound Med. Biol., vol. 41, no. 9, pp. 2435–2448, 2015.*

Red Blood Cell interaction with Microbubbles and Nanodroplets: Design of a triggered Drug Delivery Vehicle

Johnny L. Chen, Ali H. Dhanaliwala, Adam J. Dixon, Justin M. Farry, John A. Hossack, Alexander L. Klibanov

Traditionally, a combination of microbubbles and ultrasound is applied for the enhancement of delivery of external drugs (including coding and noncoding nucleic acids) into the target cells. However, an alternative task, i.e., triggered release of cell-entrapped material, may also be of interest, in a specific set of circumstances: red blood cells (RBCs) applied as a drug carrier system, where the sequestered drug should be released from RBC carrier at the specified (insonated) sites for therapeutic intervention at the desired location and time. In prior drug delivery studies, drug-loaded microbubbles were administered in combination with ultrasound [1,2,3]. Given the limitations of microbubbles as therapeutic delivery vehicles, i.e., small payload and short half-life, RBCs may become a useful alternative.

RBCs have been investigated as drug delivery vehicles for several decades. Drug entrapment strategies have been proposed, including hypo-osmotic loading [4]; targeting strategies have been investigated, including molecular targeting via antibodies attached onto the RBC surface [5], or via magnetic nanoparticles, so that RBCs would accumulate in the target tissue subjected to magnet action [6]. Recently, a CE-mark has been obtained by a cartridge-based bench-top apparatus, which loads drugs into patient's RBCs [7]. Drug-carrying RBCs, reinjected in patient's bloodstream, become a drug delivery vehicle with a circulation time of many days. However, on-demand triggered release of loaded RBC contents has been lacking. The only available example is the use of laser light in conjunction with photodegradation of the modified RBC membrane [8], but light activation does not offer good focusing or penetration depth in a clinical setting. A formulation of acoustically active RBCs (aaRBCs) may provide an ideal drug delivery system – an inherently biocompatible drug carrier, for which drug release triggered on-demand, via the interaction of ultrasound with an RBC-associated microbubble.

We have entrapped microbubbles and perfluorocarbon nanodroplets inside RBCs by an osmotic loading procedure. Upon reduction of osmotic pressure in the media, pores open up in the RBC membrane, so the drug molecules or model fluorescent dyes can enter the cells. If osmotic shock is severe, pores are large, and even micrometer-size particles, such as bubbles, could enter. Subsequent increase of osmotic pressure reseals the RBC membrane. Thus, the particles and dye/drug remain sequestered inside (which is confirmed by video microscopy). We have demonstrated ultrasound-triggered rupture and dye contents release from aaRBCs by action of ultrasound; in the absence of entrapped bubbles, dye release from "regular" RBC ghosts was minimal. However, the loading efficacy for microbubbles into RBCs is not high, and severity of the osmotic shock needed to load micrometer-size bubbles makes resulting aaRBCs less biocompatible (it lowers circulation lifetime, due to membrane reversal and phosphatidylserine exposure). Therefore, an optimized approach was developed: first, mild osmotic shock applied to RBCs to create small transient pores through which a fluorescent dye, or a drug, could enter by diffusion. The RBCs were then brought to isotonic buffer and resealed, retaining the entrapped contents. Excellent dye retention stability was demonstrated: over 90% of the entrapped calcein dye was retained within RBCs for 24 hours. To make loaded RBCs acoustically active, perfluorocarbon nanodroplets were then attached to the external surface of RBCs, for acoustic triggering.

It is already known that drug carrier nanoparticles attached to the RBCs externally do not drastically alter RBC circulation pattern, and such RBC-nanoparticle complexes may stay in the bloodstream much longer than the nanoparticles by themselves [9]. We have prepared nanodroplets (with a positively charged lipid shell, and perfluoropentane or perfluorobutane gas core, and a mean diameter ~200 nm). Nanoparticle shell has been labeled with DiI dye when it was necessary to monitor nanodroplet presence on the RBC membrane by microscopy. These particles have been adhered to RBC membrane by electrostatic interaction, and retained on cell surface. Upon the action of ultrasound, nanodroplet conversion to microbubbles and resulting microbubble/ultrasound/RBC interaction resulted in an immediate lysis of RBC and contents release. In a fluorescence video microscopy experiment, we have observed that a single ultrasound pulse (10 MHz, 11 MPa peak pressure) results in a complete release of calcein dye from the nanodroplet-carrying aaRBC, within a fraction of a second. Unlike other cell types, if a hole is created in RBC membrane, it is unable to reseal, and lysis results. A single nanodroplet is sufficient to trigger aaRBC contents release. In a bulk fluorescence quantification study, insonation allowed release of >50% of entrapped fluorescent marker from RBCs, both for perfluoropentane and perfluorobutane nanodroplets. Radiolabeled aaRBCs carrying 51-Cr radioisotope remained in the bloodstream for 2 hours (with ~90% of the administered dose present in circulation). ICG, a dye for infrared fluorescence and photoacoustic imaging, was entrapped and retained inside RBCs by the mild osmotic loading method. We were able to demonstrate that aaRBCs loaded with ICG can be imaged photoacoustically, opening the potential for new ways to monitor drug release in vivo.

Overall, aaRBCs, triggered by ultrasound, may provide the optimal choice of a biocompatible drug delivery system, with excellent payload volume, extended circulation time, with the efficient and rapid release of sequestered drugs in the insonated areas of the body.

References

1. *Lentacker I, Geers B, Demeester J, De Smedt SC, Sanders NN. Design and evaluation of doxorubicin-containing microbubbles for ultrasound-triggered doxorubicin delivery: cytotoxicity and mechanisms involved. Mol Ther. 2010;18(1):101-108*
2. *Klibanov AL, Shevchenko TI, Raju BI, Seip R, Chin CT. Ultrasound-triggered release of materials entrapped in microbubble-liposome constructs: a tool for targeted drug delivery. J Control Release. 2010;148(1):13-17.*
3. *Geers B, De Wever O, Demeester J, Bracke M, De Smedt SC, Lentacker I. Targeted liposome-loaded microbubbles for cell-specific ultrasound-triggered drug delivery. Small. 2013;9(23):4027-4035*
4. *Sprandel U, Zöllner N. Osmotic fragility of drug carrier erythrocytes. Res Exp Med (Berl). 1985;185(1):77-85.*
5. *Smirnov VN, Domogatsky SP, Dolgov VV, Hvatov VB, Klibanov AL, Koteliansky VE, Muzykantov VR, Repin VS, Samokhin GP, Shekhonin BV, et al. Carrier-directed targeting of liposomes and erythrocytes to denuded areas of vessel wall. Proc Natl Acad Sci U S A. 1986;83(17):6603-6607*
6. *Orekhov AN, Belyaev AA, Orekhova NM, Smirnov MD, Samokhin GP, Ragimov SE, Akchurin RS, Smirnov VN. Prevention of experimental carotid artery thrombosis by magnetic vectoring of aspirin. Lancet. 1987;2(8558):564-565.*
7. *Biagiotti S, Paoletti MF, Fraternale A, Rossi L, Magnani M. Drug delivery by red blood cells. IUBMB Life. 2011;63(8):621-631.*
8. *Wang C, Sun X, Cheng L, Yin S, Yang G, Li Y, Liu Z. Multifunctional theranostic red blood cells for magnetic-field-enhanced in vivo combination therapy of cancer. Adv Mater. 2014 26(28):4794-4802.*
9. *Anselmo AC, Gupta V, Zern BJ, Pan D, Zakrewsky M, Muzykantov V, Mitragotri S. Delivering nanoparticles to lungs while avoiding liver and spleen through adsorption on red blood cells. ACS Nano. 2013;7(12):11129-11137.*

The 22nd European Symposium on Ultrasound Contrast Imaging Rotterdam is sponsored by:

Bracco Suisse SA
Marco Graf, Senior
Communication Events Manager
Centro Galleria 2
Via Cantonale
CH-6928 Manno - Switzerland

GE Healthcare
Marta Gonzalez de Suso
Global Product Manager
Ultrasound Contrast Media
Life Sciences-Core Imaging
The Grove Centre, White Lion
Road, Amersham, HP7 9LL UK

Siemens Healthcare Ltd
Richard Medley
Product Manager
Ultrasound-EMEA
Sir William Siemens Square
Newton House, Frimley,
Camberley, SY GU16 8QD – UK

Philips Healthcare
John MacQuarrie
Senior Product Manager - Ultrasound
Philips Healthcare
22100 Bothell Everett Highway
Bothell, WA 98021 U.S.A.

Samsung Electronics Benelux
Luc van Dalen, Business
Development Manager
Health Medical Equipment
Evert van de Beekstraat 310
1118 CX Schiphol – Neth.

Visualsonics
Adrie Gubbels
Joop Geesinkweg 140
1114 AB Amsterdam
The Netherlands

Oldelft Ultrasound
Stefan Roggeveen
Commercial Manager
Elektronicaweg 10
2628 XG Delft
The Netherlands

Toshiba Medical Systems Europe BV
Jan de Bruijn
Marketing Communications
Zilverstraat 1
2718 RP Zoetermeer
The Netherlands

Lamepro BV
Marjan Rolffs
Business Support
Burgemeester Guljélaan 2
4837 CZ Breda
The Netherlands

Nederlandse Hartstichting
Mrs. E. Buitenhuis
Manager Research Dept.
P.O. Box 300
2501 CH Den Haag
The Netherlands

Coeur
Eric Boersma
Erasmus MC - Thoraxcenter
Dr. Molewaterplein 50
3015 GE Rotterdam
The Netherlands

Mindray Medical Germany GmbH
Hongbo Zhu
Marketing Ultrasound Europe
Goebelstrasse 21
64293 Darmstadt
Germany

Hitachi Medical Systems
Mrs. E. Bibby
European Marketing
Sumpfstrasse 24
6300 Zug
Switzerland

FIRST ANNOUNCEMENT 2018

23rd EUROPEAN SYMPOSIUM ON ULTRASOUND CONTRAST IMAGING

18-19 JANUARY 2018

ROTTERDAM, THE NETHERLANDS

Information on the 23rd **EUROPEAN SYMPOSIUM ON ULTRASOUND CONTRAST IMAGING: Mieke Pruijsten, m.pruijsten@erasmusmc.nl**

sponsors:

Golden sponsor

BRACCO
LIFE FROM INSIDE

GE Healthcare

PHILIPS

SIEMENS
Healthineers

SPONSOR

Silver sponsor

TOSHIBA
MEDICAL

LAMEPRO

SPONSOR

Oldelft
Ultrasound

mindray
healthcare within reach

SAMSUNG

HITACHI
Inspire the Next

VISUALSONICS

FUJIFILM